



## AN ABSTRACT OF THE DISSERTATION OF

Elena A. Medina for the degree of Doctor of Philosophy in Chemistry presented on February 23, 2017.

Title: The Role of Materials Chemistry in Designing Advanced Color Inorganic Pigments.

Abstract approved:

---

Munirpallam A. Subramanian

The results of the research presented in this work are related to synthesis and investigations of novel color inorganic pigments having various structures and shades. Inorganic pigments play a major role in contemporary life. They are used in paints, rubber, plastic, cosmetics etc. Searching for new, stable, environmentally benign and cheap pigments is an important task of materials science.

Several classes of colored inorganic oxides have been prepared and studied using various methods and techniques including powder X-ray (XRD) and neutron diffraction, color characterization ( $L^*a^*b^*$  parameters), optical (UV-VIS diffuse reflectance and near-IR (NIR) reflectance), magnetic and dielectric properties measurements, infrared (IR) spectroscopy.

Pigments  $A_5M'_{3-x}M_xO_{12}X$  ( $A = \text{Sr, Ba}$ ;  $M' = \text{Cr, Mn}$ ;  $M = \text{V, P}$ ;  $X = \text{F, Cl}$ ) with apatite-type structure were prepared using standard solid state, sol-gel and microwave synthesis methods. All samples have bright colors varying from white ( $x = 3.0$ ) through turquoise ( $x = 1.5$ ) to dark green ( $x = 0$ ). The color arises due to a combination of d-d interatomic transitions of  $\text{Mn}^{5+}/\text{Cr}^{5+}$  cations and transition metal- $\text{O}^{2-}$  charge transfer.  $\text{Mn}^{5+}$ ,  $\text{V}^{5+}$  and  $\text{P}^{5+}$  occupy the tetrahedral sites in the structure as shown by Rietveld structure refinement of neutron data.

Hibonite – type colored oxides with a general formula of  $AAl_{12-x}M_xO_{19}$  ( $A = \text{Ca, Sr, RE}$  (rare earths) or any combination thereof;  $M = \text{Ni, Fe, Mn, Cr, Cu}$  coupled with one of the following: Ga, In, Ti, Sn, Ge, Nb, Ta, Sb) were synthesized through A-site and M-site substitutions. Ni, Fe, Mn, Cr and Cu are chromophore ions and they are responsible for the color of the compounds.  $\text{Ni}^{2+}$  gives bright sky-blue to royal-blue colors; samples containing different amounts of Fe, Mn, Cr or Cu have diverse colors: ivory, brown, creamy, tan, pink, light turquoise and green.  $\text{Ni}^{2+}$ ,  $\text{Mn}^{2+}$  and  $\text{Fe}^{3+}$  prefer to occupy the tetrahedral site,  $\text{Mn}^{3+}$  has a preference for both tetrahedral and octahedral sites,  $\text{Ti}^{4+}$  and  $\text{Sn}^{4+}$  for octahedral site in the hibonite structure.

Compounds belong to  $\text{Li}_2\text{Mn}_{1-x}\text{Ti}_x\text{O}_3$  ( $x = 0\text{--}1.0$ ) series show bright orange colors varying from dark brick red ( $x = 0$ ) to orange ( $x = 0.5$ ) and light orange ( $x = 0.8$ ). d-d transitions of d electrons of octahedral  $\text{Mn}^{4+}$  and  $M(\text{IV})\text{--O}^{2-}$  charge transfer are responsible for the colors.

Pigments with sillenite-type structure,  $\text{Bi}_{12-x}\text{In}_x\text{TiO}_{20}$  ( $x = 0\text{--}1.5$ ),  $\text{Bi}_{12-x}\text{In}_x\text{Mn}_{0.2}\text{Ti}_{0.8}\text{O}_{20}$  ( $x = 0\text{--}5.5$ ) and  $\text{Bi}_{12}\text{Mn}_{1-x}M_x\text{O}_{20}$  ( $M = \text{Ti, Si, Ge}$ ), were prepared using standard solid state synthesis through Bi-site and M-site substitutions.  $\text{Bi}_{12-x}\text{In}_x\text{TiO}_{20}$  compounds have shades changing from light yellow ( $x = 0$ ) to beige ( $x = 1.5$ );  $\text{Bi}_{12-x}\text{In}_x\text{Mn}_{0.2}\text{Ti}_{0.8}\text{O}_{20}$  series: from forest green ( $x = 0$ ) to dark sea green ( $x = 2.5$ ) and light olive drab ( $x = 5.5$ );  $\text{Bi}_{12}\text{Mn}_{1-x}M_x\text{O}_{20}$  ( $M = \text{Ti, Si, Ge}$ ): from dark green ( $x = 0$ ) to forest green ( $x = 0.5$ ) and lawn green ( $x = 0.8$ );  $\text{Bi}_{12}M\text{O}_{20}$  ( $M = \text{Ti, Si, Ge}$ ) are light yellow.  $\text{Mn}^{4+}$  ( $T_d$ ) is a chromophore element of the solid solutions, samples become lighter when amount of manganese decreases.  $\text{Bi}_{12}\text{Mn}_{1-x}\text{Ti}_x\text{O}_{20}$  ( $x = 0.2; 0.6; 0.8$ ) phases show paramagnetic behavior in the measured temperature region (5–300 K).

All synthesized samples have relatively high reflectance in the near-IR region (700–2500 nm) and are promising candidates for “Cool pigments” applications.

©Copyright by Elena A. Medina  
February 23, 2017  
All Rights Reserved



The Role of Materials Chemistry in Designing Advanced Color Inorganic Pigments

by  
Elena A. Medina

A DISSERTATION

submitted to

Oregon State University

in partial fulfillment of  
the requirements for the  
degree of

Doctor of Philosophy

Presented February 23, 2017  
Commencement June 2017

Doctor of Philosophy dissertation of Elena A. Medina presented on February 23, 2017

APPROVED:

---

Major Professor, representing Chemistry

---

Chair of the Department of Chemistry

---

Dean of the Graduate School

I understand that my dissertation will become part of the permanent collection of Oregon State University libraries. My signature below authorizes release of my dissertation to any reader upon request.

---

Elena A. Medina, Author

## ACKNOWLEDGEMENTS

It has been an interesting, productive, sometimes difficult way filled with unexpected results, challenging tasks and great people.

I thank my research advisor Dr. Mas Subramanian for guidance, assistance during my years at OSU and for teaching me so much about solid state chemistry and my favorite pigments. His lab equipment and supplies have helped me to learn essential methods and techniques required to be professional materials chemistry researcher. The acquired knowledge will help me in my future career and life.

I express sincere appreciation to Dr. Jun Li, she has helped me a lot and taught how to perform structural refinements, how to find a hidden nature of chemical phenomena and how to write scientific papers. She is a talented crystallographer!

I appreciate Dr. David Cann, Dr. David Xiulei Ji, Dr. Michael Lerner and Dr. Sandra Loesgen for serving as my graduate committee members.

I would like to thank all faculty and staff of chemistry department, especially Margie Haak, Dr. Michael Burand, Jenna Moser, Greg Jones and Todd Stuhr, for making the department a perfect place to study and grow up as a scientist, mentor and teacher.

I would like to express my gratitude to all past and present Dr. Subramanian's research group members: Dr. Geneva Laurita, Dr. Whitney Schmidt, Dr. Rosa Grajczyk, Dr. Sandya Kumari, Sarah Synnestvedt, Stephanie Kay Ramos, Josh Flynn, Bella Giampaoli, Joseph Tang, Max Wallace, Brett Duell, Paradron Lektrakootara (Junior) and Elizabeth Sobalvarro. I am thankful for the nice working atmosphere and plenty of fruitful discussions. Special thanks to my very good friends and amazing ladies SongYi Kim, Swagata Dey and Arreerat Jiamprasertboon (Pui).

I am very thankful for my chemistry department friends: Omid Sadeghihosseinabadi, Ryan McQuade and Lauren Fullmer McQuade, Juan Carlos Ramos, Sara Goberna Ferron and Vicent Lopez Ballester, Alicia Manjon Sanz and Juan Carlos Lopez, Nadeeshani

Jayathilake (Nadee) and Chandima Bandara, Cem Celik, Hanyang Zhang. I appreciate friendship and encouragements, useful advices and fun time, which we spent together.

I am grateful to my best friend in Corvallis Deok-Hie Park. She has been at my side from our first day at OSU, I really appreciate all her help, time and support. She is the kindest person and the smartest student I've ever met. I wish her good luck in the life!

I thank my dearest friend Катя Перемыслова for constant willingness to help and share her knowledge, kindness and optimism; my "American parents" Света and Анатолий Ерофеевы and their son Владислав for vacations in Ashland and Sunriver, for our unforgettable rehearsals of Russian plays and traditional bathing in the ocean on December 31st. Thank you for accepted me as a family member!

It has been an interesting opportunity to participate in three plays of Corvallis Russian theater troupe; and I would like to appreciate our best director Vreneli Farber.

I would like to acknowledge all my friends in Corvallis and in Russia: Ваня Марченко and Вероника Vasylykivska, Oleh and Olena Taratula, Нана and Миша Яцкины, Валера Перемыслов, Марина Перемыслова and Андрей Кох, Андрей Жмогинов, Миша Яцков, Аня Кельберт, Регина Курапова, Женя Ротт, Паша and Наташа Корнилович, Галя Романцова and Паша Мордилович, Яна Исайчикова, семья Говядиновых, семья Бузденковых, Катя Круглова and Алена Самылина. I would not be able to finish this journey without their generous support.

I would like to express my sincerest gratitude to my dearest parents Марина and Саша, my sister Катя and her husband Илья. Thank you for your patience and endless faith in me. Without our daily conversations I wouldn't survive; although we have been separated by thousands of miles, you always have been on my side. All my achievements wouldn't not be reality without you. I don't take your love for granted...

Finally, I want to thank my first high school chemistry teacher Громова Тамара Борисовна, after her classes I fell in love with chemistry and decided to choose it as my major.

## CONTRIBUTION OF AUTHORS

Chapter 3: Dr. Jun Li contributed in the review of the paper manuscript on which the chapter is based: Medina, E.A., Li, J., Stalick, J.K., Subramanian, M.A. Intense turquoise colors of apatite-type compounds with  $\text{Mn}^{5+}$  in tetrahedral coordination *Solid State Sciences* 2016, 52, 97-105. Judith Stalick collected neutron data of the samples at NIST (National Institute of Standards and Technology).

Chapter 4 and Chapter 5: Dr. Mas Subramanian and Dr. Arthur Sleight contributed in the discussions, preparation and review of the two manuscripts on which these chapters are based: Li, J., Medina, E.A., Stalick, J.K., Sleight, A.W., Subramanian, M.A. Structural studies of  $\text{CaAl}_{12}\text{O}_{19}$ ,  $\text{SrAl}_{12}\text{O}_{19}$ ,  $\text{La}_{2/3+\delta}\text{Al}_{12-\delta}\text{O}_{19}$ , and  $\text{CaAl}_{10}\text{NiTiO}_{19}$  with the hibonite structure; indications of an unusual type of ferroelectricity *Zeitschrift fur Naturforschung Section B-A Journal of Chemical Sciences* 2016, 71(5), 475-484 and Li, J., Medina, E.A., Stalick, J.K., Sleight A.W., Subramanian, M.A. Colored oxides with hibonite structure: A potential route to non-cobalt blue pigments *Progress in Solid State Chemistry* 2016, 44, 107-122. Dr. Jun Li contributed in the manuscripts preparation, data analysis and neutron data refinement. Judith Stalick collected neutron data of the samples at NIST.

Chapter 6: Dr. Jun Li assisted in the data analysis and review of the manuscript on which the chapter is based: Medina, E.A., Li, J., Stalick, J.K., Subramanian, M.A. Colored oxides with hibonite structure II: Structural and optical properties of  $\text{CaAl}_{12}\text{O}_{19}$ -based pigments with Fe, Mn, Cr and Cu as chromophores *Progress in Solid State Chemistry* 2017 (submitted). Judith Stalick collected neutron data of the samples at NIST.

Chapter 7 and 8: Dr. Jun Li contributed in the discussions of the manuscript.

Chapter 8: Dr. Art Ramirez (UC Santa Cruz) assisted in magnetic data collection using MPMS (magnetic property measurement system).

## TABLE OF CONTENTS

	<u>Page</u>
1 Introduction.....	1
1.1 Transition Metal Oxides.....	1
1.2 Structure of Crystalline Compounds.....	3
1.3 Bonding in Solids.....	7
1.4 Color in Solids.....	9
1.5 Inorganic Pigments.....	16
1.6 References .....	19
2 Materials Synthesis, Properties and Characterization Methods.....	22
2.1 Synthesis .....	22
2.1.1 Solid State Synthesis .....	22
2.1.2 Sol-Gel (Pechini Method) or Low Temperature Synthesis Route.....	23
2.1.3 Microwave Method .....	24
2.2 Powder X-ray Diffraction (XRD) .....	24
2.3 Powder Neutron Diffraction.....	27
2.4 Optical Properties.....	28
2.4.1 Diffuse Reflectance Spectroscopy.....	29
2.4.2 Near-infrared (NIR) Reflectance .....	29
2.4.3 $L^*a^*b^*$ Color Space .....	30
2.5 Magnetism.....	31
2.6 Dielectric Properties Measurements .....	34
2.7 Infrared (IR) Spectroscopy.....	36
2.8 References .....	37

## TABLE OF CONTENTS (Continued)

	<u>Page</u>
3 Pigments with Apatite-type Structure.....	39
Abstract .....	39
3.1 Introduction .....	41
3.2 Results and Discussion.....	44
3.2.1 Crystal Structures by X-ray and Neutron diffraction .....	44
3.2.2 Optical Properties .....	59
3.2.3 IR Investigation .....	65
3.2.4 Magnetic Properties.....	66
3.3 Conclusion.....	68
3.4 Experimental Materials and Methods .....	68
3.5 Acknowledgements .....	70
3.6 References .....	70
4 Hibonite-type Compounds: Structural Studies .....	74
Abstract .....	74
4.1 Introduction .....	76
4.2 Results .....	78
4.2.1 $\text{CaAl}_{12}\text{O}_{19}$ .....	78
4.2.2 $\text{SrAl}_{12}\text{O}_{19}$ .....	82
4.2.3 $\text{La}_{2/3+\delta}\text{Al}_{12-\delta}\text{O}_{19}$ .....	85
4.2.4 $\text{CaAl}_{10}\text{NiTiO}_{19}$ .....	88
4.3 Discussion .....	90
4.3.1 Ferroelectric/Multiferroic Considerations .....	92

## TABLE OF CONTENTS (continued)

	<u>Page</u>
4.3.2 $\text{CaAl}_{10}\text{NiTiO}_{19}$ .....	95
4.4 Conclusion.....	97
4.5 Experimental Materials and Methods .....	98
4.6 Acknowledgements .....	99
4.7 References .....	99
5 Blue Pigments with Hibonite-type Structure: $\text{CaAl}_{12}\text{O}_{19}$ -based pigments with Ni as chromophore .....	102
Abstract .....	102
5.1 Introduction .....	104
5.2 Materials and Synthesis.....	108
5.2.1 Conventional Solid State Method.....	108
5.2.2 Other Preparation Methods.....	109
5.3 Characterization .....	109
5.3.1 Techniques Applied for Hibonites.....	109
5.3.2 For Ni-blue Hibonites in This Work .....	110
5.4 Results and Discussion.....	111
5.4.1 Colors and Phase Analyses.....	111
5.4.2 Crystal Structures .....	120
5.4.3 Optical Properties .....	127
5.4.4 Other Properties and Acid/Base Tests .....	134
5.5 Conclusion.....	140
5.6 Acknowledgements .....	140



## TABLE OF CONTENTS (Continued)

	<u>Page</u>
5.7 References .....	141
6 Color Pigments with Hibonite-type Structure: $\text{CaAl}_{12}\text{O}_{19}$ -based pigments with Fe, Mn, Cr and Cu as chromophores .....	144
Abstract .....	144
6.1 Introduction .....	146
6.2 Materials and Synthesis.....	149
6.2.1 Conventional Solid State Method.....	149
6.2.2 Other Preparation Methods.....	149
6.3 Characterization .....	150
6.3.1 Techniques Applied for Hibonites.....	150
6.3.2 For Hibonites in This Work.....	150
6.4 Results and Discussion.....	151
6.4.1 Colors and Phase Analysis .....	151
6.4.2 Crystal Structures: X-ray and Neutron Diffraction .....	154
6.4.3 Optical Properties: $L^*a^*b^*$ values, Diffuse Reflectance, NIR Reflectance ...	170
6.4.4 Magnetism .....	179
6.4.5 Dielectric Properties .....	180
6.5 Conclusion.....	182
6.6 Acknowledgements .....	182
6.7 References .....	183
7 Pigments Forming in $\text{Li}_2\text{Mn}_{1-x}\text{Ti}_x\text{O}_3$ ( $x = 0\text{--}1.0$ ) System .....	186
Abstract .....	186

## TABLE OF CONTENTS (Continued)

	<u>Page</u>
7.1 Introduction .....	187
7.2 Results and Discussion.....	189
7.3 Conclusion.....	194
7.4 Experimental Materials and Methods .....	194
7.5 Acknowledgements .....	195
7.6 References .....	195
8 Pigments with Sillenite-Type Structure .....	197
Abstract .....	197
8.1 Introduction .....	198
8.2 Results and Discussion.....	201
8.2.1 Bi-site Substitution .....	201
8.2.2 M-site Substitution .....	206
8.3 Conclusion.....	216
8.4 Experimental Materials and Methods .....	216
8.5 Acknowledgements .....	217
8.6 References .....	217
9 General Conclusions and Future Work.....	219
Bibliography .....	221

## LIST OF FIGURES

<u>Figure</u>	<u>Page</u>
1.1 (a) 2D square array and (b) 2D hexagonal array of equal atoms.....	3
1.2 (a) 1D the closest packing of equal atoms, (b) 2D AB-stacking and (c) 2D AC-stacking.....	4
1.3 (a) ABC cubic 3D close packing array and (b) ABA hexagonal 3D close packing array.....	4
1.4 (a) Formation of tetrahedral and (b) octahedral holes in close packing structure.....	5
1.5 Mutual arrangement of tetrahedral holes in hexagonal (a) and cubic (b) close packing structures.....	5
1.6 Simple cubic (a), body-centered cubic (b) and face-centered cubic (c) unit cells.....	6
1.7 Five d orbitals: $d_{x^2-y^2}$ and $d_{z^2}$ have higher energy (point along the axes) and $d_{xy}$ , $d_{xz}$ , $d_{yz}$ have lower energy (point between axes).....	7
1.8 Crystal field splitting diagrams for several common complexes.....	8
1.9 Separation of white light into the color spectrum (seven colors) after passing through the prism.....	9
1.10 Electromagnetic spectrum.....	9
1.11 Color wheel with three primary subtractive colors: red, yellow and blue.....	10
1.12 Difference between additive (a) and subtractive (b) colors.....	10
1.13 (a) An electron absorbs radiation and moves to the upper energy level; (b) emission of radiation when electron goes down to the ground state.....	11
1.14 $\text{Cr}^{3+}$ is a chromophore element in ruby (left) and emerald (right) gems.....	12
1.15 Schematic representation of charge transfer in sapphire.....	12
1.16 Structure of sapphire.....	13

## LIST OF FIGURES (Continued)

<u>Figure</u>	<u>Page</u>
1.17 (a) Schematic representation of fluorite structure, (b) fluorite with color center (trapped electron).....	14
1.18 (a) Transformation of atomic orbital into molecular orbitals and band in metal and (b) jumps of excited electrons to unoccupied levels.....	14
1.19 Band gaps in insulator, semiconductor and metal.....	15
1.20 OSU t-shirt absorbs all colors except orange and reflects only orange light....	16
1.21 Shepherd color company periodic table.....	18
1.22 The spectrum of solar radiation.....	18
1.23 All light which is not reflected, transformed into heat and transferred by conduction and convection.....	19
2.1 Solid state synthesis method.....	22
2.2 Pechini (sol-gel) method.....	23
2.3 (a) CEM MDS-81D Microwave (2.45 GHz multi-mode oven) and (b) schematic representation of the microwave method of synthesis.....	24
2.4 (a) Formation of X-ray, (b) wavelength of X-rays of some selected metals.....	25
2.5 Bragg's law illustration: X-rays diffraction from crystalline solid.....	25
2.6 Schematic setup for XRD method of analysis.....	26
2.7 Rigaku MiniFlex II diffractometer.....	27
2.8 (a) Specular and (b) diffuse reflectance.....	28
2.9 Reflectance vs. wavelength of $\text{CaAl}_{12}\text{O}_{19}$ (white), $\text{LaAl}_{11}\text{NiO}_{19}$ (blue) and $\text{CoAl}_2\text{O}_4$ (blue).....	30
2.10 $L^*a^*b^*$ color space representation.....	31
2.11 Konica Minolta CM-700d spectrophotometer.....	31

## LIST OF FIGURES (Continued)

<u>Figure</u>	<u>Page</u>
2.12 Unpaired electron spins orientation in (a) paramagnetic, (b) ferromagnetic, (c) antiferromagnetic and (d) ferrimagnetic materials placed in magnetic field.....	32
2.13 Temperature dependence of molar magnetic susceptibility ( $\chi$ ) of (a) paramagnetic, (b) ferromagnetic, (c) antiferromagnetic materials.....	33
2.14 Quantum Design Physical Property Measurement System (QD-PPMS).....	34
2.15 Dielectric material ( $h$ – thickness, and $S$ – surface area) between two parallel plates of capacitor.....	35
2.16 For ideal dielectric $I$ (electric current) outstrips the $V$ (voltage) by $90^\circ$ when external voltage applied; for non-ideal dielectric the angle between $I$ and $V$ decreases by $\delta$ and the value of the new phase angle is $90^\circ - \delta = \theta$ .....	36
2.17 (a) Stretching vibrations and (b) bending vibrations.....	37
3.1 Hexagonal unit cell of $\text{Ba}_5(\text{MnO}_4)_3\text{Cl}$ structure (left and right): Dark turquoise and yellow spheres represent two different crystallographic positions of $\text{Ba}^{2+}$ 4f (Ba1) and 6h (Ba2) accordingly, with face-sharing $\text{Ba}(1)\text{O}_9$ and edge-sharing $\text{Ba}(2)\text{O}_6\text{Cl}_2$ polyhedra forming one-dimensional chains arranged alternately along the $c$ -axis. The Mn (blue) tetrahedra are corner-shared with Ba polyhedra and the Cl (green) atoms are lined up in channels along the $c$ -axis. Oxygen atoms are omitted for clarity.....	42
3.2 Further structural description of the hexagonal unit cell of $\text{Ba}_5(\text{MnO}_4)_3\text{Cl}$ (left and right): dark turquoise and yellow spheres represent two different crystallographic positions of $\text{Ba}^{2+}$ 4f (Ba1) and 6h (Ba2) accordingly, with face-sharing $\text{Ba}(1)\text{O}_9$ and edge-sharing $\text{Ba}(2)\text{O}_6\text{Cl}_2$ polyhedra forming one-dimensional chains arranged alternately along the $c$ -axis. The Mn (blue) tetrahedra are corner-shared with Ba polyhedra and the Cl (green) atoms are lined up in channels along the $c$ -axis. Oxygen atoms are omitted for clarity.....	43
3.3 XRD patterns of $\text{Ba}_5\text{Mn}_{3-x}\text{V}_x\text{O}_{12}\text{Cl}$ (a) and $\text{Ba}_5\text{Mn}_{3-x}\text{P}_x\text{O}_{12}\text{Cl}$ (b) samples (asterisks – impurity peaks).....	45

## LIST OF FIGURES (Continued)

<u>Figure</u>	<u>Page</u>
<p>3.4 XRD patterns of (a) <math>\text{Ba}_{5-x}\text{Sr}_x\text{Mn}_3\text{O}_{12}\text{Cl}</math> (<math>x = 0-2.5</math>), <math>\text{Ba}_{5-x}\text{K}_x\text{S}_x\text{Mn}_{0.5}\text{P}_{2.5-x}\text{O}_{12}\text{Cl}</math> (<math>x = 0-0.5</math>), <math>\text{Ba}_{5-x}\text{K}_x\text{Mo}_x\text{Mn}_{0.5}\text{P}_{2.5-x}\text{O}_{12}\text{Cl}</math> (<math>x = 0-0.2</math>); (b) <math>\text{Ba}_5\text{Cr}_{3-x}\text{P}_x\text{O}_{12}\text{F}</math> (<math>x = 0.5-2.5</math>), <math>\text{Ba}_5\text{Cr}_{3-x}\text{P}_x\text{O}_{12}\text{Cl}</math> (<math>x = 1.0-2.5</math>), <math>\text{Ba}_5\text{Cr}_{3-x}\text{V}_x\text{O}_{12}\text{Cl}</math> (<math>x = 1.5-2.5</math>), <math>\text{Ba}_5\text{Mn}_{3-x}\text{Cr}_x\text{O}_{12}\text{Cl}</math> (<math>x = 0-3.0</math>); (c) <math>\text{Sr}_5\text{Cr}_{3-x}\text{P}_x\text{O}_{12}\text{Cl}</math> (<math>x = 0.5; 1.0</math>), <math>\text{Sr}_5\text{Cr}_{3-x}\text{V}_x\text{O}_{12}\text{Cl}</math> (<math>x = 0.5-1.5</math>), <math>\text{Sr}_5\text{Mn}_{3-x}\text{Cr}_x\text{O}_{12}\text{Cl}</math> (<math>x = 2.5-3.0</math>); (d) <math>\text{Sr}_5\text{Cr}_{3-x}\text{P}_x\text{O}_{12}\text{F}</math> (<math>x = 0.5-2.5</math>), <math>\text{Sr}_5\text{Cr}_{3-x}\text{V}_x\text{O}_{12}\text{F}</math> (<math>x = 0.5-2.5</math>), <math>\text{Sr}_5\text{Mn}_{3-x}\text{Cr}_x\text{O}_{12}\text{F}</math> (<math>x = 2.5-3.0</math>).....</p>	47
<p>3.5 Unit cell edges of <math>\text{Ba}_5\text{Mn}_{3-x}\text{V}_x\text{O}_{12}\text{Cl}</math> (a) and <math>\text{Ba}_5\text{Mn}_{3-x}\text{P}_x\text{O}_{12}\text{Cl}</math> (b) phases, cell volumes (c) and <math>c/a</math> ratio showing anisotropic structural change (d) of both solid solutions as a function of <math>x</math> (vanadium/phosphorus content). The estimated errors for <math>a</math>, <math>c</math>, and <math>V</math> are less than the size of the points in the figures.....</p>	48
<p>3.6 Unit cell edges <math>a</math> and <math>c</math> of <math>\text{Ba}_{5-x}\text{K}_x\text{Mo}_x\text{Mn}_{0.5}\text{P}_{2.5-x}\text{O}_{12}\text{Cl}</math> and <math>\text{Ba}_{5-x}\text{K}_x\text{S}_x\text{Mn}_{0.5}\text{P}_{2.5-x}\text{O}_{12}\text{Cl}</math> series (a), cell volumes <math>V</math> (b) and <math>c/a</math> ratio (c) as a function of <math>x</math>. The estimated errors for <math>a</math>, <math>c</math>, and <math>V</math> are less than the size of the points in the figures.....</p>	49
<p>3.7 Unit cell edges <math>a</math> and <math>c</math> of <math>\text{Ba}_{5-x}\text{Sr}_x\text{Mn}_3\text{O}_{12}\text{Cl}</math> and <math>\text{Ba}_5\text{Cr}_{3-x}\text{P}_x\text{O}_{12}\text{F}</math> series (a), cell volumes <math>V</math> (b) and <math>c/a</math> ratio (c) as a function of <math>x</math>. The estimated errors for <math>a</math>, <math>c</math>, and <math>V</math> are less than the size of the points in the figures.....</p>	50
<p>3.8 Unit cell edges <math>a</math> and <math>c</math> of <math>\text{Ba}_5\text{Mn}_{3-x}\text{Cr}_x\text{O}_{12}\text{Cl}</math>, <math>\text{Ba}_5\text{Cr}_{3-x}\text{P}_x\text{O}_{12}\text{Cl}</math> and <math>\text{Ba}_5\text{Cr}_{3-x}\text{V}_x\text{O}_{12}\text{Cl}</math> series (a), cell volumes <math>V</math> (b) and <math>c/a</math> ratio (c) as a function of <math>x</math>. The estimated errors for <math>a</math>, <math>c</math>, and <math>V</math> are less than the size of the points in the figures.....</p>	51
<p>3.9 Unit cell edges <math>a</math> and <math>c</math> of <math>\text{Sr}_5\text{Mn}_{3-x}\text{Cr}_x\text{O}_{12}\text{Cl}</math>, <math>\text{Sr}_5\text{Cr}_{3-x}\text{P}_x\text{O}_{12}\text{Cl}</math> and <math>\text{Sr}_5\text{Cr}_{3-x}\text{V}_x\text{O}_{12}\text{Cl}</math> series (a), unit cell edges <math>a</math> and <math>c</math> of <math>\text{Sr}_5\text{Mn}_{3-x}\text{Cr}_x\text{O}_{12}\text{F}</math>, <math>\text{Sr}_5\text{Cr}_{3-x}\text{P}_x\text{O}_{12}\text{F}</math> and <math>\text{Sr}_5\text{Cr}_{3-x}\text{V}_x\text{O}_{12}\text{F}</math> series (b), cell volumes <math>V</math> (c) and <math>c/a</math> ratio (d) as a function of <math>x</math>. The estimated errors for <math>a</math>, <math>c</math>, and <math>V</math> are less than the size of the points in the figures.....</p>	52
<p>3.10 Neutron data of <math>\text{Ba}_5\text{Mn}_{0.2}\text{V}_{2.8}\text{O}_{12}\text{Cl}</math> phase shown with a Rietveld fit.....</p>	52
<p>3.11 Neutron data of <math>\text{Ba}_5(\text{MnO}_4)_3\text{Cl}</math> phase shown with a Rietveld fit.....</p>	53
<p>3.12 Neutron data of <math>\text{Ba}_5\text{Mn}_{2.5}\text{V}_{0.5}\text{O}_{12}\text{Cl}</math> phase shown with a Rietveld fit.....</p>	53
<p>3.13 Neutron data of <math>\text{Ba}_5\text{Mn}_{0.5}\text{P}_{2.5}\text{O}_{12}\text{Cl}</math> phase shown with a Rietveld fit.....</p>	54

## LIST OF FIGURES (Continued)

<u>Figure</u>	<u>Page</u>
3.14 A fragment of $\text{Ba}_5\text{Mn}_{3-x}\text{V}_x\text{O}_{12}\text{Cl}$ / $\text{Ba}_5\text{Mn}_{3-x}\text{P}_x\text{O}_{12}\text{Cl}$ unit cell: big dark turquoise and yellow spheres represent different crystallographic positions of $\text{Ba}^{2+}$ – 4f and 6h accordingly, blue spheres – $\text{M}^{5+}$ , $\text{Cl}^-$ – green spheres, $\text{O}^{2-}$ – red spheres.....	58
3.15 Colors of (a) $\text{Ba}_5\text{Mn}_{3-x}\text{V}_x\text{O}_{12}\text{Cl}$ and (b) $\text{Ba}_5\text{Mn}_{3-x}\text{P}_x\text{O}_{12}\text{Cl}$ samples.....	59
3.16 Color sphere of $\text{Ba}_5\text{Mn}_{3-x}\text{V}_x\text{O}_{12}\text{Cl}$ ( $x = 0$ –2.9) samples.....	59
3.17 Color sphere of $\text{Ba}_5\text{Mn}_{3-x}\text{P}_x\text{O}_{12}\text{Cl}$ ( $x = 0$ –2.9) samples.....	60
3.18 $L^*$ (it represents a black ( $L^* = 0$ ) / white ( $L^* = 100$ ) component of color), $a^*$ (it is responsible for a red ( $a^* > 0$ ) / green ( $a^* < 0$ ) component), $b^*$ (it represents a yellow ( $b^* > 0$ ) / blue ( $b^* < 0$ ) components) parameters of samples as a function of $x$ .....	60
3.19 Diffuse-reflectance spectra of the $\text{Ba}_5\text{Mn}_{3-x}\text{V}_x\text{O}_{12}\text{Cl}$ series.....	62
3.20 Reflectance (%) of (a) $\text{Ba}_5\text{Mn}_{3-x}\text{V}_x\text{O}_{12}\text{Cl}$ , (b) $\text{Ba}_5\text{Mn}_{3-x}\text{P}_x\text{O}_{12}\text{Cl}$ , (c) $\text{Sr}_5\text{Cr}_{3-x}\text{P}_x\text{O}_{12}\text{F}$ and (d) $\text{Sr}_5\text{Cr}_{3-x}\text{V}_x\text{O}_{12}\text{F}$ samples as a function of wavelength (nm).....	63
3.21 Reflectance (%) of (a) $\text{Ba}_5\text{K}_x\text{S}_x\text{Mn}_{0.5}\text{P}_{2.5-x}\text{O}_{12}\text{Cl}$ , (b) $\text{Ba}_5\text{Cr}_{3-x}\text{P}_x\text{O}_{12}\text{Cl}$ , (c) $\text{Ba}_5\text{Mn}_{3-x}\text{Cr}_x\text{O}_{12}\text{Cl}$ and (d) $\text{Ba}_5\text{Cr}_{3-x}\text{P}_x\text{O}_{12}\text{F}$ series as a function of wavelength (nm).....	63
3.22 UV-VIS and NIR reflectance (%) of $\text{Ba}_5\text{Mn}_{3-x}\text{V}_x\text{O}_{12}\text{Cl}$ ( $x = 0, 2.5, 3.0$ ) and $\text{Ba}_5\text{Mn}_{3-x}\text{P}_x\text{O}_{12}\text{Cl}$ ( $x = 0, 2.5, 3.0$ ) samples as a function of wavelength (nm).....	64
3.23 IR spectra of $\text{Ba}_5(\text{MnO}_4)_3\text{Cl}$ , $\text{Ba}_5\text{Mn}_{2.5}\text{V}_{0.5}\text{O}_{12}\text{Cl}$ , $\text{Ba}_5\text{Mn}_{0.2}\text{V}_{2.8}\text{O}_{12}\text{Cl}$ and $\text{Ba}_5\text{Mn}_{0.5}\text{P}_{2.5}\text{O}_{12}\text{Cl}$ phases.....	65
3.24 Magnetic susceptibility and inverse magnetic susceptibility of $\text{Ba}_5\text{Mn}_3\text{O}_{12}\text{Cl}$ , $\text{Ba}_5\text{Mn}_{1.5}\text{V}_{1.5}\text{O}_{12}\text{Cl}$ and $\text{Ba}_5\text{Mn}_{1.5}\text{P}_{1.5}\text{O}_{12}\text{Cl}$ ; 1 emu (cgs units) = $10^{-3}$ A m <sup>2</sup> (SI units).....	67
3.25 Magnetic susceptibility and inverse magnetic susceptibility of $\text{Sr}_5\text{Cr}_3\text{O}_{12}\text{Cl}$ (1), $\text{Sr}_5\text{Cr}_3\text{O}_{12}\text{F}$ (2), $\text{Sr}_5\text{Mn}_{0.5}\text{Cr}_{2.5}\text{O}_{12}\text{Cl}$ (3), $\text{Sr}_5\text{Cr}_2\text{VO}_{12}\text{Cl}$ (4) and $\text{Sr}_5\text{Cr}_2\text{VO}_{12}\text{F}$ (5); 1 emu (cgs units) = $10^{-3}$ A m <sup>2</sup> (SI units).....	67

## LIST OF FIGURES (Continued)

<u>Figure</u>	<u>Page</u>
<p>4.1 The Al-O framework of the hibonite structure with the <math>c</math>-axis vertical. Dark blue octahedron at the origin with Al1. The pink unit with Al4 are face-sharing octahedra. Turquoise octahedra of Al5 forming an edge sharing sheet. Green tetrahedra with Al3. The orange trigonal bipyramidal units with Al2. (a) The paraelectric structure (<math>P6_3/mmc</math>) with random displacements along the <math>c</math>-axis. (b) Ordered dipoles in the ferroelectric structure (<math>P6_3mc</math>). (c) Ordered dipoles in the antiferroelectric structure (<math>P\bar{3}m1</math>).....</p>	76
<p>4.2 Rietveld fit of <math>\text{CaAl}_{12}\text{O}_{19}</math> neutron data at 11 K.....</p>	79
<p>4.3 Rietveld fit of <math>\text{CaAl}_{12}\text{O}_{19}</math> neutron data at 298 K.....</p>	79
<p>4.4 Shapes of anharmonic displacements for Al at (a) the Al3 site and (b) the Al4 site, both in <math>4f\bar{3}m</math>. For the Al3 site there is major anharmonicity along the <math>c</math>-axis, and minor anharmonicity perpendicular to <math>c</math>. For the Al4 site there is minor anharmonicity along <math>c</math> with more significant anharmonicity perpendicular to <math>c</math>.....</p>	82
<p>4.5 Rietveld fit of <math>\text{SrAl}_{12}\text{O}_{19}</math> neutron data at 298K. Three rows of vertical lines below the data profiles, from top to bottom, are corresponding to the major phase <math>\text{SrAl}_{12}\text{O}_{19}</math> (magenta), the impurity phase <math>\text{Al}_2\text{O}_3</math> (turquoise) and the minor hexagonal phase <math>\text{SrAl}_{12}\text{O}_{19}</math> with space group <math>P\bar{6}m2</math> (black), respectively. The amount of the impurity phase is below 2%.....</p>	83
<p>4.6 A section of the neutron diffraction pattern for <math>\text{SrAl}_{12}\text{O}_{19}</math>. High angle shoulders occur on some, but not all, peaks. These shoulders are caused by a second hexagonal phase that is structurally related to that of hibonite. These shoulders are mainly caused by shortening of the <math>c</math> cell edge in the minor hexagonal phase. (a) Without the second hexagonal phase; (b) with the second hexagonal phase. Red markers for primary phase; black markers for minor phase.....</p>	84
<p>4.7 Rietveld fit of <math>\text{LaAl}_{12}\text{O}_{19}</math> neutron data at 298K. The actual composition is refined to be <math>\text{La}_{0.91}\text{Al}_{11.66}\text{O}_{18.69}</math>. Three rows of vertical lines below the data profiles, from top to bottom, are corresponding to the major phase <math>\text{La}_{0.91}\text{Al}_{11.66}\text{O}_{18.69}</math> (magenta), the impurity phases <math>\text{LaAlO}_3</math> (turquoise) and <math>\text{Al}_2\text{O}_3</math> (black), respectively. The amount of impurity phases is below 2%.....</p>	86



## LIST OF FIGURES (Continued)

<u>Figure</u>	<u>Page</u>
4.8 Rietveld fit of $\text{CaAl}_{9.6}\text{Ti}_{1.2}\text{Ni}_{1.2}\text{O}_{19}$ neutron data at 298K. The actual composition is refined to be $\text{CaAl}_{9.98}\text{Ti}_{1.00}\text{Ni}_{1.02}\text{O}_{19}$ . Four rows of vertical lines below the data profiles, from top to bottom, are corresponding to the major phase $\text{CaAl}_{9.98}\text{Ti}_{1.00}\text{Ni}_{1.02}\text{O}_{19}$ (magenta), the impurity phases $\text{TiO}_2$ (turquoise), $\text{CaTiO}_3$ (black) and $\text{NiAl}_2\text{O}_4$ (brown), respectively. The amount of impurity phases is below 5%.....	88
5.1 Polyhedral representation of hexagonal $\text{AM}_{12}\text{O}_{19}$ ( $A = \text{Ca, Sr, RE}$ ) with hibonite-type of structure. Twelve coordinated A atoms in gray; oxygen atoms in red; $\text{MO}_6$ octahedra in pink (M1), yellow (M4), cyan (M5); $\text{MO}_5$ trigonal bipyramids in green (M2); and $\text{MO}_4$ tetrahedra in royal blue (M3). The framework can be viewed as alternating S-block (spinel layers) and R-block (constituted by A ions, trigonal bipyramids and face-sharing octahedra) stacking alternatively along the <i>c</i> -axis. (Top) Images of hibonite minerals from Madagascar and Myanmar.....	105
5.2 Colors resulted from a variety of substitutions for the hibonite host with an ideal formula $\text{CaAl}_{12}\text{O}_{19}$ . (a) $\text{CaAl}_{12-x}\text{M}_x\text{O}_{19}$ ( $M = \text{Cr, Mn, Fe, Ni, Co, Cu, Ti, V}$ ); (b) $\text{CaAl}_{12-x-y}\text{Ni}_x\text{M}_y\text{O}_{19}$ ( $M = \text{Zn, Ga, In, Si, Ti, Zr, Sn, Ge, Nb, Ta, Sb, Te}$ ); (c) $\text{Ca}_{1-x}\text{A}_x\text{Al}_{12-x}\text{Ni}_x\text{O}_{19}$ ( $A = \text{Sr, La, Y, Ce, Pr, Nd}$ ).....	112
5.3 A series of color photographs of blue pellets and powders according to the following two solid solutions: (left) $\text{CaAl}_{12-2x}\text{Ni}_x\text{Ti}_x\text{O}_{19}$ ( $x = 0-1.2$ ), and (right, inside box) $\text{Ca}_{1-x}\text{La}_x\text{Al}_{12-x}\text{Ni}_x\text{O}_{19}$ .....	113
5.4 A series of X-ray powder diffraction patterns for the (top) $\text{CaAl}_{12-2x}\text{Ni}_x\text{Ti}_x\text{O}_{19}$ ( $x = 0.2-1.2$ ), and (bottom) $\text{Ca}_{1-x}\text{La}_x\text{Al}_{12-x}\text{Ni}_x\text{O}_{19}$ ( $x = 0-1$ ) solid solutions.....	114
5.5 Cell edges of solid solution $\text{CaAl}_{12-2x}\text{Ni}_x\text{Ti}_x\text{O}_{19}$ ( $x = 0-1.2$ ) refined by X-ray and neutron powder diffraction data. Estimated uncertainties are smaller than the plotted point size.....	116
5.6 Cell edges of solid solution $\text{Ca}_{1-x}\text{La}_x\text{Al}_{12-x}\text{Ni}_x\text{O}_{19}$ ( $x = 0-1$ ) refined by X-ray and neutron powder diffraction data. Estimated uncertainties are smaller than the plotted point size.....	117
5.7 Cell edges of solid solutions $\text{Ca}_{1-x}\text{RE}_x\text{Al}_{12-x}\text{Ni}_x\text{O}_{19}$ ( $x = 0-1$ ) and $\text{Sr}_{1-x}\text{La}_x\text{Al}_{12-x}\text{Ni}_x\text{O}_{19}$ ( $x = 0-1$ ) refined by X-ray powder diffraction: 1. $\text{RE} = \text{La}$ ; 2. $\text{RE} = \text{Ce}$ ; 3. $\text{RE} = \text{Pr}$ ; 4. $\text{RE} = \text{Nd}$ ; 5. $\text{Sr}_{1-x}\text{La}_x\text{Al}_{12-x}\text{Ni}_x\text{O}_{19}$ ( $x = 0-1$ ). Estimated uncertainties are smaller than the plotted point size.....	118

## LIST OF FIGURES (Continued)

<u>Figure</u>	<u>Page</u>
<p>5.8 XRD patterns of <math>A_{1-x}RE_xAl_{12-x}Ni_xO_{19}</math> (<math>x = 0.2</math>). From bottom to top: 1. <math>A = Ca</math>, <math>RE = La</math>; 2. <math>A = Ca</math>, <math>RE = Ce</math>; 3. <math>A = Ca</math>, <math>RE = Pr</math>; 4. <math>A = Ca</math>, <math>RE = Nd</math>; 5. <math>A = Ca</math>, <math>RE = Sm</math>; 6. <math>A = Ca</math>, <math>RE = Eu</math>; 7. <math>A = Ca</math>, <math>RE = Gd</math>; 8. <math>A = Ca</math>, <math>RE = Tb</math>; 9. <math>A = Ca</math>, <math>RE = Dy</math>; 10. <math>A = Ca</math>, <math>RE = Ho</math>; 11. <math>A = Ca</math>, <math>RE = Er</math>; 12. <math>A = Ca</math>, <math>RE = Tm</math>; 13. <math>A = Ca</math>, <math>RE = Yb</math>; 14. <math>A = Ca</math>, <math>RE = Lu</math>; 15. <math>A = Sr</math>, <math>RE = La</math>; 16. <math>A = Sr</math>, <math>RE = Ce</math>; 17. <math>A = Sr</math>, <math>RE = Pr</math>; 18. <math>A = Sr</math>, <math>RE = Nd</math>; 19. <math>A = Ba</math>, <math>RE = La</math>.....</p>	119
<p>5.9 XRD patterns of <math>CaAl_{12-x-y}Ni_xM_yO_{19}</math> (For <math>M = Ti</math>, <math>Ge</math> and <math>Sn</math>, <math>x = 0.5</math>, <math>y = 0.5</math>; For <math>M = Nb</math>, <math>Ta</math> and <math>Sb</math>, <math>x = 0.4</math>, <math>y = 0.2</math>). The composition for <math>Na</math> is <math>Ca_{0.5}Na_{0.5}Al_{10.5}Ni_{0.5}TiO_{19}</math>.....</p>	120
<p>5.10 Neutron Rietveld fits of (a) <math>LaAl_{11}NiO_{19}</math> (Phase 1, ~95%). Impurity phases include: Phase 2, <math>LaAlO_3</math>; Phase 3, <math>Al_2O_3</math>; Phase 4, <math>NiAl_2O_4</math>. (b) <math>CaAl_{10}NiTiO_{19}</math> (Phase 1, ~98%). Impurity phases include: Phase 2 (<math>TiO_2</math>), Phase 3 (<math>CaTiO_3</math>), Phase 4 (<math>NiAl_2O_4</math>).....</p>	122
<p>5.11 Diffuse reflectance spectra of solid solutions (a) <math>CaAl_{12-2x}Ni_xTi_xO_{19}</math> (<math>x = 0-1.2</math>) and (b) <math>Ca_{1-x}La_xAl_{12-x}Ni_xO_{19}</math> (<math>x = 0-1</math>).....</p>	128
<p>5.12 The CIE <math>L^*a^*b^*</math> color coordinates for solid solutions (a) <math>CaAl_{12-2x}Ni_xTi_xO_{19}</math> (<math>x = 0-1.2</math>) and (b) <math>Ca_{1-x}La_xAl_{12-x}Ni_xO_{19}</math> (<math>x = 0-1</math>). Estimated uncertainties are smaller than the plotted point size.....</p>	130
<p>5.13 NIR reflectance spectra of selected Ni-containing hibonite solid solutions. (a) <math>CaAl_{12-2x}Ni_xTi_xO_{19}</math> (<math>x = 0.5, 1.0, 1.2</math>); (b) <math>Ca_{1-x}La_xAl_{12-x}Ni_xO_{19}</math> (<math>x = 0.0, 0.1, 0.3, 0.5, 0.7, 1.0</math>); (c) <math>Sr_{1-x}La_xAl_{12-x}Ni_xO_{19}</math> (<math>x = 0.0, 0.1, 0.3, 0.5, 0.7, 0.9, 1.0</math>); (d) <math>Ca_{0.5}RE_{0.5}Al_{11.5}Ni_{0.5}O_{19}</math> (<math>RE = La, Ce, Nd, Pr</math>) and <math>Sr_{0.5}La_{0.5}Al_{11.5}Ni_{0.5}O_{19}</math>.....</p>	133
<p>5.14 NIR reflectance spectra of selected Ni-containing hibonite samples. Commercial Co-blue pigment and <math>TiO_2</math> are included for comparison.....</p>	134
<p>5.15 Magnetic susceptibility (<math>\chi</math>) and inverse magnetic susceptibility (<math>1/\chi</math>) vs. temperature of (1) <math>LaAl_{11}NiO_{19}</math>; (2) <math>Ca_{0.5}La_{0.5}Al_{11.5}Ni_{0.5}O_{19}</math> and (3) <math>CaAl_{11}Ti_{0.5}Ni_{0.5}O_{19}</math>. 1 emu (cgs units) = <math>10^{-3}</math> A m<sup>2</sup> (SI units).....</p>	135
<p>5.16 (a) Temperature dependence of (a) dielectric constant <math>\kappa</math> and (b) dielectric loss <math>\tan \delta</math> for <math>CaAl_{11}Ti_{0.5}Ni_{0.5}O_{19}</math> hibonite sample.....</p>	137

## LIST OF FIGURES (Continued)

<u>Figure</u>	<u>Page</u>
5.17 (a) Temperature dependence of (a) dielectric constant $\kappa$ and (b) dielectric loss ( $\tan \delta$ ) for $\text{CaAl}_{10}\text{TiNiO}_{19}$ hibonite sample.....	137
5.18 (a) Frequency dependence of (a) dielectric constant $\kappa$ and (b) dielectric loss ( $\tan \delta$ ) for $\text{CaAl}_{11}\text{Ti}_{0.5}\text{Ni}_{0.5}\text{O}_{19}$ and $\text{CaAl}_{10}\text{TiNiO}_{19}$ hibonite samples.....	138
5.19 XRD patterns of (a) $\text{CaAl}_{11}\text{TiNiO}_{19}$ (a) and (b) $\text{LaAl}_{11}\text{NiO}_{19}$ hibonite compounds before and after exposure of various acids ( $\text{HNO}_3$ , $\text{CH}_3\text{COOH}$ , $\text{HCl}$ ) and base ( $\text{NaOH}$ ).....	139
6.1 Hexagonal structure of hibonite $\text{CaAl}_{12}\text{O}_{19}$ with five different crystallographic positions of aluminum The crystal structure consists of two blocks alternating along the $c$ -axis: the spinel layer (S-block) and the trigonal bipyramidal layer (R-block).....	146
6.2 (a) Colors resulted from iron substitutions for the hibonite host with an ideal formula $\text{CaAl}_{12}\text{O}_{19}$ . (I) $\text{CaAl}_{12-x}\text{Fe}_x\text{O}_{19}$ ; (II) $\text{CaAl}_{11-x}\text{GaFe}_x\text{O}_{19}$ ; (III) 1: $\text{CaAl}_{9.5}\text{InSn}_{0.5}\text{Cu}_{0.5}\text{Fe}_{0.5}\text{O}_{19}$ , 2: $\text{CaAl}_{9.5}\text{GaSn}_{0.5}\text{Cu}_{0.5}\text{Fe}_{0.5}\text{O}_{19}$ , 3: $\text{CaAl}_{9.5}\text{InTi}_{0.5}\text{Cu}_{0.5}\text{Fe}_{0.5}\text{O}_{19}$ , 4: $\text{CaAl}_{9.5}\text{GaTi}_{0.5}\text{Cu}_{0.5}\text{Fe}_{0.5}\text{O}_{19}$ . (b) Colors resulted from manganese substitutions for the hibonite host with an ideal formula $\text{CaAl}_{12}\text{O}_{19}$ . (I) $\text{CaAl}_{12-x}\text{Mn}_x\text{O}_{19}$ ; (II) $\text{CaAl}_{12-x}\text{Sn}_x\text{Mn}_x\text{O}_{19}$ ; (III) 1: $\text{CaAl}_{10.5}\text{Ti}_{0.5}\text{Cu}_{0.5}\text{Mn}_{0.5}\text{O}_{19}$ , 2: $\text{CaAl}_{10.5}\text{Sn}_{0.5}\text{Cu}_{0.5}\text{Mn}_{0.5}\text{O}_{19}$ , 3: $\text{CaAl}_{9.5}\text{InTi}_{0.5}\text{Cu}_{0.5}\text{Mn}_{0.5}\text{O}_{19}$ , 4: $\text{CaAl}_{9.5}\text{InSn}_{0.5}\text{Cu}_{0.5}\text{Mn}_{0.5}\text{O}_{19}$ . (c) Colors resulted from chromium substitutions for the hibonite host with an ideal formula $\text{CaAl}_{12}\text{O}_{19}$ . (I) $\text{CaAl}_{12-x}\text{Cr}_x\text{O}_{19}$ ; (II) 1: $\text{CaAl}_{10.5}\text{Sn}_{0.5}\text{Cu}_{0.5}\text{Cr}_{0.5}\text{O}_{19}$ , 2: $\text{CaAl}_{10.5}\text{GaCr}_{0.5}\text{O}_{19}$ , 3: $\text{CaAl}_{10.5}\text{Ge}_{0.5}\text{Cu}_{0.5}\text{Cr}_{0.5}\text{O}_{19}$ , 4: $\text{CaAl}_{10.5}\text{Ti}_{0.5}\text{Cu}_{0.5}\text{Cr}_{0.5}\text{O}_{19}$ ..	153
6.3 XRD patterns of $\text{CaAl}_{12-x}\text{Fe}_x\text{O}_{19}$ ( $x = 0.5\text{--}4.5$ ) series.....	156
6.4 XRD patterns of (a) $\text{CaAl}_{11-x}\text{GaM}^{\text{III}}_x\text{O}_{19}$ ( $M^{\text{III}} = \text{Cr}$ ( $x = 0.5; 1.0$ ) and $\text{Fe}$ ( $x = 0.5 - 2.5$ )) series; (b) $\text{CaAl}_{10}\text{GeM}^{\text{II}}\text{O}_{19}$ ( $M^{\text{II}} = \text{Mn}, \text{Fe}$ ), $\text{CaAl}_{12-2x}\text{Sn}_x\text{Fe}_x\text{O}_{19}$ ( $x = 0.5\text{--}1.5$ ) and $\text{CaAl}_{12-2x}\text{Ti}_x\text{M}^{\text{II}}_x\text{O}_{19}$ ( $M^{\text{II}} = \text{Mn}, \text{Fe}$ ( $x = 0.5; 1.0$ )) series; (c) $\text{CaAl}_{11-x}\text{InCr}_x\text{O}_{19}$ ( $x = 0.5; 1.0$ ) solid solution; (d) $\text{CaAl}_{11}\text{Cr}_{0.5}\text{Fe}_{0.5}\text{O}_{19}$ , $\text{CaAl}_{11}\text{Cr}_{0.5}\text{Mn}_{0.5}\text{O}_{19}$ and $\text{CaAl}_{11}\text{Fe}_{0.5}\text{Mn}_{0.5}\text{O}_{19}$ compounds.....	156
6.5 XRD patterns of $\text{CaAl}_{12-x}\text{Mn}_x\text{O}_{19}$ ( $x = 0.1\text{--}0.6$ ) solid solution.....	157
6.6 XRD patterns of $\text{CaAl}_{12-2x}\text{Sn}_x\text{Mn}_x\text{O}_{19}$ ( $x = 0.1\text{--}1.0$ ) solid solution.....	157
6.7 XRD patterns of $\text{CaAl}_{12-x}\text{Cr}_x\text{O}_{19}$ ( $x = 0.5\text{--}3.5$ ) series.....	158

## LIST OF FIGURES (Continued)

<u>Figure</u>	<u>Page</u>
6.8 XRD patterns of (a) $\text{CaAl}_{11-x}\text{Ti}_{0.5}\text{Cu}_{0.5}\text{M}^{\text{III}}_x\text{O}_{19}$ ( $\text{M}^{\text{III}}_x = \text{Cr}_{0.5}, \text{Mn}_{0.25}\text{Fe}_{0.25}, \text{Mn}_{0.5}, \text{Mn}, \text{Fe}_{0.5}$ ) compounds and (b) $\text{CaAl}_{11}\text{M}^{\text{IV}}_{0.5}\text{Cu}_{0.5}\text{O}_{19}$ ( $\text{M}^{\text{IV}} = \text{Ge}, \text{Sn}$ ) and $\text{CaAl}_{12-2x}\text{Ti}_x\text{Cu}_x\text{O}_{19}$ ( $x = 0.5-1.5$ ) solid solutions.....	158
6.9 XRD patterns of (a) $\text{CaAl}_{9.5}\text{GaTi}_{0.5}\text{Cu}_{0.5}\text{M}^{\text{III}}_{0.5}\text{O}_{19}$ and $\text{CaAl}_{9.5}\text{GaSn}_{0.5}\text{Cu}_{0.5}\text{M}^{\text{III}}_{0.5}\text{O}_{19}$ ( $\text{M}^{\text{III}} = \text{Cr}, \text{Mn}, \text{Fe}$ ) compounds; (b) $\text{CaAl}_{9.5}\text{InTi}_{0.5}\text{Cu}_{0.5}\text{M}^{\text{III}}_{0.5}\text{O}_{19}$ and $\text{CaAl}_{9.5}\text{InSn}_{0.5}\text{Cu}_{0.5}\text{M}^{\text{III}}_{0.5}\text{O}_{19}$ ( $\text{M}^{\text{III}} = \text{Cr}, \text{Mn}, \text{Fe}$ ) solid solutions and (c) $\text{CaAl}_{10.5}\text{Ge}_{0.5}\text{Cu}_{0.5}\text{M}^{\text{III}}_{0.5}\text{O}_{19}$ ( $\text{M}^{\text{III}} = \text{Cr}, \text{Mn}, \text{Fe}$ ) and $\text{CaAl}_{10.5}\text{Sn}_{0.5}\text{Cu}_{0.5}\text{M}^{\text{III}}_{0.5}\text{O}_{19}$ ( $\text{M}^{\text{III}}_{0.5} = \text{Cr}_{0.5}, \text{Mn}_{0.25}\text{Fe}_{0.25}, \text{Fe}_{0.5}, \text{Mn}_{0.5}$ ) compounds.....	159
6.10 Lattice parameters of $\text{CaAl}_{12-x}\text{Fe}_x\text{O}_{19}$ ( $x = 0.5 - 4.5$ ) and $\text{CaAl}_{12-x}\text{Cr}_x\text{O}_{19}$ ( $x = 0.5 - 3.5$ ) solid solutions: (a) unit cell edges $a$ and $c$ of $\text{CaAl}_{12-x}\text{Fe}_x\text{O}_{19}$ ( $x = 0.5-4.5$ ), (b) unit cell edges $a$ and $c$ of $\text{CaAl}_{12-x}\text{Cr}_x\text{O}_{19}$ ( $x = 0.5-3.5$ ), (c) unit cell volumes $V$ and (d) $c/a$ ratio as a function of $x$ . The estimated errors for $a$ , $c$ and $V$ are less than the size of the points in the figure.....	160
6.11 Lattice parameters of $\text{CaAl}_{12-x}\text{Mn}_x\text{O}_{19}$ ( $x = 0.1-0.6$ ): (a) unit cell edges $a$ and $c$ , (b) unit cell volumes $V$ and (c) $c/a$ ratio as a function of $x$ . The estimated errors for $a$ , $c$ and $V$ are less than the size of the points in the figure.....	161
6.12 Lattice parameters of $\text{CaAl}_{12-2x}\text{Sn}_x\text{Mn}_x\text{O}_{19}$ ( $x = 0.1-1.0$ ): (a) unit cell edges $a$ and $c$ , (b) unit cell volumes $V$ and (c) $c/a$ ratio as a function of $x$ . The estimated errors for $a$ , $c$ and $V$ are less than the size of the points in the figure.....	162
6.13 Neutron data of $\text{CaAl}_{9.5}\text{Fe}_{2.5}\text{O}_{19}$ phase shown with a Rietveld fit.....	163
6.14 Neutron data of $\text{CaAl}_{11.5}\text{Mn}_{0.5}\text{O}_{19}$ phase shown with a Rietveld fit.....	163
6.15 Neutron data of $\text{CaAl}_{10}\text{SnMnO}_{19}$ phase shown with a Rietveld fit.....	164
6.16 (a) Average M3—O bond length, and (b) average $T_d$ bond angle of $\text{CaAl}_{12-x}\text{Fe}_x\text{O}_{19}$ (1) $\text{CaAl}_6\text{Fe}_6\text{O}_{19}$ , $\text{CaAl}_{11.5}\text{Mn}_{0.5}\text{O}_{19}$ (2), $\text{CaAl}_{10}\text{SnMnO}_{19}$ (3), and $\text{CaAl}_{12-2x}\text{Ti}_x\text{Ni}_x\text{O}_{19}$ (4) as a function of $x$ as determined by Rietveld refinement ( $\text{CaAl}_{12}\text{O}_{19}$ – small orange star). The estimated error bars are less than the size of the points in the figure.....	170

## LIST OF FIGURES (Continued)

<u>Figure</u>	<u>Page</u>
6.17 Diffuse-reflectance spectra of (a) $\text{CaAl}_{12-x}\text{Fe}_x\text{O}_{19}$ ( $x = 0.5-3.0$ ); (b) $\text{CaAl}_{12-x}\text{Mn}_x\text{O}_{19}$ ( $x = 0.1-0.6$ ); (c) $\text{CaAl}_{12-2x}\text{Sn}_x\text{Mn}_x\text{O}_{19}$ ( $x = 0.1-1.0$ ) and (d) $\text{CaAl}_{12-x}\text{Cr}_x\text{O}_{19}$ ( $x = 0.5-3.5$ ) series.....	176
6.18 Diffuse-reflectance spectra of $\text{CaAl}_{10}\text{Fe}_2\text{O}_{19}$ , $\text{CaAl}_{11.5}\text{Mn}_{0.5}\text{O}_{19}$ , $\text{CaAl}_{10}\text{SnMnO}_{19}$ and $\text{CaAl}_{10}\text{Cr}_2\text{O}_{19}$ .....	177
6.19 UV-VIS and NIR reflectance (%) of (a) $\text{CaAl}_{12-x}\text{Fe}_x\text{O}_{19}$ ( $x = 0.5-3.0$ ) series and Co-blue pigment; (b) $\text{CaAl}_{12-x}\text{Mn}_x\text{O}_{19}$ ( $x = 0.1-0.6$ ); (c) $\text{CaAl}_{12-2x}\text{Sn}_x\text{Mn}_x\text{O}_{19}$ ( $x = 0.1-1.0$ ) and (d) $\text{CaAl}_{12-x}\text{Cr}_x\text{O}_{19}$ ( $x = 0.5-3.5$ ) samples as a function of wavelength (nm).....	179
6.20 Magnetic susceptibility and inverse magnetic susceptibility of $\text{CaAl}_{11.5}\text{Mn}_{0.5}\text{O}_{19}$ and $\text{CaAl}_{11}\text{Ti}_{0.5}\text{Mn}_{0.5}\text{O}_{19}$ as a function of temperature; $1 \text{ emu (cgs units)} = 10^{-3} \text{ A m}^2 \text{ (SI units)}$ .....	180
6.21 Dielectric constant (a) and dielectric loss (b) of $\text{CaAl}_{11.5}\text{Fe}_{0.5}\text{O}_{19}$ as a function of temperature ( $^{\circ}\text{C}$ ); dielectric constant (c) and dielectric loss (d) of $\text{CaAl}_{11.4}\text{Sn}_{0.3}\text{Mn}_{0.3}\text{O}_{19}$ as a function of temperature ( $^{\circ}\text{C}$ ).....	181
6.22 Frequency dependence of dielectric constants (a) and dielectric losses (b) of $\text{CaAl}_{11.5}\text{Fe}_{0.5}\text{O}_{19}$ and $\text{CaAl}_{11.4}\text{Sn}_{0.3}\text{Mn}_{0.3}\text{O}_{19}$ at room temperature.....	182
7.1 Crystal structure of $\text{Li}_2\text{MnO}_3$ .....	187
7.2 $\text{LiMn}_2$ sheet in the honeycomb lattice of $\text{Li}_2\text{MnO}_3$ .....	188
7.3 XRD patterns of $\text{Li}_2\text{Mn}_{1-x}\text{Ti}_x\text{O}_3$ solid solution.....	189
7.4 Unit cell parameters $a$ , $b$ , $c$ of $\text{Li}_2\text{Mn}_{1-x}\text{Ti}_x\text{O}_3$ solid solution as a function of $x$ . The estimated errors for $a$ , $b$ , $c$ are less than the size of the points in the figure.....	190
7.5 (a) Unit cell volume ( $V$ ) as a function of $x$ ; (b) $c/a$ value as a function of $x$ . The estimated errors for $V$ and $c/a$ ratio are less than the size of the points in the figure.....	190
7.6 Colors of $\text{Li}_2\text{Mn}_{1-x}\text{Ti}_x\text{O}_3$ samples.....	191
7.7 Diffuse reflectance spectra of $\text{Li}_2\text{Mn}_{1-x}\text{Ti}_x\text{O}_3$ ( $x = 0, 0.4, 0.6, 1.0$ ) series.....	192

## LIST OF FIGURES (Continued)

<u>Figure</u>	<u>Page</u>
7.8 Diffuse reflectance spectra of $\text{Li}_2\text{MnO}_3$ sample with all peaks assigned.....	193
7.9 $\text{Li}_2\text{Mn}_{1-x}\text{Ti}_x\text{O}_3$ ( $x = 0, 0.2, 0.5, 0.8, 1.0$ ) reflectance vs. wavelength plots.....	194
8.1 Mineral sillenite.....	198
8.2 Cristal structure of $\text{Bi}_{12}\text{MnO}_{20}$ ( $\text{Bi}^{3+}$ : magenta spheres, $\text{Mn}^{4+}$ : blue tetrahedra, $\text{O}^{2-}$ : red spheres).....	198
8.3 (a) $\text{Bi}_{12}\text{MnO}_{20}$ (polyhedral view), (b) $\square\text{BiO}_5$ distorted octahedra ( $\square$ is a lone pair) and (c) $\text{MnO}_4$ tetrahedra.....	199
8.4 XRD patterns of $\text{Bi}_{12-x}\text{In}_x\text{TiO}_{20}$ solid solution.....	201
8.5 XRD patterns of $\text{Bi}_{12-x}\text{In}_x\text{Mn}_{0.2}\text{Ti}_{0.8}\text{O}_{20}$ series.....	202
8.6 Colors of $\text{Bi}_{12-x}\text{In}_x\text{TiO}_{20}$ compounds.....	202
8.7 Colors of $\text{Bi}_{12-x}\text{In}_x\text{Mn}_{0.2}\text{Ti}_{0.8}\text{O}_{20}$ solid solution.....	203
8.8 Diffuse reflectance spectra of $\text{Bi}_{12-x}\text{In}_x\text{TiO}_{20}$ .....	203
8.9 Diffuse reflectance spectra of $\text{Bi}_{12-x}\text{In}_x\text{Mn}_{0.2}\text{Ti}_{0.8}\text{O}_{20}$ solid solution.....	204
8.10 NIR reflectance spectra of $\text{Bi}_{12-x}\text{In}_x\text{TiO}_{20}$ compounds.....	205
8.11 NIR reflectance spectra of $\text{Bi}_{12-x}\text{In}_x\text{Mn}_{0.2}\text{Ti}_{0.8}\text{O}_{20}$ solid solution.....	205
8.12 XRD patterns of $\text{Bi}_{12}\text{Mn}_{1-x}\text{Ti}_x\text{O}_{20}$ solid solution.....	206
8.13 XRD patterns of $\text{Bi}_{12}\text{Mn}_{1-x}\text{Si}_x\text{O}_{20}$ solid solution.....	206
8.14 XRD patterns of $\text{Bi}_{12}\text{Mn}_{1-x}\text{Ge}_x\text{O}_{20}$ series.....	207
8.15 Unit cell parameters $a$ vs. $x$ for $\text{Bi}_{12}\text{Mn}_{1-x}\text{M}_x\text{O}_{20}$ ( $M = \text{Ti, Si, Ge}$ ) compounds.....	208
8.16 Unit cell volume ( $V$ ) of $\text{Bi}_{12}\text{Mn}_{1-x}\text{M}_x\text{O}_{20}$ ( $M = \text{Ti, Si, Ge}$ ) series as a function of $x$ .....	208
8.17 Colors of $\text{Bi}_{12}\text{Mn}_{1-x}\text{M}_x\text{O}_{20}$ ( $M = \text{Ti, Si, Ge}$ ) compounds.....	209

## LIST OF FIGURES (Continued)

<u>Figure</u>	<u>Page</u>
8.18 $L^*a^*b^*$ parameters of $\text{Bi}_{12}\text{Mn}_{1-x}\text{Ti}_x\text{O}_{20}$ series.....	209
8.19 Diffuse reflectance spectra of (a) $\text{Bi}_{12}\text{Mn}_{1-x}\text{Ti}_x\text{O}_{20}$ solid solution, (b) $\text{Bi}_{12}\text{Mn}_{1-x}\text{Si}_x\text{O}_{20}$ series and (c) $\text{Bi}_{12}\text{Mn}_{1-x}\text{Ge}_x\text{O}_{20}$ solid solution.....	211
8.20 NIR reflectance spectra of (a) $\text{Bi}_{12}\text{Mn}_{1-x}\text{Ti}_x\text{O}_{20}$ solid solution, (b) $\text{Bi}_{12}\text{Mn}_{1-x}\text{Si}_x\text{O}_{20}$ series and (c) $\text{Bi}_{12}\text{Mn}_{1-x}\text{Ge}_x\text{O}_{20}$ compounds.....	213
8.21 Magnetic susceptibility and inverse magnetic susceptibility of $\text{Bi}_{12}\text{Mn}_{0.8}\text{Ti}_{0.2}\text{O}_{20}$ ; 1 emu (cgs units) = $10^{-3}$ A m <sup>2</sup> (SI units).....	214
8.22 Magnetic susceptibility and inverse magnetic susceptibility as a function of temperature for $\text{Bi}_{12}\text{Mn}_{1-x}\text{Ti}_x\text{O}_{20}$ ( $x = 0.2, 0.6$ and $0.8$ ) samples (from Dr. Ramirez).....	215

## LIST OF TABLES

<u>Table</u>	<u>Page</u>
1.1 List of widely used color inorganic pigments.....	16
3.1 Cell parameters by Rietveld refinement of $\text{Ba}_5\text{Mn}_{3-x}\text{M}_x\text{O}_{12}\text{Cl}$ ( $M = \text{V}, \text{P}$ ).....	54
3.2 Neutron structural refinement of $\text{Ba}_5(\text{MnO}_4)_3\text{Cl}$ . The chemical formula of compound based on the refined occupancies is $\text{Ba}_5(\text{MnO}_4)_3\text{Cl}$ .....	54
3.3 Neutron structural refinement of $\text{Ba}_5\text{Mn}_{2.5}\text{V}_{0.5}\text{O}_{12}\text{Cl}$ . The chemical formula of compound based on the refined occupancies is $\text{Ba}_5\text{Mn}_{2.6}\text{V}_{0.4}\text{O}_{12}\text{Cl}$ .....	55
3.4 Neutron structural refinement of $\text{Ba}_5\text{Mn}_{0.2}\text{V}_{2.8}\text{O}_{12}\text{Cl}$ . The chemical formula of compound based on the refined occupancies is $\text{Ba}_5\text{Mn}_{0.3}\text{V}_{2.7}\text{O}_{12}\text{Cl}$ .....	55
3.5 Neutron structural refinement of $\text{Ba}_5\text{Mn}_{0.5}\text{P}_{2.5}\text{O}_{12}\text{Cl}$ . The chemical formula of compound based on the refined occupancies is $\text{Ba}_5\text{Mn}_{0.5}\text{P}_{2.5}\text{O}_{12}\text{Cl}$ .....	55
3.6 Selected geometric parameters: bond lengths ( $\text{\AA}$ ) and angles ( $^\circ$ ) of $\text{Ba}_5\text{Mn}_{0.2}\text{V}_{2.8}\text{O}_{12}\text{Cl}$ .....	56
3.7 Selected geometric parameters: bond lengths ( $\text{\AA}$ ) and angles ( $^\circ$ ) of $\text{Ba}_5(\text{MnO}_4)_3\text{Cl}$ .....	56
3.8 Selected geometric parameters: bond lengths ( $\text{\AA}$ ) and angles ( $^\circ$ ) of $\text{Ba}_5\text{Mn}_{2.5}\text{V}_{0.5}\text{O}_{12}\text{Cl}$ .....	57
3.9 Selected geometric parameters: bond lengths ( $\text{\AA}$ ) and angles ( $^\circ$ ) of $\text{Ba}_5\text{Mn}_{0.5}\text{P}_{2.5}\text{O}_{12}\text{Cl}$ .....	57
3.10 Vibrations with wavenumbers of $\text{Ba}_5(\text{MnO}_4)_3\text{Cl}$ , $\text{Ba}_5\text{Mn}_{2.5}\text{V}_{0.5}\text{O}_{12}\text{Cl}$ , $\text{Ba}_5\text{Mn}_{0.2}\text{V}_{2.8}\text{O}_{12}\text{Cl}$ and $\text{Ba}_5\text{Mn}_{0.5}\text{P}_{2.5}\text{O}_{12}\text{Cl}$ compounds and their assignments (maximum peaks are bold).....	65
3.11 Calculated magnetic moments, Curie and Weiss constants of $\text{Ba}_5(\text{MnO}_4)_3\text{Cl}$ , $\text{Ba}_5\text{Mn}_{1.5}\text{V}_{1.5}\text{O}_{12}\text{Cl}$ , $\text{Ba}_5\text{Mn}_{1.5}\text{P}_{1.5}\text{O}_{12}\text{Cl}$ , $\text{Sr}_5\text{Cr}_3\text{O}_{12}\text{Cl}$ , $\text{Sr}_5\text{Cr}_3\text{O}_{12}\text{F}$ , $\text{Sr}_5\text{Mn}_{0.5}\text{Cr}_{2.5}\text{O}_{12}\text{Cl}$ , $\text{Sr}_5\text{Cr}_2\text{VO}_{12}\text{Cl}$ and $\text{Sr}_5\text{Cr}_2\text{VO}_{12}\text{F}$ samples (* - theoretical magnetic moment of $\text{Sr}_5\text{Mn}_{0.5}\text{Cr}_{2.5}\text{O}_{12}\text{Cl}$ compound with two magnetic ions equals $1.95\mu_B$ ).....	68



## LIST OF TABLES (Continued)

<u>Table</u>	<u>Page</u>
4.1 Summary of $\text{CaAl}_{12}\text{O}_{19}$ rietveld refinement results.....	80
4.2 Relative-permittivity $K$ of $\text{CaAl}_{12}\text{O}_{19}$ , $\text{SrAl}_{12}\text{O}_{19}$ , $\text{PbAl}_{12}\text{O}_{19}$ and $\text{CaAl}_{10}\text{NiTiO}_{19}$ .....	81
4.3 Summary of $\text{SrAl}_{12}\text{O}_{19}$ structure results ( $a = 5.5766 \text{ \AA}$ , $c = 22.143 \text{ \AA}$ ).....	85
4.4 Summary of $\text{La}_{2/3+\delta}\text{Al}_{12-\delta}\text{O}_{19}$ structure results.....	86
4.5 Comparison of structural data for $\text{La}_{2/3+\delta}\text{Al}_{12-\delta}\text{O}_{19}$ phase.....	87
4.6 Site occupations in $\text{CaAl}_{10}M\text{TiO}_{19}$ ( $M = \text{Ni}$ and $\text{Ti}$ ) samples.....	89
4.7 Bond valence sums (BVS) for $AM_{12}\text{O}_{19}$ ( $A = \text{Ca}, \text{Sr}, \text{Ba}$ ; $M = \text{Al}, \text{Ga}, \text{Fe}$ ).....	90
4.8 Comparison of refined and modeled structure for $\text{CaAl}_{12}\text{O}_{19}$ .....	91
4.9 For the M2 (TBP) cation: displacement along $c$ and bond valence sum (BVS).....	93
4.10 Comparison of interatomic distances for $\text{CaAl}_{12}\text{O}_{19}$ , $\text{CaAl}_{10}\text{NiTiO}_{19}$ , and $\text{CaAl}_{10}\text{MgTiO}_{19}$ .....	96
5.1 Rietveld refinement results of neutron powder diffraction.....	123
5.2 Average bond distances ( $\text{\AA}$ ) from neutron refinements.....	125
5.3 $L^*$ , $a^*$ , $b^*$ values of selected hibonite samples with blue colors.....	130
5.4 Calculated magnetic moments $\mu_{\text{eff}}$ , Curie and Weiss constants of $\text{LaAl}_{11}\text{NiO}_{19}$ , $\text{Ca}_{0.5}\text{La}_{0.5}\text{Al}_{11.5}\text{Ni}_{0.5}\text{O}_{19}$ and $\text{CaAl}_{11}\text{Ti}_{0.5}\text{Ni}_{0.5}\text{O}_{19}$ samples.....	135
6.1 List of synthesized compounds.....	155
6.2 Cell parameters by Rietveld refinement of $\text{CaAl}_{9.5}\text{Fe}_{2.5}\text{O}_{19}$ , $\text{CaAl}_{11.5}\text{Mn}_{0.5}\text{O}_{19}$ and $\text{CaAl}_{10}\text{SnMnO}_{19}$ samples.....	164
6.3 Neutron structural refinement of $\text{CaAl}_{9.50}\text{Fe}_{2.50}\text{O}_{19}$ . The refined chemical formula of the compound is $\text{CaAl}_{9.47}\text{Fe}_{2.53}\text{O}_{19}$ .....	164

## LIST OF TABLES (Continued)

<u>Table</u>	<u>Page</u>
6.4 Neutron structural refinement of $\text{CaAl}_{11.50}\text{Mn}_{0.50}\text{O}_{19}$ . The refined chemical formula of the compound is $\text{CaAl}_{11.62}\text{Mn}_{0.38}\text{O}_{19}$ .....	165
6.5 Neutron structural refinement of $\text{CaAl}_{10}\text{Sn}_{1.0}\text{Mn}_{1.0}\text{O}_{19}$ . The refined chemical formula of the compound is $\text{CaAl}_{10.31}\text{Sn}_{0.94}\text{Mn}_{0.75}\text{O}_{19.01}$ .....	165
6.6 Thermal displacement parameters.....	166
6.7 Selected bond lengths ( $\text{\AA}$ ) of $\text{CaAl}_{9.5}\text{Fe}_{2.5}\text{O}_{19}$ , $\text{CaAl}_{11.5}\text{Mn}_{0.5}\text{O}_{19}$ and $\text{CaAl}_{10}\text{SnMnO}_{19}$ phases.....	167
6.8 Percent of site preferences in $\text{CaAl}_{9.5}\text{Fe}_{2.5}\text{O}_{19}$ , $\text{CaAl}_{11.5}\text{Mn}_{0.5}\text{O}_{19}$ , and $\text{CaAl}_{10}\text{SnMnO}_{19}$ compounds (without site multiplicities consideration).....	168
6.9 $L^*a^*b^*$ values and pictures of compounds.....	170
6.10 Estimated crystal field splitting (eV) of selected compounds.....	178
6.11 Calculated magnetic moments, Curie and Weiss constants of $\text{CaAl}_{11.5}\text{Mn}_{0.5}\text{O}_{19}$ and $\text{CaAl}_{11}\text{Ti}_{0.5}\text{Mn}_{0.5}\text{O}_{19}$ samples.....	180
7.1 $L^*a^*b^*$ values of $\text{Li}_2\text{Mn}_{1-x}\text{Ti}_x\text{O}_3$ compounds.....	191
7.2 Estimated crystal field splitting of $\text{Li}_2\text{Mn}_{1-x}\text{Ti}_x\text{O}_3$ compounds.....	193
8.1 Estimated band gap of $\text{Bi}_{12-x}\text{In}_x\text{Mn}_{0.2}\text{Ti}_{0.8}\text{O}_{20}$ series.....	204
8.2 $L^*a^*b^*$ values of $\text{Bi}_{12}\text{Mn}_{0.2}\text{Ti}_{0.8}\text{O}_{20}$ phase before and after the sunlight exposure experiment.....	213

## DEDICATION

Не благодаря, а вопреки...

To my dearest  
parents  
Марина and Александр.  
Thank you for your endless love and support!

## CHAPTER 1

### Introduction

Materials science studies various classes of inorganic compounds and searches for ways of their uses. It *focuses on known materials* and tries to find new ways of their practical application with help of chemistry, physics and engineering.

Materials chemistry *looks for new materials* and routes of the synthesis, investigates the physical and chemical properties, and describes the structures. A fundamental task of materials chemistry is studying the relationship between structure and properties [1,2]. The structures of crystalline solids reveal their features. The structure needs to be described in order to understand reaction mechanisms, vary them to synthesize new compounds and make interesting discoveries.

Solid state chemistry mainly focuses on ceramic materials; oxides are the dominant part of the class. Materials belong to ceramics are inert, hard and have high melting points what make them useful in our everyday life (floor, walls coating, dishware, bricks etc.) [3].

This thesis mainly focuses on synthesis, structure and properties study of apatite-type, hibonite-type,  $\text{Li}_2\text{Mn}_{1-x}\text{Ti}_x\text{O}_3$  ( $x = 0-1.0$ ), and sillenite-type,  $\text{Bi}_{12}\text{Mn}_{1-x}\text{M}_x\text{O}_{20}$  ( $x = 0-1.0$ ;  $M = \text{Ti, Si, Ge}$ ), novel inorganic environmentally friendly colored oxides which are promising candidates for new, stable, non-toxic and cheap pigments. The purpose of this chapter is to give a brief introduction to structure of crystalline solids, color in solids and pigments.

### 1.1 Transition Metal Oxides

Oxides is the wide class of inorganic compounds containing oxygen in oxidation state -2 and another element. Oxides are widespread in earth crust (~50% by mass are oxides of Al, Fe, Ca, Na, K, Mg, Ti, C, P, S, Mn, Ba) and in universe [4].

Transition metal oxides are attractive materials to investigate due to their various structures and properties. Transition metal oxides consist of oxygen anions and one or more transition metal cations (d- and f-elements from the periodic table of D.I. Mendeleev). The largest group of transition metal oxides is formed by 3d metals. Most of the 3d elements

have partially filled d orbitals which leads to various oxidation states. This property dictates a possible formation of oxides with different stoichiometry and non-stoichiometric oxides, compounds where elements are not present in simple proportions [5,6]. Presence of transition metal in several oxidation states and defects in crystal structure cause non-stoichiometry.

Real crystalline solids contain a lot of defects. Presence of defects is crucial element for formation of interesting properties: electronic and ionic conductivity, colors and luminescence, chemical reactivity, hardness and strength. There are four main groups of defects: 0D (point defects), 1D (line defects), 2D (surface defects), and 3D (volume defects). Point defects are vacancies, impurities, Frenkel defects (occur in solids where cations and anions have different sizes:  $M^+ \rightarrow V_{M^+} + M_{\text{interstitial}}^+$ ) and Schottky defects (occur in solids with similar sizes of cations and anions:  $M^+ + A^- \rightarrow V_M + V_A$ ). The 1D class includes dislocations and disclinations. 2D defects are grain boundaries, twin boundaries, stacking faults, surface, and interphase boundaries. The 3D class consists of voids, cracks, faulted regions, and thermal vibrations.

Compounds containing transition metal in two oxidation states called mixed-valence compounds. There are three types of the materials:

- Oxides having easily distinguishable oxidation states in different environments ( $\text{Pb}_3\text{O}_4 = \text{Pb}^{2+}_2\text{Pb}^{4+}\text{O}_4$ );
- Compounds with “hidden” oxidation states, sites in the structure are not equivalent and there is a small activation to electron transfer ( $\text{AgO} = \text{Ag}^{1+}\text{Ag}^{3+}\text{O}_2$ );
- Oxides with indistinguishable but recognizable oxidation states ( $\text{LaTi}_2\text{O}_4$  has  $\text{Ti}^{4+}$  and  $\text{Ti}^{3+}$ ).

Transition metal oxides are fascinating compounds for investigations. For examples, transition metal oxides are widely used as catalytic agents (zeolites contain large channels, they are very useful in ion exchange and gas absorption [7,8]), superconductors ( $\text{YBa}_2\text{Cu}_3\text{O}_{7-x}$  [9]), dielectrics ( $\text{CaCu}_3\text{Ti}_4\text{O}_{12}$  [10]) and piezoelectrics ( $\text{PbZnO}_3$ — $\text{PbTiO}_3 = \text{PZT}$  [11]).

## 1.2 Structure of Crystalline Compounds

In order to find relationship between structure and properties, crystal structure of compounds needs to be characterized. The main characteristic of all crystals is 3D periodicity of structure; all crystalline solids have regular or long-range order. The structure and geometry of the smallest blocks - “bricks” used to build an endless structure reflect the properties of the whole crystal.

The common way to describe crystalline solids is usage of the close packing array of spheres, where structure might be described as a set built from layers, each layer consists of spheres (each sphere is a representation of a “construction unit”: atom, ion etc.). When atoms form a crystal they have a tendency to fill the volume with maximum efficiency and minimum amount of void space. There are two possible ways to form close packing array using atoms (spheres) with the same size (Fig. 1.1). First way called 2D square array (21.5% of void area) and the second is 2D hexagonal array (9.3% of void area). In 2D square array each atom is surrounded by four closest neighbors and in 2D hexagonal array each sphere has six atoms around it, six is the maximum number of possible neighbors into one layer. 2D square array is not the most effective way to arrange atoms in space, hexagonal array is predominant type of atomic arrangement in crystalline solids, let's focus on it.

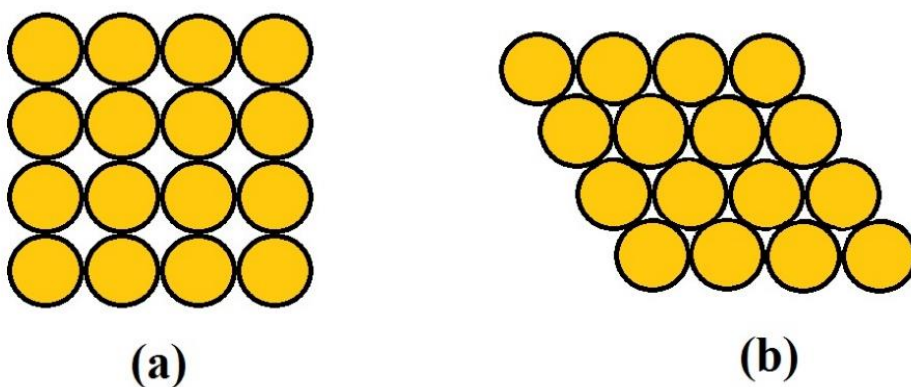


Figure 1.1 (a) 2D square array and (b) 2D hexagonal array of equal atoms.

If one continues to build 3D atoms array and want to put the second layer above the first one, there are two ways to do it: the next layer can sit into the cavities marked B (red)

and form AB-stacking or into the cavities labeled C (blue) and make AC-stacking (Fig. 1.2). Without the third layer AB-stacking and AC-stacking are indistinguishable.

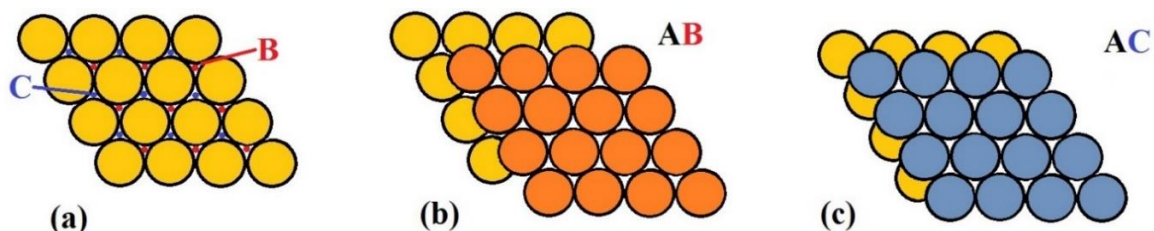


Figure 1.2 (a) 1D the closest packing of equal atoms, (b) 2D AB-stacking and (c) 2D AC-stacking.

The third layer may be built using two different ways: ABC and ABA (Fig. 1.3). ...ABCABC... stacking gives cubic close packing (*ccp*) array and ...ABABAB... sequence forms hexagonal close packing (*hcp*) array. In case of ABAB stacking, first and third layers are the same. Arrangement of the fourth layer repeats the first layer order in case of ABCABC stacking.

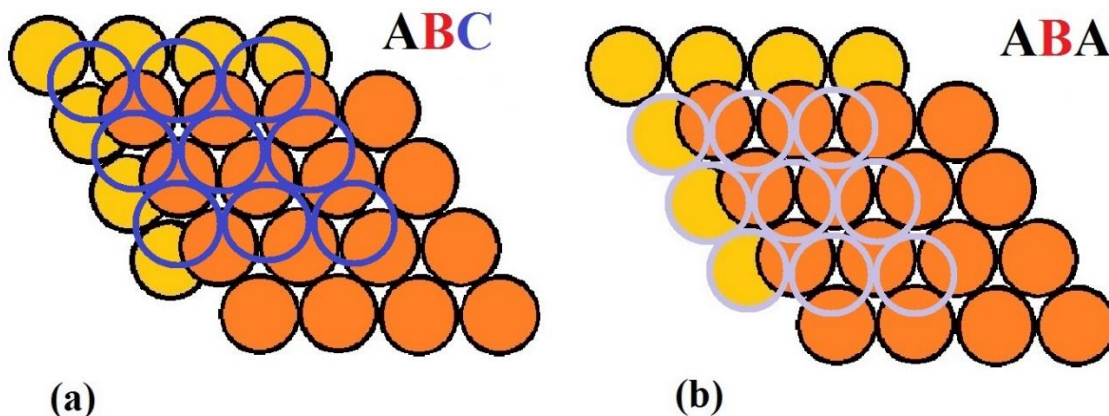


Figure 1.3 (a) ABC cubic 3D close packing array and (b) ABA hexagonal 3D close packing array.

There are two types of holes (voids) in the structure. Tetrahedral hole ( $T_d$ ) is formed between three neighboring atoms from the first layer and the fourth sphere above them belonging to the second layer (Fig. 1.4). Three spheres from the first layer and three spheres from the second layer form the octahedral hole ( $O_h$ ). Tetrahedral hole is usually smaller than octahedral hole. Holes play very important role in the crystal structures, for example,

when compound is formed from two types of atoms with big difference in ionic radii, then the larger atoms form close packing structure and the smaller atoms occupy the holes [12]. Each atom in close packing structure is associated with one octahedral site (hole) and two tetrahedral sites (holes).

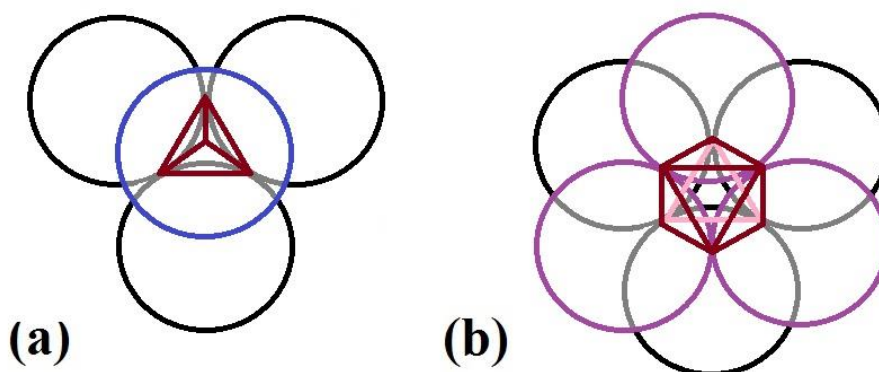


Figure 1.4 (a) Formation of tetrahedral and (b) octahedral holes in close packing structure.

There is a different mutual arrangement of tetrahedral sites in cubic and hexagonal close packing structures. In hexagonal close packing (ABA array) two tetrahedral holes might be built based on three atoms from layer B, their tops is pointing in opposite directions and they are face-shared tetrahedra (Fig. 1.5(a)). In cubic close packing (ABC array) two tetrahedra have different bases; they are edge-shared (Fig. 1.5(b)) [13].

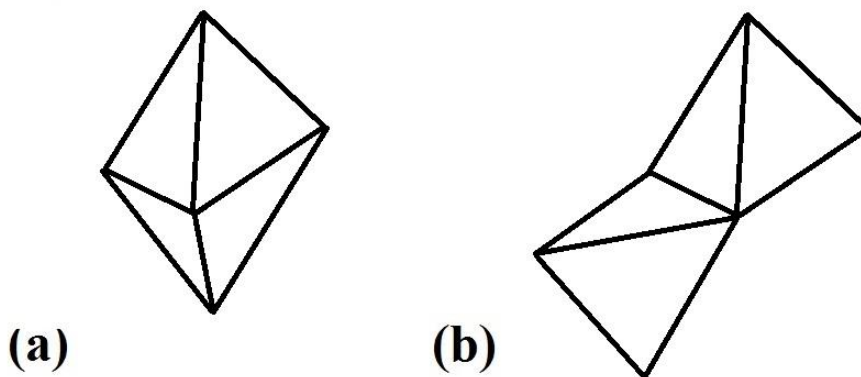


Figure 1.5 Mutual arrangement of tetrahedral holes in hexagonal (a) and cubic (b) close packing structures.



Each crystal structure can be characterized by describing the smallest unit of the 3D sequence: lattice cell or unit cell. A single unit cell fully describes the symmetry, geometry and the special arrangement of atoms in the whole crystal. There are three main types of unit cell: simple cubic (SC), body-centered cubic (BCC) and face-centered cubic (FCC) (Fig. 1.6). There is one atom at each corner in SC cell; the cell has the smallest packing efficiency equals 52% by volume and one atom per unit cell. BCC cell consists of eight atoms at corners of the cube and one atom in its center. There are two atoms per unit cell and packing efficiency is 68%. FCC cell has the largest packing efficiency (74%); eight atoms sit at the corners and one atom in the center of each face. There are four atoms per FCC cell [14].

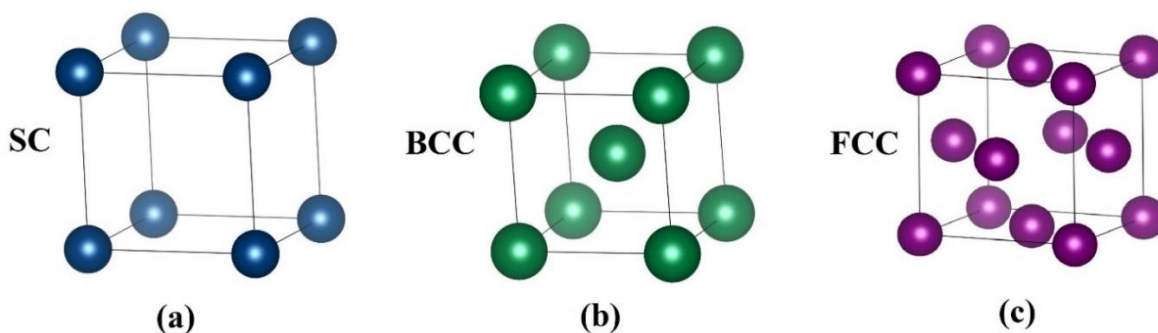


Figure 1.6 Simple cubic (a), body-centered cubic (b) and face-centered cubic (c) unit cells.

Based on various shapes of unit cells there are seven crystal systems possible, and they differ in unit cell lengths ( $a$ ,  $b$ ,  $c$ ) and unit cell angles values ( $\alpha$ ,  $\beta$ ,  $\gamma$ ):

- Cubic  $a = b = c$ ,  $\alpha = \beta = \gamma = 90^\circ$
- Tetragonal  $a = b \neq c$ ,  $\alpha = \beta = \gamma = 90^\circ$
- Hexagonal  $a = b \neq c$ ,  $\alpha = \beta = 90^\circ$ ,  $\gamma = 120^\circ$
- Orthorhombic  $a \neq b \neq c$ ,  $\alpha = \beta = \gamma = 90^\circ$
- Trigonal  $a = b \neq c$ ,  $\alpha = \beta = 90^\circ$ ,  $\gamma = 120^\circ$  or  $a = b = c$ ,  $\alpha = \beta = \gamma \neq 90^\circ$
- Monoclinic  $a \neq b \neq c$ ,  $\alpha = \gamma = 90^\circ$ ,  $\beta \neq 90^\circ$
- Triclinic  $a \neq b \neq c$ ,  $\alpha \neq \beta \neq \gamma \neq 90^\circ$

Crystalline solids can be characterized based on the type of unit cell as described above and the nature of species sit at corners of lattice. Using this principle all crystals can be

divided into three classes: molecular solids, ionic solids and atomic solids [15]. Molecules are the composite elements in molecular solids, for example  $\text{CO}_2(\text{s})$  and  $\text{H}_2\text{O}(\text{s})$ . Molecules are bonded together by very weak intermolecular forces (dispersion forces, dipole-dipole and hydrogen bonding) and these compounds have low melting points. Composite units in ionic solids are ions ( $\text{NaCl}$ ,  $\text{CsCl}$ ,  $\text{ZnS}$  etc.). These crystals have high melting points. Atoms form atomic solids: nonbonding, metallic and network covalent. Solid noble gases are nonbonding atomic solids; they are bonded by weak intermolecular dispersion forces and have low melting points. Metallic atomic solids are all metals; melting points may vary due to different strength of metallic bonds. Network covalent atomic solids are hold together by strong covalent bonds and have high melting points (diamond and graphite).

### 1.3 Bonding in Solids

To understand properties (color, magnetism, stability etc.) of solids one needs to understand the nature of bonding. Crystal field theory serves to the purpose. Crystal field theory is a model which describes how chemical environment changes configuration of transition metal d-orbitals (Fig. 1.7) [16, 17]. All d-orbitals have low electron density near the nucleus; d-orbitals lobes are located far away from each other and have weak mutual influence.

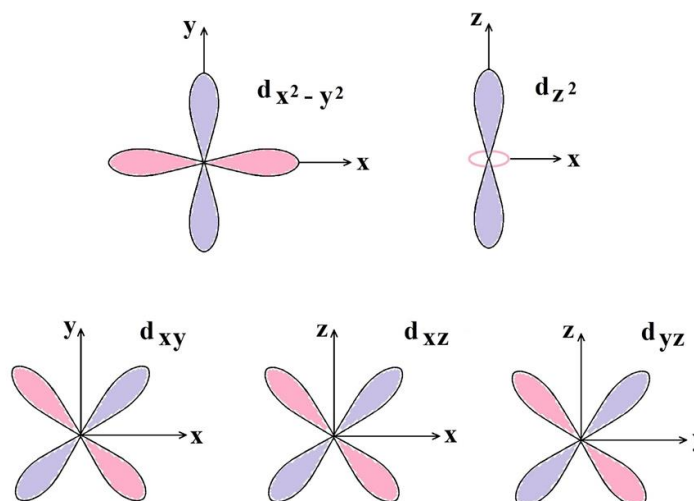


Figure 1.7 Five d orbitals:  $d_{x^2-y^2}$  and  $d_{z^2}$  have higher energy (point along the axes) and  $d_{xy}$ ,  $d_{xz}$ ,  $d_{yz}$  have lower energy (point between exes).

Free atom's d-orbitals have the same energy, they are degenerate. In crystal anions surround metal atom and cause an electric field (crystal field); there is an interaction between central atom and ligands. Let's consider a central 3d metal ion in octahedral complex (Fig. 1.8).

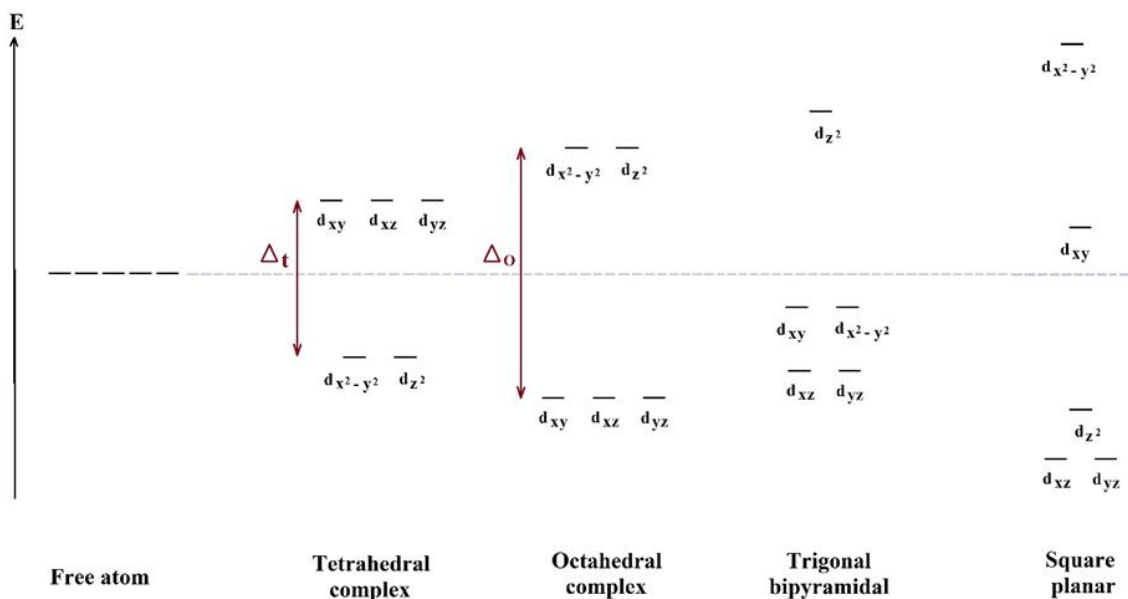


Figure 1.8 Crystal field splitting diagrams for several common complexes.

In  $O_h$  crystal field d-orbitals are splitted into two sets with different energies:  $d_{z^2}$  and  $d_{x^2-y^2}$  have higher and  $d_{xy}$ ,  $d_{yz}$  and  $d_{xz}$  have lower energy. The split is observed because  $d_{z^2}$  and  $d_{x^2-y^2}$  lobes pointing towards ligands, it increases the repulsion between them (the interaction pushes  $d_{z^2}$  and  $d_{x^2-y^2}$  orbitals up in energy);  $d_{xy}$ ,  $d_{yz}$  and  $d_{xz}$  orbitals have nodal planes in these directions and there is reduced repulsion between central atom and ligands (the interaction pushes  $d_{xy}$ ,  $d_{yz}$ ,  $d_{xz}$  orbitals down in energy). The crystal field splitting energy ( $\Delta$ ) is the difference in energy between splitted d-orbitals. If  $\Delta$  is large the complex called strong-field complex, there is a weak-field complex for small crystal field splitting energy. Geometry of complex dictates the d-orbitals splitting pattern; crystal field splitting diagrams for several common complexes are shown in Figure 1.8. The disappearance of d-orbitals degeneracy relates to the electronic, magnetic, optical and thermodynamic properties.

## 1.4 Color in Solids

Experience has shown that the prediction of the coloring properties of yet unsynthesized compounds is a very risky business which still remains in the realm of art rather than of science. So the world of color remains a mysterious and fascinating place, and the mystery only serves to deepen as we come to know more and more about it.

- Mary Virginia Orna [18]

Color is a property of material and like taste, hearing and smell it helps to understand the world around us. Using our eyes we get the largest amount of information. From ancient times the problem of visual perception and perception of color has been studied by scientists [19]. Color is the result of information taken by the eye and parsed by the brain, and light play a crucial role in the process. White light is a combination of electromagnetic waves with different wavelengths; it might be separated into spectrum by transparent prism (Fig. 1.9).

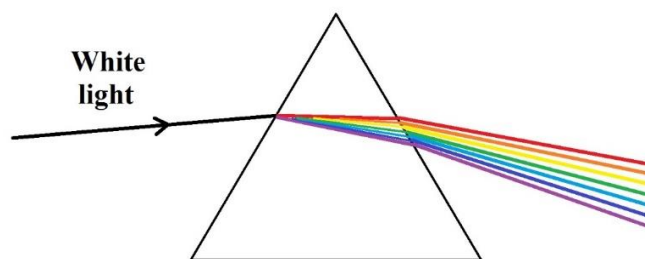


Figure 1.9 Separation of white light into the color spectrum (seven colors) after passing through the prism.

The range of electromagnetic waves which human eye is able to perceive called visible light (380 ~ 770 nm); it is very narrow region of the electromagnetic spectrum (Fig. 1.10).

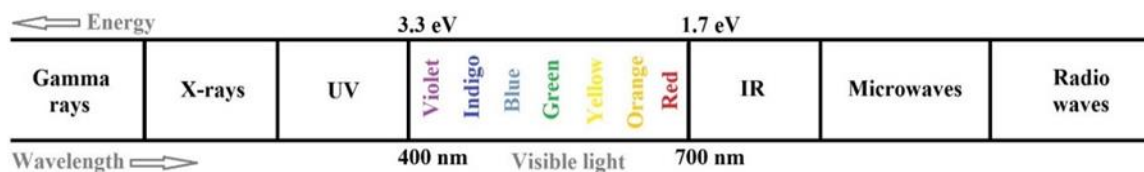


Figure 1.10 Electromagnetic spectrum.

The light with the longest wavelength we interpret as a red color, the light with the shortest wavelength: as a purple color. If material absorbs, for example, orange color, we see blue color, which is opposite or complimentary to orange (Fig. 1.11) [20].

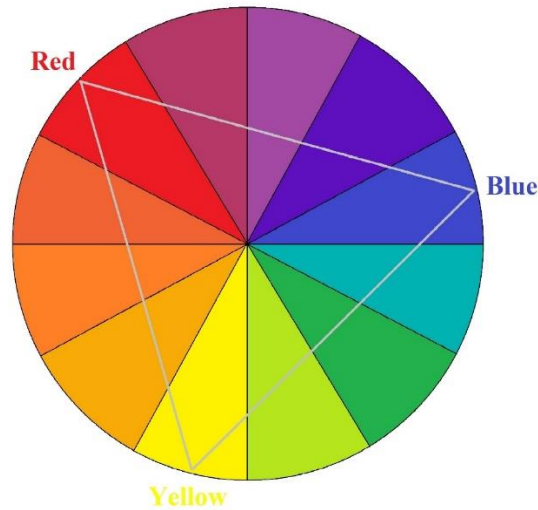


Figure 1.11 Color wheel with three primary subtractive colors: red, yellow and blue.

One must distinguish additive and subtractive color mixing (Fig. 1.12). Red, green and blue are primary colors of light. Mixing two colors gives new color, which is lighter; mixing three colors results in white light: it is additive color mixing. Work of TV, computer screens, electronic devices is based on this principle. Red, yellow and blue are main colors of subtractive color mixing. In this case mixed colors have a tendency to be darker and mixture of the three gives black color. Subtractive color scheme is used in painting and printing [21].

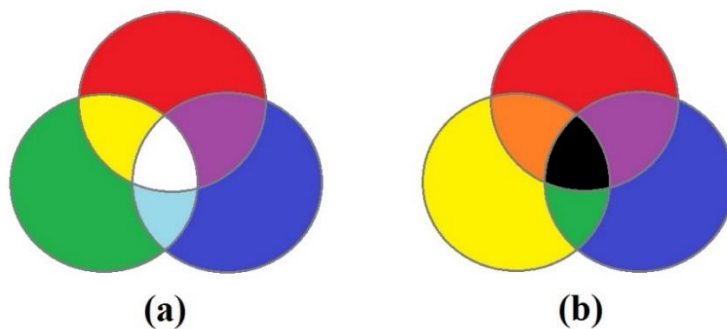


Figure 1.12 Difference between additive (a) and subtractive (b) colors.

Color is directly related to material's ability to absorb or reflect light. Changes occurring in atom during this process are crucial to understand the origin of color in inorganic compounds. When electron absorbs energy of light photon it moves to a higher energy level (Fig. 1.13). When electron comes back to the ground state, radiation emitted. If the energy falls into the visible region of the spectrum we can see a color.

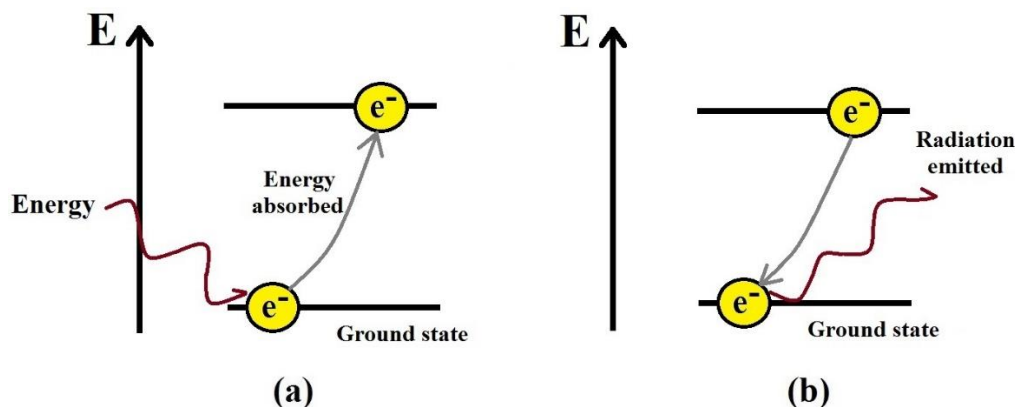


Figure 1.13 (a) An electron absorbs radiation and moves to the upper energy level; (b) emission of radiation when electron goes down to the ground state.

There are five main sources of color in inorganic solids:

1) d-d interatomic transitions.

d-block transition metals show different color in different ligand environments. d-d interatomic (localized) transitions are responsible for color in this case. During d-d transition electron moves between partially filled d-orbitals inside the same atom and as a result there is an increasing of light absorption in the visible region of the spectrum. The examples of compounds showing d-d interatomic transitions are  $\text{Cr}^{3+}$  gemstones (ruby and emerald),  $\text{Cu}^{2+}$  compounds (malachite:  $\text{Cu}_2\text{CO}_3(\text{OH})_2$  and turquoise:  $\text{CuAl}_6(\text{PO}_4)_4(\text{OH})_8 \cdot \text{H}_2\text{O}$ ),  $\text{Co}^{2+}$  compounds ( $\text{Al}_2\text{CoO}_4$ ) [22].

Gemstones ruby and emerald contain  $\text{Cr}^{3+}$  impurity substitutes for  $\text{Al}^{3+}$  on octahedral site [23]. Ruby is bright red and emerald in green. Small changes in  $\text{Cr}^{3+}$  environment cause changes in crystal field splitting energy and as a result dramatic changes occur in observed color. Doped transition metal which causes the color called chromophore element;  $\text{Cr}^{3+}$  is a chromophore in ruby and emerald gems.  $\text{Al}_2\text{O}_3$  is a host structure of ruby and

$\text{Be}_3\text{Al}_2\text{Si}_6\text{O}_{18}$  (beryl) is the structure of emerald (Fig. 1.14).  $\text{Al}_2\text{O}_3$  is a hexagonal close-packed oxygen framework where  $2/3$  of  $O_h$  holes filled by  $\text{Al}^{3+}$ . Addition of beryllium and silicon to the  $\text{Al}_2\text{O}_3$  structure results in formation of more open beryl structure. In beryl metal-oxygen bonds are more covalent comparing to ruby and  $\Delta$  is smaller ( $\Delta = 2.05$  eV in emerald and 2.23 eV in ruby) [24].

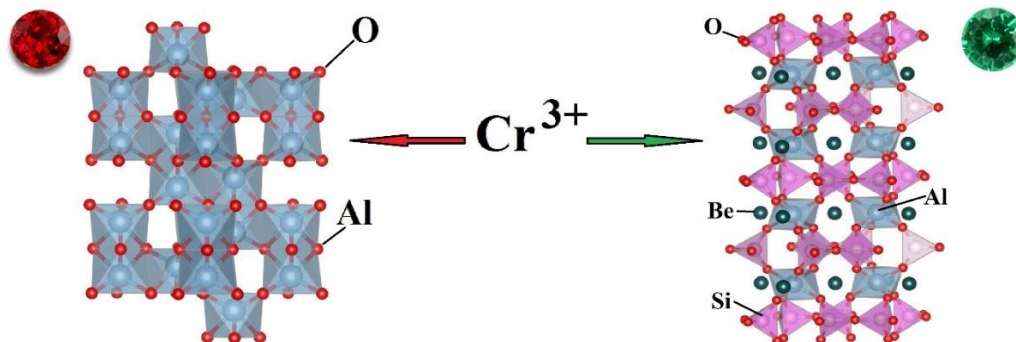


Figure 1.14  $\text{Cr}^{3+}$  is a chromophore element in ruby (left) and emerald (right) gems [25,26].

## 2) Charge transfer excitations (metal-metal, anion-metal).

Examples are  $\text{Fe}^{2+} \rightarrow \text{Ti}^{4+}$  charge transfer in sapphire and  $\text{Fe}^{2+} \rightarrow \text{Fe}^{3+}$  in Prussian blue ( $\text{Fe}_4[\text{Fe}(\text{CN})_6]_3 \cdot x\text{H}_2\text{O}$ ). Sapphire is an example of gem with metal-metal charge transfer transitions. Impurities (iron and titanium) in corundum host structure are responsible for bright blue color of the compound [27]; the color is due to metal-metal charge transfer excitations:  $\text{Fe}^{2+} + \text{Ti}^{4+} \rightarrow \text{Fe}^{3+} + \text{Ti}^{3+}$  (Fig. 1.15).

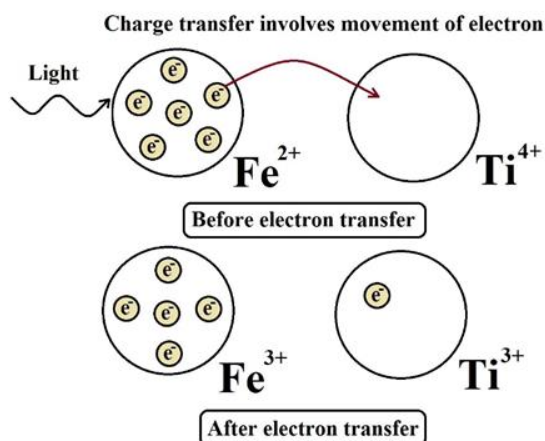


Figure 1.15 Schematic representation of charge transfer in sapphire.

The electron movement is allowed because in  $\text{Al}_2\text{O}_3$  structure titanium and iron occupy face-shared octahedra sites, which allows  $d_{z^2}$  orbitals overlap along  $c$ -axis (Fig. 1.16).

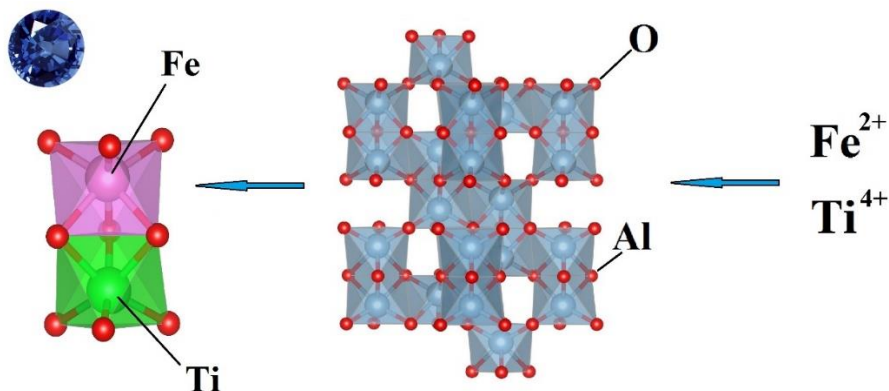


Figure 1.16 Structure of sapphire [28].

Usually wavelengths of metal-anion charge transfer excitations fall into UV region and cannot be seen by human eye. However, tetrahedrally coordinated  $d^0$  metals in high oxidation states are electronegative enough to shift wavelengths from UV to visible region. Examples are white  $\text{Ca}_3(\text{VO}_4)_2$  having tetrahedral  $\text{V}^{5+}$  and yellow  $\text{PbCrO}_4$  with  $\text{Cr}^{6+}$  in  $T_d$  coordination [29].

### 3) Color centers.

Defects, for example cation or anion vacancy, occur when crystal is exposed by radiation or heated. Electron or hole might be trapped in crystal lattice, frozen in this empty site and create color center or F-center (from German “Farbe” – color [30,31]). The energy which is absorbed by color centers usually lies in the visible region [32]. The observed color depends on the host structure. Alkali halides, “smoky” quartz, violet amethyst (doped  $\text{SiO}_2$ ) and blue topaz (doped  $\text{Al}_2\text{SiO}_4(\text{F},\text{OH})_2$ ) are examples of materials having a tendency to form color centers. Fluorite structure with and without color center is shown in Figure 1.17. Formation of Frenkel defects lead to the color centers appearance and as a result  $\text{CaF}_2$  gets purple color.



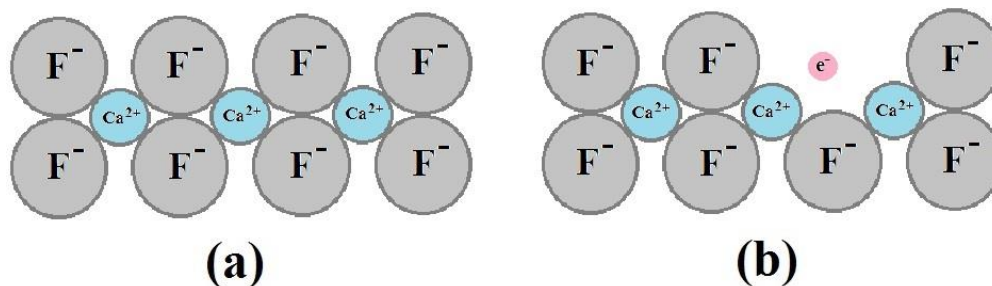


Figure 1.17 (a) Schematic representation of fluorite structure, (b) fluorite with color center (trapped electron).

#### 4) Intraband excitations in metals.

A distinctive feature of all metals is weak connection of valence electrons with nucleus and their ability to move easily to upper energy levels [33]. Transformation of atomic orbital into molecular orbitals and band in metal shown in Figure 1.18(a). When two atoms of metal interact then two molecular orbitals form instead of two atomic orbitals. Number of molecular orbitals and allowed energy states grows; gaps between them decrease with increasing of number of atoms ( $N$ ). At  $N = N_a = 10^{23}$  there are  $10^{23}$  molecular orbitals which are practically indistinguishable, they form continuous energy band; within energy band electrons can move easily. Presence of energy band determines unique properties of metals including interesting optical properties, in particular metallic luster.

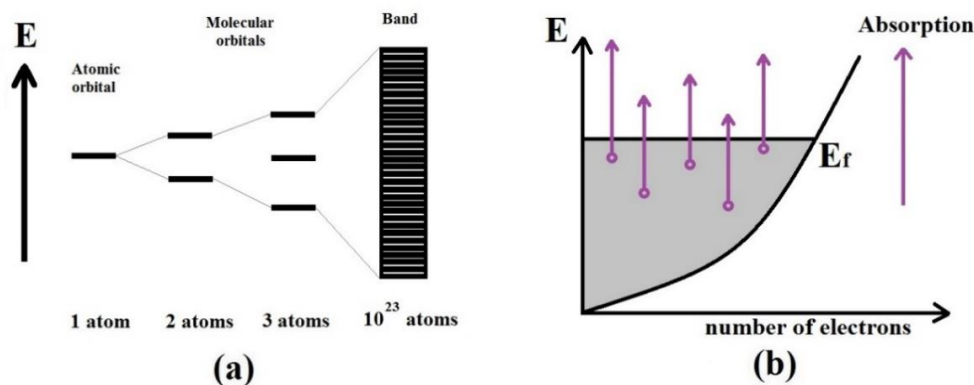


Figure 1.18 (a) Transformation of atomic orbital into molecular orbitals and band in metal and (b) jumps of excited electrons to unoccupied levels.

When metal absorbs light electrons jump from energy band through Fermi level to unoccupied upper orbitals Figure 1.18(b) [34]. Almost instantly electrons emit the same wavelength light, go down to lower levels and we can see metallic luster. This phenomenon explains the fact that most of the metals have shiny, silver color. Metals absorb and reflect light mostly on the surface, it doesn't allow light to go profoundly inside the bulk.

##### 5) Valence to conduction band transitions in semiconductors.

Energy gap between valence (occupied) band and conduction (unoccupied) band called band gap ( $E_g$ ). In Figure 1.19 a comparison of insulator, semiconductor and metal band gaps is shown. Band gap value affects the observed color of material. Compounds with large band gap ( $\sim 3$  eV and higher) reflect all incident light and appear white, for example ZnO has  $E_g = 3.0$  eV. Semiconductors with large  $E_g$  are good insulators. If material has small band gap and absorbs all wavelength it has black color (PbS:  $E_g = 0.4$  eV). Compounds with band gap varies from  $\sim 1.8$  eV to  $\sim 3$  eV show red, orange or yellow color (CdS is yellow:  $E_g = 2.6$  eV;  $\text{CdS}_{1-x}\text{Se}_x$  is orange:  $E_g = 2.3$  eV; HgS is red:  $E_g = 2.0$  eV) [35]. For instance, HgS (cinnabar, vermillion) absorbs all wavelengths with energy 2.0 eV and larger (yellow, green, blue and violet) and shows red color.

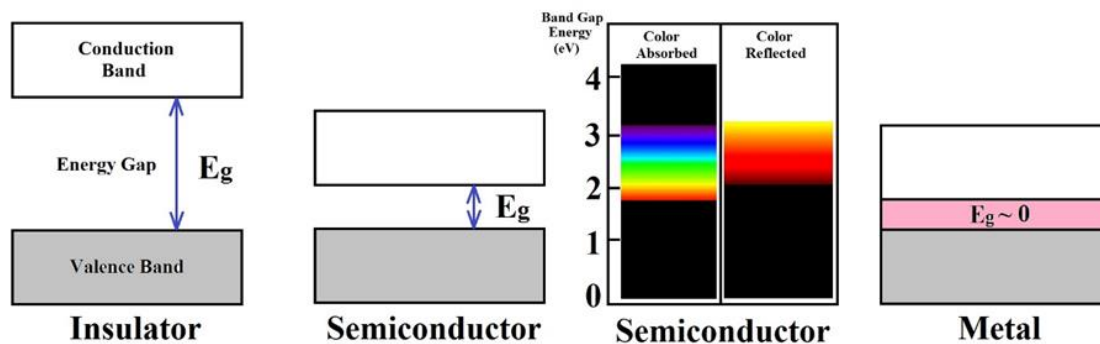


Figure 1.19 Band gaps in insulator, semiconductor and metal.

Band gap might be engineered by making solid solution of semiconductors, doping another element into the structure and changing the overlap between valence and conduction bands.

One should differentiate luminescence, fluorescence and phosphorescence. The process of light emission by the material after an energy (not from heat) has been absorbed called luminescence. There are several types of luminescence based on its origin: bio-, chemi-, electro-luminescence etc. Fluorescence (named after mineral fluorite) is one of the luminescence types. It is a process when material absorbs incident electromagnetic radiation and then emits light with different wavelength. Phosphorescence differ from fluorescence by amount of time needed for electrons to go down from excited state to the ground state. Fluorescent materials re-emit light during small portion of a second while phosphorescent compounds can emit light for several minutes or even hours [36].

### 1.5 Inorganic Pigments

Pigment from the Latin word “pigmentum” (paint), is an inorganic material with wavelength selective absorption (Fig. 1.20). Pigments impart different colors to materials; they are integral part of coating substances (paints, inks, plastics, rubber etc.) [37,38].



Figure 1.20 OSU t-shirt absorbs all colors except orange and reflects only orange light.

There are a lot of known pigments having all possible colors (Table 1.1).

Table 1.1 List of widely used color inorganic pigments [39,40].

Pigment	Color
BaCuSi <sub>2</sub> O <sub>6</sub> – Han purple, NH <sub>4</sub> MnP <sub>2</sub> O <sub>7</sub> – manganese violet, Co <sub>3</sub> (PO <sub>4</sub> ) <sub>2</sub> – cobalt (II) phosphate	purple

Na <sub>8-10</sub> Al <sub>6</sub> Si <sub>6</sub> O <sub>24</sub> S <sub>2-4</sub> – Ultramarine, CoAl <sub>2</sub> O <sub>4</sub> – cobalt blue, CaCuSi <sub>4</sub> O <sub>10</sub> – Egyptian blue, Cu <sub>3</sub> (CO <sub>3</sub> ) <sub>2</sub> (OH) <sub>2</sub> – Azurite, Fe <sub>7</sub> (CN) <sub>18</sub> – Prussian blue, YInMn blue	<b>blue</b>
Cr <sub>2</sub> O <sub>3</sub> – chrome green, CoZnO <sub>2</sub> – cobalt green, Cu <sub>2</sub> CO <sub>3</sub> (OH) <sub>2</sub> – malachite, Cu(C <sub>2</sub> H <sub>3</sub> O <sub>2</sub> ) <sub>2</sub> •3Cu(AsO <sub>2</sub> ) <sub>2</sub> – Paris green, CuHAsO <sub>3</sub> – Scheele's green, Cr <sub>2</sub> O(OH) <sub>4</sub> – Viridian green	<b>green</b>
As <sub>2</sub> S <sub>3</sub> – orpiment, CdS – cadmium sulfide, PbCrO <sub>4</sub> – lead chromate, K <sub>3</sub> Co(NO <sub>2</sub> ) <sub>6</sub> – Aureolin, Fe <sub>2</sub> O <sub>3</sub> •H <sub>2</sub> O – yellow ochre, SnS <sub>2</sub> – mosaic gold: stannic sulfide, ZnCrO <sub>4</sub> – zinc yellow	<b>yellow</b>
PbCrO <sub>4</sub> + PbO – chrome orange, Cd <sub>2</sub> SSe – cadmium sulfoselenide	<b>orange</b>
As <sub>4</sub> S <sub>4</sub> – Realgar, CdSe – cadmium red, Fe <sub>2</sub> O <sub>3</sub> – red ochre, HgS – Vermilion, Pb <sub>3</sub> O <sub>4</sub> – red lead	<b>red</b>
Fe <sub>2</sub> O <sub>3</sub> + MnO <sub>2</sub> + nH <sub>2</sub> O + Si + Al <sub>2</sub> O <sub>3</sub> – raw umber	<b>brown</b>

Unfortunately, some pigments suffer from environmental, stability and toxicity issues. As, Cd, Hg, Pb and Se containing pigments are very toxic (Fig. 1.21), ultramarine and azurite are not stable under heating and acidic conditions. Old pigments need to be improved and new pigments are waiting for the discoveries. Cation substitution in a host lattice is an important way to synthesize new inorganic pigments.



The problem with IR radiation is absence of influence on observed color; all IR radiation is converted into heat. All light energy which is not reflected, transformed into heat and transferred by conduction and convection (Fig. 1.23). There is a big disadvantage of dark cars and roofs, which don't reflect radiation at all, they heat up very quickly, but there are pigments with high reflectance rate in IR region, they called "Cool pigments".

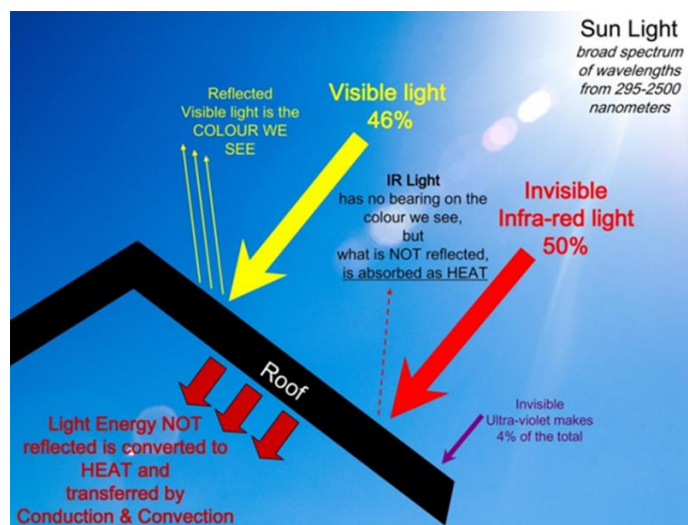


Figure 1.23 All light which is not reflected, transformed into heat and transferred by conduction and convection [42].

## 1.6 References

- [1] Weller, M.T., Inorganic Materials Chemistry, Oxford University Press, 1994, pp. 1-88.
- [2] Muller, U., Inorganic Structural Chemistry (2<sup>nd</sup> edition), John Wiley & Sons, Ltd, 2007, pp. 1-268.
- [3] [https://en.wikipedia.org/wiki/Ceramic#By\\_usage](https://en.wikipedia.org/wiki/Ceramic#By_usage) (accessed 12.01.2016).
- [4] <https://www.britannica.com/science/oxide> (accessed 12.01.2016).
- [5] Greenwood, N.N., Ionic crystals, lattice defects, and non-stoichiometry Butterworths, London, 1968
- [6] Sorensen, O.T. (Ed.), Non-stoichiometric oxides, New York: Academic Press, Incorporated, 1981, pp. 1-60.
- [7] Peterson, D.L., Helfferich, F., Blytas, G.C., J. Phys. Chem. Solids 26(5) (1965) 835.
- [8] Ilin, V.G., Rastrene, A.I., Neimark, I.E., Ukr. Khim. Zh. 36(7) (1970) 675.
- [9] Bednorz, J.G., Muller, K.A., Z. Phys. B Con. Mat. 64(2) (1986) 189.
- [10] Ramirez, A.P., Subramanian, M.A., Gardel, M. et al., Solid State Commun. 115(5) (2000) 217.
- [11] Leontsev, S.O., Eitel, R.E., Sci. Tech. Adv. Mater. 11(4) (2010) 1.

- [12] Nikolskiy, A.B., Suvorov, A.V., College Chemistry textbook, Saint Petersburg: Khimizdat, 2001, pp. 1-512 (in Russian).
- [13] Rozova, M.G., Shpanchenko, R.V., Elements of structural inorganic chemistry (textbook), Moscow State University: Moscow, 2001 (in Russian).
- [14] Tro, N.J., Chemistry: a molecular approach (3<sup>rd</sup> edition), Prentice Hall, 2013, pp. 1-1081.
- [15] Hyde, B.G., Andersson, S., Inorganic crystal structures, John Wiley & Sons, Inc., New York, 1989, pp. 1-430.
- [16] Burns, R.G., Mineralogical applications of crystal field theory (2<sup>nd</sup> edition), Putnis A., Liebermann, R.C. (Ed.), Cambridge University Press, 2005, pp. 1-576.
- [17] Tilley, R.J.D., Understanding solids: the science of materials (2<sup>nd</sup> edition), John Wiley & Sons, Ltd, 2004, pp. 1-616.
- [18] Orna, M.V., J. Chem. Ed. 5(8) (1987) 478.
- [19] <http://slideplayer.com/slide/5888177/> (accessed 12.02.2016).
- [20] <http://colory.ru/colorhistory/> (accessed 12.02.2016).
- [21] <http://www.slideshare.net/solohermelin/color-theory-39956038> (accessed 12.02.2016).
- [22] Tokura, Y., Curr. Opin. Solid State Mater. Sci. 3 (1998) 175.
- [23] [http://www.uio.no/studier/emner/matnat/kjemi/KJM3100/v06/undervisningsmateriale/optical1\\_lect21\\_pw.pdf](http://www.uio.no/studier/emner/matnat/kjemi/KJM3100/v06/undervisningsmateriale/optical1_lect21_pw.pdf) (accessed 12.02.2016).
- [24] Nassau, K., The physics and chemistry of color (2<sup>nd</sup> edition), Wiley-Interscience, 2001, pp. 1-496.
- [25] <https://bitcointalk.org/index.php?topic=1333253.0> (accessed 12.02.2016).
- [26] <http://www.agta.org/gemstones/variation-ruby.html> (accessed 12.02.2016).
- [27] <http://www.webexhibits.org/causesofcolor/8.html> (accessed 12.02.2016).
- [28] <https://en.wikipedia.org/wiki/File:Sapphire.png> (accessed 12.02.2016).
- [29] [http://www.minsocam.org/MSA/K12/K\\_12.html/MSA/collectors\\_corner/arc/color.htm](http://www.minsocam.org/MSA/K12/K_12.html/MSA/collectors_corner/arc/color.htm) (accessed 12.02.2016).
- [30] Schulman, J.H., Compton, W.D., Color centers in solids, Oxford: Pergamon Press, 1962, pp. 1-368.
- [31] Carlston, R.C., J. Chem. Ed. 42(2) (1965) 117.
- [32] West, A.R., Solid state chemistry and its applications (2<sup>nd</sup> edition), Willey & Sons, Ltd, 2014, pp. 1-556.
- [33] <http://web.mit.edu/course/6/6.732/www/opt.pdf> (accessed 12.03.2016).
- [34] <http://www.webexhibits.org/causesofcolor/9.html> (accessed 12.03.2016).
- [35] Shevell, S.K., The science of color (2<sup>nd</sup> edition), Elsevier Science, 2003, pp. 1-350.
- [36] Shcherbov, D.P., Plotnikova, R.N., Zavod. Lab. 42(12) (1976) 1429.
- [37] <https://en.wikipedia.org/wiki/Pigment> (accessed 12.03.2016).
- [38] Housecroft, C.E., Sharpe, A.G., Inorganic chemistry (4<sup>th</sup> edition), Pearson, 2012, pp. 1-1256.
- [39] [https://en.wikipedia.org/wiki/List\\_of\\_inorganic\\_pigments](https://en.wikipedia.org/wiki/List_of_inorganic_pigments) (accessed 12.03.2016).
- [40] O'Brien, D.L.J., Preparation of environmentally-friendly inorganic pigments, PhD thesis, Loughborough University, 2005.
- [41] Biernat, K., Malinowski, A., Gnat, M., Biofuels – economy, environment and sustainability, Z. Fang (Ed.), Intech, 2013, pp. 1-386.

- [42] Levinson, R., Berdahl, P., Akbari, H., Sol. Energ. Mat. Sol. Cells 89(4) (2005) 351.



## CHAPTER 2

### Materials Synthesis, Properties and Characterization Methods

#### 2.1 Synthesis

##### 2.1.1 Solid State Synthesis

Solid state synthesis or “shake and bake” method is the most common route to prepare compounds in solid state. It includes mixing and heating starting materials together at high temperature (400–1500 °C) for several hours. Solid state synthesis involves total destruction of reactants structures and formation of new lattice (crystal structure) of the product. The reaction mixture consists of reactants particles (usually oxides) and voids between them. Reaction between starting materials occurs due to ions migration throughout the crystal interfaces in places where contacts between reactants exist; as a results there is a formation of new phase. The process is accelerated by decreasing of particle sizes, palletization of starting materials mixture and increasing the temperature of synthesis [1].

Powders of starting materials are mixed together in stoichiometric amounts, ground with agate mortar and pestle, mixture is pressed into a pellet and heated in alumina (inert material) crucible for several hours. If necessary the mixture might be ground again, pelletized and reheated at higher temperature (Fig. 2.1).

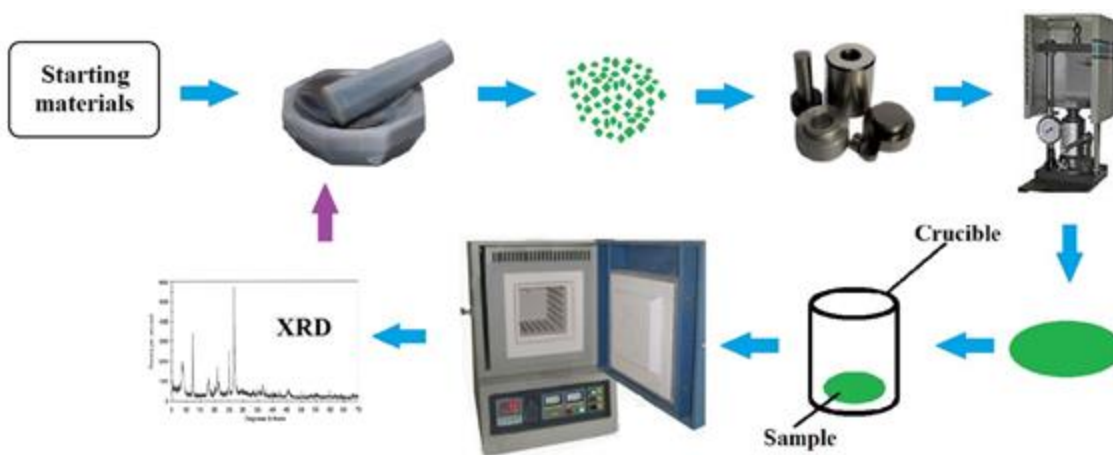


Figure 2.1 Solid state synthesis method.

### 2.1.2 Sol-Gel (Pechini Method) or Low Temperature Synthesis Route

Low temperature route of synthesis produces smaller particle size of desired product comparing to the solid state synthesis. In sol-gel method a precursor is synthesized and then decomposed at moderate temperature to produce a final product. Usually a precursor consists of nitrates, carbonates, and hydroxides of metals. The advantage of precursor is the ability to decompose with formation of very reactive particles, which interact rapidly with one another.

In this work several apatite – type pigments were made using Pechini method; details of the synthesis might be found in Chapter 3. Stoichiometric amounts of starting materials (nitrates of the metals) were mixed and dissolved in DI water. The nitrate solutions were heated while stirring, and the citric acid was added in a molar ratio of 2:1 citric acid to metal nitrates. Here citric acid plays role of a cross linking agent. The pH of the resulting solutions was then adjusted to 7 using aqueous  $\text{NH}_4\text{OH}$ , and the neutralized solutions were heated until the formation of dry gel. Dark brown amorphous powder was obtained after heating the translucent dry gel at  $250^\circ\text{C}$  for 2 h, and it was further calcined at temperature of synthesis in air for 12 h [2]. Schematic representation of Pechini method is shown in Figure 2.2.

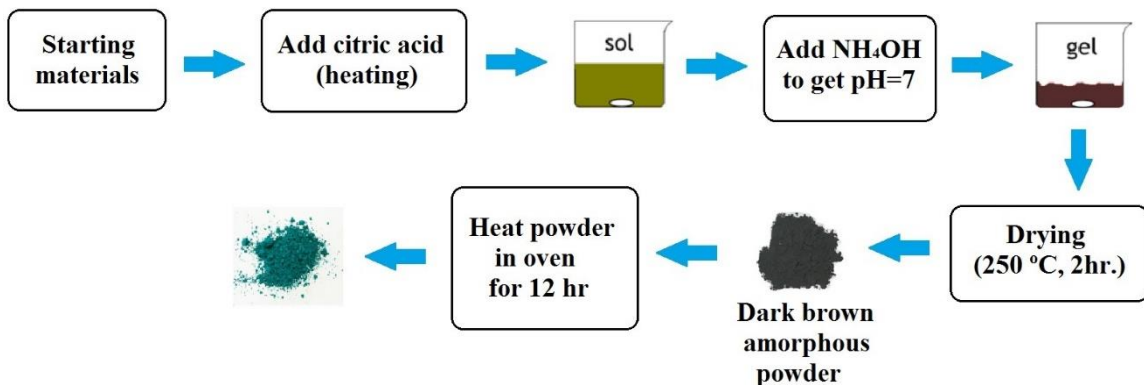


Figure 2.2 Pechini (sol-gel) method.

### 2.1.3 Microwave Method

Microwave method is applied to speed up the process of synthesis; when fast results are needed [3]. In this work some apatite – type pigments were made using microwave method. Stoichiometric mixture of starting materials was ground in an agate mortar with pestle. The powder mixture was pelletized and placed in an alumina crucible. The reaction vessel was then surrounded by carbon slug (inside a microwave high-temperature ceramic block) and placed in the microwave oven cavity. The model of microwave used is a CEM MDS-81D (2.45 GHz multi-mode oven) (Fig. 2.3). The microwave exposure was limited to 5-6 minutes intervals at 100% power (750Watts). The temperature of reaction was approximately 780-900°C, it was measured by thermocouple placing in the carbon slug directly after exposure.

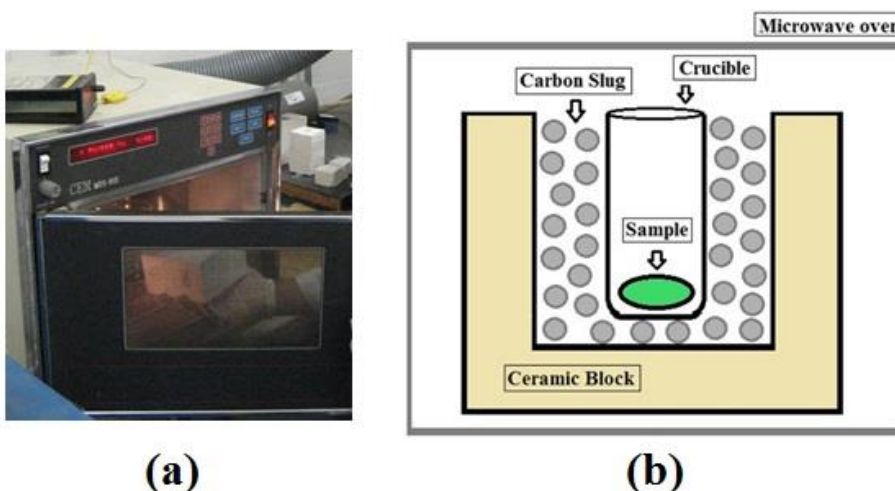


Figure 2.3 (a) CEM MDS-81D Microwave (2.45 GHz multi-mode oven) and (b) schematic representation of the microwave method of synthesis.

## 2.2 Powder X-ray Diffraction (XRD)

X-ray diffraction is the most important and useful method for characterization of polycrystalline solid inorganic materials. Using X-ray diffraction technique the arrangement of atoms in crystal can be determined and described [4].

X-rays are high energy electromagnetic beams (0.25 – 120 kV), which are formed when a metal target is bombarded by high energy electrons [5]. These electrons emboss electrons occupying the inner atomic orbitals. Electrons from remote levels move into

position of knocked-out electrons and emit X-rays. The wavelength of X-rays depend on the origin of metal, which plays a role of target [6] (Fig. 2.4).

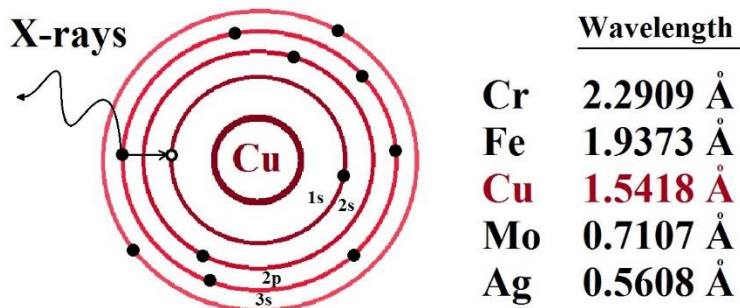


Figure 2.4 (a) Formation of X-ray, (b) wavelength of X-rays of some selected metals.

X-rays interact with electrons of atom. Atoms in crystal form periodic array, which can diffract electromagnetic waves. Amorphous materials don't have periodic long - order array and they don't have an ability to diffract. X-rays are very useful to study crystal structures because X-rays wavelength and distances between atoms in crystals have similar order of magnitude. By the interaction of X-rays with atoms diffraction pattern is obtained, which helps to determine interatomic distances. Interval between parallel planes of atoms dictates the position of diffraction peaks on the pattern. Let's consider two parallel atomic planes separated by distance  $d$  in a lattice of crystalline solid compound (Fig. 2.5).

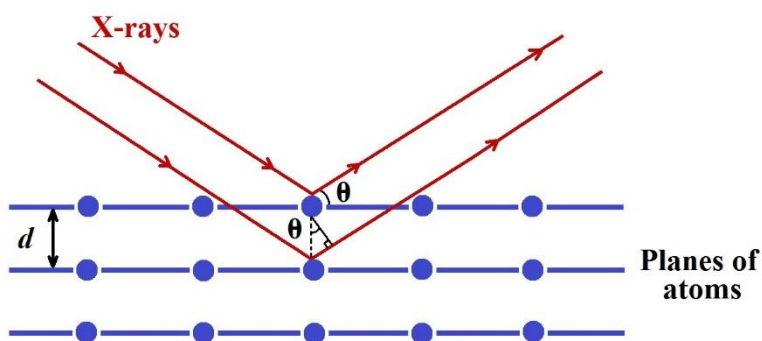


Figure 2.5 Bragg's law illustration: X-rays diffraction from crystalline solid.

When X-rays interact with the atomic planes, constructive interference occurs if the difference of path length between beams reflected from neighboring atomic planes equals a whole number of X-ray wavelengths. Bragg's law describes this relationship:

$$n\lambda = 2d\sin\theta$$

The law reveals conditions when diffraction is possible. Interatomic distance can be calculated using Bragg's law if wavelength ( $\lambda$ ) is known and angle ( $\theta$ ) is determined during experiment. There is a relationship between interatomic distance ( $d$ ) and unit cell parameters ( $a$ ,  $b$ ,  $c$ ) for each type of unit cell.

X-rays are used to analyze single crystals, powders, thin films. X-ray powder diffraction (XRD) is the most useful technique in routine phase identification of crystalline solid compounds. The possibilities of XRD method include unit cell parameters refinement, qualitative and quantitative analysis, studying of solid solutions formation, crystal size determination, solving of crystal structures. Schematic representation of XRD setup is given in Figure 2.6. Cathode (tungsten spiral) in cathode tube is heated up and emits flow of electrons, which bombards a metal anode (target, usually Cu) to produce X-rays. Monochromator (graphite) selects the most intense  $K_{\alpha 1}$  rays and leaves incident X-rays with the certain wavelength. X-rays interact with rotating sample, recording device collects diffracted X-rays to analyze a diffraction pattern by a computer.

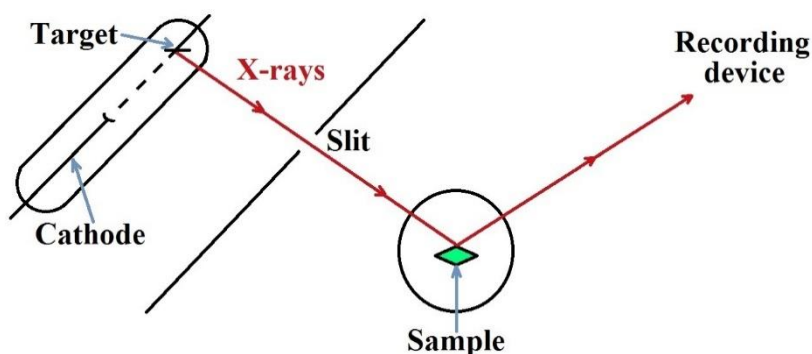


Figure 2.6 Schematic setup for XRD method of analysis.

For the present work XRD data were collected using a Rigaku MiniFlex II diffractometer (Fig. 2.7) with  $\text{CuK}\alpha$  radiation ( $\lambda = 1.5418\text{\AA}$ ) and a graphite monochromator

at room temperature. For phase identification the measurements were carried out at  $0.5^\circ/\text{min}$  within  $15^\circ$  to  $70^\circ$   $2\theta$  range. XRD data were refined using Le Bail method and GSAS-EXPGUI software [7,8].



Figure 2.7 Rigaku MiniFlex II diffractometer.

In addition to diffraction X-rays are scattered by electrons. Scattering power of atom depends on the element atomic number: it is a disadvantage of X-ray method of analysis. Light elements such as hydrogen or oxygen cannot be detected in the presence of heavier atoms.

### 2.3 Powder Neutron Diffraction

Neutron diffraction analysis is applied when extra or more detailed information about the bulk structure is required. As we mentioned above XRD method of analysis has some limitations. Neutron diffraction technique have some advantages comparing to XRD. Neutrons interact with nucleus of the atom not with electron cloud. There is no specific trend and dependence of signal intensity on atomic number of element. Positions of light atoms (oxygen in case of oxides) might be determine using this method of analysis. Also different isotopes of the same element show different ability to scatter neutrons, they can be distinguished using this technique. With neutron diffraction method one can refine atomic positions, determine atomic occupancies, find oxygen vacancies and reveal magnetic structure. Bragg's law also defines the principle of neutron diffraction. However neutron diffraction technique has a limitation, it is not suitable for materials containing high concentration of neutron-absorbing elements [9].

Powder neutron diffraction data of our samples were collected on the 32-counter high-resolution diffractometer BT-1 at the Center for Neutron Research at the National Institute of Standards and Technology (NIST), Maryland, USA. A Cu (311) monochromator, yielding a wavelength of  $1.5403(2) \text{ \AA}$ , was employed. Collimation of  $15'$  of arc was used before the monochromator,  $20'$  before the sample, and  $7'$  before the detectors. The samples were loaded into vanadium containers of 15.6 mm diameter and 50 mm length. Data were collected at room temperature over a  $2\theta$  range of  $3^\circ$  to  $167^\circ$ . Neutron data were refined using the Rietveld method, as implemented in GSAS-EXPGUI software.

## 2.4 Optical Properties

Optical properties characterization is important for pigments. The color of compound reveals specificity of electron interactions along with the structural characteristics.

When light interacts with material there are four main possible scenarios: diffuse reflectance, absorption, specular reflection, and transmittance [10].

*Specular reflectance.* In general, reflectance is a process in which incident and reflected light have the same wavelength. When material has very smooth surface, specular reflectance occurs. In this case an incident beam and reflected beam have the same angle (Fig. 2.8(a)). Metallic luster is an example of specular reflectance.

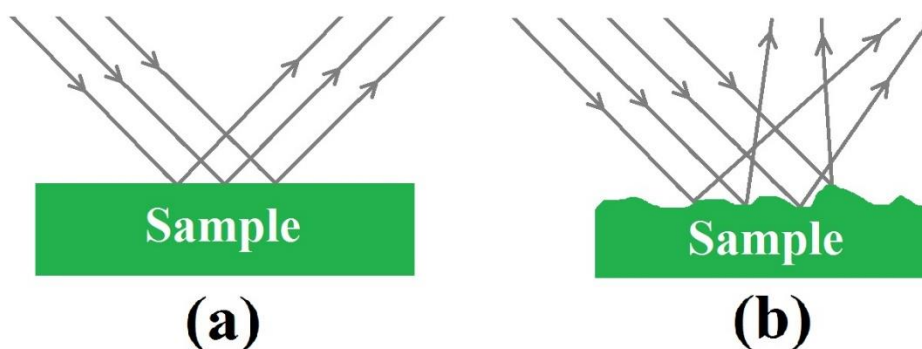


Figure 2.8 (a) Specular and (b) diffuse reflectance.

*Absorption.* Reflected light has lower intensity than incident light after interaction with material, which absorbs energy.

*Transmittance.* Only transparent materials show transmittance as a property, it is ability to transmit light with or without intensity loss.

*Diffuse reflectance* is a process when surface reflects light in all directions. It is a common characteristic of powder samples, since they have rough surface (small crystals are randomly oriented) they intensively scatter light (Fig 2.8(b)).

#### 2.4.1 Diffuse Reflectance Spectroscopy

Diffuse reflectance is a method of powders and crystals characterization, in particular to determine band gap energy ( $E_g$ ) [11]. In the diffuse reflectance spectroscopy experiment all reflected light, except specular reflected, are collected and analyzed.

All diffuse reflectance measurements were performed at Dr. McIntyre's lab, Physics Department, OSU. Diffuse reflectance data in the visible range were measured using a homemade UV-VIS spectrophotometer (MgO as the reference). Deuterium and halogen light sources were used to scan samples in 250 – 900 nm region. Diffuse reflectance was converted to absorbance using the Kubelka-Munk equation  $f(R) = (1 - R)^2/2R$ , where  $f(R)$  is absorbance and  $R$  is measured reflectance [12]. Calculated absorbance was plotted vs. wavelength (nm) or energy (eV) and linear regression was extrapolated to the  $x$ -axis and estimated band gap was determined.

#### 2.4.2 Near-infrared (NIR) Reflectance

Near-infrared (NIR) is a part of sunlight. NIR reflectance measurements are needed to be performed to characterize samples ability to reflect light (heat) in 700 ~ - 2500 nm region. It is crucial property for pigment in order to be a "Cool pigment". White pigments ( $\text{TiO}_2$ ,  $\text{CaAl}_2\text{O}_9$ ; Figure 2.9) reflect largest fraction of heat (80 ~ - 100%), show small NIR absorption and don't warm up easily. Pigments having darker colors usually reflect less amount of heat. Let's consider NIR reflectance vs. wavelength plots of commercially used Co – blue ( $\text{CoAl}_2\text{O}_4$ ) and  $\text{LaAl}_{11}\text{NiO}_{19}$  blue (it was synthesized in our lab and described in the present work, Chapter 5) pigments (Fig. 2.9).  $\text{CoAl}_2\text{O}_4$  reflects 20 ~ - 40%, while  $\text{LaAl}_{11}\text{NiO}_{19}$  reflects 50 ~ - 75% of light in NIR region; it makes the second pigment



more attractive to use.  $\text{LaAl}_{11}\text{NiO}_{19}$  outperforms  $\text{CoAl}_2\text{O}_4$  in ability to reflect heat. Also, wide use of Co – blue is not desired due to toxicity of cobalt.

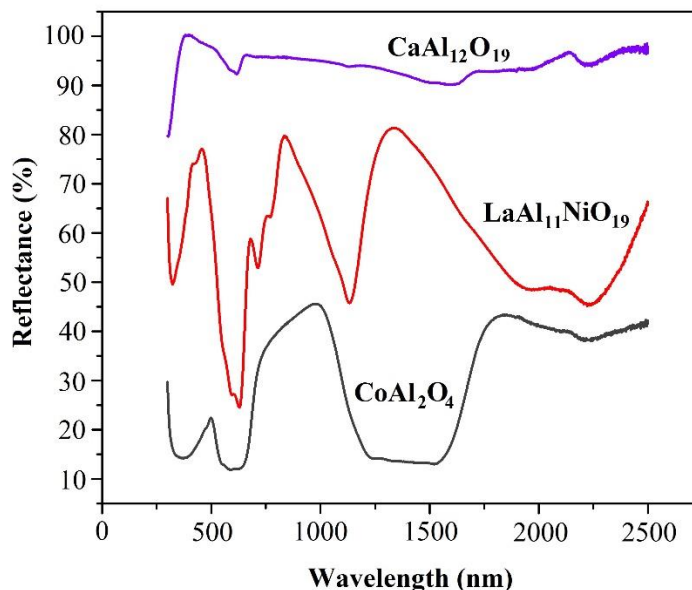


Figure 2.9 Reflectance vs. wavelength of  $\text{CaAl}_{12}\text{O}_{19}$  (white),  $\text{LaAl}_{11}\text{NiO}_{19}$  (blue) and  $\text{CoAl}_2\text{O}_4$  (blue).

NIR reflectance data (up to 2500 nm) were collected using a Jasco V-670 spectrophotometer at Dr. Chang's lab, Chemical, Biological, and Environmental Engineering Department, OSU.

#### 2.4.3 $L^*a^*b^*$ Color Space

Color perception and description is a subjective matter. Eye biology and morphology, mood, age can affect our color perception. Also, each individual describes color according to his or her verbal skills [13]. The solution to the problem is an instrument which can measure and describe color impartially.  $L^*a^*b^*$  color space is a 3D colorimetry model, which is widely used to characterize colors of paints, inks, pigments, and dyes.  $L^*$  represents a black ( $L^* = 0$ )/white ( $L^* = 100$ ) component of color,  $a^*$  is responsible for a red ( $a^* > 0$ )/green ( $a^* < 0$ ) component and  $b^*$  represents a yellow ( $b^* > 0$ )/blue ( $b^* < 0$ ) components (Fig. 2.10).  $L^*a^*b^*$  values are device independent and not based on the nature of material [14].

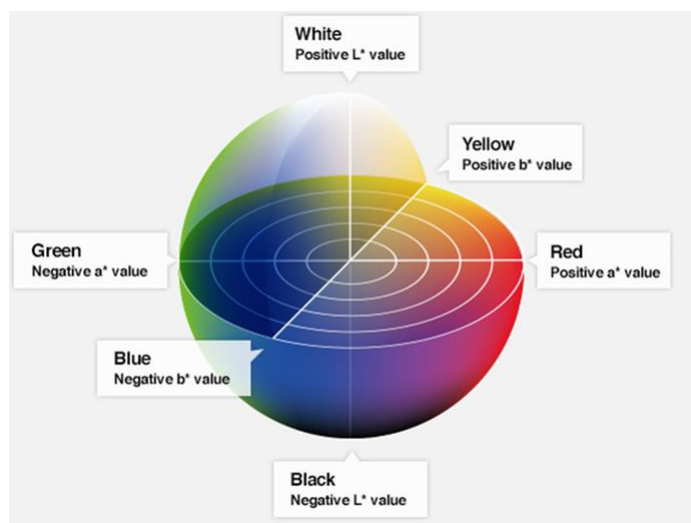


Figure 2.10  $L^*a^*b^*$  color space representation [15].

Konica Minolta CM-700d spectrophotometer (Standard illuminant  $D_{65}$ ) was used to measure  $L^*$ ,  $a^*$ ,  $b^*$  color coordinates of the synthesized samples (Fig. 2.11).



Figure 2.11 Konica Minolta CM-700d spectrophotometer.

## 2.5 Magnetism

Magnetism is a property of material dictated by certain orientation of unpaired electrons in an applied magnetic field. Let's consider an atomic orbital, Pauli principle and Hund's rule allow only two electrons (spin up and spin down) to occupy it. When all electrons are paired atom is diamagnetic, if atom has unpaired electrons in valence orbitals,

it called to be paramagnetic. Most of the paramagnetic materials contain transition metals or lanthanides. In diamagnetic atom traveling electron has small magnetic moment. In paramagnetic ion the total moment of an unpaired electron is associated with spin (S), orbital angular (L) and total momentum (J) values [16].

In paramagnetic compounds all spins are randomly oriented. If structural location of atoms allows unpaired electron spins to interact in a certain way, then three different kinds of spins orientation arise: ferromagnetism, antiferromagnetism, and ferrimagnetism (Fig. 2.12).

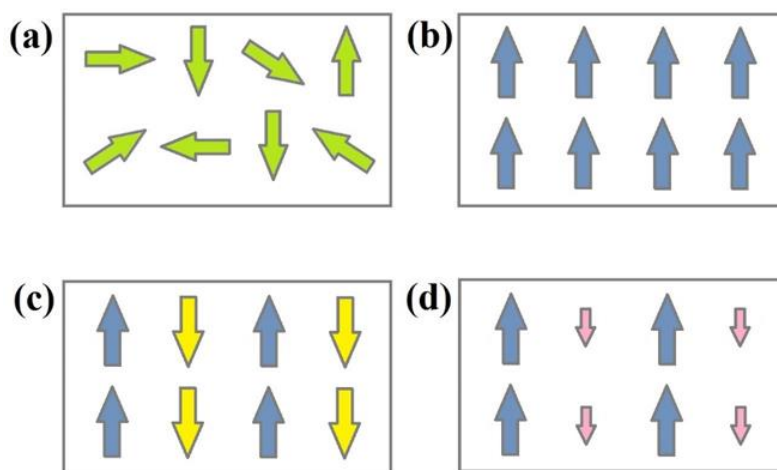


Figure 2.12 Unpaired electron spins orientation in (a) paramagnetic, (b) ferromagnetic, (c) antiferromagnetic and (d) ferrimagnetic materials placed in magnetic field.

In ferromagnetic compounds all spins are aligned in the same direction. There is an antiparallel orientation of spins in antiferromagnetic materials, spins cancel out each other. Ferrimagnetism occurs when spins are antiparallel, but they don't cancel out to zero due to their different magnitude.

For paramagnetic compounds temperature dependence of magnetic susceptibility ( $\chi$ ) follow the Curie – Weiss law:

$$\chi = C / (T + \theta)$$

where  $\chi$  is a molar susceptibility, T - temperature, C - Curie constant,  $\theta$  - Weiss constant.

Ideally,  $1/\chi$  vs. temperature plot gives a straight line, Curie constant might be obtained from the inverse slope and it equals the magnitude of magnetic moment per formula unit. Weiss constant can be found from the  $x$  – axis intercept. Its sign reveals the nature of magnetic interactions. For paramagnetic compounds  $\theta = 0$ , there are no interactions of spins, they are independent from one another. Ferromagnets have  $\theta > 0$ , spins have parallel ordering.  $\theta < 0$  for antiferromagnets, spins align antiparallel [17].

Paramagnets, ferromagnets and antiferromagnets show different behavior when temperature changes (Fig. 2.13).

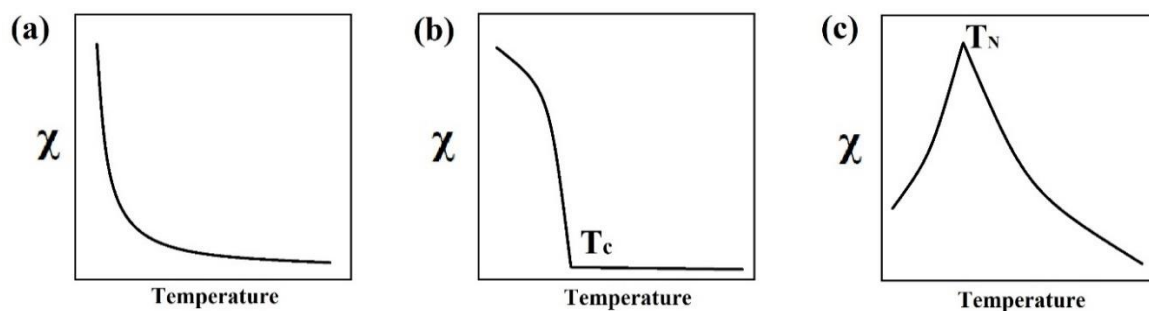


Figure 2.13 Temperature dependence of molar magnetic susceptibility ( $\chi$ ) of (a) paramagnetic, (b) ferromagnetic, (c) antiferromagnetic materials.

Molar susceptibility of paramagnetic compounds gradually decreases when temperature increases. Ferromagnets show rapid increase of  $\chi$  at Curie temperature ( $T_c$ ). As temperature decreases further the susceptibility continues to increase. Molar susceptibility of antiferromagnets starts to decrease at Neel temperature ( $T_N$ );  $\chi$  decreases further as temperature continues to decrease. Ferrimagnets have more complicated behavior [18].

Effective magnetic moment ( $\mu_{\text{eff}}$ ) defines the number of unpaired electrons in atom and determines the oxidation state of the element. The  $\mu_{\text{eff}}$  might be calculated using  $2.84 \cdot C^{1/2} \mu_B$  ( $\mu_B$  - Bohr magneton) equation.

Diamagnetic correction was made for calculations of experimental  $\mu_{\text{eff}}$ . All atoms and ions have paired electrons (diamagnetic part: repulsion from a magnetic field), they affect the measured susceptibility value ( $\chi_{\text{meas}}$ ). Diamagnetic correction is necessary to apply to

get more accurate value of effective magnetic moment:  $\chi_P = \chi_{\text{meas}} - \chi_D$  ( $\chi_P$ : paramagnetic contribution,  $\chi_D$ : diamagnetic contribution). Tabulated values of  $\chi_D$  for each cation and anion were used to obtain the sum  $\chi_D$  value for each studied compound [19].

Magnetic properties measurements were performed using a Quantum Design Physical Property Measurement System (QD-PPMS) (Fig. 2.14) at temperature range of 5 K to 300 K (zero-field cooling method, applied magnetic field is 0.5 T). Inverse magnetic susceptibility data was used to fit for Curie-Weiss law.



Figure 2.14 Quantum Design Physical Property Measurement System (QD-PPMS).

## 2.6 Dielectric Properties Measurements

Dielectric materials (dielectrics) are ceramics or polymers, which are electrical insulators [20]. They are used as embedded capacitors, gate dielectrics, chip and ceramic capacitors, FRAM (Ferroelectric Random Access Memory) in computers [21].

Dielectrics are insulators without an external electric field, but when field is applied, the charges inside the material start to shift insignificantly from their equilibrium positions, this effect called dielectric polarization. Let's consider a dielectric with thickness  $h$  and surface area  $S$  placed between two parallel plates of capacitor. When voltage is applied, the plates are charged contrarily (one plate is negative and the other is positive) (Fig. 2.15).

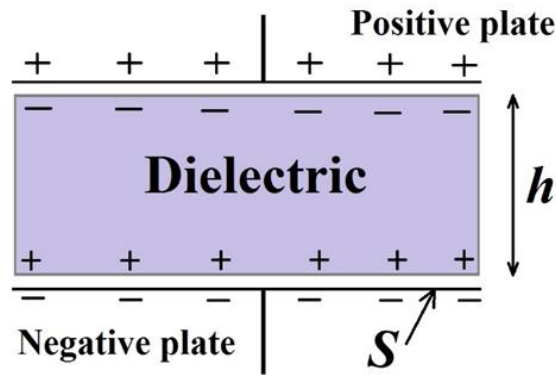


Figure 2.15 Dielectric material ( $h$  – thickness, and  $S$  – surface area) between two parallel plates of capacitor.

In this case dielectric material has capacity ( $C$ ) equals  $\epsilon_0 \epsilon_r S/h$ , where  $\epsilon_r = \epsilon/\epsilon_0$  ( $\epsilon_0$  – permittivity of free space =  $8.854 \cdot 10^{-12}$  F/m,  $\epsilon$  – permittivity of dielectric,  $\epsilon_r$  – relative permittivity), using these equations dielectric constant ( $\kappa$ ) can be defined:

$$\kappa = Ch/\epsilon_0 S$$

The ability of material to be polarized defines the magnitude of dielectric constant [22]. Crystal structure, temperature, frequency can affect the value of  $\kappa$ . Dielectric constant along with dielectric loss ( $\tan \delta$ ) are two main characteristics of each dielectric. Dielectric loss ( $\tan \delta$ ) determines an amount of electromagnetic energy, which is scattered by dielectric. For ideal dielectric  $I$  (electric current) outstrips the  $V$  (voltage) by  $90^\circ$  when external voltage applied (Fig. 2.16). Due to defects in structure, ionic motion, and electronic conductivity for real (non-ideal) dielectric the angle between  $I$  and  $V$  decreases by  $\delta$  and the value of the new phase angle is  $90^\circ - \delta = \theta$ ; as a results energy is lost in form of heat [23].

Exploration of  $\kappa$  and  $\tan \delta$  behavior when temperature/frequency changes, provides an important information about dielectric character presents in the material. To be applicable, dielectric material should have high  $\kappa$  value and small value of  $\tan \delta$ .

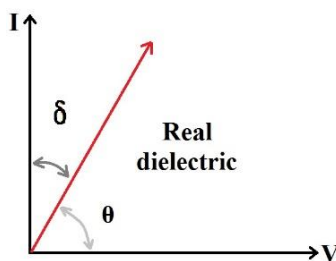


Figure 2.16 For ideal dielectric  $I$  (electric current) outstrips the  $V$  (voltage) by  $90^\circ$  when external voltage applied; for non-ideal dielectric the angle between  $I$  and  $V$  decreases by  $\delta$  and the value of the new phase angle is  $90^\circ - \delta = \theta$ .

Dielectrics which show a reversible spontaneous electric polarization called ferroelectrics. Two conditions have to be met for material to have ferroelectric properties: the presence in the structure of  $d^0$  or  $s^2p^0$  cations, which are able to respond to the external electric field and the structure shouldn't have an inversion center in order to have unbalanced displacements aligned in the same direction. Polarization of ferroelectrics is not disappear when electric field is removed. Dielectrics have ferroelectric properties below a certain temperature (Curie temperature), at this point and above material loses ferroelectricity and starts to be paraelectric [24]. For example,  $\text{BaTiO}_3$  having perovskite structure is a ferroelectric, it is used for capacitors [25]. Large  $\text{Ba}^{2+}$  cation extends the  $\text{TiO}_6$  octahedra ( $O_h$  network tolerance factor is greater than one), and  $\text{Ti}^{4+}$  moves towards one of the  $O_h$  corners. This shift might be changed by applying an external electric field.

Dielectric properties measurements were performed using home-made parallel plate capacitor setup in  $25\text{--}250^\circ\text{C}$  temperature range at 1 kHz, 10 kHz, 100 kHz, 500 kHz, 750 kHz, and 1 MHz.

## 2.7 Infrared (IR) Spectroscopy

IR or infrared spectroscopy studies molecular vibrations and rotations having low energies and high wavelengths ( $700\text{--}10^6$  nm), which we perceive as heat [26]. Each functional group has its specific resonance frequency, a point when it starts to vibrate; IR spectroscopy uses this principle to identify the bonds and functional groups present. There are two types of molecular vibrations: stretching mode (symmetric and asymmetric

stretching) and bending mode (in and out of plane) (Fig. 2.17). Stretching modes are vibrations occur along the bond axis and bending modes are changes of bond angles [27].

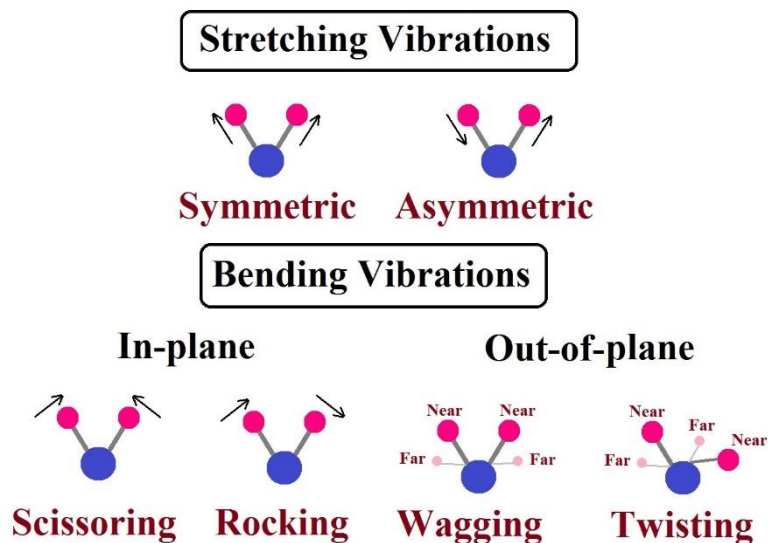


Figure 2.17 (a) Stretching vibrations and (b) bending vibrations.

Lighter atoms oscillate faster at higher energies, vibrations of bonds follow similar pattern. For example, triple bond has higher energy of oscillations than single bond. To be able to absorb in IR region molecule should have a dipole moment, it is changed during the interaction with IR radiation and absorption occurs. IR peaks belong to covalently bonded groups appear at frequencies above  $\sim 300 \text{ cm}^{-1}$ . Lattice vibrations occur at lower frequencies ( $100\text{--}300 \text{ cm}^{-1}$ ) [28].

IR measurements were performed using a Thermo Scientific Nicolet 6700 FT-IR Spectrometer in the spectral range of  $700\text{--}2500 \text{ cm}^{-1}$  (ONAMI, Corvallis, OR).

## 2.8 References

- [1] Weller, M.T., Inorganic Materials Chemistry, Oxford university press, 1994, pp. 1-88.
- [2] Li, J., Singh, U.S., Schladt, T.D. et al., Chem. Mater. 20 (2008) 6567.
- [3] Muir, S.W., Rachdi, O.D., Subramanian, M.A., Mater. Res. Bull. 47(3) (2012) 798.
- [4] Adams, D.M., Inorganic solids. An introduction to concepts in solid-state structural chemistry, John Wiley & Sons, Inc., New York, 1974, pp. 1-352.
- [5] Girolami, G.S., X-ray crystallography, Univ. Science Books, 2015, pp. 1-502.
- [6] Cullity, B.D., Elements of X-ray diffraction (2<sup>nd</sup> edition), Addison Wesley Publishing Company, Inc., MA, 1978, pp. 1-531.



- [7] Larson, A.C., Von Dreele, R.B., General Structure Analysis System (GSAS), Los Alamos National Laboratory Report LAUR (2014) 86.
- [8] Toby, B.H., EXPGUI: a graphical user interface for GSAS, *J. Appl. Crystallogr.* 34 (2001) 210.
- [9] Scott, R.A., Lukehart, C.M. (Ed.), Application of physical methods to inorganic and bioinorganic chemistry, John Wiley & Sons, Ltd., UK, 2007, pp. 1-385.
- [10] West, A.R., Solid state chemistry and its applications (2<sup>nd</sup> edition), Willey & Sons, Ltd, 2014, pp. 1-556.
- [11] <http://www.piketech.com/files/pdfs/DiffuseAN611.pdf> (accessed 12.04.2016).
- [12] Sherif, M.E., Bayoumi, O.A., Sokkar, T.Z.N., *Color Res. Appl.* 22 (1997) 32.
- [13] [http://tqmsystems.nl/uploads/Understand\\_Color\\_en.pdf](http://tqmsystems.nl/uploads/Understand_Color_en.pdf) (accessed 12.04.2016).
- [14] [https://en.wikipedia.org/wiki/Lab\\_color\\_space](https://en.wikipedia.org/wiki/Lab_color_space) (accessed 12.04.2016).
- [15] <https://www.pinterest.com/pin/184999497165632389/> (accessed 12.04.2016).
- [16] Subramanian, M.A., Magnetic properties lecture slides, 2014.
- [17] Jiles, D., Introduction to magnetism and magnetic materials, CRC Press, USA, 1998, pp. 1-570.
- [18] Tebble, R.S., Craik, D.J., Magnetic materials, John Wiley & Sons, Inc., New York, 1969.
- [19] Bain, G.A., Berry, J.F., *J. Chem. Educ.* 85 (2008) 532.
- [20] <https://en.wikipedia.org/wiki/Dielectric> (accessed 12.04.2016).
- [21] Subramanian, M.A., Dielectrics lecture slides, 2014.
- [22] Kao, K.C., Dielectric phenomena in solids (1<sup>st</sup> edition), Academic Press, Cambridge, 2004, pp. 1-579.
- [23] Hippel, A.R.V., Dielectric materials and applications, Artech House, MA, 1995, pp. 1-456.
- [24] Davis, M. (Ed.), Dielectric materials handbook, ML Books International, 2010, pp. 1-316.
- [25] Cohen, R.E., Krakauer, H., *Ferroelectrics*, 136(1-4) (1992) 65.
- [26] Cheetham, A.K., Day, P. (Ed.), Solid state chemistry: techniques, Oxford University Press, Oxford, 1987.
- [27] Schrader, B. (Ed.), Infrared and Raman spectroscopy: methods and applications, VCH, Weinheim, Germany, 1995, pp. 1-765.
- [28] Larkin, P., Infrared and Raman spectroscopy; principles and spectral interpretation (1<sup>st</sup> edition), Elsevier, 2011, pp. 1-230.

## CHAPTER 3

### Pigments with Apatite-type Structure

#### Abstract

Several  $A_5M'_{3-x}M_xO_{12}X$  ( $A = \text{Sr, Ba}$ ;  $M' = \text{Cr, Mn}$ ;  $M = \text{V, P}$ ;  $X = \text{F, Cl}$ ) solid solutions with apatite-type structures have been synthesized through solid state reactions, microwave synthesis and Pechini or sol-gel method using citric acid. The colors of the samples change from white ( $x = 3.0$ ) through turquoise ( $x = 1.5$ ) to dark green ( $x = 0$ ) with increasing amount of chromophore element (manganese or chromium). Optical measurements reveal that the origin of the color is presumably a combination of d-d transitions of  $\text{Mn}^{5+}/\text{Cr}^{5+}$  and cation-anion charge transfer from transition metals to oxygens. Near-IR reflectance measurements indicate that synthesized compounds are promising materials for “Cool pigments” applications. Magnetic measurements verify that manganese has two unpaired electrons and chromium has one unpaired electron, and they exhibit 5+ oxidation state. The IR spectra change systematically with sample compositions and the fingerprint region ( $700\text{--}1100\text{ cm}^{-1}$ ) indicates characteristic bands belonging to  $(\text{MnO}_4)^{3-}$ ,  $(\text{VO}_4)^{3-}$  and  $(\text{PO}_4)^{3-}$  functional groups. Structure refinements using neutron data confirm that  $\text{Mn}^{5+}$ ,  $\text{V}^{5+}$  and  $\text{P}^{5+}$  cations occupy the tetrahedral sites in the apatite structure.

Publications based on this chapter:

- 1) **Medina, E.A.**, Li, J., Stalick, J.K., Subramanian, M.A. Intense turquoise colors of apatite-type compounds with  $\text{Mn}^{5+}$  in tetrahedral coordination *Solid State Sciences* **2016**, 52, 97-105.

### 3.1 Introduction

The search for new, cheap, enduring and environmentally friendly inorganic pigments is a challenging task of materials science. It was discovered recently that hexagonal  $\text{YIn}_{1-x}\text{Mn}_x\text{O}_3$  solid solution with  $\text{Mn}^{3+}$  in trigonal bipyramidal coordination gives a brilliant blue color and exhibits excellent near-infrared reflectance [1]. The new blue pigments are easy to make, heat- and acid-resistant and nontoxic with great potential for “Cool pigment” applications where heating is not desirable (e.g., roofing materials). The cost of indium-based pigments however is an obstacle for practical applications. New inexpensive blue pigments with similar optical properties are needed.

Many Mn-containing compounds have been reported with vivid colors. Brownmillerite-type  $\text{Ba}_2\text{In}_{2-x}\text{Mn}_x\text{O}_{5+x}$  produces a green color with  $\text{Mn}^{5+}$  in tetrahedral coordination [2]. A minimum in the visible absorption at 500 nm is responsible for the color of these compounds. Blue [3] and green [4,5] Cr-containing pigments have been studied. The apatite-type structure  $A_5(\text{MO}_4)_3X$  ( $A = \text{Ca}^{2+}, \text{Sr}^{2+}, \text{Ba}^{2+}, \text{Pb}^{2+}$ ;  $M = \text{P}^{5+}, \text{Mn}^{5+}, \text{Cr}^{5+}, \text{V}^{5+}$ ;  $X = \text{F}^-, \text{Cl}^-, \text{OH}^-$ ) [6-15] gives a great possibility to combine different A, M and X-site elements and synthesize compounds with a wide range of useful properties. A great number of compounds with the apatite related structure occur in nature and form minerals belonging to the apatite ( $A^\text{II}_5(M^\text{V}\text{O}_4)_3X$ ), belovite ( $A^\text{II}B^\text{II}C^\text{II}_3(M^\text{V}\text{O}_4)_3X$ ), britholite ( $(A^\text{III}, B^\text{II})_5(M^\text{IV}\text{O}_4)_3X$ ) [16,17], hedyphane ( $A^\text{II}_2B^\text{II}_3(M^\text{V}\text{O}_4)_3X$ ) and ellestadite ( $A^\text{II}_5(M_1^\text{IV}\text{O}_4)_{1.5}(M_2^\text{VI}\text{O}_4)_{1.5}X$ ) mineral groups [18]. Apatite-type compounds containing  $\text{Mn}^{5+}/\text{Cr}^{5+}$  tetrahedrally coordinated by oxygen might be promising materials for pigments with deep blue and green colors [19,20]. In inorganic oxides the oxidation state 5+ of manganese and chromium is very unusual;  $\text{Mn}^{5+}$  and  $\text{Cr}^{5+}$  are unstable and have a tendency to disproportionate into more stable oxidation states 4+/7+ and 3+/6+ accordingly. Apatite-type compounds with  $\text{Mn}^{5+}/\text{Cr}^{5+}$  in tetrahedral coordination (M-site cation) exist mostly with  $\text{Ba}^{2+}$  as an A-site cation, which due to its high ( $\approx 5\text{eV}$ ) first ionization potential helps manganese and chromium to keep the unusual oxidation state [21]. Several solid solutions with the apatite host structure have been synthesized and colors of compounds were described [22,23], but no detailed and systematic structural, optical and magnetic data are reported.

The parent compound  $\text{Ba}_5(\text{MnO}_4)_3\text{Cl}$  crystallizes in  $P6_3/m$  space group ( $a = 10.48 \text{ \AA}$ ,  $c = 7.772 \text{ \AA}$ ,  $V = 739.4 \text{ \AA}^3$ ) [24-27]; it is isostructural with  $\text{Ba}_5(\text{VO}_4)_3\text{Cl}$  [28-31],  $\text{Ba}_5(\text{PO}_4)_3\text{Cl}$  [32-46],  $(\text{Ca},\text{Sr})_5(\text{PO}_4)_3\text{Cl}$  [47],  $\text{Sr}_5(\text{PO}_4)_3\text{F}$  [48],  $\text{Sr}_5(\text{CrO}_4)_3\text{F}$  [49] and  $\text{Ca}_5(\text{PO}_4)_3\text{OH}$  [50] phases (Fig. 3.1).

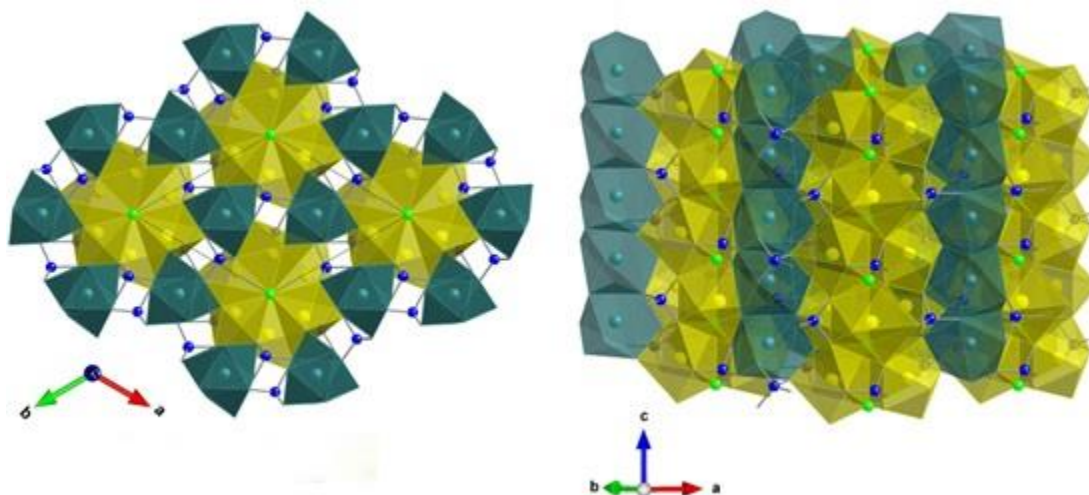


Figure 3.1 Hexagonal unit cell of  $\text{Ba}_5(\text{MnO}_4)_3\text{Cl}$  structure (left and right): Dark turquoise and yellow spheres represent two different crystallographic positions of  $\text{Ba}^{2+}$  4f (Ba1) and 6h (Ba2) accordingly, with face-sharing  $\text{Ba}(1)\text{O}_9$  and edge-sharing  $\text{Ba}(2)\text{O}_6\text{Cl}_2$  polyhedra forming one-dimensional chains arranged alternately along the  $c$ -axis. The Mn (blue) tetrahedra are corner-shared with Ba polyhedra and the Cl (green) atoms are lined up in channels along the  $c$ -axis. Oxygen atoms are omitted for clarity.

There are two crystallographic sites of  $\text{Ba}^{2+}$  in the hexagonal structure (4f and 6h) differing in coordination number and local symmetry. The Ba1 atoms occupying 4f positions have a coordination number of 9, forming face-sharing  $\text{Ba}(1)\text{O}_9$  tricapped trigonal prism chains along the  $c$  axis. The Ba2 atoms occupying 6h positions are bonded to six oxygens and two chlorines, forming edge-sharing  $\text{Ba}(2)\text{O}_6\text{Cl}_2$  bicapped trigonal prism (distorted) chains in channels of  $\text{Ba}(1)\text{O}_9$  chains. The discrete  $\text{MnO}_4$  tetrahedra interconnect the one-dimensional Ba polyhedral chains to form the three-dimensional crystal structure. Chlorine atoms are located between layers formed by  $\text{MnO}_4$  tetrahedra and stacked up in channels of Ba polyhedral chains along the  $c$ -axis. Further structural descriptions of the apatite framework is shown in Figure 3.2.

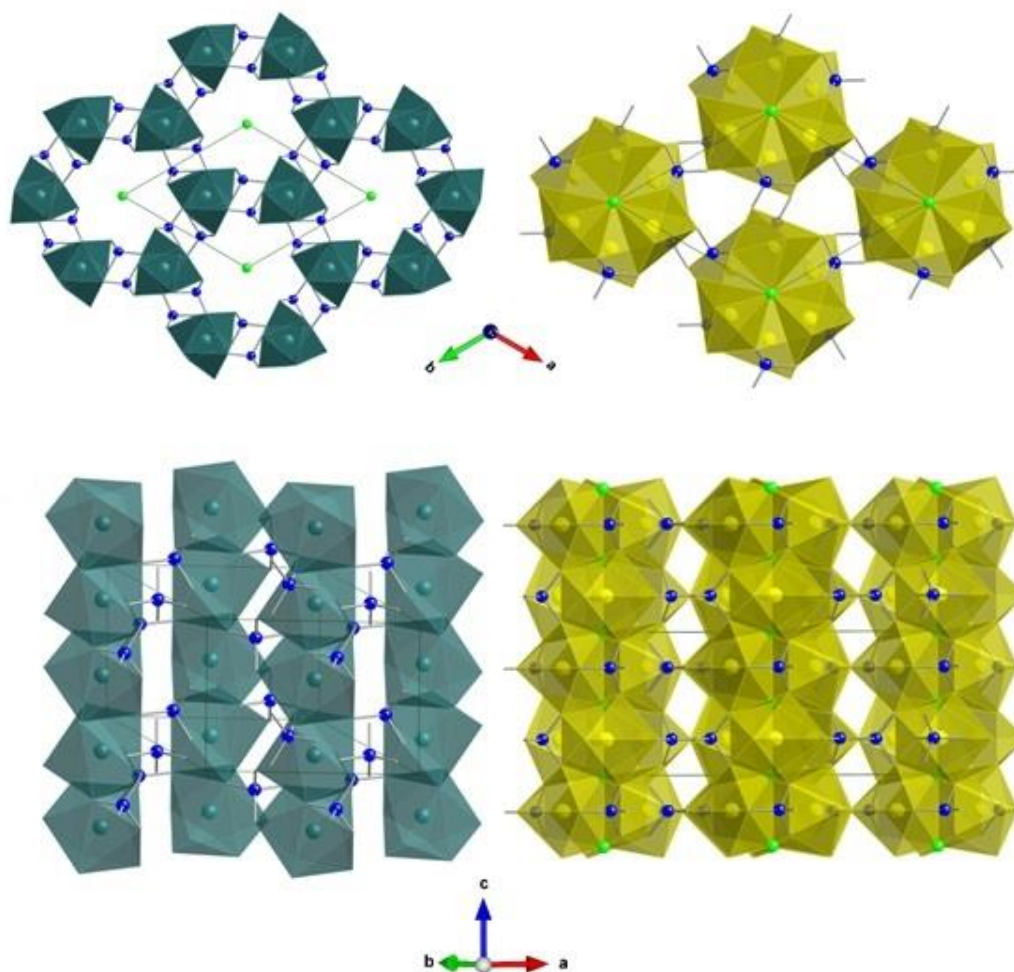


Figure 3.2 Further structural description of the hexagonal unit cell of  $\text{Ba}_5(\text{MnO}_4)_3\text{Cl}$  (left and right): dark turquoise and yellow spheres represent two different crystallographic positions of  $\text{Ba}^{2+}$  4f (Ba1) and 6h (Ba2) accordingly, with face-sharing Ba(1) $\text{O}_9$  and edge-sharing Ba(2) $\text{O}_6\text{Cl}_2$  polyhedra forming one-dimensional chains arranged alternately along the  $c$ -axis. The Mn (blue) tetrahedra are corner-shared with Ba polyhedra and the Cl (green) atoms are lined up in channels along the  $c$ -axis. Oxygen atoms are omitted for clarity.

In the present work several apatite-type solid solutions,  $\text{Sr}_5\text{Cr}_{3-x}\text{P}_x\text{O}_{12}\text{Cl}$  ( $x = 0.5; 1.0$ ),  $\text{Sr}_5\text{Cr}_{3-x}\text{V}_x\text{O}_{12}\text{Cl}$  ( $x = 0.5-1.5$ ),  $\text{Sr}_5\text{Mn}_{3-x}\text{Cr}_x\text{O}_{12}\text{Cl}$  ( $x = 2.5-3.0$ ),  $\text{Sr}_5\text{Cr}_{3-x}\text{P}_x\text{O}_{12}\text{F}$  ( $x = 0.5-2.5$ ),  $\text{Sr}_5\text{Cr}_{3-x}\text{V}_x\text{O}_{12}\text{F}$  ( $x = 0.5-2.5$ ),  $\text{Sr}_5\text{Mn}_{3-x}\text{Cr}_x\text{O}_{12}\text{F}$  ( $x = 2.5-3.0$ ),  $\text{Ba}_{5-x}\text{Sr}_x\text{Mn}_3\text{O}_{12}\text{Cl}$  ( $x = 0-2.5$ ),  $\text{Ba}_5\text{Cr}_{3-x}\text{P}_x\text{O}_{12}\text{Cl}$  ( $x = 1.0-2.5$ ),  $\text{Ba}_5\text{Cr}_{3-x}\text{V}_x\text{O}_{12}\text{Cl}$  ( $x = 1.5-2.5$ ),  $\text{Ba}_5\text{Mn}_{3-x}\text{Cr}_x\text{O}_{12}\text{Cl}$  ( $x = 0-3.0$ ),  $\text{Ba}_{5-x}\text{K}_x\text{S}_x\text{Mn}_{0.5}\text{P}_{2.5-x}\text{O}_{12}\text{Cl}$  ( $x = 0-0.5$ ),  $\text{Ba}_{5-x}\text{K}_x\text{Mo}_x\text{Mn}_{0.5}\text{P}_{2.5-x}\text{O}_{12}\text{Cl}$  ( $x = 0-0.2$ ),  $\text{Ba}_5\text{Mn}_{3-x}\text{V}_x\text{O}_{12}\text{Cl}$  ( $x = 0-3.0$ ),  $\text{Ba}_5\text{Mn}_{3-x}\text{P}_x\text{O}_{12}\text{Cl}$  ( $x = 0-3.0$ ),  $\text{Ba}_5\text{Cr}_{3-x}\text{P}_x\text{O}_{12}\text{F}$  ( $x = 0.5-2.5$ ), were successfully synthesized and their structural, optical and magnetic properties were

studied in details using various experimental methods and techniques. The end members of the solid solutions are dark green ( $\text{Ba}_5(\text{MnO}_4)_3\text{Cl}$ ) and white ( $\text{Ba}_5(\text{PO}_4)_3\text{Cl}$  and  $\text{Ba}_5(\text{VO}_4)_3\text{Cl}$ ), while the colors of the solid solutions vary from dark green to bright turquoise with different shades when  $\text{Mn}^{5+}/\text{Cr}^{5+}$  cations being gradually substituted by isovalent  $\text{V}^{5+}$  and  $\text{P}^{5+}$ . Several minerals and pigments with turquoise and green colors are well-known and used today (amazonite, vivianite, blue zircon, chalcedony, some types of spinel and beryl). The most famous among them is the opaque gem called turquoise with the formula  $\text{CuAl}_6(\text{PO}_4)_4(\text{OH})_8 \cdot 4\text{H}_2\text{O}$  [51] and bright green transparent gemstone emerald (beryl  $\text{Be}_3\text{Al}_2(\text{SiO}_3)_6$  with trace amounts of chromium) [52]. Some widely used commercial blue and turquoise pigments contain toxic cobalt [53-56]. The apatite-related pigments described here are more environmentally friendly and thermally stable with brighter colors.

### 3.2 Results and Discussion

#### 3.2.1 Crystal Structures by X-ray and Neutron diffraction

The XRD patterns are similar for the samples prepared by solid state reaction and sol-gel method. X-ray diffraction data of samples from solid state reaction were used for structural analysis:  $\text{Ba}_5\text{Mn}_{3-x}\text{V}_x\text{O}_{12}\text{Cl}$  ( $x = 0-3.0$ ) (Fig. 3.3(a)),  $\text{Ba}_5\text{Mn}_{3-x}\text{P}_x\text{O}_{12}\text{Cl}$  ( $x = 0-3.0$ ) (Fig. 3.3(b)),  $\text{Ba}_{5-x}\text{Sr}_x\text{Mn}_3\text{O}_{12}\text{Cl}$  ( $x = 0-2.5$ ) (Fig. 3.4(a)),  $\text{Ba}_{5-x}\text{K}_x\text{S}_x\text{Mn}_{0.5}\text{P}_{2.5-x}\text{O}_{12}\text{Cl}$  ( $x = 0-0.5$ ) (Fig. 3.4(a)),  $\text{Ba}_{5-x}\text{K}_x\text{Mo}_x\text{Mn}_{0.5}\text{P}_{2.5-x}\text{O}_{12}\text{Cl}$  ( $x = 0-0.2$ ) (Fig. 3.4(a)),  $\text{Ba}_5\text{Cr}_{3-x}\text{P}_x\text{O}_{12}\text{F}$  ( $x = 0.5-2.5$ ) (Fig. 3.4(b)),  $\text{Ba}_5\text{Cr}_{3-x}\text{P}_x\text{O}_{12}\text{Cl}$  ( $x = 1.0-2.5$ ) (Fig. 3.4(b)),  $\text{Ba}_5\text{Cr}_{3-x}\text{V}_x\text{O}_{12}\text{Cl}$  ( $x = 1.5-2.5$ ) (Fig. 3.4(b)),  $\text{Ba}_5\text{Mn}_{3-x}\text{Cr}_x\text{O}_{12}\text{Cl}$  ( $x = 0-3.0$ ) (Fig. 3.4(b)),  $\text{Sr}_5\text{Cr}_{3-x}\text{P}_x\text{O}_{12}\text{Cl}$  ( $x = 0.5; 1.0$ ) (Fig. 3.4(c)),  $\text{Sr}_5\text{Cr}_{3-x}\text{V}_x\text{O}_{12}\text{Cl}$  ( $x = 0.5-1.5$ ) (Fig. 3.4(c)),  $\text{Sr}_5\text{Mn}_{3-x}\text{Cr}_x\text{O}_{12}\text{Cl}$  ( $x = 2.5-3.0$ ) (Fig. 3.4(c)),  $\text{Sr}_5\text{Cr}_{3-x}\text{P}_x\text{O}_{12}\text{F}$  ( $x = 0.5-2.5$ ) (Fig. 3.4(d)),  $\text{Sr}_5\text{Cr}_{3-x}\text{V}_x\text{O}_{12}\text{F}$  ( $x = 0.5-2.5$ ) (Fig. 3.4(d)),  $\text{Sr}_5\text{Mn}_{3-x}\text{Cr}_x\text{O}_{12}\text{F}$  ( $x = 2.5-3.0$ ) (Fig. 3.4(d)). Nearly all the samples are pure with two exceptions:  $\text{Ba}_5(\text{PO}_4)_3\text{Cl}$  has two visible small impurity peaks belong to  $\text{Ba}(\text{PO}_3)_2$  and  $\text{Ba}_5(\text{VO}_4)_3\text{Cl}$  contains a small amount of  $\text{Ba}_2\text{V}_2\text{O}_7$  impurity phase. With increasing substitution of manganese and chromium with vanadium in the structures there are no visible peak shifts because the ionic radii of M-site cations differ only slightly.

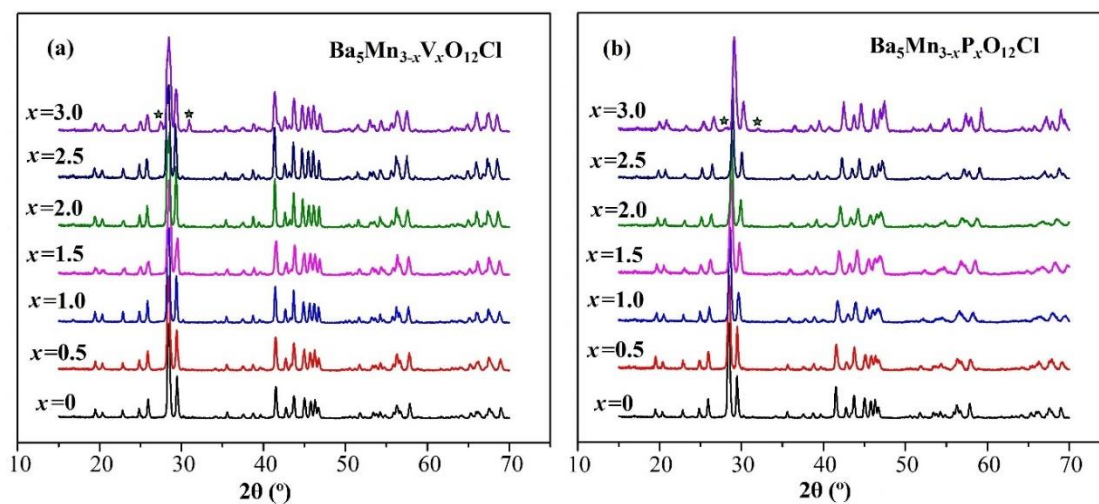
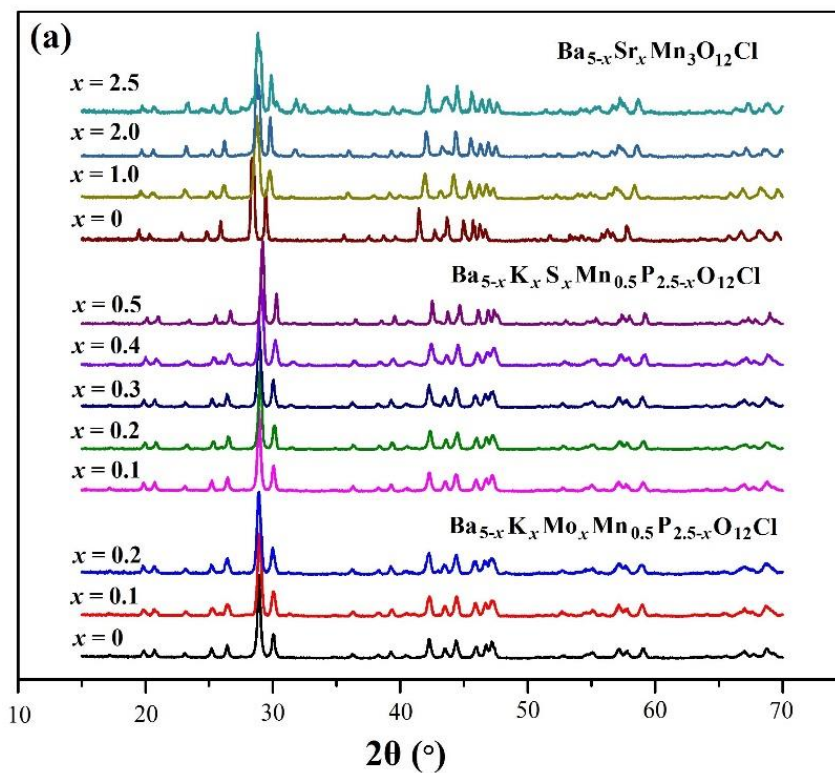
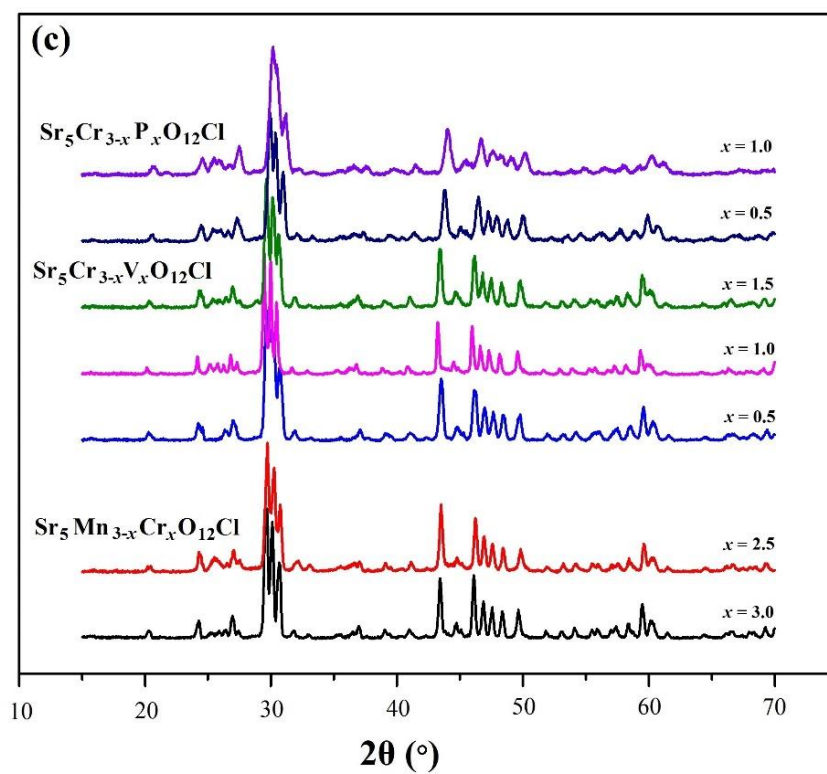
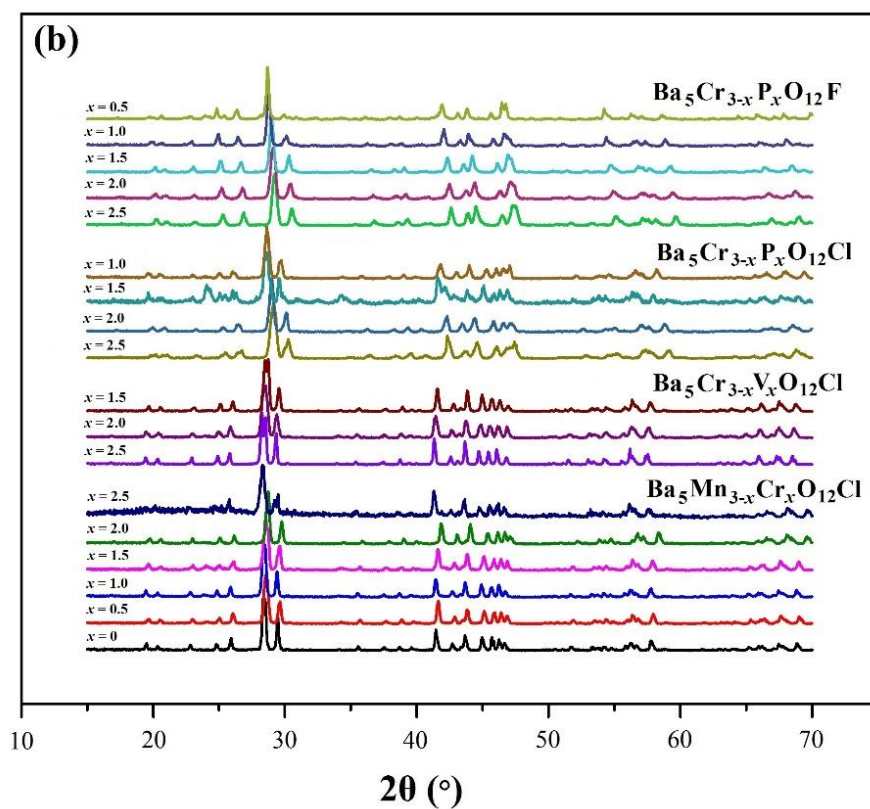


Figure 3.3 XRD patterns of  $\text{Ba}_5\text{Mn}_{3-x}\text{V}_x\text{O}_{12}\text{Cl}$  (a) and  $\text{Ba}_5\text{Mn}_{3-x}\text{P}_x\text{O}_{12}\text{Cl}$  (b) samples (asterisks – impurity peaks).







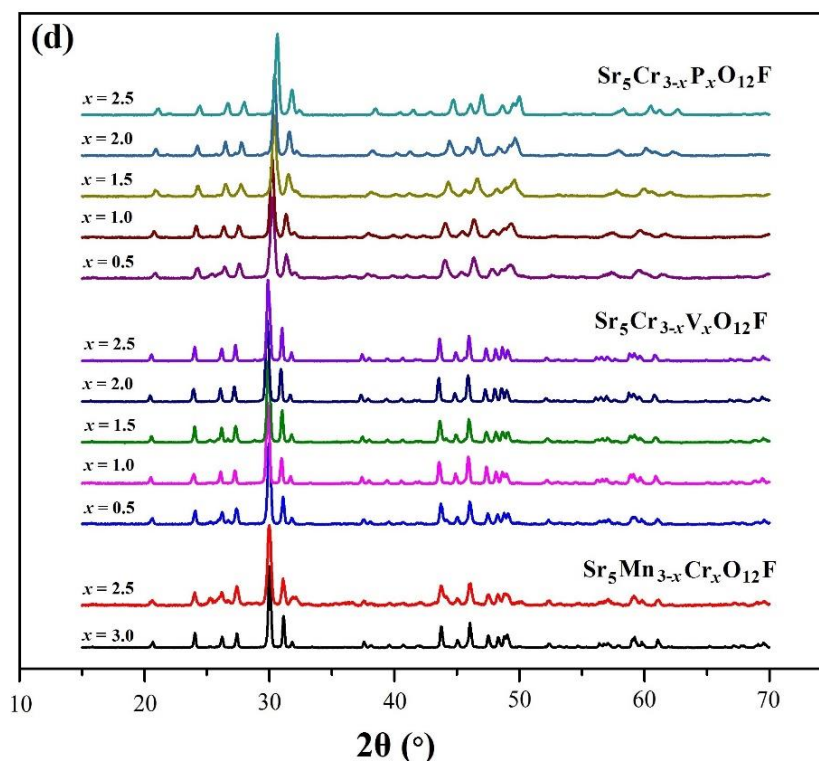


Figure 3.4 XRD patterns of (a)  $\text{Ba}_{5-x}\text{Sr}_x\text{Mn}_3\text{O}_{12}\text{Cl}$  ( $x = 0-2.5$ ),  $\text{Ba}_{5-x}\text{K}_x\text{Sr}_x\text{Mn}_{0.5}\text{P}_{2.5-x}\text{O}_{12}\text{Cl}$  ( $x = 0-0.5$ ),  $\text{Ba}_{5-x}\text{K}_x\text{Mo}_x\text{Mn}_{0.5}\text{P}_{2.5-x}\text{O}_{12}\text{Cl}$  ( $x = 0-0.2$ ); (b)  $\text{Ba}_5\text{Cr}_{3-x}\text{P}_x\text{O}_{12}\text{F}$  ( $x = 0.5-2.5$ ),  $\text{Ba}_5\text{Cr}_{3-x}\text{P}_x\text{O}_{12}\text{Cl}$  ( $x = 1.0-2.5$ ),  $\text{Ba}_5\text{Cr}_{3-x}\text{V}_x\text{O}_{12}\text{Cl}$  ( $x = 1.5-2.5$ ),  $\text{Ba}_5\text{Mn}_{3-x}\text{Cr}_x\text{O}_{12}\text{Cl}$  ( $x = 0-3.0$ ); (c)  $\text{Sr}_5\text{Cr}_{3-x}\text{P}_x\text{O}_{12}\text{Cl}$  ( $x = 0.5; 1.0$ ),  $\text{Sr}_5\text{Cr}_{3-x}\text{V}_x\text{O}_{12}\text{Cl}$  ( $x = 0.5-1.5$ ),  $\text{Sr}_5\text{Mn}_{3-x}\text{Cr}_x\text{O}_{12}\text{Cl}$  ( $x = 2.5-3.0$ ); (d)  $\text{Sr}_5\text{Cr}_{3-x}\text{P}_x\text{O}_{12}\text{F}$  ( $x = 0.5-2.5$ ),  $\text{Sr}_5\text{Cr}_{3-x}\text{V}_x\text{O}_{12}\text{F}$  ( $x = 0.5-2.5$ ),  $\text{Sr}_5\text{Mn}_{3-x}\text{Cr}_x\text{O}_{12}\text{F}$  ( $x = 2.5-3.0$ ).

Based on structure refinements all members of the series are isostructural, with the same hexagonal  $P6_3/m$  unit cell as the parent compounds or end-members of the series. The unit cell parameters ( $a$ ,  $c$ , cell volume  $V$ , and  $c/a$  ratio) variations with  $x$  (vanadium/phosphorus content) for  $\text{Ba}_5\text{Mn}_{3-x}\text{M}_x\text{O}_{12}\text{Cl}$  ( $M = \text{V}, \text{P}$ ) solid solutions are shown in Figure 3.5. There is a gradual increase of the  $a$  cell parameter and  $V$  in the case of  $\text{Ba}_5\text{Mn}_{3-x}\text{V}_x\text{O}_{12}\text{Cl}$  solid solution with substitution of smaller cations  $\text{Mn}^{5+}$  ( $0.33\text{\AA}$ ) ion by larger cations  $\text{V}^{5+}$  ( $0.355\text{\AA}$ ) [57]. Cell edge  $c$ , however, decreases slightly with increasing vanadium substitution. There is a slight deviation from Vegard's law in the case of  $\text{Ba}_5\text{Mn}_{3-x}\text{P}_x\text{O}_{12}\text{Cl}$  solid solution; unit cell edges  $a$ ,  $c$  and cell volume  $V$  progressively decrease with increasing of  $\text{P}^{5+}$  ( $0.17\text{\AA}$ ) content. The unit cell parameter  $c$  decreases with increasing  $x$  value for both solid solutions. Generally, the  $a$  parameter changes faster than  $c$  with  $x$  or

an increase/decrease in the size of M has a more pronounced impact on the  $a$  cell edge. This phenomenon is a consequence of the fact that the apatite structure is more amenable to expansion/compression in the direction of the  $a$  axis due to the difference in connection of barium polyhedra along the  $a$  and  $c$  axes: along the  $c$ -axis the structure is more rigid. The  $c/a$  ratio varies strongly because of the difference in average V-O/P-O and Mn-O bond lengths. All experimentally obtained unit cell parameters are in a good agreement with the literature data.

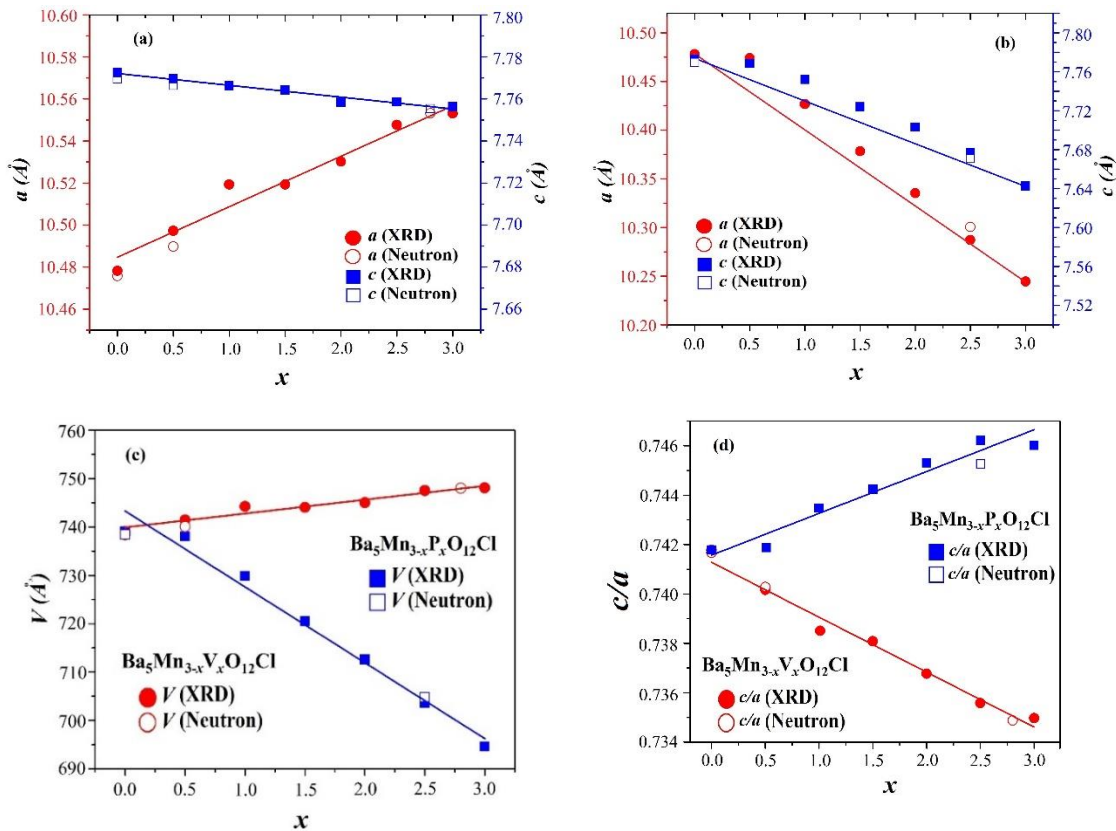


Figure 3.5 Unit cell edges of  $\text{Ba}_5\text{Mn}_{3-x}\text{V}_x\text{O}_{12}\text{Cl}$  (a) and  $\text{Ba}_5\text{Mn}_{3-x}\text{P}_x\text{O}_{12}\text{Cl}$  (b) phases, cell volumes (c) and  $c/a$  ratio showing anisotropic structural change (d) of both solid solutions as a function of  $x$  (vanadium/phosphorus content). The estimated errors for  $a$ ,  $c$ , and  $V$  are less than the size of the points in the figures.

Unit cell parameters of  $\text{Ba}_{5-x}\text{K}_x\text{Mo}_x\text{Mn}_{0.5}\text{P}_{2.5-x}\text{O}_{12}\text{Cl}$  and  $\text{Ba}_{5-x}\text{K}_x\text{S}_x\text{Mn}_{0.5}\text{P}_{2.5-x}\text{O}_{12}\text{Cl}$  series are given in Figure 3.6. The  $a$ ,  $c$ ,  $V$  and  $c/a$  are almost constant and just slightly decrease with increasing of  $x$  in case of  $\text{Ba}_{5-x}\text{K}_x\text{S}_x\text{Mn}_{0.5}\text{P}_{2.5-x}\text{O}_{12}\text{Cl}$  solid solution, when  $\text{Ba}^{2+}$  (CN (VIII) = 1.42 Å and CN (IX) = 1.47 Å) substituted with  $\text{K}^+$  (CN (VIII) = 1.51 Å and CN

(IX) = 1.55Å) and  $P^{5+}$  (CN (IV) = 0.17Å) replaced by  $S^{6+}$  (CN (IV) = 0.12Å). Unit cell parameters ( $a$ ,  $c$ ,  $V$  and  $c/a$ ) of  $Ba_{5-x}K_xMo_xMn_{0.5}P_{2.5-x}O_{12}Cl$  compounds increase with  $x$  (ionic radius of  $Mo^{6+}$  (IV) = 0.41Å).

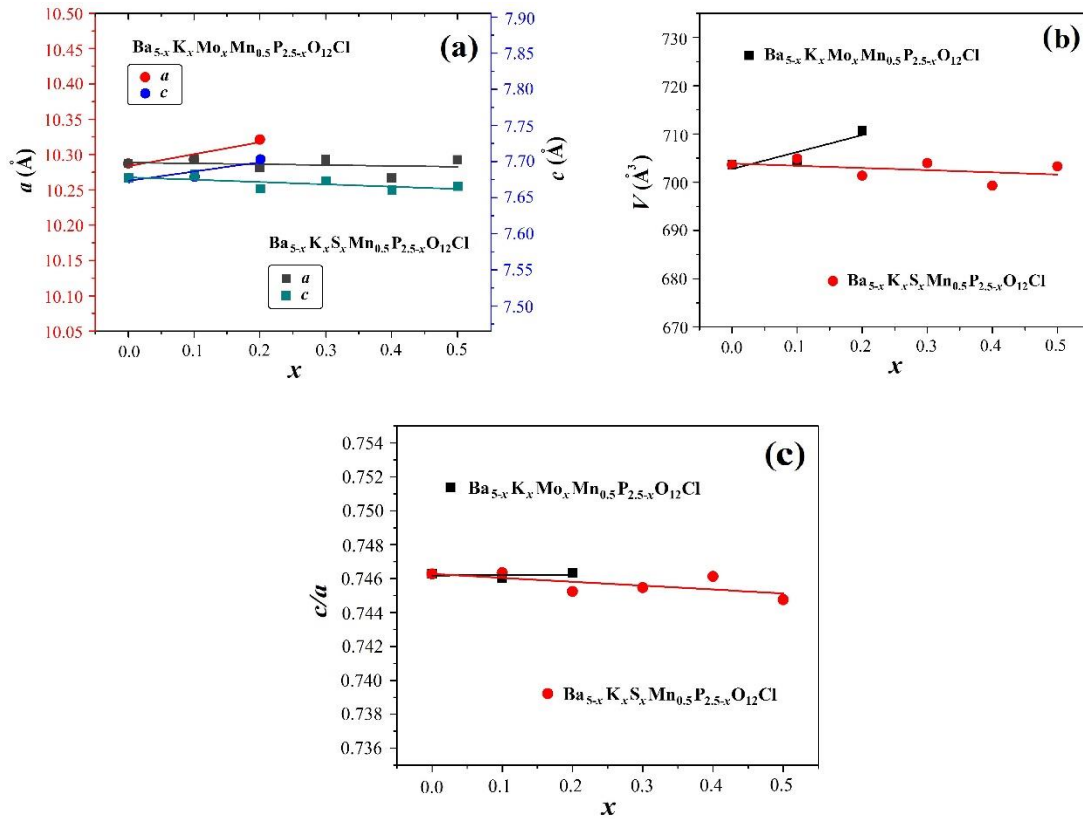


Figure 3.6 Unit cell edges  $a$  and  $c$  of  $Ba_{5-x}K_xMo_xMn_{0.5}P_{2.5-x}O_{12}Cl$  and  $Ba_{5-x}K_xS_xMn_{0.5}P_{2.5-x}O_{12}Cl$  series (a), cell volumes  $V$  (b) and  $c/a$  ratio (c) as a function of  $x$ . The estimated errors for  $a$ ,  $c$ , and  $V$  are less than the size of the points in the figures.

Unit cell parameters of  $Ba_{5-x}Sr_xMn_3O_{12}Cl$  and  $Ba_5Cr_{3-x}P_xO_{12}F$  compounds are shown in Figure 3.7. The  $a$  and  $V$  values of  $Ba_{5-x}Sr_xMn_3O_{12}Cl$  decrease with increasing of strontium amount in the structure (Shannon ionic radii of  $Sr^{2+}$  = 1.26Å (CN = VIII) and  $Sr^{2+}$  = 1.31Å (CN = IX));  $c$  and  $c/a$  parameters gradually increase with  $x$ . In case of  $Ba_5Cr_{3-x}P_xO_{12}F$  solid solution  $a$ ,  $c$  and  $V$  go down with increasing of  $x$  value. Reduction of cell parameters is related to a decrease of ionic radius, when larger  $Cr^{5+}$  (CN (IV) = 0.345Å) is replaced by smaller  $P^{5+}$ . The  $c/a$  ratio progressively goes up, because  $a$  parameter reduces faster comparing to  $c$  value.

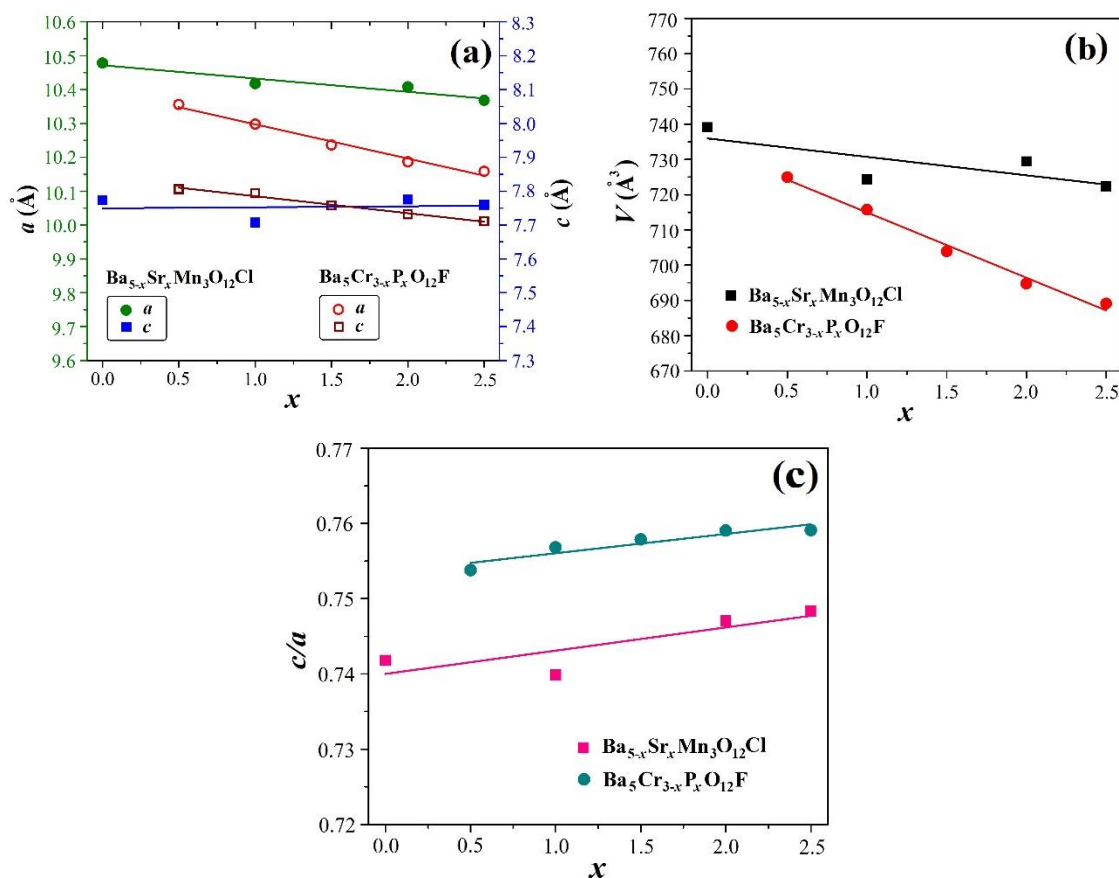
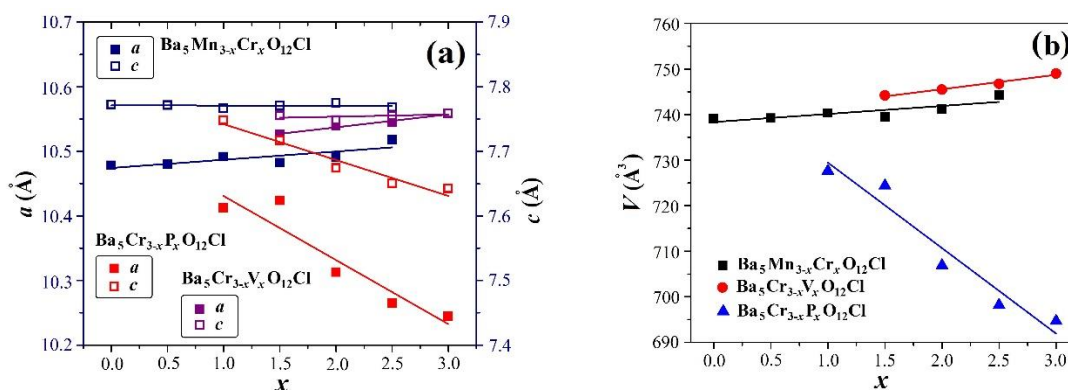


Figure 3.7 Unit cell edges  $a$  and  $c$  of  $\text{Ba}_{5-x}\text{Sr}_x\text{Mn}_3\text{O}_{12}\text{Cl}$  and  $\text{Ba}_5\text{Cr}_{3-x}\text{P}_x\text{O}_{12}\text{F}$  series (a), cell volumes  $V$  (b) and  $c/a$  ratio (c) as a function of  $x$ . The estimated errors for  $a$ ,  $c$ , and  $V$  are less than the size of the points in the figures.

Cell parameters of  $\text{Ba}_5\text{Mn}_{3-x}\text{Cr}_x\text{O}_{12}\text{Cl}$ ,  $\text{Ba}_5\text{Cr}_{3-x}\text{P}_x\text{O}_{12}\text{Cl}$  and  $\text{Ba}_5\text{Cr}_{3-x}\text{V}_x\text{O}_{12}\text{Cl}$  series are given in Figure 3.8. The  $a$ ,  $c$  and  $V$  values progressively increase in case of  $\text{Ba}_5\text{Mn}_{3-x}\text{Cr}_x\text{O}_{12}\text{Cl}$  and  $\text{Ba}_5\text{Cr}_{3-x}\text{V}_x\text{O}_{12}\text{Cl}$  compounds when smaller cations are substituted with larger elements; the  $a$ ,  $c$ , and  $V$  parameters decrease with  $x$  in case of  $\text{Ba}_5\text{Cr}_{3-x}\text{P}_x\text{O}_{12}\text{Cl}$ .



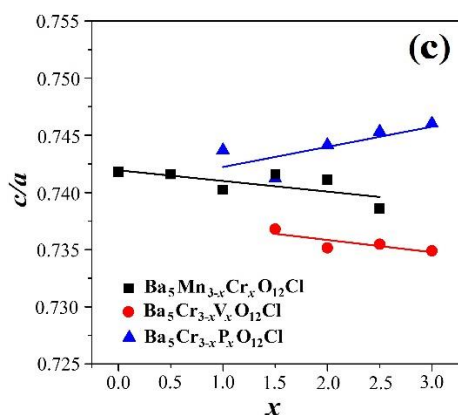
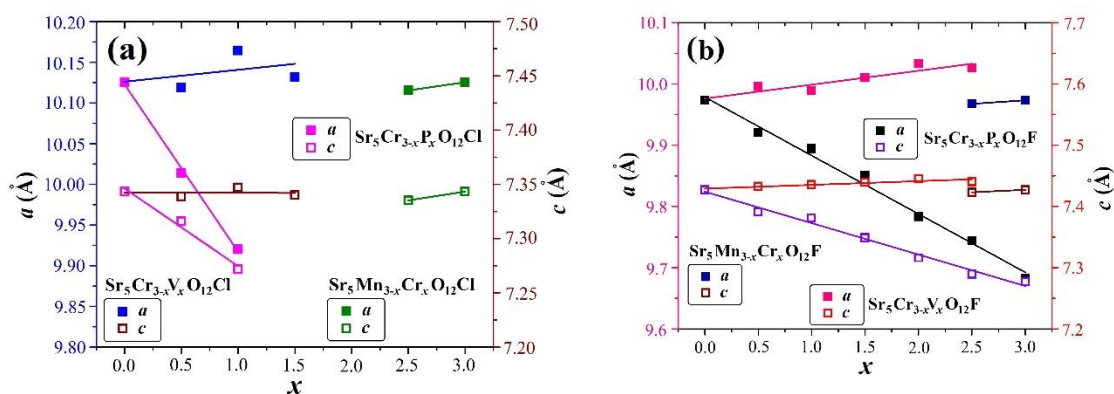


Figure 3.8 Unit cell edges  $a$  and  $c$  of Ba<sub>5</sub>Mn<sub>3-x</sub>Cr<sub>x</sub>O<sub>12</sub>Cl, Ba<sub>5</sub>Cr<sub>3-x</sub>P<sub>x</sub>O<sub>12</sub>Cl and Ba<sub>5</sub>Cr<sub>3-x</sub>V<sub>x</sub>O<sub>12</sub>Cl series (a), cell volumes  $V$  (b) and  $c/a$  ratio (c) as a function of  $x$ . The estimated errors for  $a$ ,  $c$ , and  $V$  are less than the size of the points in the figures.

Unit cell edges  $a$  and  $c$ , unit cell volume  $V$  and  $c/a$  ratio of Sr<sub>5</sub>Mn<sub>3-x</sub>Cr<sub>x</sub>O<sub>12</sub>Cl, Sr<sub>5</sub>Cr<sub>3-x</sub>P<sub>x</sub>O<sub>12</sub>Cl, Sr<sub>5</sub>Cr<sub>3-x</sub>V<sub>x</sub>O<sub>12</sub>Cl, Sr<sub>5</sub>Mn<sub>3-x</sub>Cr<sub>x</sub>O<sub>12</sub>F, Sr<sub>5</sub>Cr<sub>3-x</sub>P<sub>x</sub>O<sub>12</sub>F and Sr<sub>5</sub>Cr<sub>3-x</sub>V<sub>x</sub>O<sub>12</sub>F series are shown in Figure 3.9. Unit cell parameters decrease with increasing  $x$  when Cr<sup>5+</sup> is substituted with P<sup>5+</sup> (Sr<sub>5</sub>Cr<sub>3-x</sub>P<sub>x</sub>O<sub>12</sub>Cl and Sr<sub>5</sub>Cr<sub>3-x</sub>P<sub>x</sub>O<sub>12</sub>F); and  $a$ ,  $c$  and  $V$  values go up with replacement of Cr<sup>5+</sup> by V<sup>5+</sup> (Sr<sub>5</sub>Cr<sub>3-x</sub>V<sub>x</sub>O<sub>12</sub>Cl and Sr<sub>5</sub>Cr<sub>3-x</sub>V<sub>x</sub>O<sub>12</sub>F) and Mn<sup>5+</sup> by Cr<sup>5+</sup> (Sr<sub>5</sub>Mn<sub>3-x</sub>Cr<sub>x</sub>O<sub>12</sub>Cl and Sr<sub>5</sub>Mn<sub>3-x</sub>Cr<sub>x</sub>O<sub>12</sub>F). This trend was expected based on ionic radii difference.





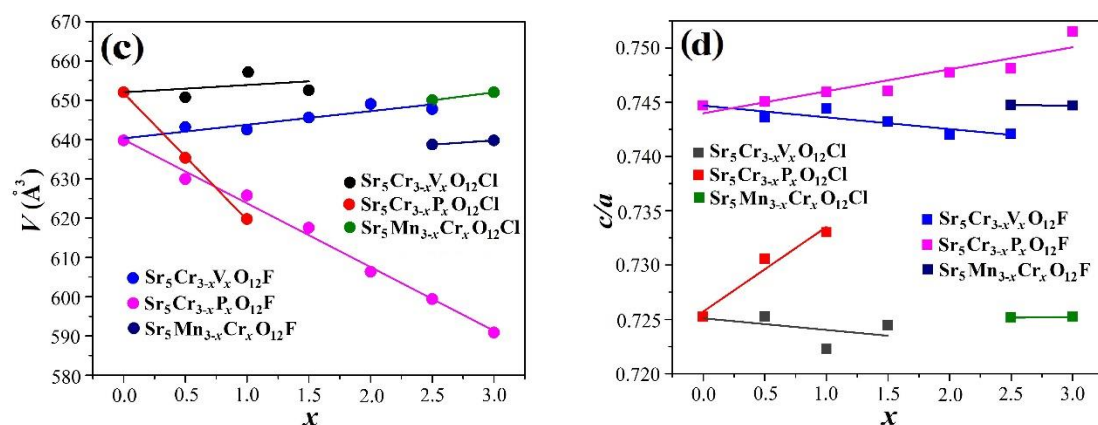


Figure 3.9 Unit cell edges  $a$  and  $c$  of  $\text{Sr}_5\text{Mn}_{3-x}\text{Cr}_x\text{O}_{12}\text{Cl}$ ,  $\text{Sr}_5\text{Cr}_{3-x}\text{P}_x\text{O}_{12}\text{Cl}$  and  $\text{Sr}_5\text{Cr}_{3-x}\text{V}_x\text{O}_{12}\text{Cl}$  series (a), unit cell edges  $a$  and  $c$  of  $\text{Sr}_5\text{Mn}_{3-x}\text{Cr}_x\text{O}_{12}\text{F}$ ,  $\text{Sr}_5\text{Cr}_{3-x}\text{P}_x\text{O}_{12}\text{F}$  and  $\text{Sr}_5\text{Cr}_{3-x}\text{V}_x\text{O}_{12}\text{F}$  series (b), cell volumes  $V$  (c) and  $c/a$  ratio (d) as a function of  $x$ . The estimated errors for  $a$ ,  $c$ , and  $V$  are less than the size of the points in the figures.

Neutron diffraction data on  $\text{Ba}_5\text{Mn}_{3-x}\text{V}_x\text{O}_{12}\text{Cl}$  ( $x = 0, 0.5, 2.8$ ) and  $\text{Ba}_5\text{Mn}_{0.5}\text{P}_{2.5}\text{O}_{12}\text{Cl}$  samples were collected and the crystal structures were refined using the Rietveld fitting method. The observed and calculated diffraction patterns for  $\text{Ba}_5\text{Mn}_{0.2}\text{V}_{2.8}\text{O}_{12}\text{Cl}$  are shown in Figure 3.10 and those for  $\text{Ba}_5(\text{MnO}_4)_3\text{Cl}$ ,  $\text{Ba}_5\text{Mn}_{2.5}\text{V}_{0.5}\text{O}_{12}\text{Cl}$  and  $\text{Ba}_5\text{Mn}_{0.5}\text{P}_{2.5}\text{O}_{12}\text{Cl}$  can be found in Figures 3.11-3.13 accordingly.

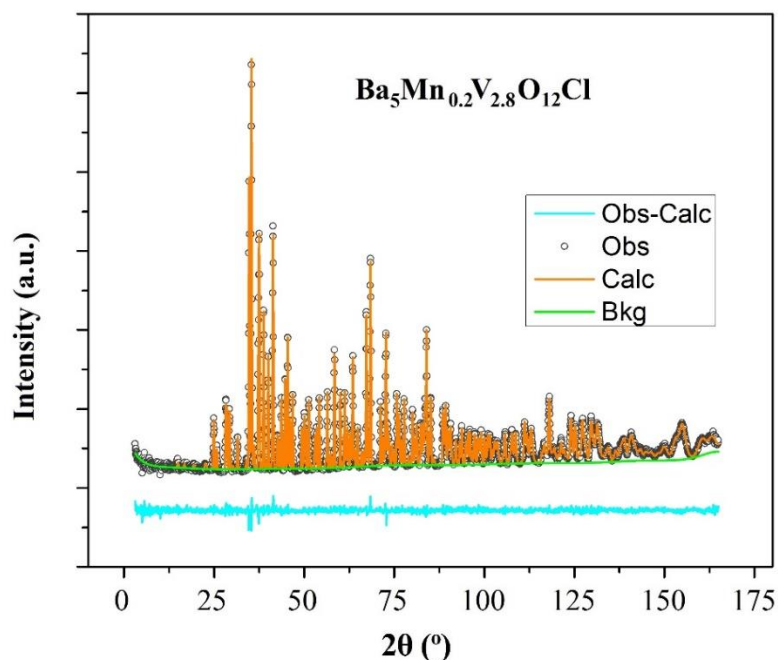


Figure 3.10 Neutron data of  $\text{Ba}_5\text{Mn}_{0.2}\text{V}_{2.8}\text{O}_{12}\text{Cl}$  phase shown with a Rietveld fit.

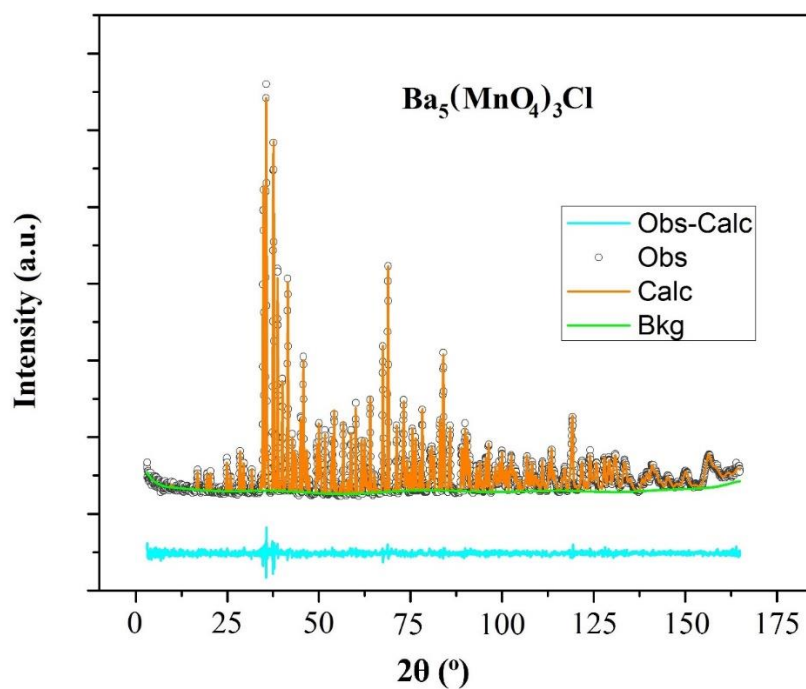


Figure 3.11 Neutron data of  $\text{Ba}_5(\text{MnO}_4)_3\text{Cl}$  phase shown with a Rietveld fit.

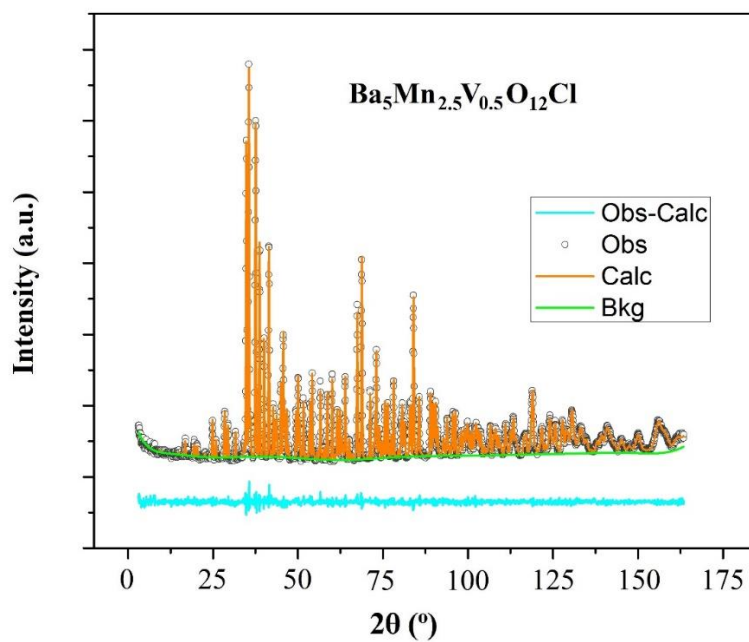


Figure 3.12 Neutron data of  $\text{Ba}_5\text{Mn}_{2.5}\text{V}_{0.5}\text{O}_{12}\text{Cl}$  phase shown with a Rietveld fit.



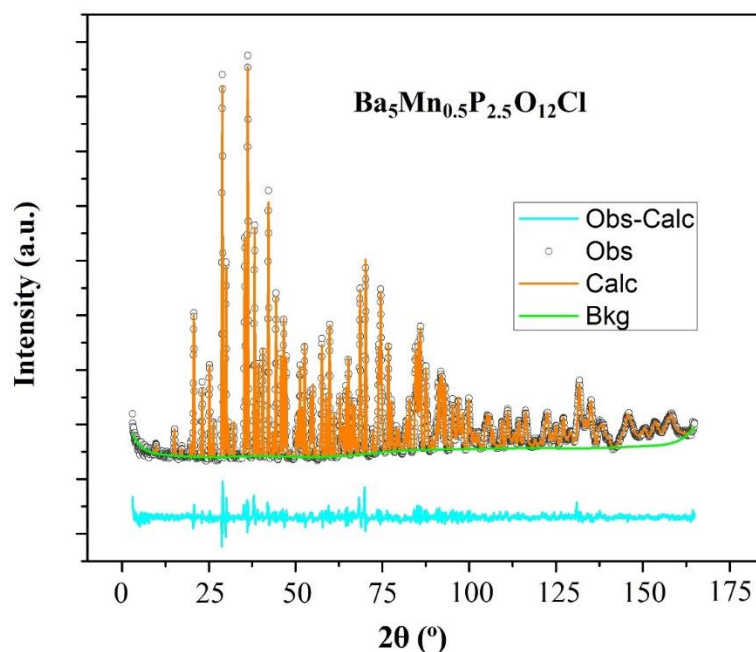


Figure 3.13 Neutron data of  $\text{Ba}_5\text{Mn}_{0.5}\text{P}_{2.5}\text{O}_{12}\text{Cl}$  phase shown with a Rietveld fit.

The structural refinement results are shown in Tables 3.1-3.5; bond valence sums (BVS) were calculated using the bond-valence calculator.

Table 3.1 Cell parameters by Rietveld refinement of  $\text{Ba}_5\text{Mn}_{3-x}\text{M}_x\text{O}_{12}\text{Cl}$  ( $M = \text{V}, \text{P}$ ).

Composition	$x = 0$	$M = \text{V}, x = 0.5$	$M = \text{V}, x = 2.8$	$M = \text{P}, x = 2.5$
$a$ (Å)	10.482(5)	10.490(7)	10.553(2)	10.301(0)
$c$ (Å)	7.7744(7)	7.7660(7)	7.7553(5)	7.6702(4)
$V$ (Å <sup>3</sup> )	739.82(4)	740.19(1)	748.00(2)	704.85(3)
$R_{\text{wp}}$ (%)	4.67	4.64	4.41	5.75
$\chi^2$	1.08	1.12	1.00	2.99

Table 3.2 Neutron structural refinement of  $\text{Ba}_5(\text{MnO}_4)_3\text{Cl}$ . The chemical formula of compound based on the refined occupancies is  $\text{Ba}_5(\text{MnO}_4)_3\text{Cl}$ .

Atoms	Wyckoff position	BVS	$x$	$y$	$z$	Occupancy	$U_{\text{iso}}$ (Å <sup>2</sup> )
Ba1	4f	2.1	1/3	2/3	0	1.00	0.009(4)
Ba2	6h	1.9	0.2585(8)	0.0132(1)	1/4	1.00	0.009(3)
Mn1	6h	4.7	0.3706(6)	0.4046(5)	1/4	1.00	0.009(4)
Cl1	2b	1.2	0	0	0	1.00	0.012(8)
O1	6h	1.9	0.4798(0)	0.3267(8)	1/4	1.00	0.016(6)

<b>O2</b>	6 <i>h</i>	2.1	0.4688(9)	0.5925(8)	1/4	1.00	0.009(0)
<b>O3</b>	12 <i>i</i>	1.9	0.2589(7)	0.3543(5)	0.0757(7)	1.00	0.014(1)

Table 3.3 Neutron structural refinement of Ba<sub>5</sub>Mn<sub>2.5</sub>V<sub>0.5</sub>O<sub>12</sub>Cl. The chemical formula of compound based on the refined occupancies is Ba<sub>5</sub>Mn<sub>2.6</sub>V<sub>0.4</sub>O<sub>12</sub>Cl.

Atoms	Wyckoff position	BVS	<i>x</i>	<i>y</i>	<i>z</i>	Occupancy	<i>U</i> <sub>iso</sub> (Å <sup>2</sup> )
<b>Ba1</b>	4 <i>f</i>	2.1	1/3	2/3	0	1.00	0.008(8)
<b>Ba2</b>	6 <i>h</i>	1.9	0.2576(6)	0.0120(6)	1/4	1.00	0.012(3)
<b>Mn1</b>	6 <i>h</i>		0.3717(2)	0.4051(2)	1/4	0.85(2)	0.008(0)
<b>V1</b>	6 <i>h</i>		0.3717(2)	0.4051(2)	1/4	0.15	0.006(8)
<b>Cl1</b>	2 <i>b</i>	1.0	0	0	0	1.00	0.011(3)
<b>O1</b>	6 <i>h</i>	1.9	0.4796(9)	0.3272(4)	1/4	1.00	0.019(2)
<b>O2</b>	6 <i>h</i>	2.1	0.4693(8)	0.5920(1)	1/4	1.00	0.011(2)
<b>O3</b>	12 <i>i</i>	1.8	0.2586(6)	0.3545(4)	0.0760(4)	1.00	0.000(3)

Table 3.4 Neutron structural refinement of Ba<sub>5</sub>Mn<sub>0.2</sub>V<sub>2.8</sub>O<sub>12</sub>Cl. The chemical formula of compound based on the refined occupancies is Ba<sub>5</sub>Mn<sub>0.3</sub>V<sub>2.7</sub>O<sub>12</sub>Cl.

Atoms	Wyckoff position	BVS	<i>x</i>	<i>y</i>	<i>z</i>	Occupancy	<i>U</i> <sub>iso</sub> (Å <sup>2</sup> )
<b>Ba1</b>	4 <i>f</i>	2.1	1/3	2/3	0	1.00	0.011(1)
<b>Ba2</b>	6 <i>h</i>	1.8	0.2455(1)	0.9884(7)	1/4	1.00	0.006(2)
<b>V1</b>	6 <i>h</i>		0.4055(1)	0.3717(2)	1/4	0.90	0.010(2)
<b>Mn1</b>	6 <i>h</i>		0.4055(1)	0.3717(2)	1/4	0.10(1)	0.007(1)
<b>Cl1</b>	2 <i>b</i>	1.0	0	0	0	1.00	0.013(1)
<b>O1</b>	6 <i>h</i>	1.8	0.3267(0)	0.4802(1)	1/4	1.00	0.018(8)
<b>O2</b>	6 <i>h</i>	2.1	0.5926(5)	0.4694(9)	1/4	1.00	0.007(0)
<b>O3</b>	12 <i>i</i>	1.8	0.3540(3)	0.2590(5)	0.0743(1)	1.00	0.020(9)

Table 3.5 Neutron structural refinement of Ba<sub>5</sub>Mn<sub>0.5</sub>P<sub>2.5</sub>O<sub>12</sub>Cl. The chemical formula of compound based on the refined occupancies is Ba<sub>5</sub>Mn<sub>0.5</sub>P<sub>2.5</sub>O<sub>12</sub>Cl.

Atoms	Wyckoff position	BVS	<i>x</i>	<i>y</i>	<i>z</i>	Occupancy	<i>U</i> <sub>iso</sub> (Å <sup>2</sup> )
<b>Ba1</b>	4 <i>f</i>	2.1	1/3	2/3	0	1.00	0.010(3)
<b>Ba2</b>	6 <i>h</i>	1.8	0.2453(4)	0.2592(4)	1/4	1.00	0.013(9)
<b>P1</b>	6 <i>h</i>		0.4049(7)	0.0350(2)	1/4	0.84(9)	0.007(0)
<b>Mn1</b>	6 <i>h</i>		0.4049(7)	0.0350(2)	1/4	0.15(1)	0.031(6)
<b>Cl1</b>	2 <i>b</i>	1.0	0	0	0	1.00	0.008(9)
<b>O1</b>	6 <i>h</i>	1.9	0.3397(1)	-0.1388(7)	1/4	1.00	0.024(3)
<b>O2</b>	6 <i>h</i>	2.1	0.5821(7)	0.1189(5)	1/4	1.00	0.010(6)

<b>O3</b>	12i	1.9	0.3547(5)	0.0855(4)	0.0855(9)	1.00	0.021(7)
-----------	-----	-----	-----------	-----------	-----------	------	----------

The refinement of atomic site occupancies shows that there are no oxygen or chlorine vacancies in the structures, i.e. oxygen and chlorine sites are fully occupied. Occupancies of vanadium atoms in the compounds were not refined because vanadium doesn't scatter neutrons much; all vanadium occupancies shown in the tables were calculated based on refined manganese occupancies. Refined atomic displacement parameter  $U$  values are reasonable and calculated bond valence sums are as expected.  $\text{Mn}^{5+}$ ,  $\text{V}^{5+}$ ,  $\text{P}^{5+}$  occupy the same crystallographic sites in the structure and have tetrahedral coordination, bonded to four oxygen atoms.

Bond distances and angles for  $\text{Ba}_5\text{Mn}_{0.2}\text{V}_{2.8}\text{O}_{12}\text{Cl}$  are shown in Table 3.6 and those for  $\text{Ba}_5(\text{MnO}_4)_3\text{Cl}$ ,  $\text{Ba}_5\text{Mn}_{2.5}\text{V}_{0.5}\text{O}_{12}\text{Cl}$ , and  $\text{Ba}_5\text{Mn}_{0.5}\text{P}_{2.5}\text{O}_{12}\text{Cl}$  are given in Tables 3.7-3.9 correspondingly. The M-O bonds in  $(\text{MO}_4)^{3-}$  tetrahedra become shorter and more covalent with increasing of Mn content in the case of  $\text{Ba}_5\text{Mn}_{3-x}\text{V}_x\text{O}_{12}\text{Cl}$  solid solution (average M-O bond length of  $\text{Ba}_5(\text{MnO}_4)_3\text{Cl}$  equals 1.699(5) Å and 1.711(8) Å for  $\text{Ba}_5\text{Mn}_{0.2}\text{V}_{2.8}\text{O}_{12}\text{Cl}$ ).

Table 3.6 Selected geometric parameters: bond lengths (Å) and angles (°) of  $\text{Ba}_5\text{Mn}_{0.2}\text{V}_{2.8}\text{O}_{12}\text{Cl}$ .

<b>Ba1—O1×3</b>	2.737(2)	<b>Ba2—O1</b>	2.962(4)
<b>Ba1—O2×3</b>	2.749(8)	<b>Ba2—O2</b>	2.606(0)
<b>Ba1—O3×3</b>	3.040(9)	<b>Ba2—O3×2</b>	2.692(1)
<b>Mn1/V1—O3×2</b>	1.708(6)	<b>Ba2—O3×2</b>	2.837(5)
<b>Mn1/V1—O2</b>	1.710(9)	<b>Ba2—Cl1×2</b>	3.286(6)
<b>Mn1/V1—O1</b>	1.718(9)		
<b>O1—Mn1/V1—O3</b>	111.8(4)	<b>Cl1—Ba2—Cl1</b>	72.30(1)
<b>Ba1—O3—Mn1/V1</b>	92.61(5)	<b>O2—Mn1/V1—O3</b>	106.8(0)
<b>Ba2—O1—Mn1/V1</b>	101.2(6)		

Table 3.7 Selected geometric parameters: bond lengths (Å) and angles (°) of  $\text{Ba}_5(\text{MnO}_4)_3\text{Cl}$ .

<b>Ba1—O1×3</b>	2.739(7)	<b>Ba2—O1</b>	2.925(7)
<b>Ba1—O2×3</b>	2.735(4)	<b>Ba2—O2</b>	2.594(8)
<b>Ba1—O3×3</b>	3.019(1)	<b>Ba2—O3×2</b>	2.701(7)
<b>Mn1—O3×2</b>	1.692(9)	<b>Ba2—O3×2</b>	2.832(1)
<b>Mn1—O2</b>	1.706(7)	<b>Ba2—Cl1×2</b>	3.281(5)

<b>Mn1—O1</b>	1.705(6)		
<b>O1—Mn1—O3</b>	112.1(7)	<b>Cl1—Ba2—Cl1</b>	72.63(7)
<b>Ba1—O3—Mn1</b>	93.06(8)	<b>O2—Mn1—O3</b>	106.4(8)
<b>Ba2—O1—Mn1</b>	101.1(3)		

Table 3.8 Selected geometric parameters: bond lengths (Å) and angles (°) of Ba<sub>5</sub>Mn<sub>2.5</sub>V<sub>0.5</sub>O<sub>12</sub>Cl.

<b>Ba1—O1×3</b>	2.748(0)	<b>Ba2—O1</b>	2.942(2)
<b>Ba1—O2×3</b>	2.735(3)	<b>Ba2—O2</b>	2.590(7)
<b>Ba1—O3×3</b>	3.017(0)	<b>Ba2—O3×2</b>	2.706(2)
<b>Mn1/V1—O3×2</b>	1.698(2)	<b>Ba2—O3×2</b>	2.819(2)
<b>Mn1/V1—O2</b>	1.698(5)	<b>Ba2—Cl1×2</b>	3.278(7)
<b>Mn1/V1—O1</b>	1.695(8)		
<b>O1—Mn1/V1—O3</b>	112.3(2)	<b>Cl1—Ba2—Cl1</b>	72.62(0)
<b>Ba1—O3—Mn1/V1</b>	92.92(5)	<b>O2—Mn1/V1—O3</b>	106.5(3)
<b>Ba2—O1—Mn1/V1</b>	101.3(7)		

Table 3.9 Selected geometric parameters: bond lengths (Å) and angles (°) of Ba<sub>5</sub>Mn<sub>0.5</sub>P<sub>2.5</sub>O<sub>12</sub>Cl.

<b>Ba1—O1×3</b>	2.746(7)	<b>Ba2—O1</b>	2.964(1)
<b>Ba1—O2×3</b>	2.721(5)	<b>Ba2—O2</b>	2.603(3)
<b>Ba1—O3×3</b>	3.012(4)	<b>Ba2—O3×2</b>	2.722(5)
<b>Mn1/P1—O3×2</b>	1.548(5)	<b>Ba2—O3×2</b>	2.842(3)
<b>Mn1/P1—O2</b>	1.581(4)	<b>Ba2—Cl1×2</b>	3.232(1)
<b>Mn1/P1—O1</b>	1.567(3)		
<b>O1—Mn1/P1—O3</b>	111.0(7)	<b>Cl1—Ba2—Cl1</b>	72.78(0)
<b>Ba1—O3—Mn1/P1</b>	93.98(2)	<b>O2—Mn1/P1—O3</b>	107.7(2)
<b>Ba2—O1—Mn1/P1</b>	100.4(9)		

The main differences in the studied structures occur in the tetrahedrally coordinated M-atoms (Fig. 3.14). A change of the tetrahedral central atom leads to modifications of polyhedra parameters (bond lengths and bond angles). To describe the distortion of tetrahedra the bond angle variance (BAV) and bond length distortion (BLD) parameters might be used [58,59]. BAV and BLD are used to characterize any polyhedra deviations from the ideal geometry.

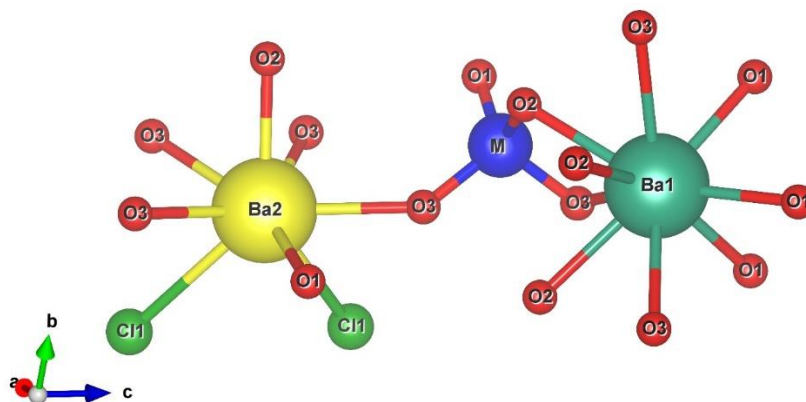


Figure 3.14 A fragment of  $\text{Ba}_5\text{Mn}_{3-x}\text{V}_x\text{O}_{12}\text{Cl}/\text{Ba}_5\text{Mn}_{3-x}\text{P}_x\text{O}_{12}\text{Cl}$  unit cell: big dark turquoise and yellow spheres represent different crystallographic positions of  $\text{Ba}^{2+}$  – 4f and 6h accordingly, blue spheres –  $\text{M}^{5+}$ ,  $\text{Cl}^-$  – green spheres,  $\text{O}^{2-}$  – red spheres.

The bond angle variance (BAV) can be calculated using  $\sum_{i=1}^n (\theta_i - \theta_0)^2 / (n-1)$  equation ( $\theta_0$  = ideal bond angle for a regular polyhedron,  $n$  = number of bond angles in polyhedron and  $\theta_i$  = individual bond angles).  $\text{BLD} = 100/n \sum_{i=1}^n |((\text{M}-\text{X})_i - (\text{M}-\text{X})_m) / (\text{M}-\text{X})_m|$  ( $i$  = individual bond lengths,  $m$  = average bond length and  $n$  = number of bonds). These parameters were calculated for  $\text{Ba}_5\text{Mn}_{0.2}\text{V}_{2.8}\text{O}_{12}\text{Cl}$ ,  $\text{Ba}_5(\text{MnO}_4)_3\text{Cl}$  and  $\text{Ba}_5\text{Mn}_{0.5}\text{P}_{2.5}\text{O}_{12}\text{Cl}$  phases based on our Rietveld refinement and compared with the same parameters for  $\text{Ba}_5(\text{VO}_4)_3\text{Cl}$  and  $\text{Ba}_5(\text{PO}_4)_3\text{Cl}$  compounds, which were calculated based on the literature data. The average bond angles O–M–O in  $(\text{MO}_4)^{3-}$  tetrahedra slightly varies for both series with increasing  $x$  value (V/P content). The mean O–M–O angle equals  $108.72^\circ$ ,  $109.40^\circ$ ,  $109.45^\circ$ ,  $109.48^\circ$  and  $109.47^\circ$  for  $\text{Ba}_5(\text{VO}_4)_3\text{Cl}$ ,  $\text{Ba}_5\text{Mn}_{0.2}\text{V}_{2.8}\text{O}_{12}\text{Cl}$ ,  $\text{Ba}_5(\text{MnO}_4)_3\text{Cl}$ ,  $\text{Ba}_5\text{Mn}_{0.5}\text{P}_{2.5}\text{O}_{12}\text{Cl}$  and  $\text{Ba}_5(\text{PO}_4)_3\text{Cl}$ , respectively (ideal tetrahedral angle is  $109.47^\circ$ ). The O–M–O bond angle for the larger  $(\text{VO}_4)^{3-}$  tetrahedra deviate more from  $109.47^\circ$ ; this fact is confirmed by BAV values (BAV ( $\text{Ba}_5(\text{VO}_4)_3\text{Cl}$ ) = 13.7, BAV ( $\text{Ba}_5\text{Mn}_{0.2}\text{V}_{2.8}\text{O}_{12}\text{Cl}$ ) = 13.5, BAV ( $\text{Ba}_5(\text{MnO}_4)_3\text{Cl}$ ) = 12.8, BAV ( $\text{Ba}_5\text{Mn}_{0.5}\text{P}_{2.5}\text{O}_{12}\text{Cl}$ ) = 2.93 and BAV ( $\text{Ba}_5(\text{PO}_4)_3\text{Cl}$ ) = 2.35). There is an opposite trend in the case of BLD values; with decreasing of  $\text{M}^{5+}$  ionic radius BLD increases. The smaller tetrahedral  $(\text{PO}_4)^{3-}$  anion is more distorted, where  $\text{Ba}_5(\text{PO}_4)_3\text{Cl}$  has the highest value of BLD = 0.83 (BLD ( $\text{Ba}_5(\text{VO}_4)_3\text{Cl}$ ) = 0.19, BLD ( $\text{Ba}_5\text{Mn}_{0.2}\text{V}_{2.8}\text{O}_{12}\text{Cl}$ ) = 0.21, BLD ( $\text{Ba}_5(\text{MnO}_4)_3\text{Cl}$ ) = 0.39 and BLD ( $\text{Ba}_5\text{Mn}_{0.5}\text{P}_{2.5}\text{O}_{12}\text{Cl}$ ) = 0.82).

### 3.2.2 Optical Properties

Optical properties were characterized to study the evolution of the solid solutions colors and understand structure-property relationships. The substituted samples have very bright colors, varying from light to dark turquoise and dark green (Mn-rich ends of solid solutions); the end members  $\text{Ba}_5(\text{PO}_4)_3\text{Cl}$  and  $\text{Ba}_5(\text{VO}_4)_3\text{Cl}$  have a white color (Fig. 3.15).

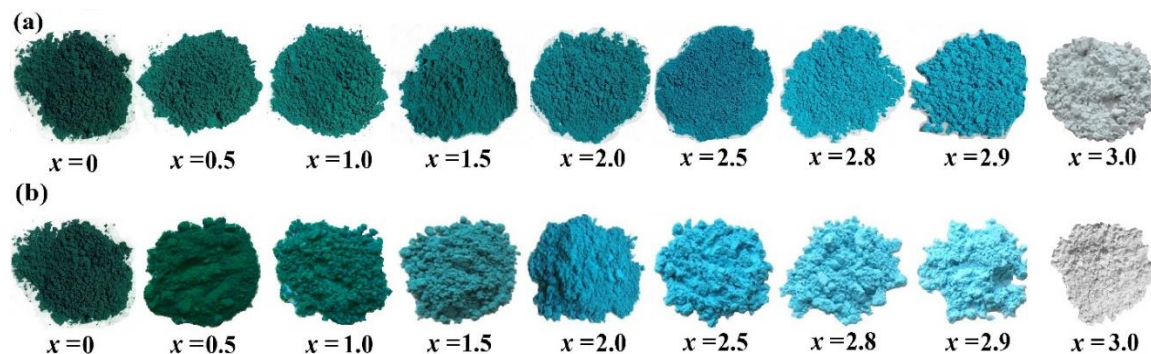


Figure 3.15 Colors of (a)  $\text{Ba}_5\text{Mn}_{3-x}\text{V}_x\text{O}_{12}\text{Cl}$  and (b)  $\text{Ba}_5\text{Mn}_{3-x}\text{P}_x\text{O}_{12}\text{Cl}$  samples.

To characterize the color of  $\text{Ba}_5\text{Mn}_{3-x}\text{M}_x\text{O}_{12}\text{Cl}$  ( $M = \text{V}, \text{P}$ ) samples, the  $L^*$ ,  $a^*$ ,  $b^*$  color coordinates were measured [60] ( $L^*a^*b^*$  color spheres of  $\text{Ba}_5\text{Mn}_{3-x}\text{M}_x\text{O}_{12}\text{Cl}$  ( $M = \text{V}, \text{P}$ ) series are given in Fig. 3.16 and Fig. 3.17).

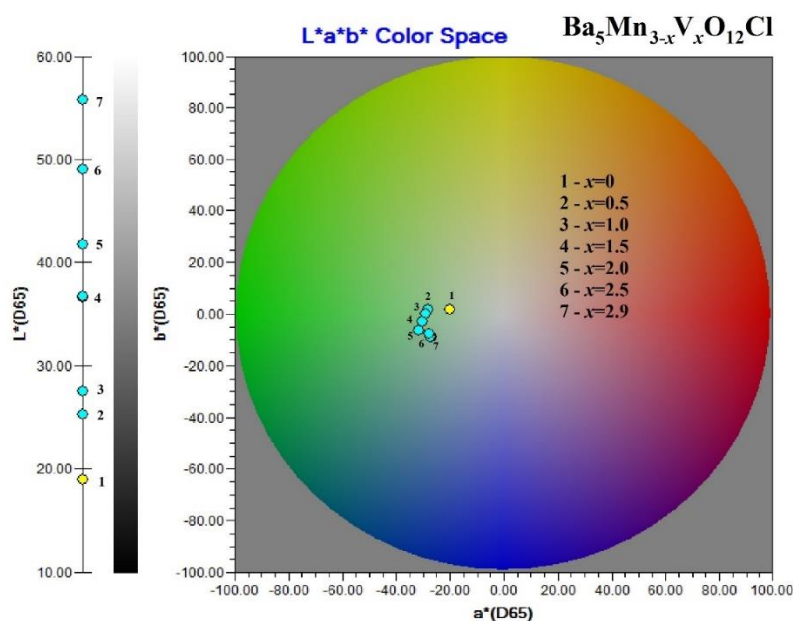


Figure 3.16 Color sphere of  $\text{Ba}_5\text{Mn}_{3-x}\text{V}_x\text{O}_{12}\text{Cl}$  ( $x = 0-2.9$ ) samples.

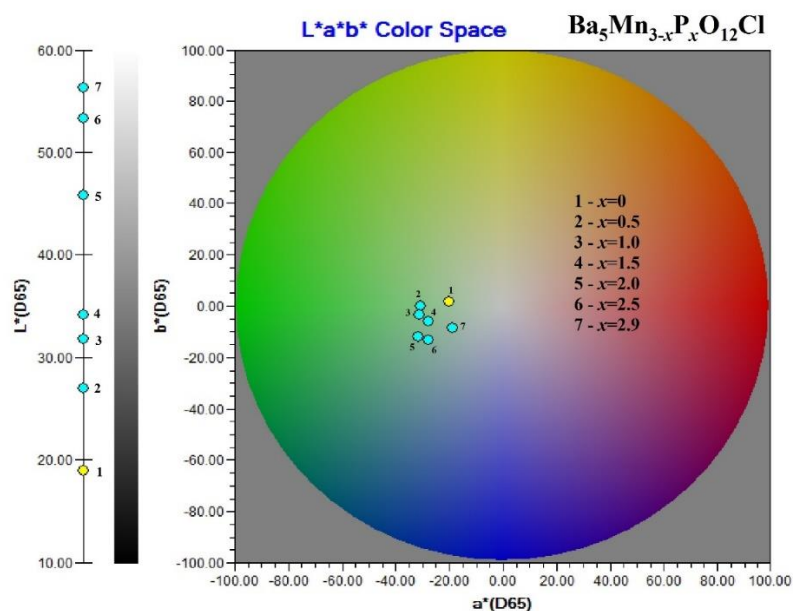


Figure 3.17 Color sphere of  $\text{Ba}_5\text{Mn}_{3-x}\text{P}_x\text{O}_{12}\text{Cl}$  ( $x = 0-2.9$ ) samples.

As shown in Figure 3.18, the  $L^*$  and  $a^*$  values gradually increase with increasing of  $x$  value, while the  $b^*$  values decrease as  $x$  moves to the vanadium/phosphorous-rich sides of the solid solutions.

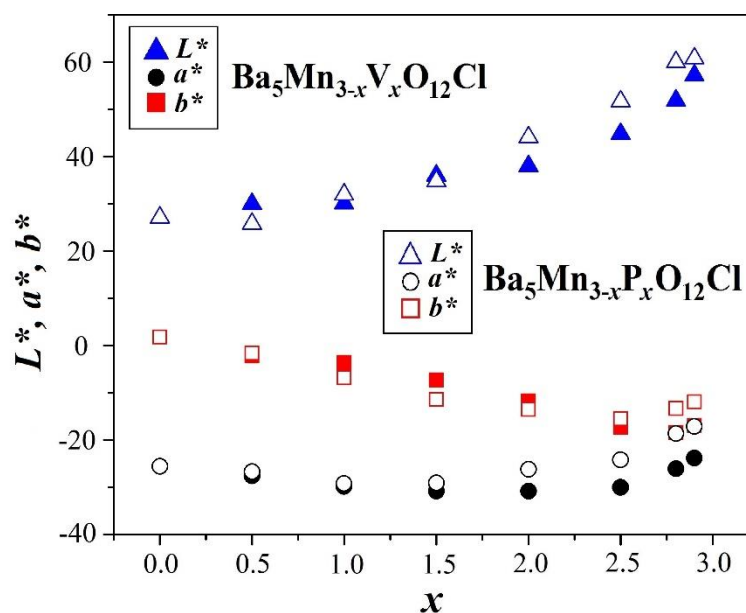


Figure 3.18  $L^*$  (it represents a black ( $L^* = 0$ ) / white ( $L^* = 100$ ) component of color),  $a^*$  (it is responsible for a red ( $a^* > 0$ ) / green ( $a^* < 0$ ) component),  $b^*$  (it represents a yellow ( $b^* > 0$ ) / blue ( $b^* < 0$ ) components) parameters of samples as a function of  $x$ .

Interatomic excitations (d-d transitions) in  $\text{Mn}^{5+}$  (tetrahedral coordination) are mainly responsible for the color of the samples. There are two transitions that significantly impact the visible spectrum and thus color. The ground state  $e_2$  has two states with two unpaired electrons. There are just two fully allowed transitions to examine: one electron up to  $t_2$  ( $e^1t^1_2$ ) and two electrons up to  $t_2$  ( $e^0t^2_2$ ). The one-electron transition gives the blue color. The two-electron transition has a higher energy and lower probability. Consequently, the second transition is what changes blue to blue-green (turquoise) color. It is possible that this less probable two-electron transition is intensified by the high oxidation state (5+) of the manganese ion and this is the reason it is most enhanced for barium containing compounds where Mn–O covalency is very high.

Diffuse reflectance spectra of the  $\text{Ba}_5\text{Mn}_{3-x}\text{V}_x\text{O}_{12}\text{Cl}$  series are shown in Figure 3.19. All  $\text{Ba}_5\text{Mn}_{3-x}\text{V}_x\text{O}_{12}\text{Cl}$  ( $x = 0\text{--}2.9$ ) samples show two maximum peaks in the red-orange (~630 nm) and purple (~380 nm) regions and one minimum in the green-blue region (~500 nm to 520 nm); this combination causes the green or turquoise color of the compounds.  $\text{Ba}_5\text{V}_3\text{O}_{12}\text{Cl}$  and  $\text{Ba}_5\text{P}_3\text{O}_{12}\text{Cl}$  don't absorb in the visible region and the color of these samples is white. On each absorbance vs. wavelength spectrum there are two shoulders; which are present in the high- and low-energy regions of the visible spectrum. The low-energy peak is due to the allowed transitions of electrons (d-d transitions) inside the manganese atom and the high-energy peak is due to a  $\text{Mn}^{5+}\text{--O}^{2-}$  charge transfer transition. The intensity of the samples' absorbance goes down with decreasing of manganese content ( $x$  increases), because the d-d transition's contribution becomes smaller, and the samples become lighter. At the same time the minimum of absorbance becomes broader, though it still exists in the spectrum of the lightest sample ( $x = 2.5$ ) and completely disappears for white samples ( $x = 3$ ), which do not absorb in the visible region.



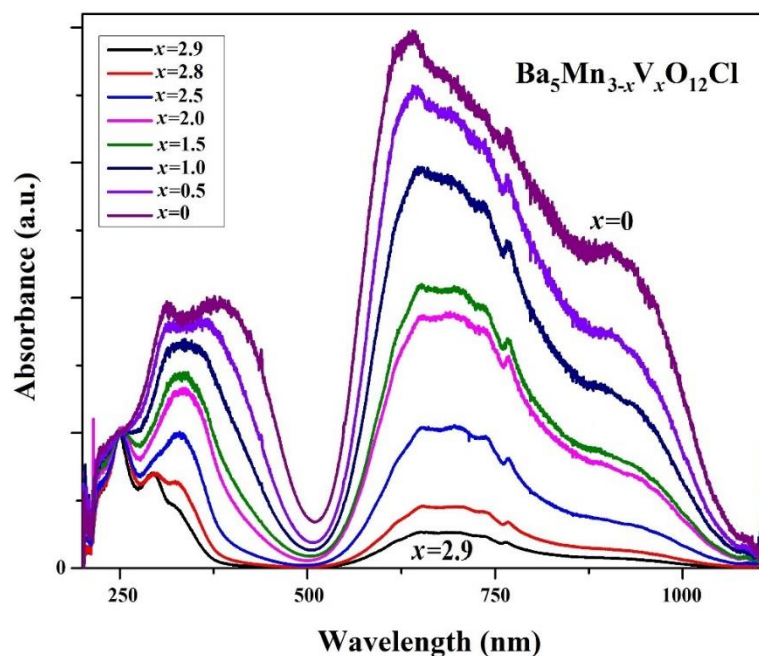
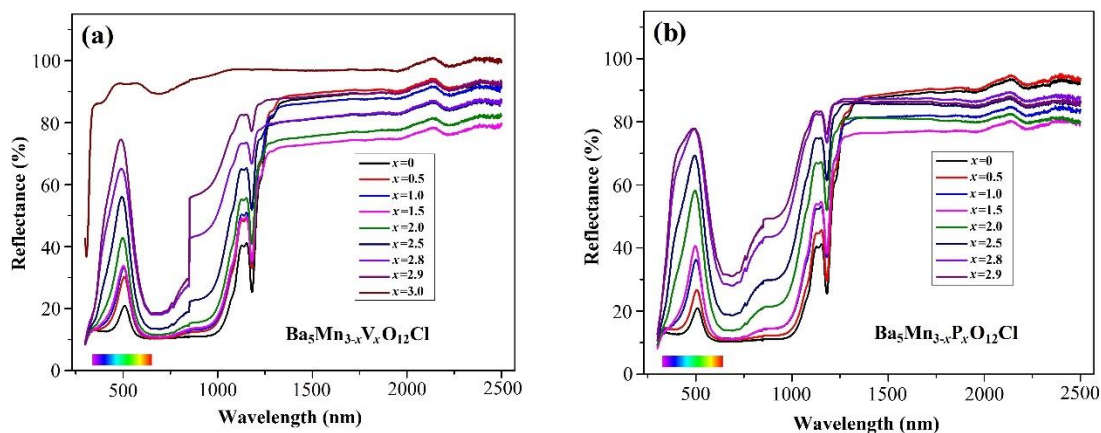


Figure 3.19 Diffuse-reflectance spectra of the  $\text{Ba}_5\text{Mn}_{3-x}\text{V}_x\text{O}_{12}\text{Cl}$  series.

Near-infrared (NIR) reflectance spectra were measured to examine the potential “Cool pigment” application of the samples ( $\text{Ba}_5\text{Mn}_{3-x}\text{V}_x\text{O}_{12}\text{Cl}$ : Fig. 3.20(a),  $\text{Ba}_5\text{Mn}_{3-x}\text{P}_x\text{O}_{12}\text{Cl}$ : Fig. 3.20(b),  $\text{Sr}_5\text{Cr}_{3-x}\text{P}_x\text{O}_{12}\text{F}$ : Fig. 3.20(c),  $\text{Sr}_5\text{Cr}_{3-x}\text{V}_x\text{O}_{12}\text{F}$ : Fig. 3.20(d),  $\text{Ba}_5\text{K}_x\text{S}_x\text{Mn}_{0.5}\text{P}_{2.5-x}\text{O}_{12}\text{Cl}$ : Fig. 3.21(a),  $\text{Ba}_5\text{Cr}_{3-x}\text{P}_x\text{O}_{12}\text{Cl}$ : Fig. 3.21(b),  $\text{Ba}_5\text{Mn}_{3-x}\text{Cr}_x\text{O}_{12}\text{Cl}$ : Fig. 3.21(c) and  $\text{Ba}_5\text{Cr}_{3-x}\text{P}_x\text{O}_{12}\text{F}$ : Fig. 3.21(d)).



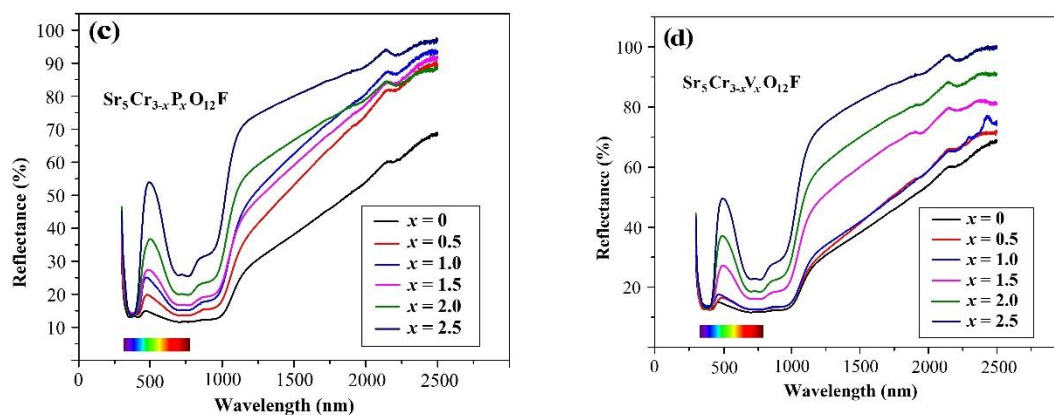


Figure 3.20 Reflectance (%) of (a)  $\text{Ba}_5\text{Mn}_{3-x}\text{V}_x\text{O}_{12}\text{Cl}$ , (b)  $\text{Ba}_5\text{Mn}_{3-x}\text{P}_x\text{O}_{12}\text{Cl}$ , (c)  $\text{Sr}_5\text{Cr}_{3-x}\text{P}_x\text{O}_{12}\text{F}$  and (d)  $\text{Sr}_5\text{Cr}_{3-x}\text{V}_x\text{O}_{12}\text{F}$  samples as a function of wavelength (nm).

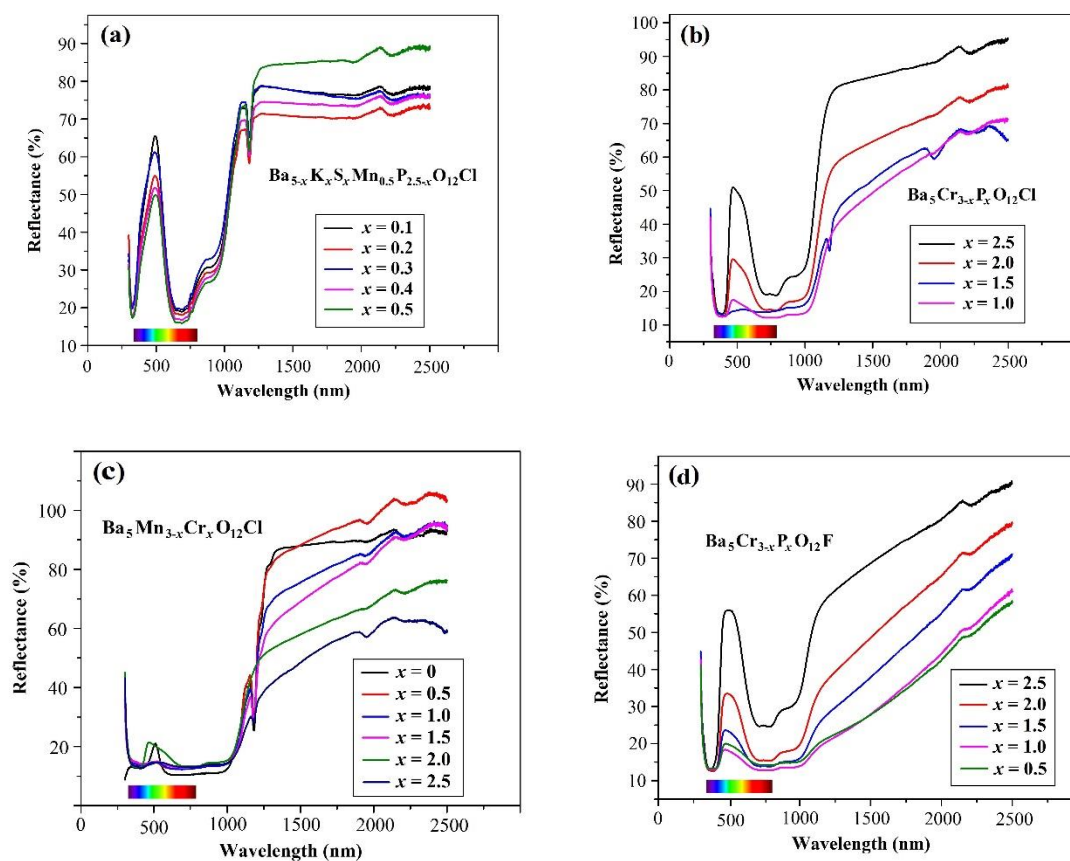


Figure 3.21 Reflectance (%) of (a)  $\text{Ba}_5\text{K}_x\text{S}_x\text{Mn}_{0.5}\text{P}_{2.5-x}\text{O}_{12}\text{Cl}$ , (b)  $\text{Ba}_5\text{Cr}_{3-x}\text{P}_x\text{O}_{12}\text{Cl}$ , (c)  $\text{Ba}_5\text{Mn}_{3-x}\text{Cr}_x\text{O}_{12}\text{Cl}$  and (d)  $\text{Ba}_5\text{Cr}_{3-x}\text{P}_x\text{O}_{12}\text{F}$  series as a function of wavelength (nm).

UV-VIS and NIR reflectance of  $\text{Ba}_5\text{Mn}_{3-x}\text{V}_x\text{O}_{12}\text{Cl}$  ( $x = 0, 2.5, 3.0$ ) and  $\text{Ba}_5\text{Mn}_{3-x}\text{P}_x\text{O}_{12}\text{Cl}$  ( $x = 0, 2.5, 3.0$ ) samples as a function of wavelength are shown in Figure 3.22. There is one peak around 500 nm in the visible region for the colored samples, and the

maximum of this peak shifts toward longer wavelength with increasing manganese content as the sample color goes from turquoise to dark green. With decreasing amount of vanadium/phosphorus (when  $x$  value decreases) metal-oxygen M–O bonds become more covalent and the crystal field around the M-atom changes resulting in the peak shifting. The  $(\text{MnO}_4)^{3-}$  group shows five reflectance peaks and absorbance valleys in the 400 nm to 1400 nm region, which are related to five interatomic transitions of the  $\text{Mn}^{5+}$  cation [61–64]. All synthesized samples show these transitions in the studied region:  $e^2(^3A_2) \rightarrow t_2^2(^3T_1 = ^3P)$  ( $\sim 300$  nm);  $e^2(^3A_2) \rightarrow e^1t_2^1(^3T_1 = ^3F)$  ( $\sim 700$  nm) and  $e^2(^3A_2) \rightarrow e^1t_2^1(^3T_2)$  ( $\sim 900$  nm) are spin allowed transitions and two are spin forbidden:  $e^2(^3A_2) \rightarrow e^2(^1A_1)$  ( $\sim 800$  nm) and there is minimum peak around 1200 nm, which corresponds to  $e^2(^3A_2) \rightarrow e^2(^1E)$  transition. Intensity of reflectance goes down from light turquoise to dark-green samples. The abrupt change in the IR reflectance of  $\text{Ba}_5\text{Mn}_{3-x}\text{V}_x\text{O}_{12}\text{Cl}$  solid solution near 800 nm is probably due to the effect of fluorescence in samples containing manganese and vanadium together; samples with  $x = 0$  and  $x = 3.0$  do not show this phenomenon.

The reflectance of all manganese containing samples in the 750 nm to 2500 nm region where “Cool pigments” display high reflectance is around 70 % to 85 %. The samples with chromium show slightly smaller reflectance ( $\sim 50\%$ – $80\%$ ). All synthesized compounds are promising materials for “Cool pigments” application.

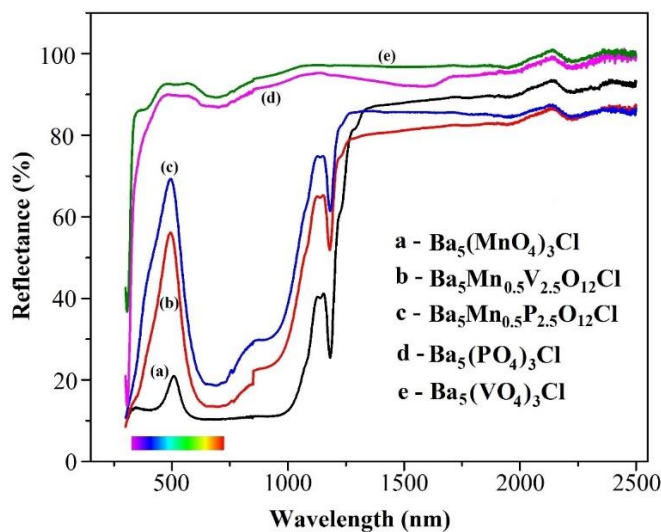


Figure 3.22 UV-VIS and NIR reflectance (%) of  $\text{Ba}_5\text{Mn}_{3-x}\text{V}_x\text{O}_{12}\text{Cl}$  ( $x = 0, 2.5, 3.0$ ) and  $\text{Ba}_5\text{Mn}_{3-x}\text{P}_x\text{O}_{12}\text{Cl}$  ( $x = 0, 2.5, 3.0$ ) samples as a function of wavelength (nm).

### 3.2.3 IR Investigation

Based on literature data the most intense vibrational modes in apatite-type compounds are due to vibrations of  $(\text{MO}_4)^{3-}$  tetrahedra; the group has characteristic bands in the  $700\text{ cm}^{-1}$  to  $1100\text{ cm}^{-1}$  IR region [65-67]. Positions and shapes of vibrational peaks depend on symmetry of the group, distortion of atoms from ideal tetrahedral coordination and origin of atoms surrounding M cation. IR spectra of  $\text{Ba}_5\text{Mn}_3\text{O}_{12}\text{Cl}$ ,  $\text{Ba}_5\text{Mn}_{2.5}\text{V}_{0.5}\text{O}_{12}\text{Cl}$ ,  $\text{Ba}_5\text{Mn}_{0.2}\text{V}_{2.8}\text{O}_{12}\text{Cl}$  and  $\text{Ba}_5\text{Mn}_{0.5}\text{P}_{2.5}\text{O}_{12}\text{Cl}$  phases were obtained. Measured spectra of the compounds, all vibrations and their wavenumbers for these phases are given in Figure 3.23.

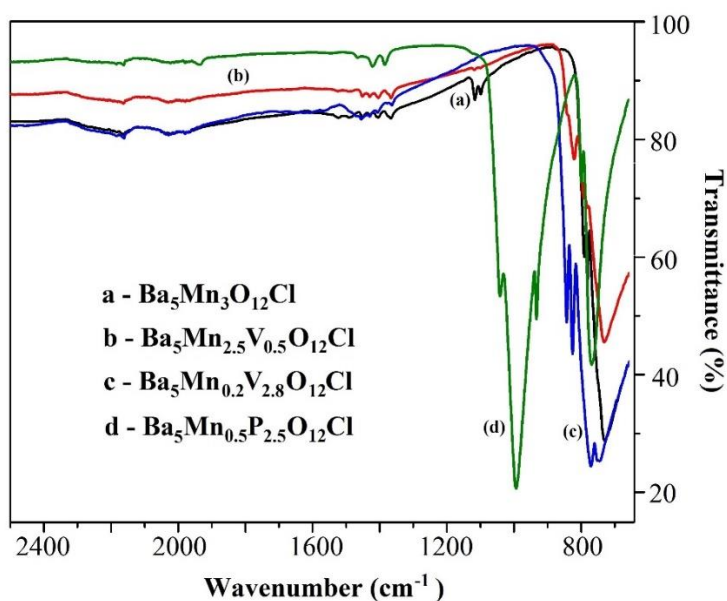


Figure 3.23 IR spectra of  $\text{Ba}_5(\text{MnO}_4)_3\text{Cl}$ ,  $\text{Ba}_5\text{Mn}_{2.5}\text{V}_{0.5}\text{O}_{12}\text{Cl}$ ,  $\text{Ba}_5\text{Mn}_{0.2}\text{V}_{2.8}\text{O}_{12}\text{Cl}$  and  $\text{Ba}_5\text{Mn}_{0.5}\text{P}_{2.5}\text{O}_{12}\text{Cl}$  phases.

All vibrations and their wavenumbers for all studied compounds are shown in Table 3.10. We compared all founded in IR spectra vibrations with spectra of known Apatite-related compounds and assigned vibrations into groups.

Table 3.10 Vibrations with wavenumbers of  $\text{Ba}_5(\text{MnO}_4)_3\text{Cl}$ ,  $\text{Ba}_5\text{Mn}_{2.5}\text{V}_{0.5}\text{O}_{12}\text{Cl}$ ,  $\text{Ba}_5\text{Mn}_{0.2}\text{V}_{2.8}\text{O}_{12}\text{Cl}$  and  $\text{Ba}_5\text{Mn}_{0.5}\text{P}_{2.5}\text{O}_{12}\text{Cl}$  compounds and their assignments (maximum peaks are bold).

Assignment		Wavenumber, $\text{cm}^{-1}$ <b><math>\text{Ba}_5(\text{MnO}_4)_3\text{Cl}</math></b>	Wavenumber, $\text{cm}^{-1}$ <b><math>\text{Ba}_5\text{Mn}_{2.5}\text{V}_{0.5}\text{O}_{12}\text{Cl}</math></b>	Wavenumber, $\text{cm}^{-1}$ <b><math>\text{Ba}_5\text{Mn}_{0.2}\text{V}_{2.8}\text{O}_{12}\text{Cl}</math></b>	Wavenumber, $\text{cm}^{-1}$ <b><math>\text{Ba}_5\text{Mn}_{0.5}\text{P}_{2.5}\text{O}_{12}\text{Cl}</math></b>
$(\text{VO}_4)^{3-}$	<b><math>\nu_1</math></b>		840	843	

	<b>v<sub>3</sub></b>		820	825, <b>774</b>	
<b>(PO<sub>4</sub>)<sup>3-</sup></b>	<b>v<sub>1</sub></b>				952
	<b>v<sub>3</sub></b>				<b>996, 1043</b>
<b>(MnO<sub>4</sub>)<sup>3-</sup></b>	<b>v<sub>1</sub></b>	781	782	overlay with v <sub>3</sub> (VO <sub>4</sub> ) <sup>3-</sup>	
	<b>v<sub>3</sub></b>	<b>729</b>	<b>730</b>	769	768

Vibrations with higher wavenumbers (from 300 cm<sup>-1</sup> to 900 cm<sup>-1</sup>) belong to deformation vibrations (v<sub>1</sub> – symmetrical and v<sub>3</sub> – asymmetrical) of (VO<sub>4</sub>)<sup>3-</sup> group; modes with smaller wavenumbers (from 420 cm<sup>-1</sup> to 290 cm<sup>-1</sup>) pertain to stretching vibrations (v<sub>2</sub> - symmetrical and v<sub>4</sub> - asymmetrical). Mn–O and V–O bond distances are very similar and vibrational peaks of (VO<sub>4</sub>)<sup>3-</sup> and (MnO<sub>4</sub>)<sup>3-</sup> functional groups might be overlapped. (PO<sub>4</sub>)<sup>3-</sup> group's deformation modes lie in the region with higher wavenumbers (from 1000 cm<sup>-1</sup> to 1200 cm<sup>-1</sup>), because the P–O bond is shorter than V–O and Mn–O bonds. All vibrations located below these regions are vibrations of the lattice, and vibrations lying above are composite vibrations. Due to the large mass of the chlorine atom, its vibrations cannot be detected in the measured region; they are shifted towards the smaller wavenumbers and lie below 200 cm<sup>-1</sup>. The Ba<sub>5</sub>Mn<sub>0.5</sub>P<sub>2.5</sub>O<sub>12</sub>Cl sample shows three (PO<sub>4</sub>)<sup>3-</sup> group vibrational modes around 1000 cm<sup>-1</sup> (fingerprint region of the group), which correspond to v<sub>1</sub> and v<sub>3</sub> modes. All samples have the v<sub>3</sub> vibrational peak of (MnO<sub>4</sub>)<sup>3-</sup> from 730 cm<sup>-1</sup> to 770 cm<sup>-1</sup>. Vanadium containing samples Ba<sub>5</sub>Mn<sub>2.5</sub>V<sub>0.5</sub>O<sub>12</sub>Cl and Ba<sub>5</sub>Mn<sub>0.2</sub>V<sub>2.8</sub>O<sub>12</sub>Cl show the v<sub>3</sub> vibrational mode of (VO<sub>4</sub>)<sup>3-</sup> group around 800 cm<sup>-1</sup>.

### 3.2.4 Magnetic Properties

Magnetic properties of the parent compound Ba<sub>5</sub>Mn<sub>3</sub>O<sub>12</sub>Cl were reported earlier [24]; however those of the solid solutions have not been studied systematically. We measured magnetic susceptibilities of Ba<sub>5</sub>Mn<sub>3</sub>O<sub>12</sub>Cl, Ba<sub>5</sub>Mn<sub>1.5</sub>V<sub>1.5</sub>O<sub>12</sub>Cl, Ba<sub>5</sub>Mn<sub>1.5</sub>P<sub>1.5</sub>O<sub>12</sub>Cl, Sr<sub>5</sub>Cr<sub>3</sub>O<sub>12</sub>Cl, Sr<sub>5</sub>Cr<sub>3</sub>O<sub>12</sub>F, Sr<sub>5</sub>Mn<sub>0.5</sub>Cr<sub>2.5</sub>O<sub>12</sub>Cl, Sr<sub>5</sub>Cr<sub>2</sub>VO<sub>12</sub>Cl and Sr<sub>5</sub>Cr<sub>2</sub>VO<sub>12</sub>F phases. Based on magnetic susceptibility ( $\chi$ ) versus temperature and inverse magnetic susceptibility (1/ $\chi$ ) versus temperature graphs (Fig. 3.24 and Fig. 3.25) all samples show paramagnetic behavior in the measured temperature region (from 5 K to 300 K).

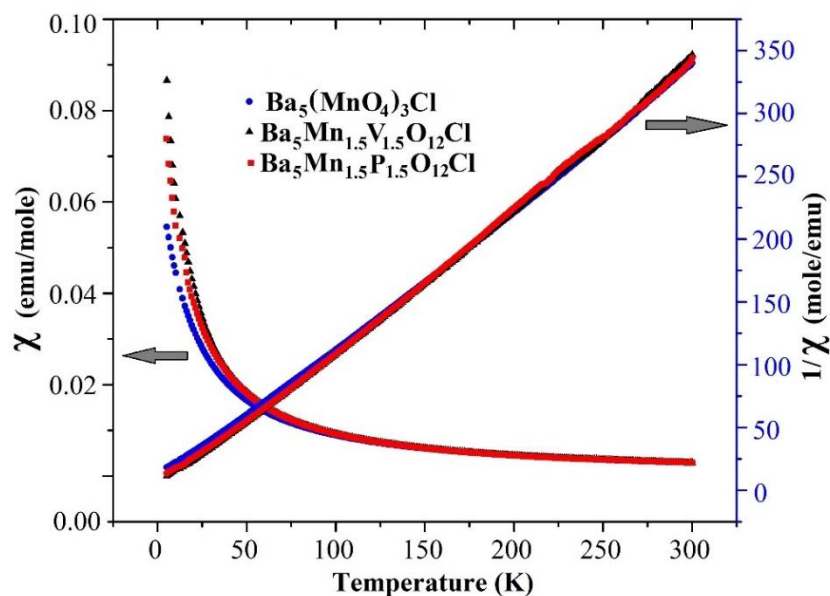


Figure 3.24 Magnetic susceptibility and inverse magnetic susceptibility of  $\text{Ba}_5\text{Mn}_3\text{O}_{12}\text{Cl}$ ,  $\text{Ba}_5\text{Mn}_{1.5}\text{V}_{1.5}\text{O}_{12}\text{Cl}$  and  $\text{Ba}_5\text{Mn}_{1.5}\text{P}_{1.5}\text{O}_{12}\text{Cl}$ ; 1 emu (cgs units) =  $10^{-3}$  A m<sup>2</sup> (SI units).

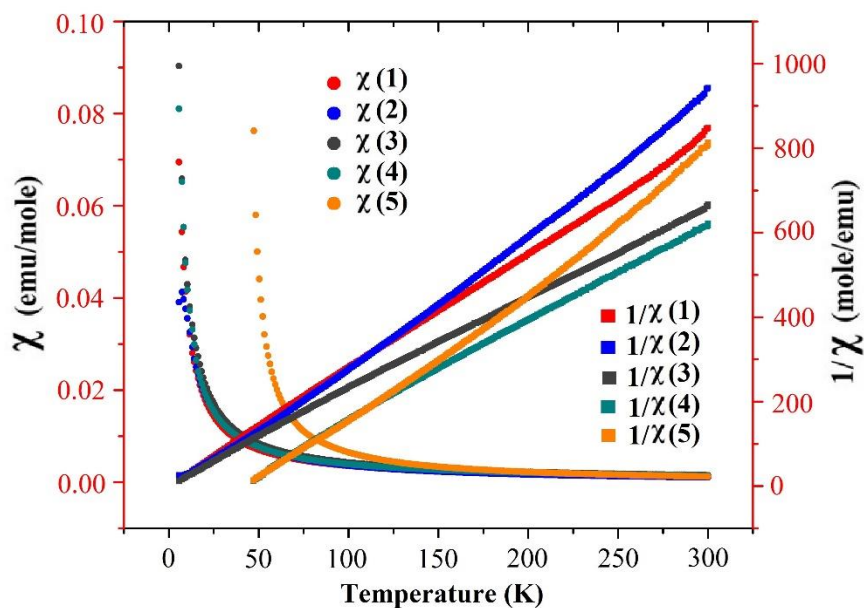


Figure 3.25 Magnetic susceptibility and inverse magnetic susceptibility of  $\text{Sr}_5\text{Cr}_3\text{O}_{12}\text{Cl}$  (1),  $\text{Sr}_5\text{Cr}_3\text{O}_{12}\text{F}$  (2),  $\text{Sr}_5\text{Mn}_{0.5}\text{Cr}_{2.5}\text{O}_{12}\text{Cl}$  (3),  $\text{Sr}_5\text{Cr}_2\text{VO}_{12}\text{Cl}$  (4) and  $\text{Sr}_5\text{Cr}_2\text{VO}_{12}\text{F}$  (5); 1 emu (cgs units) =  $10^{-3}$  A m<sup>2</sup> (SI units).

Calculated magnetic moments are listed in Table 3.11; the calculated moments are in agreement with the theoretical magnetic moment of  $\text{Mn}^{5+}$  ( $\mu_{\text{th}} = 2.83$ ) and  $\text{Cr}^{5+}$  ( $\mu_{\text{th}} = 1.73$ ); this indicates that manganese and chromium in all samples show an oxidation state equals

5+ with two or one unpaired electrons accordingly. The Curie and Weiss constants were calculated from the slope and intercept of the linear region of  $1/\chi$  versus temperature.

Table 3.11 Calculated magnetic moments, Curie and Weiss constants of  $\text{Ba}_5(\text{MnO}_4)_3\text{Cl}$ ,  $\text{Ba}_5\text{Mn}_{1.5}\text{V}_{1.5}\text{O}_{12}\text{Cl}$ ,  $\text{Ba}_5\text{Mn}_{1.5}\text{P}_{1.5}\text{O}_{12}\text{Cl}$ ,  $\text{Sr}_5\text{Cr}_3\text{O}_{12}\text{Cl}$ ,  $\text{Sr}_5\text{Cr}_3\text{O}_{12}\text{F}$ ,  $\text{Sr}_5\text{Mn}_{0.5}\text{Cr}_{2.5}\text{O}_{12}\text{Cl}$ ,  $\text{Sr}_5\text{Cr}_2\text{VO}_{12}\text{Cl}$  and  $\text{Sr}_5\text{Cr}_2\text{VO}_{12}\text{F}$  samples (\* - theoretical magnetic moment of  $\text{Sr}_5\text{Mn}_{0.5}\text{Cr}_{2.5}\text{O}_{12}\text{Cl}$  compound with two magnetic ions equals  $1.95\mu_B$ ).

Compound	T region (K)	C	$\theta$ (K)	$\mu_{\text{eff}}$ ( $\mu_B$ )
<b><math>\text{Ba}_5(\text{MnO}_4)_3\text{Cl}</math></b>	200–300	0.8424	14.92	2.61
<b><math>\text{Ba}_5\text{Mn}_{1.5}\text{V}_{1.5}\text{O}_{12}\text{Cl}</math></b>	200–300	0.8107	19.37	2.57
<b><math>\text{Ba}_5\text{Mn}_{1.5}\text{P}_{1.5}\text{O}_{12}\text{Cl}</math></b>	200–300	1.0314	-18.27	2.84
<b><math>\text{Sr}_5\text{Cr}_3\text{O}_{12}\text{Cl}</math></b>	250–300	0.4579	-11.49	1.92
<b><math>\text{Sr}_5\text{Cr}_3\text{O}_{12}\text{F}</math></b>	200–300	0.4171	-12.43	1.83
<b><math>\text{Sr}_5\text{Mn}_{0.5}\text{Cr}_{2.5}\text{O}_{12}\text{Cl}</math></b>	250–300	0.4542	-1.037	1.91*
<b><math>\text{Sr}_5\text{Cr}_2\text{VO}_{12}\text{Cl}</math></b>	250–300	0.3996	12.16	1.79
<b><math>\text{Sr}_5\text{Cr}_2\text{VO}_{12}\text{F}</math></b>	200–300	0.3850	3.499	1.76

### 3.3 Conclusion

We have successfully synthesized several solid solutions  $\text{Sr}_5\text{Cr}_{3-x}\text{P}_x\text{O}_{12}\text{Cl}$  ( $x = 0.5$ ; 1.0),  $\text{Sr}_5\text{Cr}_{3-x}\text{V}_x\text{O}_{12}\text{Cl}$  ( $x = 0.5$ –1.5),  $\text{Sr}_5\text{Mn}_{3-x}\text{Cr}_x\text{O}_{12}\text{Cl}$  ( $x = 2.5$ –3.0),  $\text{Sr}_5\text{Cr}_{3-x}\text{P}_x\text{O}_{12}\text{F}$  ( $x = 0.5$ –2.5),  $\text{Sr}_5\text{Cr}_{3-x}\text{V}_x\text{O}_{12}\text{F}$  ( $x = 0.5$ –2.5),  $\text{Sr}_5\text{Mn}_{3-x}\text{Cr}_x\text{O}_{12}\text{F}$  ( $x = 2.5$ –3.0),  $\text{Ba}_{5-x}\text{Sr}_x\text{Mn}_3\text{O}_{12}\text{Cl}$  ( $x = 0$ –2.5),  $\text{Ba}_5\text{Cr}_{3-x}\text{P}_x\text{O}_{12}\text{Cl}$  ( $x = 1.0$ –2.5),  $\text{Ba}_5\text{Cr}_{3-x}\text{V}_x\text{O}_{12}\text{Cl}$  ( $x = 1.5$ –2.5),  $\text{Ba}_5\text{Mn}_{3-x}\text{Cr}_x\text{O}_{12}\text{Cl}$  ( $x = 0$ –3.0),  $\text{Ba}_{5-x}\text{K}_x\text{Sr}_x\text{Mn}_{0.5}\text{P}_{2.5-x}\text{O}_{12}\text{Cl}$  ( $x = 0$ –0.5),  $\text{Ba}_{5-x}\text{K}_x\text{Mo}_x\text{Mn}_{0.5}\text{P}_{2.5-x}\text{O}_{12}\text{Cl}$  ( $x = 0$ –0.2),  $\text{Ba}_5\text{Mn}_{3-x}\text{V}_x\text{O}_{12}\text{Cl}$  ( $x = 0$ –3.0),  $\text{Ba}_5\text{Mn}_{3-x}\text{P}_x\text{O}_{12}\text{Cl}$  ( $x = 0$ –3.0),  $\text{Ba}_5\text{Cr}_{3-x}\text{P}_x\text{O}_{12}\text{F}$  ( $x = 0.5$ –2.5) with apatite-type structure. All samples show intense turquoise and green colors. All phases were characterized using X-ray diffraction technique and optical, magnetic and IR measurements were performed for selected compounds; for four samples ( $\text{Ba}_5(\text{MnO}_4)_3\text{Cl}$ ;  $\text{Ba}_5\text{Mn}_{2.5}\text{V}_{0.5}\text{O}_{12}\text{Cl}$ ;  $\text{Ba}_5\text{Mn}_{0.2}\text{V}_{2.8}\text{O}_{12}\text{Cl}$  and  $\text{Ba}_5\text{Mn}_{0.5}\text{P}_{2.5}\text{O}_{12}\text{Cl}$ ) neutron data were collected and their structures were refined. The synthesized compounds show great potential as environmentally benign inorganic “Cool pigments”.

### 3.4 Experimental Materials and Methods

All samples were synthesized using standard solid state synthesis. Stoichiometric amounts of  $\text{BaCO}_3$  (Cerac, 99.9%),  $\text{MnO}_2$  (Alfa Aesar, 99.9%),  $\text{V}_2\text{O}_5$  (Cerac, 99.9%),  $\text{BaCl}_2 \cdot 2\text{H}_2\text{O}$  (Mallinckrodt, 99.9%) and  $(\text{NH}_4)_2\text{HPO}_4$  (Mallinckrodt, 99.9%) were ground



in an agate mortar, pelletized and heated in an alumina crucible at 800°C for 12 h in air. The mixture was then ground again, pelletized and reheated at 850°C for 12 h.

Microwave synthesis was applied to prepare  $\text{Ba}_5\text{Mn}_{3-x}\text{V}_x\text{O}_{12}\text{Cl}$  samples. Stoichiometric mixture of starting materials ( $\text{BaCO}_3$  (Cerac, 99.9%),  $\text{MnO}_2$  (Alfa Aesar, 99.9%),  $\text{V}_2\text{O}_5$  (Cerac, 99.9%) and  $\text{BaCl}_2 \cdot 2\text{H}_2\text{O}$  (Mallinckrodt, 99.9%)) was ground, pelletized and placed in an alumina crucible. The reaction vessel was then surrounded by carbon slug (inside a microwave high-temperature ceramic block) and placed in the microwave oven cavity. The microwave exposure was limited to 5-6 minutes intervals at 100% power (750Watts). The temperature of reaction was approximately 780-900°C.

Low temperature synthesis (sol-gel method) was also attempted for the  $\text{Ba}_5\text{Mn}_{3-x}\text{V}_x\text{O}_{12}\text{Cl}$  system. Stoichiometric amounts of  $\text{Ba}(\text{NO}_3)_2$  (Mallinckrodt, 99.9%),  $\text{Mn}(\text{NO}_3)_2 \cdot 4\text{H}_2\text{O}$  (Aldrich, 99.99%),  $\text{NH}_4\text{Cl}$  (Macron, 99.9%) were mixed and dissolved in DI water. The nitrate solutions were heated while stirring, and the citric acid (Sigma-Aldrich,  $\geq 99.5\%$ ) was added in a molar ratio of 2:1 citric acid to metal nitrates. Here citric acid is used as a cross linking agent. The pH of the resulting solutions was then adjusted to 7 using aqueous  $\text{NH}_4\text{OH}$  (ACS, 28–30% solution), and the neutralized solutions were heated until the formation of dry gel. Dark brown amorphous powder was obtained after heating the translucent dry gel at 250°C for 2 h, and it was further calcined at 700–750°C in air for 12 h.

XRD data were collected using a Rigaku MiniFlex II diffractometer with  $\text{CuK}\alpha$  radiation ( $\lambda = 1.5418\text{\AA}$ ) and a graphite monochromator at room temperature. For phase identification the measurements were carried out at 0.5°/min within 15° to 70°  $2\theta$  range. For lattice parameter calculation the data were collected with an internal standard such as Si. Powder neutron diffraction data were collected on the 32-counter high-resolution diffractometer BT-1 at the Center for Neutron Research at the National Institute of Standards and Technology. A  $\text{Cu}(311)$  monochromator, yielding a wavelength of  $1.5403(2)\text{\AA}$ , was employed. Collimation of 15' of arc was used before the monochromator, 20' before the sample, and 7' before the detectors. The samples were loaded into vanadium containers of 15.6 mm diameter and 50 mm length. Data were collected at room



temperature over a  $2\theta$  range of  $3^\circ$  to  $167^\circ$ . XRD and neutron data were refined using the Rietveld method, as implemented in GSAS-EXPGUI software [68,69]. Bond-valence analysis of the neutron structures made use of the bond-valence calculator [70].

Konica Minolta CM-700d Spectrophotometer (Standard illuminant D<sub>65</sub>) was used to measure  $L^*$ ,  $a^*$ ,  $b^*$  color coordinates. Diffuse reflectance data in the visible range were measured using a homemade UV-VIS spectrophotometer (Department of Physics, OSU); MgO was used as the reference; diffuse reflectance was converted to absorbance using the Kubelka-Munk equation [71]. Near-infrared reflectance data (up to 2500 nm) were collected using a Jasco V-670 Spectrophotometer (Chemical Engineering Department, OSU). IR measurements were performed using a Thermo Scientific Nicolet 6700 FT-IR Spectrometer in the spectral range of 700–2500  $\text{cm}^{-1}$  (ONAMI, Corvallis, OR).

Magnetic properties measurements were made using a Quantum Design Physical Property Measurement System (QD-PPMS) at temperature range of 5–300 K (zero-field cooling, applied magnetic field 0.5 T). Inverse magnetic susceptibility data was used to fit for Curie-Weiss law. Diamagnetic corrections were made for calculations of experimental  $\mu_B$  [72].

### 3.5 Acknowledgements

Text and figures within this chapter have been used in part or whole from the publication:

**Medina, E.A.**, Li, J., Stalick, J.K., Subramanian, M.A. Intense turquoise colors of apatite-type compounds with  $\text{Mn}^{5+}$  in tetrahedral coordination *Solid State Sciences* **2016**, 52, 97-105.

This research was supported by National Science Foundation (DMR-1508527). The identification of any commercial product or trade name does not imply endorsement or recommendation by the National Institute of Standards and Technology.

### 3.6 References

[1] Smith, A.E., Mizoguchi, H., Delaney, K., Spaldin, N.A., Sleight, A.W., Subramanian, M.A., J. Am. Chem. Soc. 131 (2009) 17084.

- [2] Jiang, P., Li, J., Ozarowski, A., Sleight, A.W., Subramanian, M.A., *Inorg. Chem.* 52 (2013) 1349.
- [3] Ivanyuk, E.V., Astrelin, I.M., Suprunchuk, V.I., *Russian J. Appl. Chem.* 72(9) (1999) 1508.
- [4] Kablukov, V.I., Sukhov, A.V., Kaminskaya, N.A., Fetisov, G.N., Russian Patent No. 2023716 (30 November 1994).
- [5] Sereda, B.P., Soloshenko, A.A., Popov, B.A., Sekirazh, V.M., Churkin, V.I., Pakhomov, B.A., *Trudy Ural'skogo Nauchno-Issledovatel'skogo Khimicheskogo Instituta* 27 (1973) 190 (in Russian).
- [6] Elliott, J.C., Wilson, R.M., Dowker, S.E.P., *Adv. X-ray Anal.* 45 (2002) 172.
- [7] Knyazev, A.V., Chernorukov, N.G., Bulanov, E.N., *Materials Chem. and Phys.* 132 (2012) 773.
- [8] Wu, P., Zeng, Y.Z., Wang, C.M., *Biomaterials* 25 (2004) 1123.
- [9] Baker, W.E., *Am. Mineral.* 51 (1966) 1712.
- [10] Chernorukov, N.G., Knyazev, A.V., Bulanov, E.N., *Inorg. Mater.* 47(2) (2011) 172.
- [11] Cooray, P.G., *Am. Mineral.* 55 (1970) 2038.
- [12] Guillemin, C., Prouvist, J., Wintenberger, M., *Bull. Soc. Franc. Miner. Crist.* LXXVIII (1955) 301 (in French).
- [13] Laufec, F., Romanskala, Haloda, J., Cisarova, I., *J. Czech Geol. Soc.* 51(3-4) (2006) 271.
- [14] Merker, V.L., Wondratshek, H., *Z. Anorg. Allg. Chem.* 300 (1959) 41 (in German).
- [15] Rao, J.S.R.K., Raju, R.D., *J. Indian Geo. Assoc.* 13 (1971) 79.
- [16] Buvaneswari, G., Varadaraju, U.V., *J. Solid State Chem.* 149 (2000) 133.
- [17] Knyazev, A.V., Bulanov, E.N., Korshunov, A.O., Krashenninnikova, O.V., *Inorg. Mater.* 49(11) (2013) 1133.
- [18] Pasero, M., Kampf, A.R., Ferraris, C., Pekov, I. et al., *Eur. J. Mineral* 22 (2010) 163.
- [19] Knyazev, A.V., Maczka, M., Bulanov, E.N., Ptak, M., Belopolskaya, S.S., *Dyes and Pigments* 91(3) (2011) 286.
- [20] Johnson, P.D., Prener, J.S., Kingsley, J.D., *Science* 141 (1963) 1179.
- [21] Knyazev, A.V., Chernorukov, N.G., Bulanov, E.N., *Vestnik of Lobachevsky State University of Nizhni Novgorod* 6 (2010) 82 (in Russian).
- [22] Grisafe, D.A., Hummel, F.A., *J. Solid Sate Chem. Part B. Color* 2 (1970) 167.
- [23] Dardenne, K., Vivien, D., Huguenin, D., *J. Solid State Chem.* 146 (1999) 464.
- [24] Brixner, L., Weiher, J.F., *Inorg. Chem.* 7 (1968) 1474.
- [25] Reinen, D., Lachwa, H., Allmann, R., *Z. Anorg. Allg. Chem.* 542 (1986) 71 (in German).
- [26] Fielder, D.A., Albering, J.H., Besenhard, J.O., *J. Solid State Electrochem.* 2 (1998) 413.
- [27] White, T.J., Dong, Z.L., *Acta Crystallogr. Sect. B* 59 (2003) 1.
- [28] Roh, Y.H., Hong, S.T., *Acta Crystallogr.* 61 (2005) i140.
- [29] Xia, Z., Liang, Y., Huang, W. et al., *J. Mater. Sci. Mater. Electron.* 24 (2013) 5111.
- [30] Kruzhalov, A.V., Gavrilov, F.F., Kordyukov, N.I. et al., *Z. Prikladnoj Spektroskopii* 21 (1974) 631 (in Russian).
- [31] Beck, H.P., Douiheche, M., Haberkorn, R., Kohlmann, H., *Solid State Sci.* 8 (2006) 64.

- [32] Hata, M., Marumo, F., Iwai, S., Aoki, H., *Acta Crystallogr. Sect. B* 35 (1979) 2382.
- [33] Li, C., Li, Y., Wang, X., *Materials Chem. and Phys.* 139 (2013) 220.
- [34] Ju, G., Hu, Y., Li, C., Wang, X., *J. of Appl. Phys.* 3 (2012) 113508.
- [35] Yoo, H.S., Vaidyanathan, S., Kim, S.W., Jeon, D.Y., *Opt. Mater.* 31 (2009) 1555.
- [36] Xiao-Long, J., *J. of Luminescence* 4 (2014) 409 (in Chinese).
- [37] Yue, S.J., Cui, D.Pe., Xue, B. et al., *Mechanics and Materials* 401 (2013) 796.
- [38] Guifang, J., Hu, Y., Li, C. et al., *Mater. Res. Bull.* 48 (2013) 2598.
- [39] Ju, G., Hu, Y., Chen, L., Wang, X., *J. of Photochem. Photobiology A: Chem.* 251 (2013) 100.
- [40] Noginov, M.A., Loutts, G.B., Bonner, C.E. et al., *JOSA B* 17 (2000) 1329.
- [41] Sato, M., Tanaka, T., Ohta, M., *J. Electrochem. Soc.* 141 (1994) 1851.
- [42] Herren, M., Gudel, H.U., *Chem. Phys. Lett.* 183 (2001) 98.
- [43] Forster, K., Greenblatt, M., Pifer, J., *J. Solid State Chem.* 30 (1979) 121.
- [44] Suchow, L., *J. Electrochem. Soc.* 108 (1961) 847.
- [45] Shang, M., Geng, D., Yang, D., Kang, X., Zhang, Y., Lin, J., *Inorg. Chem.* 52 (2013) 3102.
- [46] Bai, G., Tsang, M.K., Hao, J., *Adv. Opt. Mater.* 3 (2015) 431.
- [47] Sudarsanan, K., Young, R.A., *Acta Crystallogr., Sect. B: Struct. Sci.* 36 (1980) 1525.
- [48] Pekov, I.V., Britvin, S.N., Zubkova, N.V., Pushcharovsky, D.Y., Pasero, M., *Eur. J. Mineral.* 22(6) (2010) 869.
- [49] Baikie, T., Ahmad, Z., Srinivasan, M., et al., *J. Solid State Chem.* 180(5) (2007) 1538.
- [50] Paluszkiwicz, C., Slosarczyk, A., Pijocha, D., et al., *J. Mol. Struct.* 976 (1-3) (2010) 301.
- [51] <http://en.wikipedia.org/wiki/Turquoise> (accessed 09/12/2016).
- [52] <https://en.wikipedia.org/wiki/Emerald> (accessed 01/04/2017).
- [53] Kukushkina, G.N., Demidovskaya, A.N., Irklievskaya, O.T., Mokhort, V.N., Kurlovich, T.I., Stepanova, L.N., Gizun, N.M., U.S.S.R. Patent No. 1273338 (30 November 1986).
- [54] Kukushkina, G.N., Demidovskaya, A.N., Irklievskaya, O.T., Mokhort, V.N., Kurlovich, T.I., Stepanova, L.N., Petrushev, V.L., U.S.S.R. Patent No. 1281534 (7 January 1987).
- [55] Pishch, I.V., Biryukova, K.E., Slepukhova, L.V., U.S.S.R. Patent No. 1065358 (7 January 1984).
- [56] [https://en.wikipedia.org/wiki/Cobalt\\_blue](https://en.wikipedia.org/wiki/Cobalt_blue) (accessed 01/04/2017).
- [57] Shannon, R.D., *Acta Crystallogr. Sect. A* 32 (1976) 751.
- [58] Robinson, K., Gibbs, G.V., Ribbe, P.H., *Science* 172 (1971) 567.
- [59] Fleet, M.E., *Mineral. Mag.* 40 (1976) 531.
- [60] Schanda, J., *Colorimetry: Understanding the CIE system*, 1<sup>st</sup> ed., Wiley-Interscience, 2007.
- [61] Kingsley, J.D., Prener, J.S., Segall, B., *APS* 137 (1965) 189.
- [62] Borromei, R., Oleari, L., Day, P., *J. Chem. Soc.* 77 (1981) 1563.
- [63] Scott, M.A., Henerson, B., Gallaghen, H.G., Han, T.P.J., *J. Phys. Condens. Matter* 9 (1997) 9893.
- [64] Dardenne, K., Vivien, D., Ribot, F., et al., *Eur. J. Solid State Inorg. Chem.* 35 (1998) 419.

- [65] Knyazev, A.V., Bulanov, E.N., Lapshin, A.N., Vestnik of Lobachevsky State University of Nizhni Novgorod 3 (2012) 87 (in Russian).
- [66] Nakamoto, K., Mir, Moscow (1991) 121 (in Russian).
- [67] Boechat, C., Eon, J.-G., Rossi, A., et al., J. Phys. Chem. A 2 (2000) 4225.
- [68] Larson, A.C., Von Dreele, R.B., General Structure Analysis System (GSAS), Los Alamos National Laboratory Report LAUR (1994) 86.
- [69] EXPGUI, a graphical user interface for GSAS: Toby, B.H., J. Appl. Crystallogr. 34 (2001) 210.
- [70] Hormillosa, C., Healy, S., Stephen, T., Brown, I.D., Bond Valence Calculator, Version 2.0 (1993) <http://www.ccp14.ac.uk> (accessed 07/15/2016).
- [71] Sherif, M.E., Bayoumi, A.O., Sokkar, T.Z.N., Color Res. Appl. 22 (1997) 32.
- [72] Bain, G.A., Berry, J.F., J. Chem. Educ. 85 (2008) 532.

## CHAPTER 4

### Hibonite-type Compounds: Structural Studies

#### Abstract

Various oxides with the hibonite structure were synthesized and structurally analyzed using powder neutron diffraction. The structure of  $\text{CaAl}_{12}\text{O}_{19}$  at 298 K and 10 K shows dipoles that are apparently too dilute to order unless subjected to a suitable electric field. Magnetoplumbites, such as  $\text{BaFe}_{12}\text{O}_{19}$ , are isostructural with hibonite. These compounds possess ferromagnetic properties, which combined with the electric dipoles may influence multiferroic behavior. Our  $\text{SrAl}_{12}\text{O}_{19}$  sample showed two distinct hexagonal phases, a major phase with the normal hibonite structure and a minor phase having a closely related structure. Our sample of the defect hibonite  $\text{La}_{2/3+\delta}\text{Al}_{12-\delta}\text{O}_{19}$  phase shows a distinctly higher  $\delta$  value (0.25) vs. that reported ( $\sim 0.15$ ) for samples made from the melt. Finally, we used to advantage the negative scattering length of Ti to determine the site occupancies of Ni and Ti in  $\text{CaAl}_{10}\text{NiTiO}_{19}$ .

Publications based on this chapter:

- 1) Li, J., **Medina, E.A.**, Stalick, J.K., Sleight, A.W., Subramanian, M.A. Structural studies of  $\text{CaAl}_{12}\text{O}_{19}$ ,  $\text{SrAl}_{12}\text{O}_{19}$ ,  $\text{La}_{2/3+\delta}\text{Al}_{12-\delta}\text{O}_{19}$ , and  $\text{CaAl}_{10}\text{NiTiO}_{19}$  with the hibonite structure; indications of an unusual type of ferroelectricity *Zeitschrift fur Naturforschung Section B-A Journal of Chemical Sciences* **2016**, 71(5), 475-484.

## 4.1 Introduction

The mineral hibonite only rarely occurs naturally on our planet, but it is frequently found in chondritic meteorites that impact our planet [1,2]. The ideal hibonite formula is  $\text{CaAl}_{12}\text{O}_{19}$ , but minerals occur with Si, Ti, V, Cr, Fe, Mn, Zn, and Mg substituting for Al [1-3]. The compounds  $\text{SrAl}_{12}\text{O}_{19}$ ,  $\text{PbAl}_{12}\text{O}_{19}$ ,  $\text{SrGa}_{12}\text{O}_{19}$ , and  $\text{BaGa}_{12}\text{O}_{19}$  with the hibonite structure have been synthesized [4,5]. The hibonite structure is also the structure found for magnetoplumbites such as  $\text{BaFe}_{12}\text{O}_{19}$  [6].

The hibonite structure (Figure 4.1) is hexagonal and contains five different sites for Al.

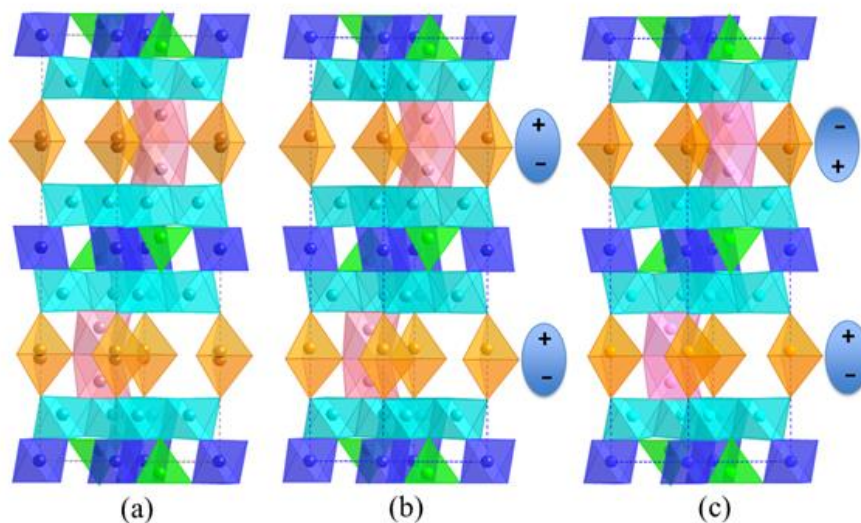


Figure 4.1 The Al-O framework of the hibonite structure with the  $c$ -axis vertical. Dark blue octahedron at the origin with Al1. The pink unit with Al4 are face-sharing octahedra. Turquoise octahedra of Al5 forming an edge sharing sheet. Green tetrahedra with Al3. The orange trigonal bipyramidal units with Al2. (a) The paraelectric structure ( $P6_3/mmc$ ) with random displacements along the  $c$ -axis. (b) Ordered dipoles in the ferroelectric structure ( $P6_3mc$ ). (c) Ordered dipoles in the antiferroelectric structure ( $P\bar{3}m1$ ).

The Al coordination number (CN) is 6 for three of these sites and 4 for one of these sites. The 5<sup>th</sup> site (Al2) ideally has trigonal bipyramidal (TBP) symmetry with very long apical distances. However, the most recent diffraction studies conclude that the cation at the TBP site is always displaced toward one of the apical O atoms giving it a CN of 4 [4,7,8]. This has been confirmed by  $^{27}\text{Al}$  NMR studies in the case of  $\text{SrAl}_{12}\text{O}_{19}$  [9]. The

three Al sites with CN 6 are described as octahedral but none have ideal octahedral symmetry, which cannot occur strictly in hexagonal symmetry. The Al (Al1) atom at the origin (an inversion center) has ideal trigonal antiprismatic symmetry. Two  $\text{AlO}_6$  octahedra share a common face utilizing the Al4 site. The  $\text{AlO}_6$  octahedra based on the Al5 site form a sheet perpendicular to the  $c$ -axis. Each of these octahedra shares edges with four other  $\text{AlO}_6$  octahedra. These sheets together with the tetrahedral Al atoms of the Al3 site form a slab that occurs in the spinel and  $\beta$ -alumina structures. Reported bond valence sum (BVS) calculations for  $\text{CaAl}_{12}\text{O}_{19}$  have shown that Al at the tetrahedral (Al3) site is underbonded [10], and we find that the Ca site and Al2 site are also underbonded and that the Al1 site is overbonded.

$\text{CaAl}_{12}\text{O}_{19}$  melts incongruently at  $1850^\circ\text{C}$  [11]. However, there are many reports of growing large single crystals of substituted hibonite compositions from the melt [4,5,12-16]. These include  $A\text{Al}_{12}\text{O}_{19}$  ( $A = \text{Ca, Sr, Pb}$ ) and  $Ln\text{Al}_{11}M\text{O}_{19}$  compositions where  $Ln$  is La, Pr, Nd, Sm, or Eu and  $M$  is Mg, Mn, Fe, Co, Ni, or Cu. Several characteristics of hibonite compositions suggest that they are generally not thermodynamically stable at lower temperatures. One of these is that all successful  $\text{CaAl}_{12}\text{O}_{19}$  syntheses require a temperature of at least  $1300^\circ\text{C}$ , and hibonite mineral samples apparently have been formed at very high temperatures. Another factor is the poor bond valence sums for several atoms in this structure. Still another factor pointing toward metastability is that there is always disorder at the Al2 site. The issue of metastability has been controversial, and the most recent evaluation of the situation concluded that present thermodynamic data cannot unambiguously determine whether or not hibonite is an entropy-stabilized phase, such as “FeO” [17].

The situation for magnetoplumbites such as  $\text{BaFe}_{12}\text{O}_{19}$  is very similar to that of hibonites. Structural studies show that Fe in the TBP (Al2) site is actually displaced toward one of the apical O atoms in a disordered manner [7]. Mössbauer spectroscopic studies of  $^{57}\text{Fe}$  as a function of temperature indicate that the disorder is dynamic at room temperature and above, but well below room temperature these Fe atoms become trapped on one side of the basal plane triangle of O atoms [18]. There have apparently been no structural or  $^{27}\text{Al}$  NMR studies for hibonites as a function of temperature. One aspect of our current



study was to investigate the structure of  $\text{CaAl}_{12}\text{O}_{19}$  as function of temperature looking for evidence that the disorder of Al at the Al2 site might change with temperature.

Two studies have reported a hibonite structure in the La/Al/O system [12,13]. A formula of  $\text{La}_{2/3}\text{Al}_{12}\text{O}_{19}$  might be expected for this phase; however, the structural analyses have shown a significantly higher La content. Our sample examined by neutron diffraction shows even higher La content, and we discuss how the extra positive charge is compensated.

We have been interested in the optical properties of transition metal cations in TBP sites of oxides [19-21]. Our studies of the optical properties hibonites containing partial transition metal substitutions for Al are presented elsewhere.

## 4.2 Results

### 4.2.1 $\text{CaAl}_{12}\text{O}_{19}$

The structure of  $\text{CaAl}_{12}\text{O}_{19}$  was refined from neutron diffraction data obtained at 11 K and 298 K. Three different structures were considered: paraelectric in space group  $P6_3/mmc$  with disordered dipoles (Fig. 4.1(a)), ferroelectric in space group  $P6_3mc$  (Fig. 4.1(b)), and antiferroelectric in space group  $P\bar{3}m1$  (Fig. 4.1(c)). Good Rietveld fits (Fig. 4.2 and Fig. 4.3) at both temperatures were obtained regardless of the space group assumed. No new peaks were observed in the low temperature diffraction pattern. For spaces groups  $P6_3/mmc$  and  $P6_3mc$  the only systematic absence is for  $hhl$  reflections when  $l$  is odd.

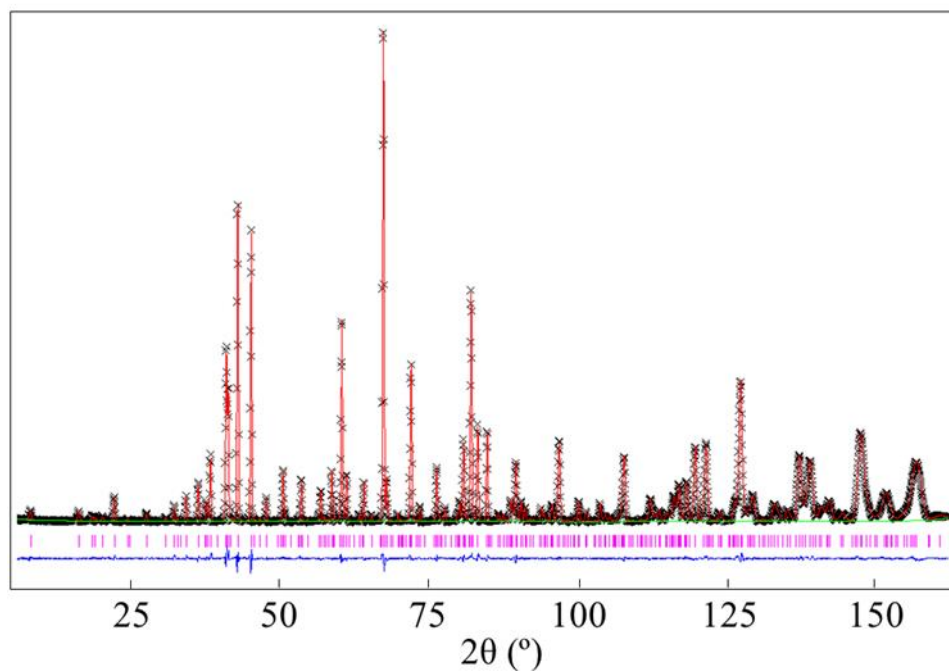


Figure 4.2 Rietveld fit of  $\text{CaAl}_{12}\text{O}_{19}$  neutron data at 11 K.

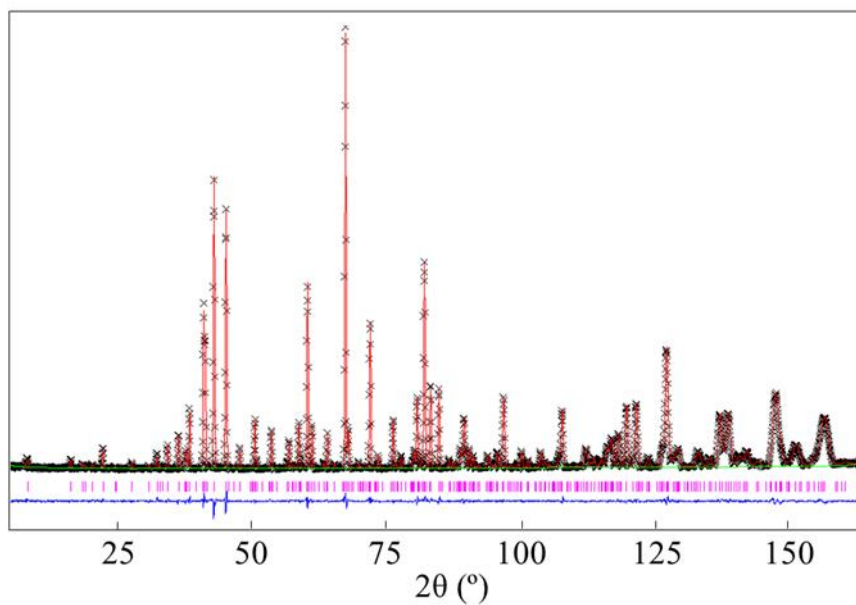


Figure 4.3 Rietveld fit of  $\text{CaAl}_{12}\text{O}_{19}$  neutron data at 298 K.

There are no systematic absences in space group  $P\bar{3}m1$ , but intensities calculated for  $hhl$  reflections with  $l$  odd are so weak ( $< 0.1\%$  relative to strongest peak) that they would

not be observed even if present. The refinement in space group  $P6_3mc$  did not converge due to correlations between atomic positions caused by the increased number of variables in the lower space group. The refinement converged in space group  $P\bar{3}m1$ . However, the fit did not improve significantly despite the six additional positional parameters. The structure was essentially unchanged except that now Al2 cations are ordered; there are no partially occupied sites. There was no improvement in the BVS values relative to the refinement in  $P6_3/mmc$ . Thus, we conclude that the structure is best described in  $P6_3/mmc$  at 298 and 11 K (Table 4.1).

Table 4.1 Summary of  $\text{CaAl}_{12}\text{O}_{19}$  rietveld refinement results.

	<b>298 K</b>	<b>11 K</b>
wRp (%)	4.72	3.90
Rp (%)	3.65	3.12
$\chi^2$	1.57	2.29
$a$ (Å)	5.5592(1)	5.5564(1)
$c$ (Å)	21.902(1)	21.867(1)
Ca: $x$	2/3	2/3
Ca: $z$	1/4	1/4
Ca: $U$ (Å <sup>2</sup> )	0.015(1)	0.0091(6)
Al1: $x$	0	0
Al1: $z$	0	0
Al1: $U$ (Å <sup>2</sup> )	0.0040(4)	0.0042(5)
Al2: $x$	0	0
Al2: $z$	0.2585(2)	0.2582(2)
Al2: $U$ (Å <sup>2</sup> )	0.0018(9)	0.0010(9)
Al3: $x$	1/3	1/3
Al3: $z$	0.0286(1)	0.0283(1)
Al3: $U$ (Å <sup>2</sup> )	0.0039(6)	0.0020(3)
Al4: $x$	1/3	1/3
Al4: $z$	0.1908(1)	0.1911(1)
Al4: $U$ (Å <sup>2</sup> )	0.0051(8)	0.0010(9)
Al5: $x$	0.1688(2)	0.1680(1)
Al5: $z$	0.8909(1)	0.8909(4)
Al5: $U$ (Å <sup>2</sup> )	0.0051(3)	0.0030(4)
O1: $x$	0	0
O1: $z$	0.1490(1)	0.1494(1)
O1: $U$ (Å <sup>2</sup> )	0.0071(3)	0.0036(3)

O2: $x$	2/3	2/3
O2: $z$	0.0547(1)	0.0547(1)
O2: $U$ ( $\text{\AA}^2$ )	0.0053(5)	0.0045(4)
O3: $x$	0.1807(1)	0.1815(1)
O3: $z$	1/4	1/4
O3: $U$ ( $\text{\AA}^2$ )	0.0065(4)	0.0027(3)
O4: $x$	0.1547(1)	0.1550(1)
O4: $z$	0.0523(1)	0.0523(1)
O4: $U$ ( $\text{\AA}^2$ )	0.0047(3)	0.0025(2)
O5: $x$	0.5034(1)	0.5034(1)
O5: $z$	0.1493(1)	0.1495(1)
O5: $U$ ( $\text{\AA}^2$ )	0.0050(3)	0.0032(3)

Therefore, the dipoles are disordered at both 11 and 298 K. This does not preclude a model with considerable dipole ordering in chains along the  $c$ -axis, but with a random polarity between adjacent chains. The lack of a second harmonic generation signal (SHG) at room temperature for  $\text{CaAl}_{12}\text{O}_{19}$ ,  $\text{SrAl}_{12}\text{O}_{19}$ , and  $\text{PbAl}_{12}\text{O}_{19}$  indicates all are centric at room temperature. This rules out ferroelectric ordering at room temperature but does not rule out antiferroelectric ordering. Our room temperature relative-permittivity data on pellets of these three compounds do not suggest enhanced polarizability (Table 4.2), but the concentration of dipoles is very low and they are only expected to be active in one direction.

Table 4.2 Relative-permittivity  $K$  of  $\text{CaAl}_{12}\text{O}_{19}$ ,  $\text{SrAl}_{12}\text{O}_{19}$ ,  $\text{PbAl}_{12}\text{O}_{19}$  and  $\text{CaAl}_{10}\text{NiTiO}_{19}$ .

Composition	Density, %	$K$ , <i>experimental</i>	$K$ , <i>corrected</i>	$K$ , <i>theoretical</i>
<b><math>\text{CaAl}_{12}\text{O}_{19}</math></b>	75	7.75	10.0	8.98
<b><math>\text{SrAl}_{12}\text{O}_{19}</math></b>	81	11.0	13.3	9.42
<b><math>\text{PbAl}_{12}\text{O}_{19}</math></b>	63	6.24	9.62	10.9
<b><math>\text{CaAl}_{10}\text{TiNiO}_{19}</math></b>	88	9.94	11.2	10.6

Notes: (1) The  $K$  (*experimental*) values were measured at room temperature at 1MHz, (2) The  $K$  (*corrected*) values after porosity correction were calculated using the equation from Ref. [22] assuming the 2<sup>nd</sup> phase is air with  $K(\text{air}) = 1$ , (3) The  $K$  (*theoretical*) values were calculated using dielectric polarizability data.

Bond valence sum calculations for the refinement in space group  $P6_3/mmc$  have shown low BVS values for Al3 in tetrahedral coordination and for Ca. These atoms would then be loosely bound and would be expected to show larger thermal displacement parameters

than the atoms showing BVS values close to those expected. The  $U$  value for Ca is much higher than the values obtained for Al or O (Table 4.1). However, high displacement values for Al3 were not observed when using harmonic terms only. This is not surprising because an ellipsoid is not an appropriate shape for displacements of an atom at a tetrahedral site. Figure 4.4 shows the result of refining displacement factors incorporating anharmonic terms for Al3 and Al4, but Al4 is not at a tetrahedral site. We see that in fact the shape obtained for Al3 is very anharmonic. The Zn atom in hexagonal ZnO is in the same type of site as Al3 in  $\text{CaAl}_{12}\text{O}_{19}$ . But in ZnO the BVS for Zn and O are normal, and applying anharmonic terms shown that an isotropic description of displacement factors is adequate [23].

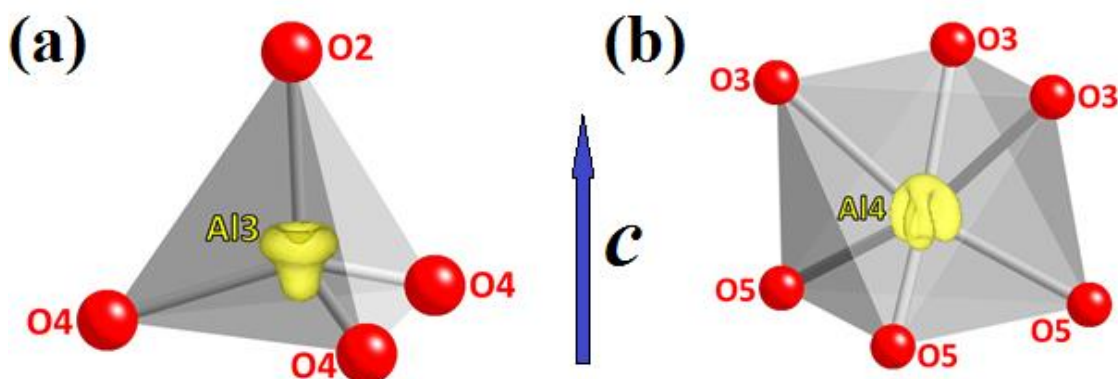


Figure 4.4 Shapes of anharmonic displacements for Al at (a) the Al3 site and (b) the Al4 site, both in  $4f3m$ . For the Al3 site there is major anharmonicity along the  $c$ -axis, and minor anharmonicity perpendicular to  $c$ . For the Al4 site there is minor anharmonicity along  $c$  with more significant anharmonicity perpendicular to  $c$ .

#### 4.2.2 $\text{SrAl}_{12}\text{O}_{19}$

Rietveld fit of  $\text{SrAl}_{12}\text{O}_{19}$  neutron data is shown in Figure 4.5.

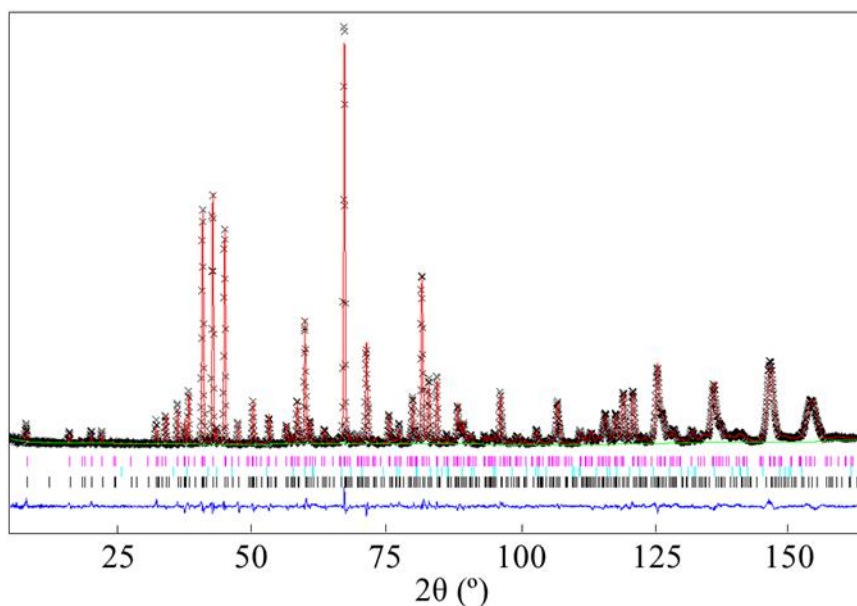


Figure 4.5 Rietveld fit of  $\text{SrAl}_{12}\text{O}_{19}$  neutron data at 298K. Three rows of vertical lines below the data profiles, from top to bottom, are corresponding to the major phase  $\text{SrAl}_{12}\text{O}_{19}$  (magenta), the impurity phase  $\text{Al}_2\text{O}_3$  (turquoise) and the minor hexagonal phase  $\text{SrAl}_{12}\text{O}_{19}$  with space group  $P-6m2$  (black), respectively. The amount of the impurity phase is below 2%.

Our neutron diffraction pattern for  $\text{SrAl}_{12}\text{O}_{19}$  showed high angle shoulders for some, but not all, peaks (Fig. 4.6).

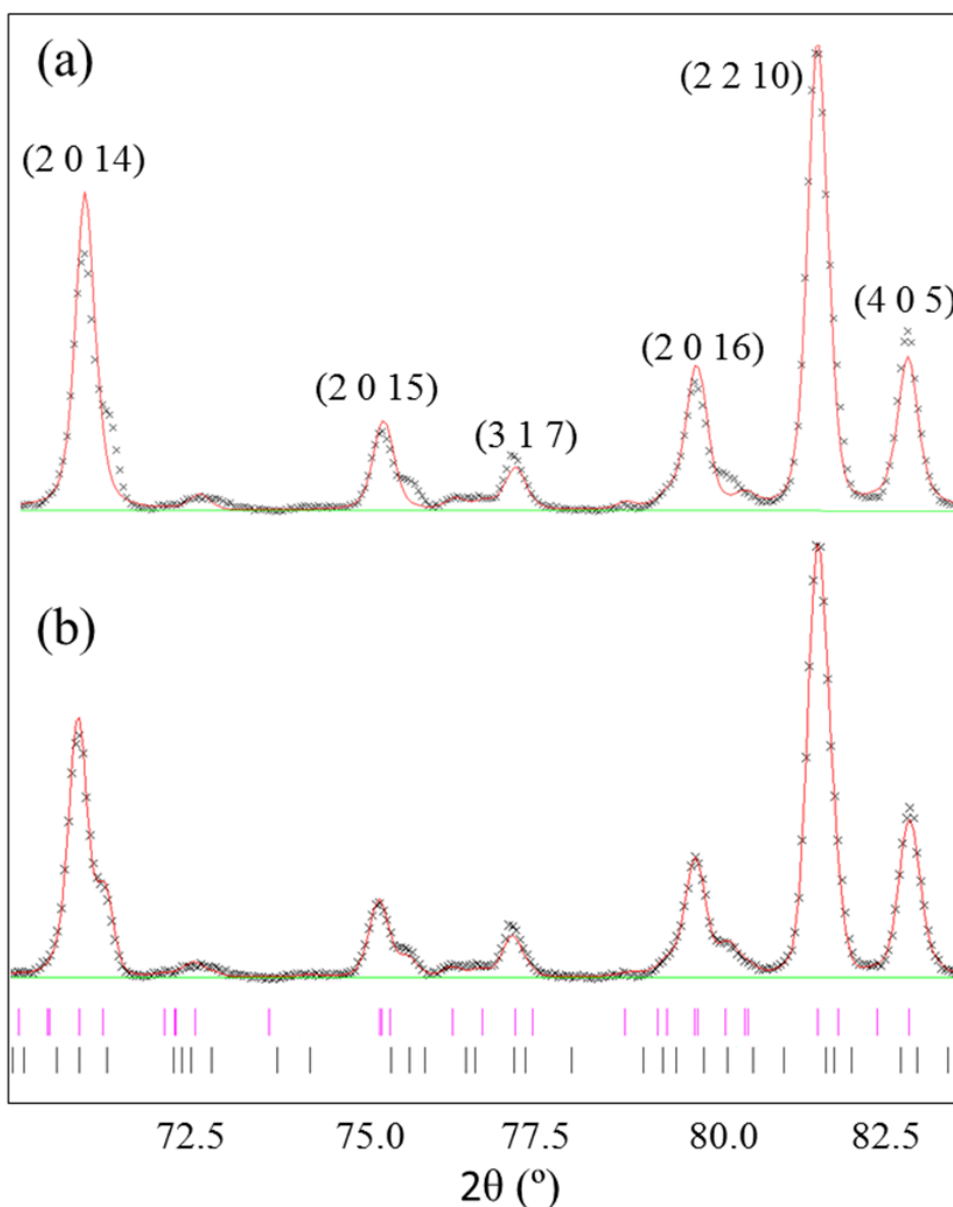


Figure 4.6 A section of the neutron diffraction pattern for  $\text{SrAl}_{12}\text{O}_{19}$ . High angle shoulders occur on some, but not all, peaks. These shoulders are caused by a second hexagonal phase that is structurally related to that of hibonite. These shoulders are mainly caused by shortening of the  $c$  cell edge in the minor hexagonal phase. (a) Without the second hexagonal phase; (b) with the second hexagonal phase. Red markers for primary phase; black markers for minor phase.

Such shoulders can in some cases be modeled as anisotropic strain resulting from a sample with inhomogeneous composition. However, the shape of the peaks with shoulders in this case required a two-phase refinement. The cell dimensions of the main hexagonal

phase and the minor hexagonal phase are  $a = 5.5766 \text{ \AA}$ ,  $c = 22.143 \text{ \AA}$  and  $a = 5.5718 \text{ \AA}$ ,  $c = 22.012 \text{ \AA}$ , respectively. The ratio of the two phases was about 4:1. The minor phase is contracted relative to the major phase 0.6% along  $c$  and only 0.09% along  $a$ . Thus, the peak shoulders are caused almost exclusively by the contraction along  $c$ . Refinement of the primary phase indicated  $\text{SrAl}_{12}\text{O}_{19}$  with the hibonite structure (Table 4.3).

Table 4.3 Summary of  $\text{SrAl}_{12}\text{O}_{19}$  structure results ( $a = 5.5766 \text{ \AA}$ ,  $c = 22.143 \text{ \AA}$ ).

Atom	Wyckoff site	$x^a$	$z$	$U_{\text{iso}} (\text{\AA}^2)$
Sr	$2d$	$2/3$	$1/4$	0.010(1)
Al1	$2a$	0	0	0.003(1)
Al2	$4e$	0	0.2644(4)	0.009 (3)
Al3	$4f$	$1/3$	0.0268(3)	0.001(1)
Al4	$4f$	$1/3$	0.1883(3)	0.008(1)
Al5	$12k$	0.1694(4)	0.8922(1)	0.0077(5)
O1	$4e$	0	0.1485(2)	0.0002(7)
O2	$4f$	$2/3$	0.0556(2)	0.0015(6)
O3	$6h$	0.1828(4)	$1/4$	0.022(1)
O4	$12k$	0.1552(2)	0.0515(1)	0.0058(4)
O5	$12k$	0.5022(4)	0.1481(1)	0.0070(3)

<sup>a</sup> $y = 2x$ .

Possibilities for the minor phase are suggested by findings in the Sr-Al-Mg-O system [24]. Single crystal studies in this system established both a  $\beta$ -alumina structure and a structure based on alternating layers of  $\beta$ -alumina and hibonite structures with ideal formulas of  $\text{SrMgAl}_{10}\text{O}_{17}$  and  $\text{Sr}_2\text{MgAl}_{22}\text{O}_{36}$ , respectively. Without Mg and compensating with Sr vacancies, these formulas become  $\text{Sr}_{0.5}\text{Al}_{11}\text{O}_{17}$  and  $\text{Sr}_{1.5}\text{Al}_{23}\text{O}_{36}$ . Both of these were evaluated as the possible minor phase in our sample with the conclusion being that both structures gave an equivalently good result.

#### 4.2.3 $\text{La}_{2/3+\delta}\text{Al}_{12-\delta}\text{O}_{19}$

Rietveld fit of  $\text{La}_{2/3+\delta}\text{Al}_{12-\delta}\text{O}_{19}$  neutron data is shown in Figure 4.7.



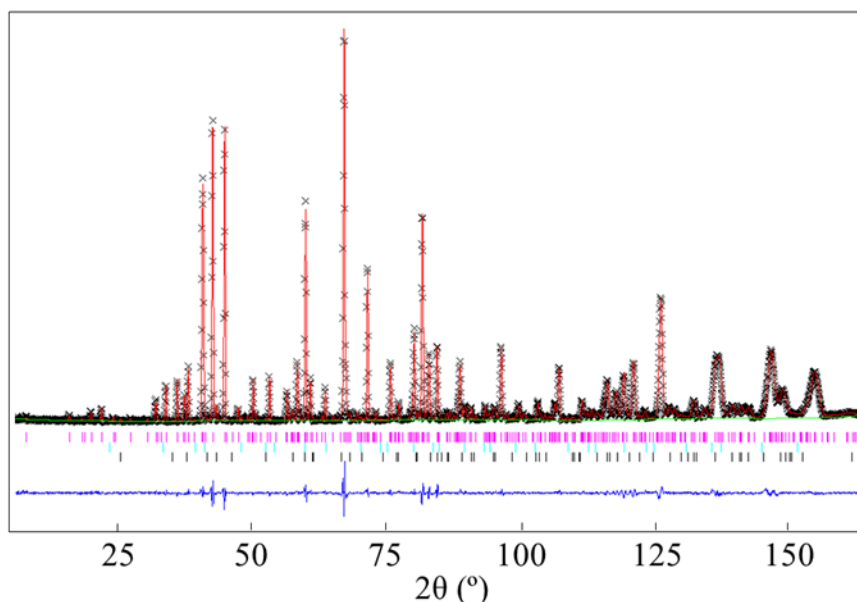


Figure 4.7 Rietveld fit of  $\text{LaAl}_{12}\text{O}_{19}$  neutron data at 298 K. The actual composition is refined to be  $\text{La}_{0.91}\text{Al}_{11.66}\text{O}_{18.69}$ . Three rows of vertical lines below the data profiles, from top to bottom, are corresponding to the major phase  $\text{La}_{0.91}\text{Al}_{11.66}\text{O}_{18.69}$  (magenta), the impurity phases  $\text{LaAlO}_3$  (turquoise) and  $\text{Al}_2\text{O}_3$  (black), respectively. The amount of impurity phases is below 2%.

Refinement of our neutron diffraction data on the hibonite structure in the La/Al/O system gave results (Table 4.4 and 4.5) similar to those obtained from two different single crystal XRD studies reported in 1984 [13,14].

Table 4.4 Summary of  $\text{La}_{2/3+\delta}\text{Al}_{12-\delta}\text{O}_{19}$  structure results.

Atom	$x^a$	$z$	$U_{\text{iso}} (\text{\AA}^2)$	Occupancy <sup>b</sup>	Occupancy <sup>c</sup>
La1	2/3	1/4	0.005(1)	0.63(3)	0.64
La2	0.720(3)	1/4	0.005(1)	0.28(1) <sup>d</sup>	0.28
Al1	0	0	0.010(1)	1.0	1.016
Al2	0	0.2378(3)	0.009(2)	0.99(1) <sup>d</sup>	1.006
Al3	1/3	0.0270(2)	0.0010(6)	1.0	1.016
Al4	1/3	0.1898(2)	0.003(1)	1.0	1.016
Al5	0.1673(3)	0.8923(2)	0.0036(5)	0.946(9)	0.961
O1	0	0.1492(1)	0.0058(7)	1.0	1.016
O2	2/3	0.0569(1)	0.0061(5)	1.0	1.016
O3	0.1818(2)	1/4	0.007(1)	0.965(8)	0.980
O4	0.1540(2)	0.0524(1)	0.0057(5)	0.965(6)	0.980
O5	0.5047(2)	0.1502(1)	0.0056(5)	1.0	1.016

<sup>a</sup> $y = 2x$ ; <sup>b</sup>based on  $\text{La}_{0.91}\text{Al}_{11.66}\text{O}_{18.69}$ ; <sup>c</sup>rescaled to  $\text{La}_{0.92}\text{Al}_{11.85}\text{O}_{19}$ ; <sup>d</sup>sum of the split site.

Table 4.5 Comparison of structural data for  $\text{La}_{2/3+\delta}\text{Al}_{12-\delta}\text{O}_{19}$  phase.

	<b>XRD1<sup>a</sup></b>	<b>XRD2<sup>b</sup></b>	<b>Neutron</b>
$a$ (Å)	5.550	5.561(2)	5.5756(1)
$c$ (Å)	22.031	22.07(1)	22.046(1)
$c/a$	3.970	3.969	3.954
La1 occup. ( $1/3, 2/3, 3/4$ )	0.55	0.49(2)	0.63(3)
La2 occup. <sup>c</sup> ( $x, 2x, 3/4$ )	0.3	0.34(2)	0.28(1)
Total La	0.85	0.83(2)	0.91(3)
$\delta$	0.18	0.16	0.25
$x$ (La2)	0.717	0.718(7)	0.720(3)
Al5 occup.	0.95	0.92(2)	0.946(9)
Al2 occup. <sup>c</sup>	0.82	0.85(7)	0.99(1) <sup>c</sup>

<sup>a</sup>Ref. [13], standard deviations not reported; <sup>b</sup>ref. [14]; <sup>c</sup>sum of the split site.

The approximate formula can be represented as  $\text{La}_{2/3+\delta}\text{Al}_{12-\delta}\text{O}_{19}$  with the Al vacancies confined to Al sites in the edge shared sheets. Based on the refined La content, the values of  $\delta$  obtained from the two XRD single crystal studies are 0.16 and 0.18. Our refinement gives a  $\delta$  value of 0.25. One can expect the value of  $\delta$  to vary with synthesis conditions, which were different. The single crystals were prepared from the melt at temperatures higher than 1700 °C. Our polycrystalline powders were prepared at 1500 °C. The vacancies on La and Al5 sites cause general disorder in the structure, which impedes an accurate description of the structure. The disorder in the plane at the  $z = 1/4$  and  $3/4$  includes disorder within the plane for La, disorder of Al2 displaced from the plane, and a partial occupancy for O3. In addition, our difference Fourier map shows a peak just above and below this plane at  $x = 0.18, y = 0.36$  with an intensity of about 6% of an O atom. The disorder caused by the Al vacancies in the Al5 layer also causes apparent O vacancies at the O4 position, which is bonded to two Al5 atoms. Peaks in our difference Fourier map near the plane of Al5 atoms can also be attributed to the disorder at and near the Al5 plane. The refined composition yields a positive charge about 1% too high for charge balance, but this as close as could be expected based on the uncertainties of the occupation factors for several cation and anion sites.

Our results are compared to those of the two previous studies in Table 4.5. Due to common systematic errors, the  $c/a$  ratio is more reliable than the values of  $a$  and  $c$

themselves. This ratio is essentially the same for the two XRD studies, consistent with the fact that their value of  $\delta$  is nearly the same. The  $c/a$  ratio for our sample is significantly smaller (Table 4.5), consistent with our higher La content. All three studies have found that an atomic fraction of 30-40% of the La is displaced about 0.5 Å from the ideal site. We did not observe such displacements of La for  $\text{LaAl}_{11}\text{NiO}_{19}$  hibonite where there are no La vacancies. We conclude that the displacements of some La atoms from the ideal site are caused by adjacent La site vacancies.

#### 4.2.4 $\text{CaAl}_{10}\text{NiTiO}_{19}$

Rietveld fit of  $\text{CaAl}_{10}\text{NiTiO}_{19}$  neutron data is shown in Figure 4.8.

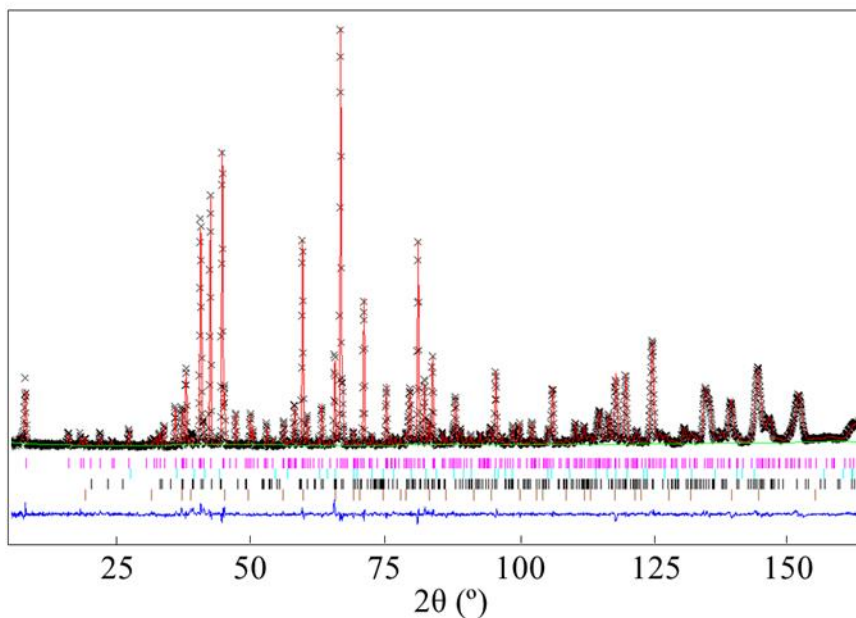


Figure 4.8 Rietveld fit of  $\text{CaAl}_{9.6}\text{Ti}_{1.2}\text{Ni}_{1.2}\text{O}_{19}$  neutron data at 298 K. The actual composition is refined to be  $\text{CaAl}_{9.98}\text{Ti}_{1.00}\text{Ni}_{1.02}\text{O}_{19}$ . Four rows of vertical lines below the data profiles, from top to bottom, are corresponding to the major phase  $\text{CaAl}_{9.98}\text{Ti}_{1.00}\text{Ni}_{1.02}\text{O}_{19}$  (magenta), the impurity phases  $\text{TiO}_2$  (turquoise),  $\text{CaTiO}_3$  (black) and  $\text{NiAl}_2\text{O}_4$  (brown), respectively. The amount of impurity phases is below 5%.

We have prepared and structurally characterized many hibonite phases where Al has been partially substituted by various 3d transition elements. Most of this work is shown in the Chapter 5 and Chapter 6, they focus on the optical properties of these phases, which show promise as pigments. Here we present our structural results on one such substitution,

$\text{CaAl}_{10}\text{NiTiO}_{19}$ . Determination of the distribution of Ni and Ti on the five different Al sites is challenging because one cannot refine the occupancies of Al, Ni, and Ti on one site even if one constrains the total site occupancies to be 100% and constrains the overall stoichiometry of the compound. An unconstrained refinement of the three elements would require additional information, such as XRD data. One can, however, take advantage of the fact that whereas the scattering lengths for Al and Ni are positive with a much higher value for Ni, the scattering length of Ti is negative. Our strategy was to first refine the structure of a  $\text{CaAl}_{10}\text{NiTiO}_{19}$  composition using 100% Al in all five Al sites. Assuming that the Ca and O sites are essentially fully occupied, the scale factor would be set and the total scattering powers at the five Al sites would be determined. If the refined Al occupancy at a given site decreased, there must be Ti on that site with this assumption. If the refined Al occupancy on a given site increased above 100%, there must be Ni on that site. The possibility that some Ni and Ti are both substituting on the same site is at first ignored except in the case of the TBP site where we fixed the Ni occupancy to the value we found for  $\text{LaAl}_{11}\text{NiO}_{19}$  and  $\text{Ca}_{0.5}\text{La}_{0.5}\text{Al}_{11.5}\text{Ni}_{0.5}\text{O}_{19}$ . Next the sites with decreased scattering power were refined as a mixture of Al and Ti, and the sites with increased scattering power are refined as a mixture Al and Ni. The results of this refinement are presented in Table 4.6.

Table 4.6 Site occupations in  $\text{CaAl}_{10}M\text{TiO}_{19}$  ( $M = \text{Ni}$  and  $\text{Ti}$ ) samples.

Site	$M = \text{Ni}^a$	$M = \text{Mg}^b$
M1: trigonal antiprism	Ni: 0.06(1)	
M2: “trigonal bipyramid”	Ti: 0.112(5); Ni: 0.02 <sup>c</sup>	Ti: 0.130(3)
M3: tetrahedral	Ni: 0.245(5)	Mg: 0.46(1)
M4: face-shared octahedra	Ti: 0.44(1)	Ti: 0.403(3)
M5: edge-shared octahedra	Ni: 0.073(4)	

<sup>a</sup>This work; refined composition:  $\text{CaAl}_{10.02}\text{Ni}_{0.98}\text{Ti}_{1.00}\text{O}_{19}$ ; <sup>b</sup>Ref. [51]; refined composition with amounts of Mg and Ti constrained to be equal:  $\text{CaAl}_{9.96}\text{Mn}_{0.98}\text{Ti}_{0.98}\text{O}_{19}$ ; <sup>c</sup>Ni fixed at value found for  $\text{LaAl}_{11}\text{NiO}_{19}$  and  $\text{Ca}_{0.5}\text{La}_{0.5}\text{Al}_{11.5}\text{Ni}_{0.5}\text{O}_{19}$ .

The composition obtained from this refinement is  $\text{CaAl}_{10.02}\text{Ni}_{0.98}\text{Ti}_{1.00}\text{O}_{19}$ , which is very close to a nominal  $\text{CaAl}_{10}\text{NiTiO}_{19}$  composition. We see that Ni is showing a strong preference for the tetrahedral site (Al3), and that Ti is showing a strong preference for the site with face-shared octahedra (Al4). Significant Ti substitution also occurs at the Al2

(TBP) site. The results indicate some Ni on the Al1 and Al5 sites, and there could possibly be a very small amount of Ni on the Al4 site that is dominated by Ti substitution.

### 4.3 Discussion

A common feature of all simple  $AM_{12}O_{19}$  compounds ( $A^{2+} = \text{Pb, Ca, Sr, or Ba}$ ;  $M^{3+} = \text{Al, Ga, or Fe}$ ) with the hibonite structure is that the  $M$  cations at both the tetrahedral site (M3) and the trigonal bipyramid site (M2) are severely underbonded (Table 4.7).

Table 4.7 Bond valence sums (BVS)<sup>a</sup> for  $AM_{12}O_{19}$  ( $A = \text{Ca, Sr, Ba}$ ;  $M = \text{Al, Ga, Fe}$ ).

Site	PbAl [26]	CaAl This work	SrAl [6]	SrAl This work	SrGa [6,56]	BaGa [7]	SrFe [6]	BaFe [8]
A	<b>1.97</b>	<b>1.49</b>	2.09	2.03	<b>1.67</b>	2.39	<b>1.54</b>	2.27
Al1: trigonal antiprism	3.24	3.23	3.33	3.20	3.16	3.14	3.12	3.13
Al2: “trigonal bipyramid”	<b>2.64</b>	<b>2.77</b>	<b>2.82</b>	<b>2.60</b>	<b>2.76</b>	<b>2.62</b>	<b>2.82</b>	<b>2.76</b>
Al3: tetrahedral	<b>2.63</b>	<b>2.68</b>	<b>2.58</b>	<b>2.61</b>	<b>2.69</b>	<b>2.62</b>	<b>2.76</b>	<b>2.78</b>
Al4: face-shared octahedra	2.89	3.00	3.16	2.89	2.96	2.83	3.05	2.99
Al5: edge-shared octahedra	3.09	3.09	3.09	3.02	3.09	3.05	3.02	2.97
O1: 3Al5, 1Al2 <sup>b</sup>	1.96	2.02	1.94	<b>1.87</b>	2.01	1.95	1.92	<b>1.86</b>
O2: 1Al1, 3Al5	<b>1.86</b>	<b>1.85</b>	1.91	1.92	<b>1.88</b>	<b>1.84</b>	1.92	1.91
O3: 1Al2, 2Al4	<b>1.92</b>	<b>1.87</b>	<b>1.41</b>	<b>1.84</b>	<b>1.87</b>	1.93	<b>1.88</b>	1.96
O4: 1Al3, 1Al1, 2Al5	2.00	2.01	1.98	1.96	1.98	1.95	1.98	1.98
O5: 2Al5, 1Al4	2.00	1.99	2.40	2.02	2.03	2.05	2.00	2.03

<sup>a</sup>Underbonded values in bold; overbonded value in italics; <sup>b</sup>cations bonded to oxygen.

In some structures, such as the perovskite structure, such a poor bonding situation can be relieved by a distortion to a structure with lower symmetry. This option apparently is not available to the hibonite structure because no such distortions have ever been observed. A partial solution to this problem is to introduce larger cations into the structure that will locate mainly on the tetrahedral and/or the TBP sites. Examples are  $\text{LaAl}_{11}\text{NiO}_{19}$  and  $\text{CaAl}_{10}\text{NiTiO}_{19}$ . Such substitutions also lower the required synthesis temperature.

The failure of the hibonite structure to adjust in a way that would give good BVS values at the M2 and M3 sites was explored by modeling with DLS software [25]. The results are given in Table 4.8.

Table 4.8 Comparison of refined and modeled structure for  $\text{CaAl}_{12}\text{O}_{19}$ .

	Refined Structure	DLS Al2: CN4	DLS Al2: CN5
$a$ , Å	5.5592	5.5517	5.6320
$c$ , Å	21.902	21.969	20.238
$z$ , Al2	0.258	0.270	0.25
$z$ , Al3	0.0286	0.0277	0.0399
$z$ , Al4	0.1908	0.1911	0.1822
$x$ , Al5	0.1686	0.1700	0.1705
$z$ , Al5	0.1090	0.1091	0.1126
$z$ , O1	0.1493	0.1493	0.1493
$z$ , O2	0.0547	0.0534	0.0534
$x$ , O3	0.1813	0.1779	0.1804
$x$ , O4	0.1552	0.1550	0.1550
$z$ , O4	0.0522	0.0523	0.0534
$x$ , O5	0.5031	0.5030	0.5030
$z$ , O5	0.1492	0.1493	0.1493
Al1-O4 $\times$ 6	<b>1.882</b>	<b>1.882</b>	<b>1.86</b>
Al2-O3 $\times$ 3	1.755	1.7673	1.78
Al2-O1	2.027	1.7694	2.04
Al2-O1'	2.384		2.04
Al2-Oave	<b>1.935</b>	<b>1.768</b>	<b>1.88</b>
Al3- O4 $\times$ 3	1.792	1.7985	1.78
Al3- O2	1.823	1.781	1.77
Al3-Oave	<b>1.800</b>	<b>1.794</b>	<b>1.78</b>
Al4-O5 $\times$ 3	1.871	1.873	1.82
Al4-O3 $\times$ 3	1.956	1.977	1.957
Al4-Oave	<b>1.914</b>	<b>1.925</b>	<b>1.887</b>
Al5-O5 $\times$ 2	1.809	1.803	1.773
Al5-O1	1.847	1.858	1.884
Al5-O2	1.984	1.991	1.970
Al5-O4 $\times$ 2	1.998	2.003	1.971
Al5-Oave	<b>1.906</b>	<b>1.910</b>	<b>1.890</b>
BVS Ca $\times$ 2	1.47	1.46	1.71
BVS Al1 $\times$ 2	3.24	3.21	3.42
BVS Al2 $\times$ 2	2.79	2.98	2.81
BVS Al3 $\times$ 4	2.65	2.72	2.94

BVS Al4 × 4	2.95	2.89	3.23
BVS Al5 × 12	3.10	3.07	3.31
BVS O1 × 4	2.14, 1.91	2.44, 1.78	2.18
BVS O2 × 4	1.85	1.90	1.99
BVS O3 × 6	1.85	1.78	1.78
BVS O4 × 12	2.00	1.98	2.12
BVS O5 × 12	2.00	2.01	2.30
Ave BVS   $\delta$   <sup>a</sup>	<b>0.08</b>	<b>0.13</b>	<b>0.20</b>

<sup>a</sup>Average BVS uses absolute differences between BVS of Al with 3.0 and of O with 2.0. The multiplicities of atoms incorporated. Values higher than ~0.1 suggest incorrect structure. Bond values indicate average bond length values.

In one example, we see that obtaining a good BVS for tetrahedral Al2 can be get with small variations of  $a$ ,  $c$ , and positional parameters. However, this is at a cost of changes in other BVS values that cause the overall BVS situation to degrade. The differences between the expected and observed BVS values were averaged based on the multiplicities of the atoms. Note that the BVS values based on the refined structure are close to those expected for the atoms with high multiplicity (Al5, O4, and O5). The failed attempt to obtain a good BVS for Al2 at an ideal TBP site (Table 4.8) demonstrates that the structure strongly resists such a variation.

The most significant factor resisting the adoption of a BVS close to 3.0 for Al2 appears to be the BVS for O1. As Al2 is displaced off the mirror plane ( $z = 1/4$ ), it moves toward one O1 increasing its BVS and away from another O1 decreasing its BVS. The O1 values for the refined structure are 2.14 and 1.91, both marginally acceptable values. The further displacement of Al2 to produce a good BVS for Al leads to BVS values of 2.44 and 1.78 for O1 (Table 4.8). These can be viewed as unacceptable deviations for 2.0. Thus, a displacement of Al2 large enough to produce a good BVS for Al does not occur.

#### 4.3.1 Ferroelectric/Multiferroic Considerations

The situation in magnetopumbites is the same as in hibonite compounds. Table 4.9 gives the displacements of the “TBP cations” from the ideal value of  $0\ 0\ 1/4$  in the center of the O triangle.

Table 4.9 For the M2 (TBP) cation: displacement along  $c$  and bond valence sum (BVS).

Compound	Displacement ( $\text{\AA}$ ) <sup>a</sup>	BVS <sup>b</sup>
CaAl <sub>12</sub> O <sub>19</sub>	0.17	2.77, 2.77, 2.80
SrAl <sub>12</sub> O <sub>19</sub>	0.21	2.60, 2.60, 2.61
PbAl <sub>12</sub> O <sub>19</sub> [30]	0.21	2.64, 2.64, 2.65
SrGa <sub>12</sub> O <sub>19</sub> [31]	0.17	2.76, 2.76, 2.80
BaGa <sub>12</sub> O <sub>19</sub> [7]	0.22	2.62, 2.62, 2.63
SrFe <sub>12</sub> O <sub>19</sub> [6]	0.10	2.82, 2.82, 2.87
BaFe <sub>12</sub> O <sub>19</sub> [8]	0.26	2.75, 2.76, 2.80

<sup>a</sup>Displacement of TBP cation from the ideal site ( $z = 1/4$ ) based on refinement of single crystal X-ray data; <sup>b</sup>bond valence sum for TBP cation at (1) ideal site, (2) reported site, and (3) site with four equal M-O bond lengths, respectively.

The situation for hibonite/magnetoplumbite compounds is very much like the situation in LiNbO<sub>3</sub> and LiTaO<sub>3</sub>. Switching polarity in an electric field causes in both cases a cation to move through the center of a triangle of O atoms. The displacements from the ideal paraelectric position are much greater for Li ( $\sim 0.65 \text{ \AA}$ ) than for the TBP cations in the hibonite/magnetoplumbite compounds. However, if net polarization for the dipoles is calculated based on formal charges, as is frequently practiced, the net polarization caused by the large displacements of Li and the smaller displacements for TBP cations is about the same. It is generally accepted that Li in the paraelectric states of LiNbO<sub>3</sub> and LiTaO<sub>3</sub> does not reside in the center of the O triangle, but is instead randomly distributed above and below this triangle [26]. The same situation apparently pertains to the “TBP cation” in hibonite/magnetoplumbite compounds.

Table 4.9 also gives the bond valence sum for the TBP cation (M2) at various sites along the  $c$ -axis. The first BVS value is with this cation placed at the ideal site ( $z = 1/4$ ). The second BVS value pertains to this cation placed according the reported structure refinement. The final BVS value pushes this cation even further from the ideal site to a position where one of the apical distances is now equal to the three equatorial distances, a tetrahedral situation but with only one 3-fold axis. Note first that the BVS values are always much lower than the expected value of 3.0. Also note that the BVS does not change significantly as the TBP cation moves from the ideal TBP symmetry to a position where there would be four equal distances for tetrahedral coordination. We conclude from this



that the TBP cation is loosely bound and that any barrier preventing its movement through the O triangle of the TBP unit is very small.

In situations where dipoles orient along a particular direction, simple electrostatic considerations favor ferroelectric chains as in Figure 1b. This occurs in tetragonal  $\text{BaTiO}_3$  and hexagonal  $\text{LiNbO}_3$  where all the chains along the  $c$ -axis are polarized the same direction. However, simple electrostatic considerations would have half the chain dipoles ordered in one direction and half in another direction, as occurs in  $\text{PbZrO}_3$  [27]. The triangular orientation of the chains in  $\text{YInO}_3$  type structures causes a frustration, the result of which is that  $1/3$  of the chains polarized up and  $2/3$  down. In some cases it has been demonstrated that the application of an electric field can cause such antiferroelectric or ferrielectric structures to become ferroelectric [28]. Thus even if the stable form of hibonite were antiferroelectric or ferrielectric, it would likely exhibit ferroelectric behavior when an electric field is applied along the  $c$ -axis.

A very unusual aspect of the hibonite structure is the dilution of the dipoles. Only 1 out of 12 Al atoms participates, and the distance between such atoms is about  $5.5 \text{ \AA}$  in the  $ab$  plane. The more important direction for dipole ordering is along the  $c$ -axis where the distance between dipoles is about  $11 \text{ \AA}$ . There are no O atoms that link the TBP units together. Ferroelectricity is well established in the hexagonal (again  $P6_3/mmc$ ) oxides such as  $\text{YInO}_3$ , where also again there are no empty  $d$  levels close to the Fermi level, a condition frequently regarded as essential for ferroelectricity in oxides [29]. The dipoles in this  $\text{YInO}_3$  structure are separated by only somewhat more than  $3 \text{ \AA}$ , and they remain ordered up very high temperatures ( $\sim 1000^\circ\text{C}$ ).

Mössbauer spectroscopic studies of  $^{57}\text{Fe}$  in  $\text{BaFe}_{12}\text{O}_{19}$  confirm that Fe at the TBP site is actually in tetrahedral coordination [18]. At higher temperatures it is jumping back and forth between sites on either side of the triangle of the TBP site. At temperatures well below room temperature the Fe atoms become trapped on one side of the triangle. The behavior of Al in hibonites is likely very much the same as that of Fe in  $\text{BaFe}_{12}\text{O}_{19}$ . The trapping of Fe at low temperatures does not infer that these displacements will necessarily produce an ordered arrangement of the dipoles.

The lack of dipole ordering in hibonite phases cannot be taken as evidence that they are not ferroelectrics. Amorphous materials with dipoles can develop ferroelectric properties by ordering of the dipoles in the presence of an electric field [30,31]. The expected ferroelectric moment in hibonites is low due to the low concentration of dipoles and because the dipoles only occur along the *c*-axis. However, in a dipole ordered structure, displacements of the loosely bound M3 cations can be expected to occur and contribute to the moment. Enhancement of a ferroelectric moment might also occur in  $\text{PbAl}_{12}\text{O}_{19}$  due to the high polarizability of  $\text{Pb}^{2+}$ .

There are many reports of multiferroic behavior in magnetoplumbite phases [31-49]. The electrical conductivity, attributed to very small amounts of  $\text{Fe}^{2+}$  in such ferrites, is generally too high at room temperature to support ferroelectric behavior. However, the conductivity decreases with decreasing temperature allowing multiferroic behavior to be observed below room temperature. Some reports of multiferroic behavior at room temperature and above are most likely due to space charge polarization owing to electrical conductivity rather than actual ferroelectricity [50]. The polarization observed for the confirmed multiferroic magnetoplumbites is perpendicular to the *c*-axis and thus cannot be related to the dipoles shown in Figure 1. The observed polarization is instead attributed to mutually canted interacting spins producing the local electric polarization by a spin-orbit interaction [43]. It could be that spin-orbit interactions dominate for all the magnetoplumbite phases. Further studies on insulating single crystals are required to fully understand how the dipoles at the TBP sites in magnetoplumbites have an impact on their properties.

#### 4.3.2 $\text{CaAl}_{10}\text{NiTiO}_{19}$

A very recent study described neutron diffraction refinements of  $\text{CaAl}_{12}\text{O}_{19}$  samples with substitutions of Ti and Mg for Al [51]. Most of the compositions were purposely prepared under reducing conditions to produce some  $\text{Ti}^{3+}$ , but one composition,  $\text{CaAl}_{19.96}\text{Mg}_{0.98}\text{Ti}_{0.98}\text{O}_{19}$ , contained only  $\text{Ti}^{4+}$  and can thus be considered for comparison to our results for  $\text{CaAl}_{10}\text{NiTiO}_{19}$  (Tables 4.6 and 4.10).

Table 4.10 Comparison of interatomic distances for  $\text{CaAl}_{12}\text{O}_{19}$ ,  $\text{CaAl}_{10}\text{NiTiO}_{19}$ , and  $\text{CaAl}_{10}\text{MgTiO}_{19}$ .

<b>Distances (Å)</b>	<b><math>\text{CaAl}_{12}\text{O}_{19}</math></b>	<b><math>\text{CaAl}_{11}\text{NiTiO}_{19}</math></b>	<b><math>\text{CaAl}_{11}\text{MgTiO}_{19}</math> [51]</b>
M1-O4 $\times$ 6	<b>1.8821(8)</b>	<b>1.8949(15)</b>	<b>1.888</b>
M2-O3 $\times$ 3	1.755(1)	1.7843(25)	1.776
M2-O1	2.027(5)	1.888(8)	1.924
M2-O1'	2.384(5)	2.580(8)	2.547
M2-Oave	<b>1.935</b>	<b>1.964</b>	<b>1.960</b>
M3-O4 $\times$ 3	1.792(1)	1.824(2)	1.825
M3-O2	1.823(3)	1.855(4)	1.849
M3-Oave	<b>1.800</b>	<b>1.832</b>	<b>1.831</b>
M4-M4	<b>2.595(5)</b>	<b>2.84(7)</b>	<b>2.80</b>
M4-O5 $\times$ 3	1.871(2)	1.84(1)	1.84
M4-O3 $\times$ 3	1.956(2)	2.06(6)	2.045
M4-Oave	<b>1.914</b>	<b>1.95</b>	<b>1.94</b>
M5-M5	2.748(3) $\times$ 2	2.786(5) $\times$ 2	2.770 $\times$ 2
M5-M5'	2.811(3) $\times$ 2	2.819(5) $\times$ 2	2.837 $\times$ 2
M5-M5ave	<b>2.780</b>	<b>2.803</b>	<b>2.804</b>
M5-O5 $\times$ 2	1.809(1)	1.855(2)	1.849
M5-O1	1.847(2)	1.879(3)	1.876
M5-O2	1.984(2)	1.957(3)	1.962
M5-O4 $\times$ 2	1.998(1)	1.980(2)	1.985
M5-Oave	<b>1.906</b>	<b>1.918</b>	<b>1.917</b>

Bond values indicate average bond length values.

These studies show a strong preference of Mg and Ni for the tetrahedral site. This might be expected considering that Mg and Ni also prefer the tetrahedral sites in the spinels  $\text{MgAl}_2\text{O}_4$  and  $\text{NiAl}_2\text{O}_4$ . Both studies also show a strong preference of Ti for the face sharing octahedral units, and both studies found about the same amount of Ti on the TBP M2 site. The two studies, however, differ with respect to the octahedral M1 and M5 sites. No substitution is reported for Al1 and Al5 in the study of  $\text{CaAl}_{9.96}\text{Mg}_{0.98}\text{Ti}_{0.98}\text{O}_{19}$ , but we find small but significant amounts of Ni on these two sites (Table 4.6). The very high scattering length of Ni (10.3 fm) vs. Al (3.449 fm), Mg (5.38 fm), and Ti (-3.438 fm) provides high accuracy to the amount of Ni on the M1 and M5 sites. A rather dramatic increase of the M2 cation distance from the triangle of the TBP unit has occurred with Ni and Mg substitution. This displacement, which was 0.17 Å in  $\text{CaAl}_{12}\text{O}_{19}$ , has become 0.31 Å in

$\text{CaAl}_{10}\text{MgTiO}_{19}$  and 0.35 Å in  $\text{CaAl}_{10}\text{NiTiO}_{19}$ . Since  $\text{Mg}^{2+}$ ,  $\text{Ni}^{2+}$ , and  $\text{Ti}^{4+}$  are all significantly larger than  $\text{Al}^{3+}$ , one might expect that bonding distances would increase as any of these cations replace  $\text{Al}^{3+}$ . In fact, such increases are observed for all five Al sites in the case of  $\text{CaAl}_{10}\text{NiTiO}_{19}$  (Table 4.6). In the case of  $\text{CaAl}_{10}\text{MgTiO}_{19}$ , the M-O distance at the M1 site has not increased significantly indicating any Mg substitution at that site is very small, in agreement with the report on  $\text{CaAl}_{10}\text{MgTiO}_{19}$  [51]. However, in  $\text{CaAl}_{10}\text{MgTiO}_{19}$  there is a significant increase in the average M5-O distance suggesting some Mg at this site, which was not reported [51]. It is not surprising that little or no Ti occupies the tetrahedral site because this is a rare site for Ti. Both studies have indicated that Ti also avoids the M1 octahedral site. Possibly, this is due to the overbonded situation at this site, which would worsen if Ti were introduced. Some Ti is expected to enter the M2 site because  $\text{Ti}^{4+}$  readily accepts TBP symmetry. There are strong cation-cation repulsive interactions across the edge-sharing octahedra in the case of M5 cation and across face-sharing octahedra in the case of M4 cations. One might then expect that the higher charge of  $\text{Ti}^{4+}$  would inhibit its substitution into the M4 and M5 sites. But in fact, Ti strongly prefers the M4 site to all other sites. Relative to the M5 site, there are two important factors. One is that the M4-M4 distance across the shared face is relatively free to increase as the Al-Ti interactions are introduced (Table 4.6). This distance actually increases to about the same value as found for the edge-sharing case of M5 cations. The other relevant factor is that a M5 cation shares edges with four other M5 cations whereas the M4 cation shares a face with only one M4 cation. Thus, cation-cation repulsion consideration is far more important for the M5 site relative to the M4 site. The Ti concentration at the M4 does not exceed 50%; thus, it is likely that Ti-Ti interactions do not occur at this site, and this may be a factor that limits the Ti substitution into  $\text{CaAl}_{12}\text{O}_{19}$ .

#### 4.4 Conclusion

Hibonite-type oxides,  $\text{CaAl}_{12}\text{O}_{19}$ ,  $\text{SrAl}_{12}\text{O}_{19}$ ,  $\text{La}_{2/3+\delta}\text{Al}_{12-\delta}\text{O}_{19}$  and  $\text{CaAl}_{10}\text{NiTiO}_{19}$ , were prepared and their structures were refined using neutron diffraction data.  $\text{CaAl}_{12}\text{O}_{19}$  structure was studied at 11 K and at 298 K; the room temperature relative-permittivity data of the phase showed that the dipoles concentration is low.  $\text{SrAl}_{12}\text{O}_{19}$  sample has a second hexagonal phase, which is structurally related to that of hibonite. Our  $\text{La}_{2/3+\delta}\text{Al}_{12-\delta}\text{O}_{19}$

structure refinement gives a  $\delta$  value of 0.25. Ni and Ti site occupancies were determined in  $\text{CaAl}_{10}\text{NiTiO}_{19}$  compound:  $\text{Ni}^{2+}$  cations prefer to occupy the tetrahedral M3 sites and  $\text{Ti}^{4+}$  strongly prefers M4 sites (face-sharing octahedra).  $\text{Ni}^{2+}$  cations provide a bright blue color to  $\text{CaAl}_{10}\text{NiTiO}_{19}$  sample.

#### 4.5 Experimental Materials and Methods

Reactants were  $\text{CaCO}_3$  (Spectrum, 99%),  $\text{SrCO}_3$  (Aldrich, 99.9%),  $\text{La}_2\text{O}_3$  (Alfa Aesar, 99.99%),  $\text{Al}_2\text{O}_3$  (Cerac, 99.99%),  $\text{NiO}$  (Alfa Aesar, 99.998%), and  $\text{TiO}_2$  (Aldrich, 99.9%). Appropriate quantities were ground together in an agate mortar and then pelleted. The pellets were then heated at a range of 1300-1500 °C in air several times with intermediate grinding. Ramp rates were 300 °C h<sup>-1</sup>. The synthesis temperature was 1300 °C for  $\text{CaAl}_{10}\text{NiTiO}_{19}$  and 1500 °C for  $\text{CaAl}_{12}\text{O}_{19}$ ,  $\text{SrAl}_{12}\text{O}_{19}$ , and  $\text{La}_{2/3+\delta}\text{Al}_{12-\delta}\text{O}_{19}$ .

The products were characterized by a Rigaku Miniflex X-ray diffractometer using  $\text{Cu K}_\alpha$  radiation and a graphite monochromator on the diffracted beam. Powder neutron diffraction data were collected on the 32-counter high-resolution diffractometer BT-1 at the Center for Neutron Research at the National Institute of Standards and Technology. A  $\text{Cu}(311)$  monochromator, yielding a wavelength of 1.5401(2) Å, was employed. Collimation of 15' of arc was used before the monochromator, 20' before the sample, and 7' before the detectors. The samples were loaded into vanadium containers of 15.6 mm diameter and 50 mm length. Data were collected at room temperature over a  $2\theta$  range of 3–167°. In the case of  $\text{CaAl}_{12}\text{O}_{19}$ , data were also collected at 11 K. Structure refinements of XRD and neutron data by the Rietveld approach were carried out using GSAS-EXPGUI software [52,53].

Final structures were evaluated with difference Fourier maps. Anharmonic refinements used Jana2006 software [54].

Bond valence sums were calculated with the software EUTAX [55]. This software does not deal directly with the issues arising from split atoms. However, the bond valence sums produced can be corrected for the extra bonds produced utilizing the individual bond valences, which are provided by the software.

## 4.6 Acknowledgements

Text and figures within this chapter have been used in part or whole from the publication:

Li, J., **Medina, E.A.**, Stalick, J.K., Sleight, A.W., Subramanian, M.A. Structural studies of  $\text{CaAl}_{12}\text{O}_{19}$ ,  $\text{SrAl}_{12}\text{O}_{19}$ ,  $\text{La}_{2/3+\delta}\text{Al}_{12-\delta}\text{O}_{19}$ , and  $\text{CaAl}_{10}\text{NiTiO}_{19}$  with the hibonite structure; indications of an unusual type of ferroelectricity *Zeitschrift fur Naturforschung Section B-A Journal of Chemical Sciences* **2016**, 71(5), 475-484.

This research done at Oregon State University was supported by National Science Foundation grant (DMR - 1508527). The identification of any commercial product or trade name does not imply endorsement or recommendation by the National Institute of Standards and Technology.

## 4.7 References

- [1] Keil, K., Fuchs, L.H., *Earth Planet. Sci. Lett.* 12 (1971) 184.
- [2] Burns, R.G., Burns, V.M., Virginia, J. *Geophys. Res.*, B 89(Suppl.) (1984) C313.
- [3] Nagashima, M., Armbruster, T., Hainschwang, T., *Miner. Mag.* 74 (2010) 871.
- [4] Kimura, K., Ohgaki, M., Tanaka, K., Morikawa, H., Marumo, F., *J. Solid State Chem.* 87 (1990) 186.
- [5] Comer, J.J., Croft, W.J., Kestigian, M., Carter, J.R., *Mat. Res. Bull.* 2 (1967) 293.
- [6] Wagner, T.R., *J. Solid State Chem.* 136 (1998) 120.
- [7] Obradors, X., Collomb, A., Pernet, M., Samaras, D., Joubert, J.C., *J. Solid State Chem.* 56 (1985) 171.
- [8] Du, L-S., Stebbins, J.F., *J. Phys. Chem. B* 108 (2004) 3681.
- [9] Harindranath, K., Viswanath, K.A., Chandranb, C.V., Bräuniger, T., Madhuc, P.K., Ajithkumar, T.G., Joy, P.A., *Solid State Commun.* 150 (2010) 262.
- [10] Wagner, T.R., O’Keeffe, M., *J. Solid State Chem.* 73 (1988) 211.
- [11] Geiger, C.A., Kleppa, O.J., Mysen, B.O., Laitimer, J.M., Grossman, L., *Geochim. Cosmo. Acta*, 52 (1988) 1729.
- [12] Saber, D., Lejus, A.M., *Mat. Res. Bull.* 16 (1981) 1325.
- [13] Gasperin, M., Saine, M.C., Kahn, A., Laville, F., Lejus, A.M., *J. Solid State Chem.* 54 (1984) 61.
- [14] Iyi, N., Inoue, Z., Takekawa, S., Kimura, S., *J. Solid State Chem.* 54 (1984) 70.
- [15] Kahn, A., Lejus, A.M., Madsac, M., Théry, J., Vivien, D., Bernier, J.C., *J. Appl. Phys.* 52 (1981) 6864.
- [16] Laville, F., Perrin, M., Lejus, A.M., Gasperin, M., Moncorge, R., Vivien, D., *J. Solid State Chem.* 65 (1986) 301.
- [17] Mao, H.H., Hillert, M., Selleby, M., Sundman, B., *J. Amer. Cer. Soc.* 89 (2006) 298.

- [18] Kreber, E., Gonser, U., Trauwein, A., Harris, F.E., *J. Phys. Chem. Solids* 36 (1975) 265.
- [19] Smith, A.E., Mizoguchi, H., Delaney, K., Spaldin, N.A., Sleight, A.W., Subramanian, M.A., *J. Am. Chem. Soc.* 131 (2009) 17084.
- [20] Mizoguchi, H., Sleight, A.W., Subramanian, M.A., *Inorg. Chem.* 50 (2011) 10.
- [21] Jiang, P., Li, J., Sleight, A.W., Subramanian, M.A., *Inorg. Chem.*, 50 (2011) 5858.
- [22] Kingery, W.D., *Introduction to Ceramics*, New York: John Wiley & Sons, Inc., 1960, pp. 1-719.
- [23] Kihara, K., Donnay, G., *Canad. Miner.* 23 (1985) 647654.
- [24] Iyi, N., Göbbels, M., *J. Solid State Chem.* 122 (1996) 46.
- [25] Meier, W.M., Villiger, H., *Z. Kristallogr.* 129 (1969) 411.
- [26] Sanna, S., Schmidt, W.G., *IEEE Trans. Ultra. Ferroelec. Freq. Cont.* 59 (2012) 1925.
- [27] Sawaguchi, E., Maniwa, H., Hoshino, S., *Phys. Rev.* 83 (1951) 1078.
- [28] Sawaguchi, E., Shirane, G., Takagi, Y., *J. Phys. Soc. Jpn.* 6 (1951) 333.
- [29] Sleight, A.W., *Prog. Solid State Chem.* 37 (2009) 251.
- [30] Lines, M.E., *Phys. Rev. B* 15 (1977) 388.
- [31] Xu, Y., Mackenzie, J.D., *J. Non-Crys. Solids* 246 (1999) 136.
- [32] Tan, G.-L., Wang, M., *J. Electrocer.* 26 (2011) 170.
- [33] Ebnabbasi, K., Mohebbi, M., Vittoria, C., *J. Appl. Phys.* 113 (2013) 17C703.
- [34] Wang, L., Wang, D., Cao, Q., Zheng, Y., Xuan, H., Gao, J., Du, Y., *Sci. Rep.* 2 (2012) 223.
- [35] Ebnabbasi, K., Vittoria, C., Widom, A., *Phys. Rev. B* 86 (2012) 024430.
- [36] Ebnabbasi, K., Chen, Y., Geiler, A., Harris, V., Vittoria, C., *J. Appl. Phys.* 111 (2012) 07C719.
- [37] Ebnabbasi, K., Mohebbi, M., Vittoria, C., *Appl. Phys. Lett.* 101 (2012) 062406.
- [38] Ishiwata, S., Taguchi, Y., Murakawa, H., Onose, Y., Tokura, Y., *Science* 319 (2008) 1643.
- [39] Ishiwata, S., Taguchi, Y., Tokunaga, Y., Murakawa, H., Onose, Y., Tokura, Y., *Phys Rev B* 79 (2009) 180408(R).
- [40] Chun, S.H., Chai, Y.S., Jaiswal-Nagar, D., Haam, S.Y., Kim, I., *Phys. Rev. Lett.* 104 (2010) 037204.
- [41] Kitagawa, Y., Hiraoka, Y., Honda, T., Ishikura, T., Nakamura, H., Kimura, T., *Nat. Mater.* 9 (2010) 797.
- [42] Okumura, K., Ishikura, T., Soda, M., Asaka, T., Nakamura, H., Wakabayashi, Y., Kimura, T., *Appl. Phys. Lett.* 98 (2011) 212504.
- [43] Tokunaga, Y., Kaneko, Y., Okuyama, D., Ishiwata, S., Arima, T., Wakimoto, S., Kakurai, K., Taguchi, Y., Tokura, Y., *Phys. Rev. Lett.* 105 (2010) 257201.
- [44] Iqbal, M.J., Ashiq, M.N., Gomez, P.H., Munoz, J.M., *J. Magn. Magn. Mater.* 320 (2008) 881.
- [45] Na, E.H., Lee, J.H., Ahn, S.J., Hong, K.P., Koo, Y.M., Jang, H.M., *J. Magn. Magn. Mater.* 324 (2012) 2866.
- [46] Utsumi, S., Yoshida, D., Momozawa, N., *J. Phys. Soc. Jpn.* 76 (2007) 034704.
- [47] Kimura, T., Lawes, G., Ramirez, A.P., *Phys. Rev. Lett.* 94 (2005) 137201.
- [48] Kimura, T., Goto, T., Shintani, H., Ishizaka, K., Arima, T., Tokura, Y., *Nature* 426 (2003) 55.

- [49] Na, E.H., Song, S., Koo, Y.-M., Jang, H.M., *Acta Mater.* 61 (2013) 7705.
- [50] Magione, M., Subramanian, M.A., *Appl. Phys. Lett.* 93 (2008) 032902.
- [51] Doyle, P.M., Schofield, P.F., Berry, A.J., Walker, A.M., Knight, K.S., *Amer. Mineral.* 201 (1999) 1369.
- [52] Larson, A.C., Von Dreele, R.B., *General Structure Analysis System (GSAS)*; Report LAUR 86-748; Los Alamos National Laboratory, Los Alamos, NM, 1994.
- [53] Toby, B.H., *J. Appl. Crystallogr.* 34 (2001) 210.
- [54] Petricek, V., Dusek, M., Palatinus, L., *Z. Kristallogr. – Cryst. Mater.* 229 (2014) 345.
- [55] O’Keeffe, M., Eutax; <http://www1.iucr.org/sincris-top/logiciel/prg-eutax.html> (accessed 02/17/2016).
- [56] Iyi, N., Takekawa, S., Kimura, S., *J. Solid State Chem.* 85 (1990) 318.



## CHAPTER 5

### Blue Pigments with Hibonite-type Structure: $\text{CaAl}_{12}\text{O}_{19}$ -based pigments with Ni as chromophore

#### Abstract

The crystal structure of hibonite with an ideal formula  $\text{CaAl}_{12}\text{O}_{19}$  is hexagonal  $P6_3/mmc$ , isostructural with magnetoplumbite. Natural and synthetic hibonites have been widely studied for their formation, compositions, crystal structures, properties and applications. Recent increasing interest in its coloration has led to the search of inorganic pigments based on the hibonite structure. We present here the syntheses and characterization of hibonite compounds with a general formula of  $A\text{Al}_{12-x}M_x\text{O}_{19}$  ( $A = \text{Ca}, \text{Sr}, \text{RE}$  (rare earths) or any combination thereof; and  $M = \text{Ni}$  or  $\text{Ni}$  coupled with one of the following:  $\text{Ti}, \text{Sn}, \text{Ge}, \text{Nb}, \text{Ta}, \text{Sb}$ ). Bright sky-blue to royal-blue colors are induced in these oxides prepared by conventional solid state reactions, as demonstrated in the solid solutions of  $\text{CaAl}_{12-2x}\text{Ni}_x\text{Ti}_x\text{O}_{19}$  ( $x = 0-1$ ) and  $\text{Ca}_{1-x}\text{La}_x\text{Al}_{12-x}\text{Ni}_x\text{O}_{19}$  ( $x = 0-1$ ). The values of color coordinates  $L^*a^*b^*$  range from 64.5,  $-5.3$ ,  $-18.5$  to 57,  $-11.33$ ,  $-30.38$ . Structure refinements of neutron powder diffraction data reveal that Ni preferably occupies the tetrahedral site in the hibonite structure, and magnetic susceptibility analysis confirms that this Ni is  $\text{Ni}^{2+}$ . Optical measurements further verifies that the observed blue color is due to d-d transitions of tetrahedral  $\text{Ni}^{2+}$ . The preference of  $\text{Ni}^{2+}$  for the tetrahedral site is unusual because  $\text{Ni}^{2+}$  prefers the octahedral site in the spinel  $\text{NiAl}_2\text{O}_4$ . We attribute this unexpected behavior to the unusually large Al–O distances for the tetrahedral site in the hibonite structure. These blue hibonites exhibit excellent thermal stability, superior acid/base durability and better near-infrared reflectance than that of the commercial cobalt blue pigment. Our results suggest a potential route to the development of inexpensive, enduring and cobalt-free blue pigments. Synthesis and characterization methods are briefly reviewed for hibonite type of oxides, especially those with blue colors.

Publication based on this chapter:

- 1) Li, J., **Medina, E.A.**, Stalick, J.K., Sleight A.W., Subramanian, M.A. Colored oxides with hibonite structure: A potential route to non-cobalt blue pigments *Progress in Solid State Chemistry* **2016**, 44, 107-122.

## 5.1 Introduction

The mineral hibonite was discovered in Madagascar by a French prospector Paul Hibon in 1953 [1,2]. The compositions and crystal structure of these naturally occurring hibonite samples were reported three years later as  $[(\text{Ca}, \text{RE})](\text{Al}, \text{Fe}^{3+}, \text{Ti}, \text{Si}, \text{Mg}, \text{Fe}^{2+})_{12}\text{O}_{19}$  with a hexagonal structure that is identical to that of the magnetoplumbite [2]. Although found primarily in high-grade metamorphic rocks from Madagascar to Siberia, Tanzania, Kenya, South India, China and Myanmar, terrestrial hibonites are rare compared with their meteoritic analogue (mostly in chondritic meteorites) that landed on our earth [3,4]. The formation of metamorphic rocks was associated with high temperatures and pressure underneath the Earth's surface, and early studies on origin of hibonite inclusions in meteorites favored a vapor condensation mechanism that also required extremely high temperatures [5]. Hibonite is considered as one of the earliest condensation products from the solar nebula compared with other major CAI (Ca-Al-rich inclusion) minerals found in carbonaceous chondrite meteorites [3,5].

Research on nature hibonites has been focused on their texture, compositions, crystal structures and some physical properties, the major objective of which is to ascertain the origin of hibonite-bearing meteoritic assemblages in hope of understanding the evolution of the primitive solar nebula [3–9]. Crystal structures of synthetic hibonites have been extensively studied and determined to be isostructural with the mineral magnetoplumbite [10–18]. Although the ideal formula is  $\text{CaAl}_{12}\text{O}_{19}$ , various oxides with the hibonite structure have also been synthesized, including  $\text{PbAl}_{12}\text{O}_{19}$ ,  $\text{BaGa}_{12}\text{O}_{19}$ ,  $\text{SrAl}_{12}\text{O}_{19}$ ,  $\text{SrGa}_{12}\text{O}_{19}$  and the defect hibonite phase  $\text{La}_{2/3+\delta}\text{Al}_{12-\delta}\text{O}_{19}$  [12–18]. The hexagonal structure of hibonite  $\text{AM}_{12}\text{O}_{19}$  can be described as, along the  $c$ -axis, alternating “spinel slabs” or S-blocks (similar to those in  $\beta$ -alumina) and intermediate layers or R-blocks (containing  $\text{A}^{2+}$  ions, 5-coordinated  $\text{MO}_5$  and isolated face-sharing  $\text{MO}_6$  pairs) [5,8]. As depicted in Figure 5.1, the A ( $\text{A} = \text{Ca}, \text{Sr}, \text{RE}$ ) cations are in 12-fold coordination in the center of the R-blocks while the M ( $M = \text{Al}, \text{Ga}$  etc.) cations are distributed over three crystallographically distinct octahedral sites (M1, M4 and M5), one tetrahedral site (M3), and one trigonal bipyramidal site (M2). None of the three M sites with coordination number (CN) 6 have ideal octahedral

symmetry. The M1 atom at the origin has ideal trigonal antiprismatic symmetry, two  $\text{MO}_6$  (M4) octahedra form a face-sharing dimer, and the  $\text{MO}_6$  octahedra based on the M5 site form a sheet perpendicular to the  $c$ -axis [18].

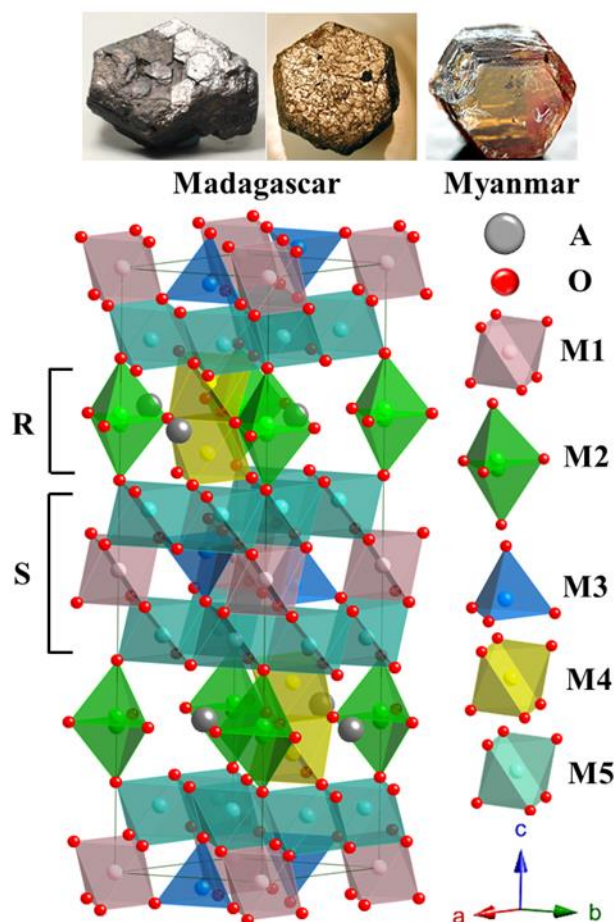


Figure 5.1 Polyhedral representation of hexagonal  $\text{AM}_{12}\text{O}_{19}$  ( $A = \text{Ca}, \text{Sr}, \text{RE}$ ) with hibonite-type of structure. Twelve coordinated  $A$  atoms in gray; oxygen atoms in red;  $\text{MO}_6$  octahedra in pink (M1), yellow (M4), cyan (M5);  $\text{MO}_5$  trigonal bipyramids in green (M2); and  $\text{MO}_4$  tetrahedra in royal blue (M3). The framework can be viewed as alternating S-block (spinel layers) and R-block (constituted by  $A$  ions, trigonal bipyramids and face-sharing octahedra) stacking alternatively along the  $c$ -axis. (Top) Images of hibonite minerals from Madagascar [1] and Myanmar [32].

The tetrahedral M3 cation inside the “spinel slabs” was found underbonded for  $M = \text{Al}$  [10,18]. The M2 ( $M = \text{Al}, \text{Ga}$ ) cation with trigonal bipyramidal (TBP) symmetry was reported to displace toward one of the apical oxygen atoms and hence be treated with a split-atom model [8,11,15–18]. This has been confirmed by  $^{27}\text{Al}$  NMR studies for

$\text{CaAl}_{12}\text{O}_{19}$  and  $\text{SrAl}_{12}\text{O}_{19}$  [19], and the disorder between two adjacent pseudotetrahedral sites was demonstrated to be dynamic in magnetoplumbite  $\text{BaFe}_{12}\text{O}_{19}$  at room temperature using  $^{57}\text{Fe}$  Mössbauer spectroscopy [20].

The unique structural features of hibonite make it an excellent host material to accommodate ions of various sizes, coordinations and valences. Hibonite minerals are known to occur with many impurity elements such as Mg, Ti, Si, V, Cr, Fe, Mn, Zn, Sr, Na, K and rare earth (RE) cations [3,4,8]. Meteoritic hibonite  $\text{Ca}(\text{Al,Ti,Mg})_{12}\text{O}_{19}$  was found to emit a bright red-orange or bright blue luminescence depending on the composition [3], and substituted synthetic hibonites have been of great interest as phosphor or laser materials [21–25]. Whereas the “ideal” hibonites are colorless, natural and synthetic hibonites often display a variety of colors (Fig.1, top): black, brownish black, reddish brown, orange, blue, green, yellow etc., as a result of the variation in occurrences and/or chemical compositions [5,26–32]. There are several studies on the pleochroism of hibonites especially the origin of the blue color [5,27–29]. The first row transition metals are responsible for the colors of many minerals, and in the case of the Blue Angel (blue hibonite-containing inclusion from the Murchison meteorite) the origin of the color has been attributed to several mechanisms: crystal field transitions within  $\text{V}^{3+}$  or  $\text{Ti}^{3+}$ , color centers and the  $\text{Fe}^{2+} \rightarrow \text{Ti}^{4+}$  charge transfer analogous to that occurring in blue sapphires [5,27,29]. The presence of  $\text{Ti}^{3+}$  in blue hibonites has been inferred by electron spin resonance (ESR) spectroscopy, Ti K-edge X-ray absorption near edge structure (XANES) spectra and X-ray and neutron structural studies [33–36]. The concentration of  $\text{Ti}^{3+}$  was found to increase with decreasing oxygen fugacity, giving rise to the growth of an absorption band that is associated with the blue color [28].

The occurrence of nickel within natural hibonites is very rare, and it is not related to the observed blue color as found in hexagonal grains of Fe-Ni metal in the core of the meteoritic hibonite inclusion [27]. Ni-substituted oxides with hibonite structure have been synthesized since early 1980s [23,37–42], and the resulting blue color has recently prompted interest in its application as inorganic pigments [43–47]. Although it is not uncommon for nickel to be utilized as a chromophore in ceramic pigments with spinel or

rutile structures [48-49], the hibonite-based oxides incorporated with Ni have not been extensively investigated as potential blue pigments and the reported colors are more turquoise than blue [43-47]. The Ni-containing pigments prepared with anorthite fluxing agent and cassiterite tin buffer or from the industrial waste comprised of only ~55% hibonite phase and exhibited a very light turquoise color [44]. The color of Ni-Ti codoped hibonite samples by combustion synthesis was described as “greenish-blue, close to cyan or turquoise” [47].

Given the complexity and flexibility of the host structure, it would be of considerable interest to examine the distribution of numerous ions including  $\text{Ni}^{2+}$  substituted for Al in the  $\text{AAl}_{12-x}\text{M}_x\text{O}_{19}$  ( $A = \text{Ca, Sr, RE}$ ;  $M = \text{Ni etc.}$ ) hibonite lattice. We have previously reported on one example,  $\text{CaAl}_{10}\text{NiTiO}_{19}$ , where we revealed from neutron diffraction data that  $\text{Ni}^{2+}$  on the tetrahedral sites in hibonite provides a bright blue color [18]. Here we report on many more  $\text{Ni}^{2+}$  containing hibonite phases. To ensure charge neutrality of the system heterovalent substitution for  $\text{Al}^{3+}$  can be achieved combining divalent ions ( $M = \text{Ni, Mn, Fe, Co, Cu, Cr etc.}$ ) with tetravalent and pentavalent ions ( $M = \text{Si, Ti, Sn, Ge, Zr, V, Nb, Ta, Sb etc.}$ ) such that  $\text{M}^{2+} + \text{M}^{4+} \rightarrow 2\text{Al}^{3+}$  or  $2\text{M}^{2+} + \text{M}^{5+} = 3\text{Al}^{3+}$ , and substituent ions of other valences may also be introduced to  $A$  or  $M$  site for charge compensation. We have tried coupled substitutions of various types and discovered different colors in addition to blue [50]. The details about those hibonite phases with colors other than blue can be found in the Chapter 6. The present work is particularly devoted to syntheses and characterization of Ni-containing hibonite solid solutions  $\text{AAl}_{12-2x}\text{Ni}_x\text{Ti}_x\text{O}_{19}$  ( $A = \text{Ca, Sr, } x = 0-1$ ) and  $\text{Ca}_{1-x}\text{RE}_x\text{Al}_{12-x}\text{Ni}_x\text{O}_{19}$  ( $\text{RE} = \text{La, Ce, Nd, Pr, } x = 0-1$ ) as well as compositions that display a range of blue colors. A brief review of synthesis and characterization methods will be given for hibonite type of oxides.

The Co-doped blue hibonites have been explored for pigment application [45,51,52]. Like commercial cobalt blue ( $\text{CoAl}_2\text{O}_4$ ), they may cause some environmental issues since cobalt is considered to be a human carcinogen. We expect that our results of hibonite-based Ni-blue will lead to routes for the development of Co-free pigments. The ultimate goal of our research is to design environmentally benign pigments with intense blue color, great

durability and excellent near infrared reflectance comparable to the YInMn Blue ( $\text{YIn}_{1-x}\text{Mn}_x\text{O}_3$ ) [53] but with less cost.

## 5.2 Materials and Synthesis

Hibonite is frequently found in meteorites and apparently forms on cooling from a liquid phase [54], and laboratory synthesis of compounds with the hibonite structure generally requires temperatures of about 1200 °C or higher. There are indications that  $\text{CaAl}_{12}\text{O}_{19}$  synthesis requires very high temperatures because it is actually entropy stabilized. Attempts to employ low temperature synthesis methods, such as a sol-gel precursor, still require a final temperature of about 1200 °C or higher. The issue of the metastability of hibonite has been controversial, and the most recent evaluation of the situation concluded that present thermodynamic data cannot unambiguously determine whether or not hibonite is an entropy-stabilized phase, such as “FeO” [55].

### 5.2.1 Conventional Solid State Method

Hibonite compounds can be synthesized in many ways. The most convenient preparative method, especially for pigment manufacturing, would be calcination directly of the starting materials in powder or pellet form at high temperatures in air [18,44–46].

We prepared all the colored oxides with hibonite structure via conventional solid state reactions. The general formula is  $A\text{Al}_{12-y}M_y\text{O}_{19}$  where  $A$  and  $M$  stand for one or more than one cations depending on charge compensation requirement. Stoichiometric amount of dried, reagent-grade  $\text{ACO}_3$  ( $A = \text{Ca}, \text{Sr}, \text{Ba}$ ),  $\text{A}_2\text{CO}_3$  ( $A = \text{Na}$ ),  $\text{RE}_2\text{O}_3$  ( $\text{RE} = \text{La}, \text{Nd}, \text{Sm}, \text{Eu}, \text{Gd}, \text{Dy}, \text{Ho}, \text{Er}, \text{Tm}, \text{Yb}, \text{Lu}, \text{Y}$ ),  $\text{CeO}_2$ ,  $\text{Pr}_6\text{O}_{11}$ ,  $\text{Tb}_4\text{O}_7$ ,  $\text{MO}$  ( $M = \text{Ni}, \text{Cu}, \text{Zn}$ ),  $\text{M}_2\text{O}_3$  ( $M = \text{Mn}, \text{Fe}, \text{In}, \text{Ga}, \text{Cr}, \text{Zn}$ ),  $\text{MO}_2$  ( $M = \text{Si}, \text{Ti}, \text{Sn}, \text{Ge}, \text{Te}$ ),  $\text{M}_2\text{O}_5$  ( $M = \text{Sb}, \text{V}, \text{Nb}, \text{Ta}$ ) and  $\text{Co}_3\text{O}_4$  were mixed, ground and pelletized. The resulting pellets were then heated in alumina crucibles for 12 h at a range of 1300–1500°C in air several times with intermediate grinding. Ramp rates were 300°C/h. Starting materials like rare earth oxides were preheated in an oven to remove moisture and carbonate content before use. To obtain pure  $\text{CaAl}_{12-2x}\text{Ni}_x\text{Ti}_x\text{O}_{19}$  ( $x = 0-1$ ) phases, the synthesis temperatures were 1300–1350 °C for high Ni content ( $x \geq 0.4$ ) samples, 1400–1450 °C for low Ni content ( $x < 0.4$ ) samples, and

1500–1550 °C for the end member  $\text{CaAl}_{12}\text{O}_{19}$ . Entire range of solid solutions  $\text{A}_{1-x}\text{RE}_x\text{Al}_{12-x}\text{Ni}_x\text{O}_{19}$  ( $\text{A} = \text{Ca}, \text{Sr}, \text{RE} = \text{La}, \text{Ce}, \text{Pr}, \text{Nd}, x = 0-1$ ) were prepared in a similar way at 1400–1550 °C with longer heating time.

The M-site substitutions of  $\text{CaAl}_{12-x}\text{M}_x\text{O}_{19}$  with chromophore cations other than Ni were attempted for  $M = \text{Co}, \text{Fe}, \text{Mn}, \text{Cr}, \text{V}$  and small amount of substitution resulted in colors including purplish blue, ivory, brown, creamy, pink and light turquoise, respectively. The detailed results can be found in the Chapter 6. Reduction of certain samples was carried out at 900 °C in 5% $\text{H}_2$ /95% $\text{N}_2$  for 5 h in an alumina tube furnace.

### 5.2.2 Other Preparation Methods

In addition to the standard ceramic method, hibonite type of oxides can also be prepared using wet techniques through citrate-based sol-gel precursors followed by thermal decomposition at 1300–1550 °C [35,41,42], or by coprecipitation of mixed metal hydroxides and then heating at 1350–1500 °C [22]. A very recent study of  $\text{CaAl}_{12-2x}\text{Ni}_x\text{Ti}_x\text{O}_{19}$  phases employed a combustion synthesis route, a technique that is generally not considered to be a viable commercial route [47]. Furthermore, this route still employed a final heating at 1200 °C.

Single crystals are sometimes preferred for different applications such as substrates for electronics [25]. Crystal growth can be realized by floating zone method [11,12,23,26,37,39], Verneuil method [17,23,26,37,39], Czochralski technique [13] or heating the ingredients with a flux in Pt crucibles up to high temperatures [15,30].

## 5.3 Characterization

### 5.3.1 Techniques Applied for Hibonites

In this chapter we focus on characterization of structure and various properties: color, magnetic, dielectric, and stability. Crystal structures of hibonite type of oxides have been characterized extensively by lab X-ray [8,10–17,23,30,35,39], synchrotron [41] and neutron [18,36] diffractions. Other techniques have also been employed to characterize hibonite phases. Electron Energy Loss Spectroscopy (EELS) in the TEM [56,57] and high-



resolution solid state  $^{27}\text{Al}$  Nuclear Magnetic Resonance Spectroscopy (NMR) [19] were used to probe the local symmetry fingerprints for hibonite structures and local environment of Al atoms. Lattice information and defects such as dislocations were explored by TEM with electron diffraction [14,42,54]. Chemical compositions of mineral samples were normally determined by SEM equipped with EDX [32,34,36,44,51,52], Electron Probe Microanalysis (EMPA) [3,31,33,35], X-ray Fluorescence (XRF) [44,45,51] and even Inductively Coupled Plasma (ICP) with mass spectrometer [4]. The morphology, texture and elemental distribution were obtained through electron microscopic studies like Scanning Electron Microscopy (SEM), Transmission Electron Microscopy (TEM) and Backscattered Electron (BSE) imaging [31,35,54]. Mossbauer [5,29], XANES [34], Fourier Transform Infrared Spectroscopy (FTIR)/IR [24,32,58] and Raman spectra [32,46] were utilized for obtaining additional structure information. Electron Spin Resonance (ESR) was used to make the first direct determination of  $\text{Ti}^{3+}$  [33]. Optical properties were investigated by Ultraviolet-visible (UV-Vis) and Near-infrared (NIR) spectra [24,28,32,39,44,45,47,51,52].

### 5.3.2 For Ni-blue Hibonites in This Work

The calcined powders were characterized by a Rigaku Miniflex X-ray diffractometer using  $\text{Cu K}\alpha$  radiation and a graphite monochromator. For lattice parameter calculation the XRD data were collected with Si as the internal standard. Powder neutron diffraction data were collected on the 32-counter high-resolution diffractometer BT-1 at the Center for Neutron Research at the National Institute of Standards and Technology. A  $\text{Cu}(311)$  monochromator, yielding a wavelength of  $1.5403(2) \text{ \AA}$ , was employed. Collimation of  $15'$  of arc was used before the monochromator,  $20'$  before the sample, and  $7'$  before the detectors. The samples were loaded into vanadium containers of 15.6 mm diameter and 50 mm length. Data were collected at room temperature over a  $2\theta$  range of  $3\text{--}167^\circ$ . Structure refinements of XRD and neutron data were carried out using GSAS-EXPGUI software [59,60]. Bond-valence analysis of the neutron structures made use of the bond-valence calculator [61].

Diffuse Reflectance data of the polycrystalline samples were measured in the visible range using a homemade UV-VIS spectrophotometer (MgO as the reference) and converted to absorbance using Kubelka-Munk equation [62]. Near-infrared reflectance data (up to 2500 nm) were collected using a Jasco V-670 Spectrophotometer. Konica Minolta CM-700d Spectrophotometer (Standard illuminant D65) was used to measure the  $L^*$ ,  $a^*$ ,  $b^*$  color coordinates.

Magnetic data were obtained on a Quantum Design, Physical Property Measuring System (QD-PPMS) over a temperature range of 5–300 K. Data were collected using the zero field cooling (ZFC) method with an applied magnetic field of 0.5T. Inverse magnetic susceptibility data were used to fit for the Curie-Weiss law. Diamagnetic corrections were made for calculating the effective magnetic moments [63].

Dielectric properties were measured on a HP Precision LCR Meter 4284A instrument with a frequency range of 20 Hz–1 MHz and a temperature range of 25–250 °C. The sample pellets were sintered at a temperature slightly higher than the synthesis temperature to achieve a reasonably high density. Both sides of the pellets were smoothed with fine sand paper and coated with silver electrode. The pellets were then let dry in the oven overnight and cool to room temperature before the measurement.

## 5.4 Results and Discussion

### 5.4.1 Colors and Phase Analyses

A wide variety of substitutions were attempted on both A and M sites of the hibonite host with an ideal formula  $\text{CaAl}_{12}\text{O}_{19}$ . Representative colors of the resulting powders  $(\text{Ca},\text{A})(\text{Al},\text{M})_{12}\text{O}_{19}$  are demonstrated in Figure 5.2. As we can see in Figure 2(a), only Co gives rise to a purplish blue color, whereas the color induced by Ni is light turquoise. However when charge compensation is achieved by adding some trivalent, tetravalent or pentavalent ions, a range of blue colors are produced in Ni-containing samples  $\text{CaAl}_{12-x-y}\text{Ni}_x\text{M}_y\text{O}_{19}$  ( $M = \text{Zn, Ga, In, Si, Ti, Zr, Sn, Ge, Nb, Ta, Sb, Te}$ ), among which the most intense blue colors are found with Ti, Ge and Nb (Fig. 2(b)). In the case of  $(\text{Ca},\text{A})\text{Al}_{12-x-y}\text{Ni}_x\text{Ti}_y\text{O}_{19}$ , if Ca is partially replaced by Sr the color becomes less intense and lighter, while

the addition of Na helps to give a slightly darker color at low Ni content (Fig. 2(c)). All the A site substitutions of  $\text{Ca}_{1-x}\text{RE}_x\text{Al}_{12-x}\text{Ni}_x\text{O}_{19}$  by rare earth ions result in bright blue colors as shown in Figure 2(c).

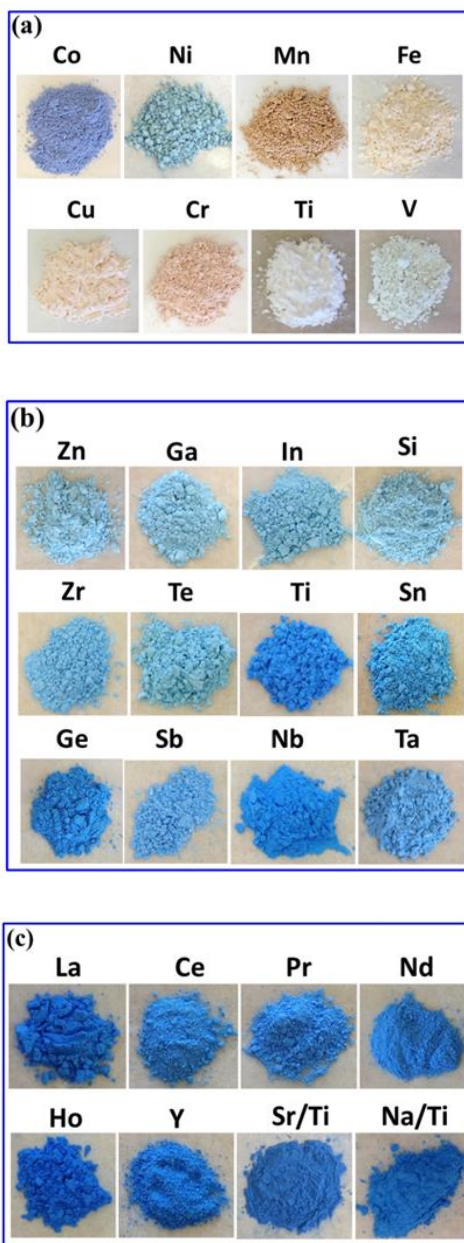


Figure 5.2 Colors resulted from a variety of substitutions for the hiconite host with an ideal formula  $\text{CaAl}_{12}\text{O}_{19}$ . (a)  $\text{CaAl}_{12-x}\text{M}_x\text{O}_{19}$  ( $M = \text{Cr, Mn, Fe, Ni, Co, Cu, Ti, V}$ ); (b)  $\text{CaAl}_{12-x-y}\text{Ni}_x\text{M}_y\text{O}_{19}$  ( $M = \text{Zn, Ga, In, Si, Zr, Sn, Ge, Nb, Ta, Sb, Te}$ ); (c)  $\text{Ca}_{1-x}\text{A}_x\text{Al}_{12-x}\text{Ni}_x\text{O}_{19}$  ( $A = \text{Sr, La, Y, Ce, Pr, Nd}$ ).

Phase identification by X-ray powder diffraction (XRD) confirms the formation of full solid solutions of  $\text{CaAl}_{12-2x}\text{Ni}_x\text{Ti}_x\text{O}_{19}$  ( $x = 0-1$ ),  $\text{Ca}_{1-x}\text{Sr}_x\text{Al}_{12-2x}\text{Ni}_x\text{Ti}_x\text{O}_{19}$  ( $x = 0-1$ ),  $\text{SrAl}_{12-2x}\text{Ni}_x\text{Ti}_x\text{O}_{19}$  ( $x = 0-2$ ),  $\text{Ca}_{1-x}\text{RE}_x\text{Al}_{12-x}\text{Ni}_x\text{O}_{19}$  ( $\text{RE} = \text{La, Ce, Pr, Nd}, x = 0-1$ ) and  $\text{Sr}_{1-x}\text{La}_x\text{Al}_{12-x}\text{Ni}_x\text{O}_{19}$  ( $x = 0-1$ ). Blue pellets and powders of selected solid solutions are shown in Figure 5.3.

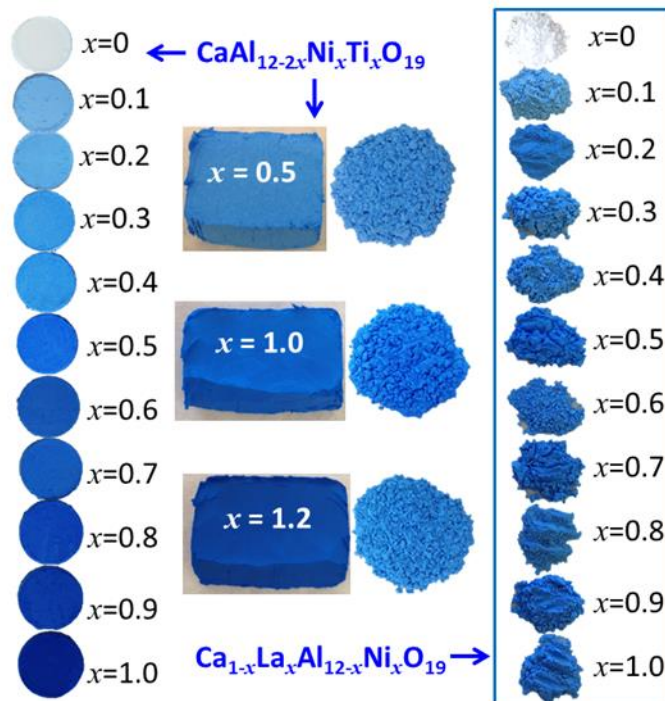


Figure 5.3 A series of color photographs of blue pellets and powders according to the following two solid solutions: (left)  $\text{CaAl}_{12-2x}\text{Ni}_x\text{Ti}_x\text{O}_{19}$  ( $x = 0-1.2$ ), and (right, inside box)  $\text{Ca}_{1-x}\text{La}_x\text{Al}_{12-x}\text{Ni}_x\text{O}_{19}$ .

X-ray diffraction patterns of these two solid solutions are shown in Figure 5.4.

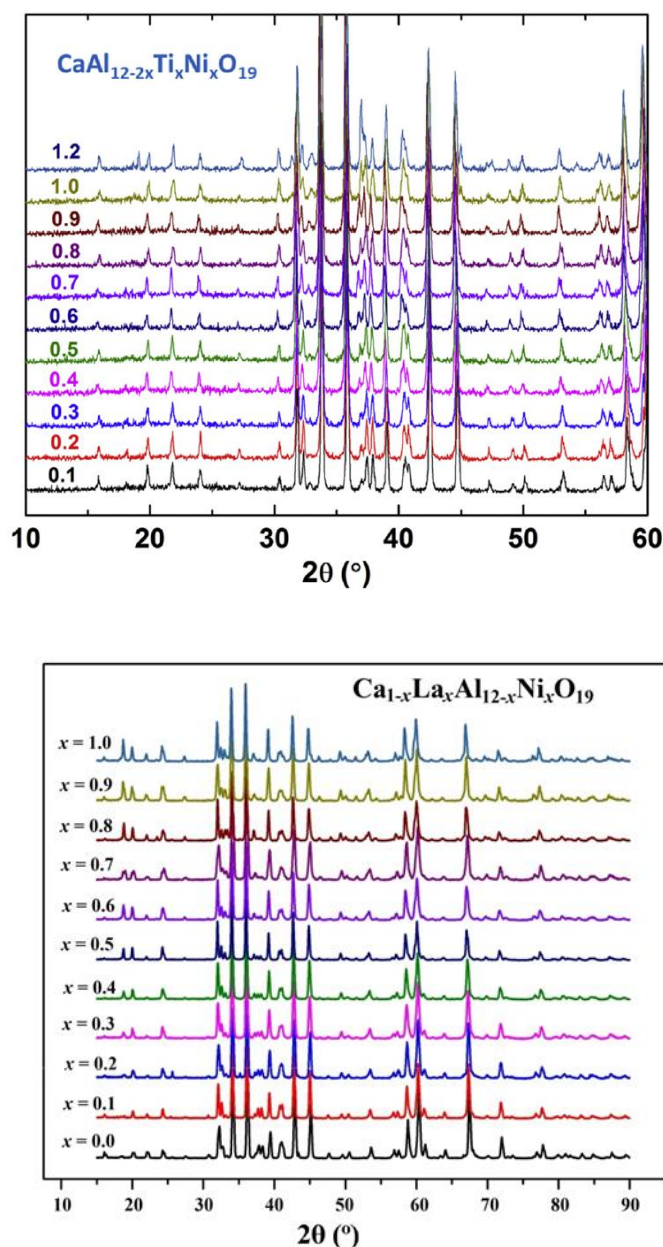
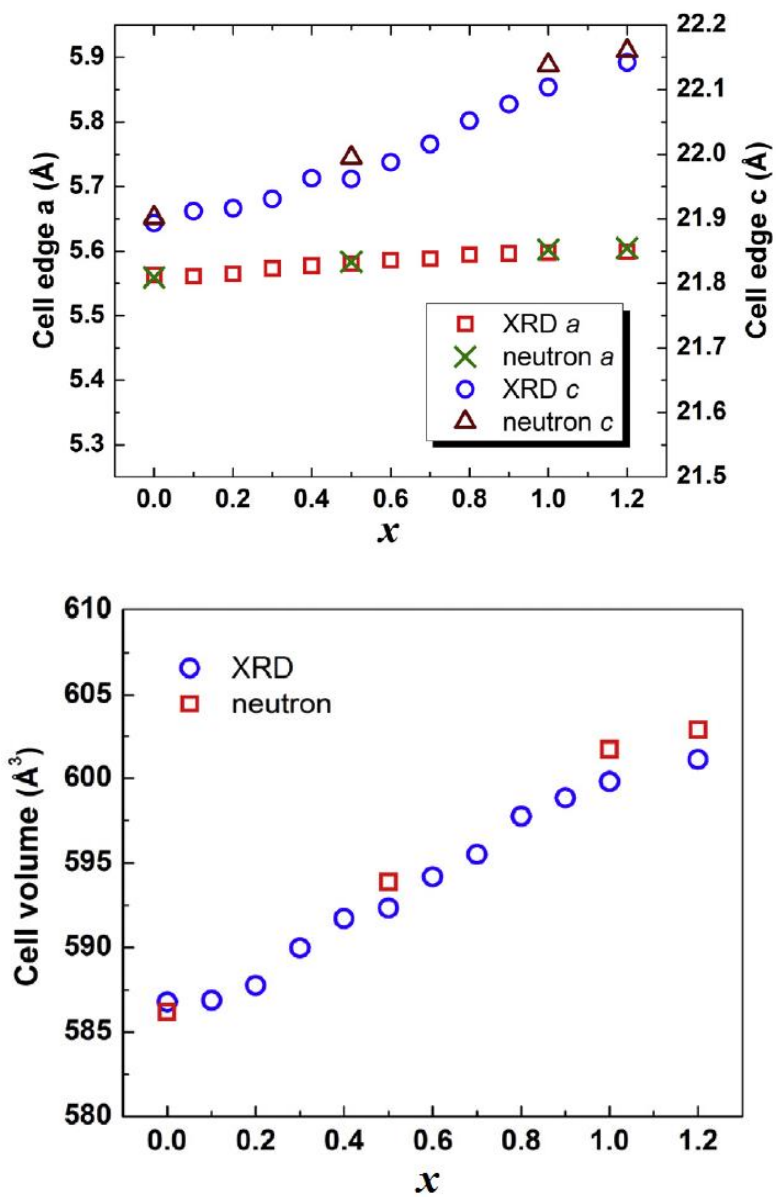


Figure 5.4 A series of X-ray powder diffraction patterns for the (top)  $\text{CaAl}_{12-2x}\text{Ti}_x\text{Ni}_x\text{O}_{19}$  ( $x = 0.2-1.2$ ), and (bottom)  $\text{Ca}_{1-x}\text{La}_x\text{Al}_{12-x}\text{Ni}_x\text{O}_{19}$  ( $x = 0-1$ ) solid solutions.

The lattice parameters are calculated by whole pattern fitting of XRD data as shown in Figures 5.5 and 5.6. The increase of cell edges  $a$ ,  $c$  and cell volume  $V$  is consistent with the substitution of small  $\text{Ca}^{2+}$  and  $\text{Al}^{3+}$  ions with larger  $\text{La}^{3+}$  and  $\text{Ni}^{2+}/\text{Ti}^{4+}$  ions. The lattice parameters from neutron Rietveld refinement are plotted for comparison, and the discrepancy between X-ray and neutron is simply sample related. The samples for neutron

experiment, darker in color, were heated for longer hours with more intermediate grindings, the relatively higher cell expansion shown by neutron samples hence indicating higher level of Ni and Ni/Ti incorporation than samples examined by XRD.



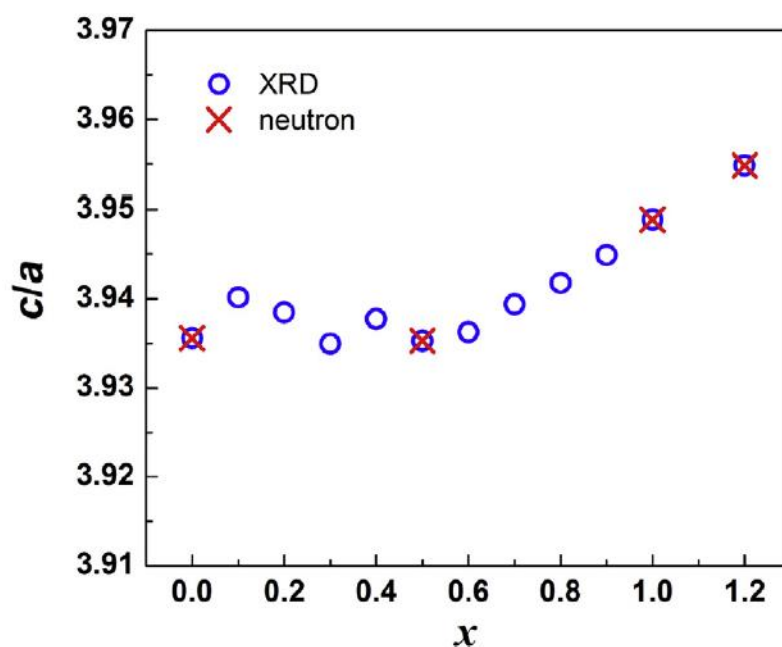
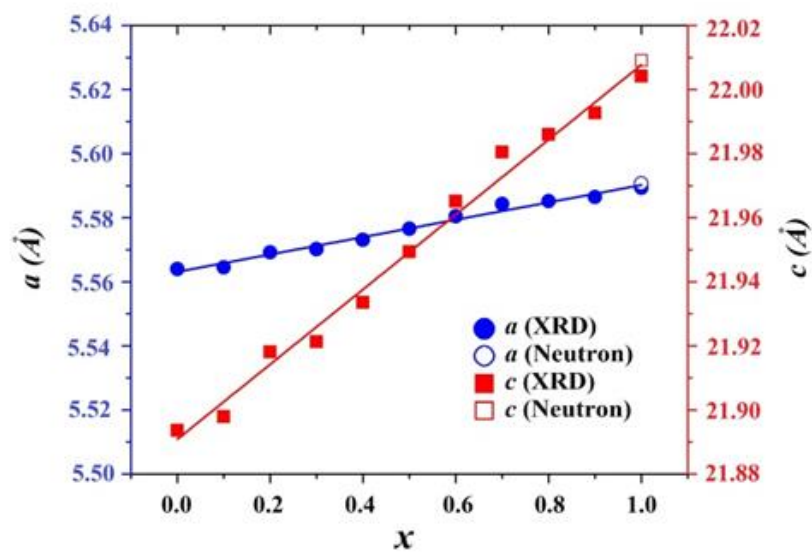


Figure 5.5 Cell edges of solid solution  $\text{CaAl}_{12-2x}\text{Ni}_x\text{Ti}_x\text{O}_{19}$  ( $x = 0-1.2$ ) refined by X-ray and neutron powder diffraction data. Estimated uncertainties are smaller than the plotted point size.



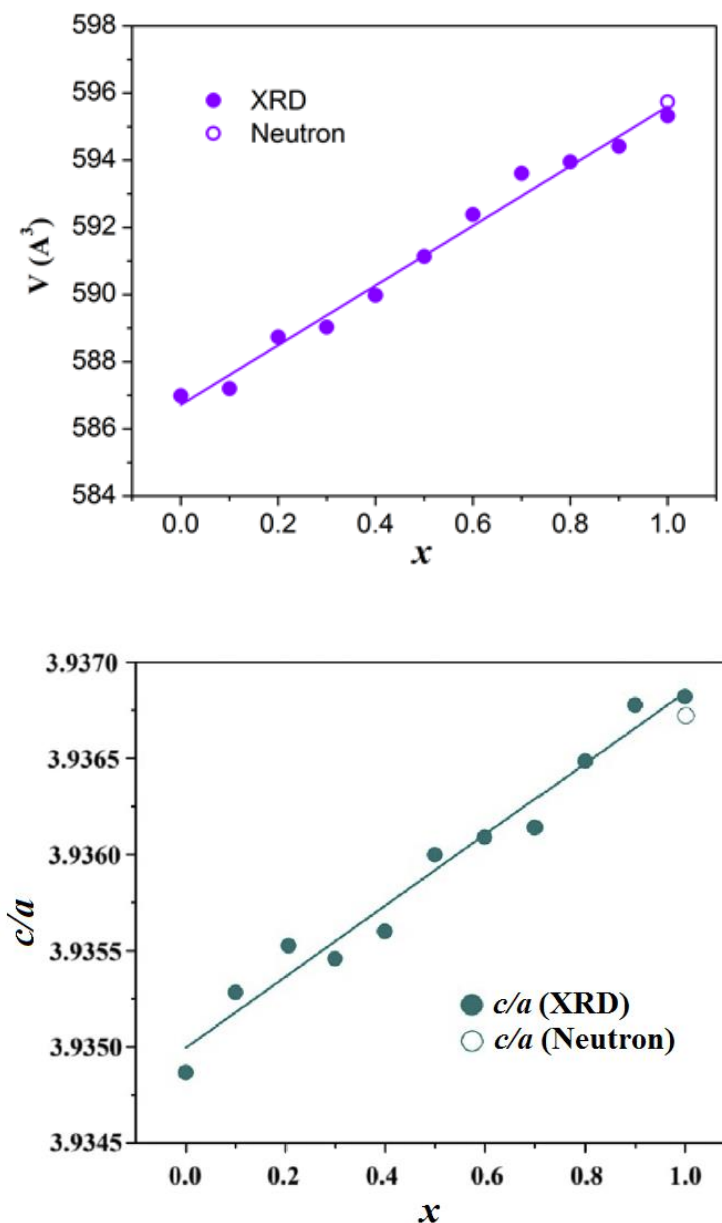


Figure 5.6 Cell edges of solid solution  $\text{Ca}_{1-x}\text{La}_x\text{Al}_{12-x}\text{Ni}_x\text{O}_{19}$  ( $x = 0-1$ ) refined by X-ray and neutron powder diffraction data. Estimated uncertainties are smaller than the plotted point size.

Cell edges of solid solutions  $\text{Ca}_{1-x}\text{RE}_x\text{Al}_{12-x}\text{Ni}_x\text{O}_{19}$  ( $\text{RE} = \text{La}, \text{Ce}, \text{Pr}, \text{Nd}, x = 0-1$ ) and  $\text{Sr}_{1-x}\text{La}_x\text{Al}_{12-x}\text{Ni}_x\text{O}_{19}$  ( $x = 0-1$ ) refined by XRD data are shown in Figure 5.7. The ionic radius of Sr is  $1.44 \text{ \AA}$  ( $\text{CN} = 12$ ), larger than that of La,  $1.36 \text{ \AA}$  ( $\text{CN} = 12$ ), and La is the largest among all the rare earth ions [64].



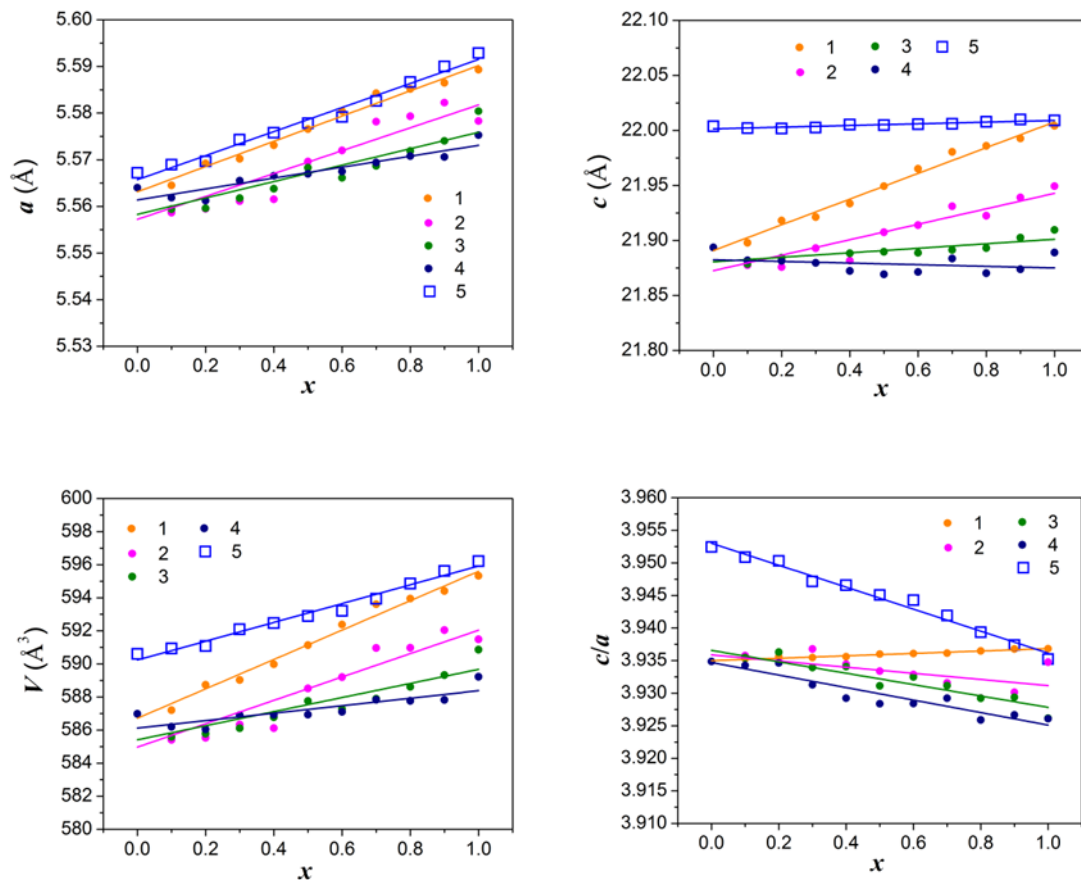


Figure 5.7 Cell edges of solid solutions  $\text{Ca}_{1-x}\text{RE}_x\text{Al}_{12-x}\text{Ni}_x\text{O}_{19}$  ( $x = 0-1$ ) and  $\text{Sr}_{1-x}\text{La}_x\text{Al}_{12-x}\text{Ni}_x\text{O}_{19}$  ( $x = 0-1$ ) refined by X-ray powder diffraction: 1. RE = La; 2. RE = Ce; 3. RE = Pr; 4. RE = Nd; 5.  $\text{Sr}_{1-x}\text{La}_x\text{Al}_{12-x}\text{Ni}_x\text{O}_{19}$  ( $x = 0-1$ ). Estimated uncertainties are smaller than the plotted point size.

This can explain why the cell edges of Sr and La containing samples are larger than the rest of the members in the Figure 5.7. In addition, the Sr-bearing samples exhibit the least change in  $c$ -axis with increasing level of coupled substitution (La and Ni), which could be attributed to the canceling effect of some contraction on A site and some expansion on M site. This effect however does not influence the change in cell edge  $a$ . Interestingly, the trend of  $c/a$  ratio decreases with substitution for all members in Figure 5.7 except for La, contrary to those in Figures 5.5 and 5.6, implying more rapid increase upon substitution along  $c$ -axis than  $a$ -axis for  $\text{CaAl}_{12-2x}\text{Ni}_x\text{Ti}_x\text{O}_{19}$  ( $x = 0-1$ ) and  $\text{Ca}_{1-x}\text{RE}_x\text{Al}_{12-x}\text{Ni}_x\text{O}_{19}$  (RE = La, Ce, Pr, Nd,  $x = 0-1$ ) series. The existence of  $\text{Ce}^{3+}$  is inferred by the observed trend of cell edges in Figure 5.7 since the ionic radius of  $\text{Ce}^{4+}$  is smaller

than those of the trivalent Pr and Nd ions [64]. The reduction of  $\text{Ce}^{4+}$  to  $\text{Ce}^{3+}$  most likely occurred during the formation of hibonite phases at high temperatures, and some  $\text{Ce}^{3+}$  might be oxidized again during sample cooling, leading to slightly varied  $\text{Ce}^{3+}/\text{Ce}^{4+}$  ratio from sample to sample and hence relatively scattered data points in the Ce series.

Although samples of  $\text{SrAl}_{12-2x}\text{Ni}_x\text{Ti}_x\text{O}_{19}$  are prepared nearly phase pure in the composition range of  $0 \leq x \leq 2$ , the color of the powder changes from light sky blue to turquoise above  $x = 1.0$ . Other rare earth containing samples  $\text{Ca}_{1-x}\text{RE}_x\text{Al}_{12-x}\text{Ni}_x\text{O}_{19}$  were only made phase pure up to  $x = 0.2$  under similar reaction conditions (Fig. 5.8). It is difficult to obtain pure hibonite phase when replacing Ca with Y, and it seems to work better with larger A ions like Sr.

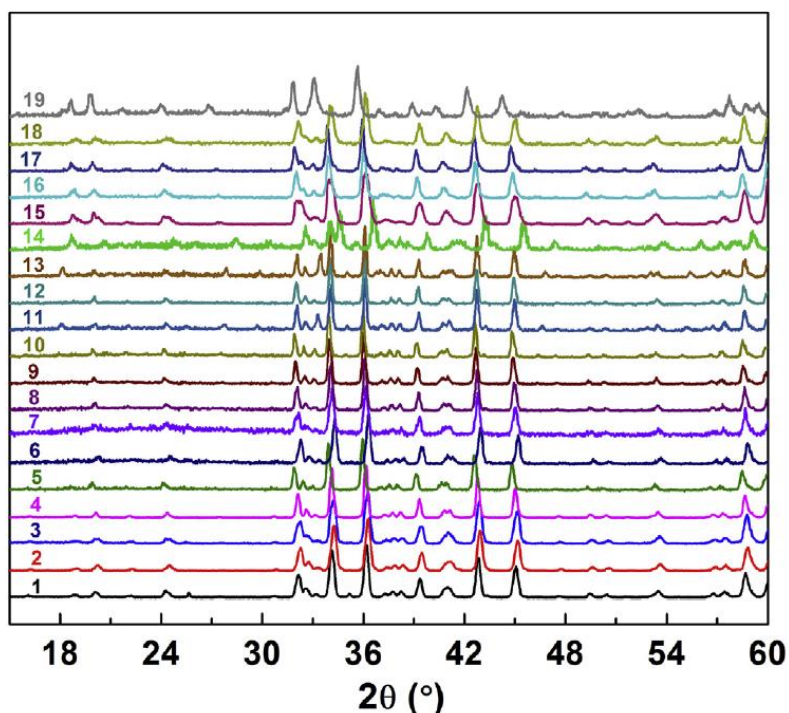


Figure 5.8 XRD patterns of  $A_{1-x}\text{RE}_x\text{Al}_{12-x}\text{Ni}_x\text{O}_{19}$  ( $x = 0.2$ ). From bottom to top: 1.  $A = \text{Ca}$ ,  $\text{RE} = \text{La}$ ; 2.  $A = \text{Ca}$ ,  $\text{RE} = \text{Ce}$ ; 3.  $A = \text{Ca}$ ,  $\text{RE} = \text{Pr}$ ; 4.  $A = \text{Ca}$ ,  $\text{RE} = \text{Nd}$ ; 5.  $A = \text{Ca}$ ,  $\text{RE} = \text{Sm}$ ; 6.  $A = \text{Ca}$ ,  $\text{RE} = \text{Eu}$ ; 7.  $A = \text{Ca}$ ,  $\text{RE} = \text{Gd}$ ; 8.  $A = \text{Ca}$ ,  $\text{RE} = \text{Tb}$ ; 9.  $A = \text{Ca}$ ,  $\text{RE} = \text{Dy}$ ; 10.  $A = \text{Ca}$ ,  $\text{RE} = \text{Ho}$ ; 11.  $A = \text{Ca}$ ,  $\text{RE} = \text{Er}$ ; 12.  $A = \text{Ca}$ ,  $\text{RE} = \text{Tm}$ ; 13.  $A = \text{Ca}$ ,  $\text{RE} = \text{Yb}$ ; 14.  $A = \text{Ca}$ ,  $\text{RE} = \text{Lu}$ ; 15.  $A = \text{Sr}$ ,  $\text{RE} = \text{La}$ ; 16.  $A = \text{Sr}$ ,  $\text{RE} = \text{Ce}$ ; 17.  $A = \text{Sr}$ ,  $\text{RE} = \text{Pr}$ ; 18.  $A = \text{Sr}$ ,  $\text{RE} = \text{Nd}$ ; 19.  $A = \text{Ba}$ ,  $\text{RE} = \text{La}$ .

The M-site substitution other than Ti produced single-phase products only up to  $y = 0.2$  or  $0.5$  for  $\text{CaAl}_{12-x-y}\text{Ni}_x\text{M}_y\text{O}_{19}$  ( $M = \text{Sn, Ge, Sb, Nb, Ta}$ ) (Fig. 5.9). The best blue color is given by Ge or Nb containing samples, and the presence of Na helps to enhance the blue color although the sample is not a single phase.

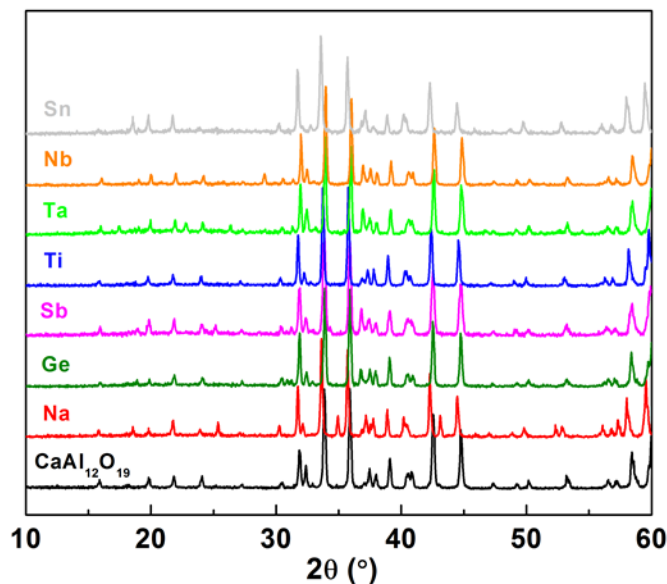


Figure 5.9 XRD patterns of  $\text{CaAl}_{12-x-y}\text{Ni}_x\text{M}_y\text{O}_{19}$  (For  $M = \text{Ti, Ge and Sn}$ ,  $x = 0.5$ ,  $y = 0.5$ ; For  $M = \text{Nb, Ta and Sb}$ ,  $x = 0.4$ ,  $y = 0.2$ ). The composition for Na is  $\text{Ca}_{0.5}\text{Na}_{0.5}\text{Al}_{10.5}\text{Ni}_{0.5}\text{TiO}_{19}$ .

To check the effect of  $\text{Ti}^{3+}$  on color, we prepared the  $\text{CaAl}_{11.8}\text{Ti}_{0.2}\text{O}_{19}$  sample at  $1450^\circ\text{C}$  in air followed by heating the white powder in  $5\%\text{H}_2/95\%\text{N}_2$  at  $900^\circ\text{C}$  for 5 h. The color of the powder changed to a very light turquoise blue after reduction. The resulting color would probably be more blue if the sample were treated under severe reducing conditions [28].

#### 5.4.2 Crystal Structures

The complex structure of hibonite  $\text{CaAl}_{12}\text{O}_{19}$  is shown in Figure 5.1. There are five different sites for Al: three have octahedral coordination (M1, M4, and M5), one has tetrahedral coordination (M3), and one site ideally has trigonal bipyramidal (TBP) coordination (M2). Early structural studies placed Al at the center of this TBP site, but recent studies have this Al displaced off this center along the  $c$ -axis, up and down in

disordered manner [11,16–18]. At high temperatures this TBP Al moves back and forth between the up and down positions. At low temperature this Al becomes trapped in one of the two positions. In addition to corner sharing of the various  $\text{AlO}_4$ ,  $\text{AlO}_5$  and  $\text{AlO}_6$  polyhedra, the two  $\text{AlO}_6$  octahedra at the M4 site share a common face and the  $\text{AlO}_6$  octahedra at the M5 site share edges to form a sheet perpendicular to the  $c$ -axis. Examination of the bond valence sums (BVS) for certain atoms indicates considerable mismatch when connecting these polyhedral [18,65]. Serious underbonding for Al occurs at the M2 (2.77) and M3 (2.68) sites as well as for two O sites (1.85 and 1.87). And at the M1 site there is significant overbonding of Al (3.23). The BVS at the A site for Ca is 1.49 but becomes normal (2.09) when Ca is replaced with Sr. These poor BVS values indicating a misfit of the polyhedra is one of the factors suggesting that  $\text{CaAl}_{12}\text{O}_{19}$  and some other oxides with the hibonite structure are entropy stabilized phases that are metastable at room temperature and below.

The TBP site in  $\text{CaAl}_{12}\text{O}_{19}$  has much longer Al–O apical distances (2.21 Å) than Al–O basal plane distances (1.755 Å). Moving this Al atom off the ideal site along the  $c$ -axis to a site with 4 equal “tetrahedral” Al–O distances has little impact on the low BVS value for Al, but it increases the BVS for the apical O from 2.02 to 2.44 [18]. Such overbonding of this O would explain the lower displacement of Al actually observed.

Another factor complicating the structures of oxides with the hibonite structure is defects related to stacking faults. The  $\beta$ -alumina structure has the same spinel type blocks that occur in hibonite. Intergrowth between the hibonite and the  $\beta$ -alumina structures has been observed and likely occurs to some extent in most hibonite compositions [54,66].

This chapter focuses on substitutions of  $\text{Ni}^{2+}$  for  $\text{Al}^{3+}$  in  $\text{CaAl}_{12}\text{O}_{19}$ . This substitution is charge compensated by a cosubstitution on the Ca site or the Al sites according to the formulas such as  $\text{Ca}_{1-x}\text{La}_x\text{Al}_{12-x}\text{Ni}_x\text{O}_{19}$  and  $\text{CaAl}_{12-2x}\text{Ni}_x\text{Ti}_x\text{O}_{19}$ . Structural analysis utilized Rietveld refinement of neutron diffraction data and the representative Rietveld fits are shown in Figure 5.10.

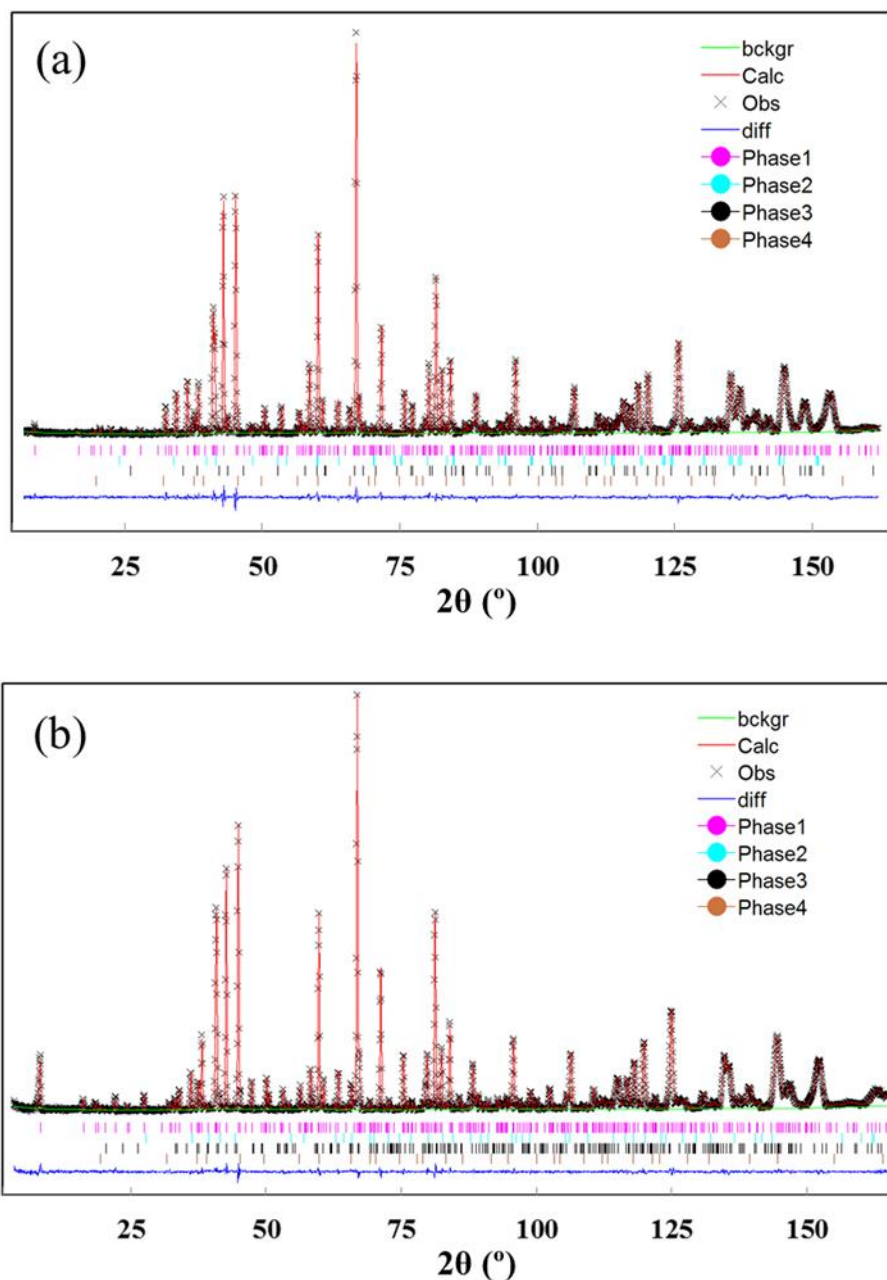


Figure 5.10 Neutron Rietveld fits of (a)  $\text{LaAl}_{11}\text{NiO}_{19}$  (Phase 1, ~95%). Impurity phases include: Phase 2,  $\text{LaAlO}_3$ ; Phase 3,  $\text{Al}_2\text{O}_3$ ; Phase 4,  $\text{NiAl}_2\text{O}_4$ . (b)  $\text{CaAl}_{10}\text{NiTiO}_{19}$  (Phase 1, ~98%). Impurity phases include: Phase 2 ( $\text{TiO}_2$ ), Phase 3 ( $\text{CaTiO}_3$ ), Phase 4 ( $\text{NiAl}_2\text{O}_4$ ).

Details of this procedure were previously given [18]. Results are summarized in Table 5.1. Relative to X-ray diffraction, neutron diffraction has much greater sensitivity to Ni and Ti substitution for Al due to the scattering lengths of 10.3 fm for Ni and -3.438 fm for Ti vs 3.449 fm for Al. Also, the negative value for Ti vs the very high positive value for

Ni is of great value in separating the contributions of Ni and Ti. Furthermore, the relative scattering power of O is much greater when using neutrons, and this leads to more accurate bond distances.

Table 5.1 Rietveld refinement results of neutron powder diffraction.<sup>a</sup>

Composition	La <sub>0.5</sub> Ca <sub>0.5</sub> Al <sub>11.5</sub> Ni <sub>0.5</sub> O <sub>19</sub>	LaAl <sub>11</sub> NiO <sub>19</sub>	CaAl <sub>11</sub> Ti <sub>0.5</sub> Ni <sub>0.5</sub> O <sub>19</sub>	CaAl <sub>10</sub> TiNiO <sub>19</sub>	CaAl <sub>9.6</sub> Ti <sub>1.2</sub> Ni <sub>1.2</sub> O <sub>19</sub>
$\chi^2$	2.00	1.32	1.67	1.23	1.94
R <sub>wp</sub> (%)	5.25	4.10	4.68	3.85	4.92
R <sub>p</sub> (%)	4.06	3.34	3.86	3.12	3.84
$a = b$ (Å)	5.5750(1)	5.5906(1)	5.5837(1)	5.6024(2)	5.6049(2)
$c$ (Å)	21.952(1)	22.009(1)	21.995(1)	22.138(2)	22.160(2)
$V$ (Å <sup>3</sup> )	590.87(1)	595.73(1)	593.87(1)	601.73(1)	602.88(1)
Al2, $z$	0.2390(4)	0.2399(2)	0.2608(2)	0.2643(2)	0.2656(3)
Al3, $z$	0.0284(2)	0.0273(1)	0.0280(1)	0.0273(1)	0.0271(1)
Al4, $z$	0.1904(2)	0.1894(1)	0.1900(2)	0.1889(7)	0.1870(8)
Al5, $x$	0.1670(4)	0.1673(2)	0.1672(2)	0.1676(2)	0.1677(3)
Al5, $z$	0.8917(1)	0.8921(1)	0.8919(1)	0.8930(1)	0.8931(1)
A, <sup>b</sup> $U_{\text{iso}}$ (Å <sup>2</sup> )	0.0096(8)	0.0092(4)	0.022(1)	0.029(2)	0.026(2)
Al1, $U_{\text{iso}}$ (Å <sup>2</sup> )	0.007(2)	0.002(1)	0.005(1)	0.005(1)	0.005(1)
Al2, $U_{\text{iso}}$ (Å <sup>2</sup> )	0.008(5)	0.003(1)	0.003(2)	0.004(3)	0.004(3)
Al3, $U_{\text{iso}}$ (Å <sup>2</sup> )	0.0059(8)	0.0042(5)	0.0038(5)	0.0041(4)	0.0065(6)
Al4, $U_{\text{iso}}$ (Å <sup>2</sup> )	0.008(2)	0.003(1)	0.002(1)	0.003(2)	0.007(6)
Al5, $U_{\text{iso}}$ (Å <sup>2</sup> )	0.0031(6)	0.0054(4)	0.0041(4)	0.0049(3)	0.0060(4)
Ni(Al1) Occ. <sup>c</sup>	0.026(9)	0.053(9)	0.028(7)	0.049(8)	0.050(8)
Ti(Al2) Occ.	-	-	0.056(3)	0.064(3)	0.067(3)
Ni(Al2) Occ.	0.023(7)	0.015(5)	0.010(3)	0.012(3)	0.020(3)
Ni(Al3) Occ.	0.188(8)	0.283(7)	0.180(5)	0.234(5)	0.245(5)
Ti(Al4) Occ.	-	-	0.191(6)	0.408(6)	0.445(6)
Ni(Al4) Occ.	0.016(8)	0.010(8)	0.0	0	0
Ni(Al5) Occ.	0.005(4)	0.053(5)	0.016(3)	0.065(3)	0.075(4)
La(Ca) Occ.	0.492(26)	1	-	-	-
Refined FOR. <sup>d</sup>	La <sub>0.49</sub> Ca <sub>0.51</sub> Al <sub>11.49</sub> Ni <sub>0.51</sub> O <sub>19</sub>	LaAl <sub>11.01</sub> Ni <sub>0.99</sub> O <sub>19</sub>	CaAl <sub>11.01</sub> Ti <sub>0.49</sub> Ni <sub>0.50</sub> O <sub>19</sub>	CaAl <sub>10.13</sub> Ti <sub>0.94</sub> Ni <sub>0.93</sub> O <sub>19</sub>	CaAl <sub>9.95</sub> Ti <sub>1.02</sub> Ni <sub>1.03</sub> O <sub>19</sub>
A–O3 $\times$ 6, Å	2.7914(1)	2.7990(1)	2.7952(1)	2.8042(1)	2.8055(1)
A–O5 $\times$ 6, Å	2.689(2)	2.674(1)	2.708(1)	2.725(1)	2.728(2)
Al1–O4 $\times$ 6, Å	1.886(2)	1.895(1)	1.883(1)	1.892(1)	1.894(1)
Al2–O1, Å	2.444(9)	2.417(5)	2.443(6)	2.552(5)	2.576(8)
Al2–O1, Å	1.960(8)	1.974(5)	1.969(6)	1.918(5)	1.895(8)
Al2–O3 $\times$ 3, Å	1.774(3)	1.771(2)	1.765(2)	1.777(2)	1.783(3)
Al3–O2, Å	1.862(4)	1.866(3)	1.854(3)	1.860(3)	1.855(4)
Al3–O4 $\times$ 3, Å	1.807(2)	1.828(1)	1.815(1)	1.824(1)	1.823(2)
Al4–O3 $\times$ 3, Å	1.961(4)	1.986(2)	1.978(3)	2.009(8)	2.039(2)
Al4–O5 $\times$ 3, Å	1.869(3)	1.863(2)	1.874(2)	1.868(7)	1.851(2)

Al5–O1, Å	1.851(4)	1.870(2)	1.858(2)	1.874(2)	1.878(3)
Al5–O2, Å	1.969(4)	1.953(2)	1.970(2)	1.956(2)	1.955(3)
Al5–O4 × 2, Å	1.978(2)	1.971(1)	1.982(1)	1.979(1)	1.981(2)
Al5–O5 × 2, Å	1.838(2)	1.853(2)	1.835(1)	1.854(1)	1.855(2)
Al2–Al2, <sup>e</sup> Å	0.48(2)	0.44(1)	0.47(1)	0.63(1)	0.68(1)
Al4–Al4, <sup>f</sup> Å	2.62(1)	2.67(2)	2.64(2)	2.71(3)	2.79(2)
A, BVS <sup>g</sup>	-	2.65	1.45	1.40	1.39
Hibonite phase <sup>h</sup>	97%	95%	99%	98%	98%

Notes: (a) All refined in space group  $P6_3/mmc$ . Ca at 2d (1/3, 2/3, 3/4), Al1 at 2a (0, 0, 0), Al2 and O1 at 4e (0, 0, z), Al3, Al4 and O2 at 4f (1/3, 2/3, z), Al5, O4 and O5 at 12k (x, 2x, z), O3 at 6h (x, 2x, 1/4). Octahedral sites: Al1, Al4 and Al5; TBP site: Al2; tetrahedral site: Al3. (b) A = La, Ca. Atomic displacement parameters are constrained to be the same for atoms at the same site. (c) Ni(Al1) means Ni at the site of Al1 and so forth. Occ. stands for site occupancy. (d) Refined formulas, as opposed to nominal compositions. (e) Distances between two split sites of TBP Al2. (f) Distances between two adjacent Al4 sites in face-sharing  $\text{AlO}_6$  octahedra. (g) BVS stands for bond valence sum [61]. (h) Impurity phases for La-containing samples are:  $\text{Al}_2\text{O}_3$ ,  $\text{LaAlO}_3$ ,  $\text{NiAl}_2\text{O}_4$ ; for Ti-containing phases are:  $\text{TiO}_2$ ,  $\text{CaTiO}_3$ ,  $\text{NiAl}_2\text{O}_4$ .

The analysis of  $\text{Ca}_{1-x}\text{La}_x\text{Al}_{12-x}\text{Ni}_x\text{O}_{19}$  phases with  $x = 0.5$  and  $1.0$  shows that 57–75% of the  $\text{Ni}^{2+}$  substituted enters the tetrahedral site (M3). The remainder of the  $\text{Ni}^{2+}$  is distributed over the M1, M2, and M5 sites. A statistically significant amount of Ni is not found at the M4 site. The expected increase in M3–O distances with  $x$  is observed. The refined formulas of  $\text{La}_{0.49}\text{Ca}_{0.51}\text{Al}_{11.49}\text{Ni}_{0.51}\text{O}_{19}$  and  $\text{LaAl}_{11.01}\text{Ni}_{0.99}\text{O}_{19}$  agree well with the intended compositions. A previous study of  $\text{LaAl}_{11}\text{NiO}_{19}$  using powder X-ray diffraction reported Ni only on the tetrahedral site (M4) [41].

Structural analysis of  $\text{CaAl}_{12-2x}\text{Ni}_x\text{Ti}_x\text{O}_{19}$  phases is much more challenging. When using X-ray diffraction, both Ni and Ti have stronger scattering powers than Al. Thus if the scattering power increases at a given M site, there is no way that this increase can be attributed to just Ni or Ti because either could cause this increase. The situation is dramatically more favorable when using neutron diffraction because the scattering lengths of all atoms present are positive with the exception of Ti, which has a negative scattering length. Thus, for  $\text{CaAl}_{12-2x}\text{Ni}_x\text{Ti}_x\text{O}_{19}$  phases if the scattering power of a given M site decreases, this must be due to Ti substitution. If there is an increase in scattering power at a site, there must be Ni substitution at that site. There is still a complication when both Ti

and Ni enter the same site, but this complication can be resolved by utilizing the results found for  $\text{Ca}_{1-x}\text{La}_x\text{Al}_{12-x}\text{Ni}_x\text{O}_{19}$  phases where Ti is not present.

Our refinements indicate that the maximum value of  $x$  for  $\text{CaAl}_{12-2x}\text{Ni}_x\text{Ti}_x\text{O}_{19}$  phases is close to 1.0 for samples prepared under our conditions [18]. Tables 5.1 and 5.2 summarize our results for samples with nominal  $x$  values of 0.5, 1.0, and 1.2. We find for  $\text{CaAl}_{12-2x}\text{Ni}_x\text{Ti}_x\text{O}_{19}$  phases that the scattering power at the tetrahedral site (M3) increases rapidly with  $x$ . This indicates Ni on this site, which was anticipated based on our results for the  $\text{Ca}_{1-x}\text{La}_x\text{Al}_{12-x}\text{Ni}_x\text{O}_{19}$  phases. For the  $\text{CaAl}_{12-2x}\text{Ni}_x\text{Ti}_x\text{O}_{19}$  phases we found a large decrease in scattering power for the site with face-sharing octahedra, and this must be due to Ti entering this site (M4). Small amounts of Ni enter both the M1 and M5 sites. The amount of Ni on the M5 site is much greater than that on the M1 site simply because the multiplicity of the M5 site is six times greater than that of the M1 site. Our results for  $\text{Ca}_{1-x}\text{La}_x\text{Al}_{12-x}\text{Ni}_x\text{O}_{19}$  samples with  $x = 0.5$  and 1.0 indicate statistically insignificant amount of Ni on the M4 site, and this is apparently also true for  $\text{CaAl}_{12-2x}\text{Ni}_x\text{Ti}_x\text{O}_{19}$  phases.

Table 5.2 Average bond distances ( $\text{\AA}$ ) from neutron refinements.

Refined composition	A–O	M1–O	M2–O	M3–O	M4–O	M5–O	M4–M4	M2dis <sup>a</sup>
$\text{La}_{0.49}\text{Ca}_{0.51}\text{Al}_{11.49}\text{Ni}_{0.51}\text{O}_{19}$	2.740	1.886	1.945	1.821	1.915	1.909	2.62	0.242(16)
$\text{LaAl}_{11.01}\text{Ni}_{0.99}\text{O}_{19}$	2.737	1.895	1.941	1.838	1.925	1.912	2.67	0.221(10)
$\text{CaAl}_{12}\text{O}_{19}$	2.745	1.879	1.934	1.804	1.916	1.906	2.595	0.185(11)
$\text{CaAl}_{11.04}\text{Ti}_{0.48}\text{Ni}_{0.49}\text{O}_{19}$	2.752	1.883	1.941	1.825	1.926	1.910	2.64	0.237(11)
$\text{CaAl}_{10.14}\text{Ti}_{0.95}\text{Ni}_{0.93}\text{O}_{19}$	2.765	1.892	1.960	1.833	1.939	1.916	2.71	0.315(10)
$\text{CaAl}_{9.95}\text{Ti}_{1.02}\text{Ni}_{1.03}\text{O}_{19}$	2.767	1.894	1.964	1.831	1.945	1.918	2.79	0.341(14)

<sup>a</sup>Displacement of M2 from the ideal TBP site in  $\text{\AA}$ .

An X-ray diffraction study on  $\text{Ca}_{1-x}\text{La}_x\text{Al}_{12-x}\text{Ni}_x\text{O}_{19}$  phases also concluded that Ni went mainly to the M3 site and that Ti went mainly to the M4 site [47]. However, the site occupancies were inferred, not actually refined. The occupancies of Ni and Ti given often do not agree well with our findings using neutron diffraction. This X-ray diffraction study did not detect the presence of Ni on the M1 and M5 sites, which we show is readily detected using neutron diffraction.



The M1–O distance and the average of M5–O distances increase by about 0.01 Å with Ni substitution, consistent with significant amount of Ni<sup>2+</sup> substitution on the M1 and M5 sites. The average M3–O distances increase by about 0.03 Å due to the much greater Ni substitution at the M3 site. This distance increase would be even greater if it were not for the fact that this site has larger M3–O distances than expected when this site is occupied by Al only. The average M4–O distance also increases by about 0.03 Å as Ti<sup>4+</sup> enters the M4 site. Although Ti<sup>4+</sup> is larger than Al<sup>3+</sup>, this increase in average distance is in part due to an increase in the difference between the two different M4–O distances. This difference is 0.10 Å in CaAl<sub>12</sub>O<sub>19</sub> and increases to 0.19 Å with the Ni/Ti substitution. The smaller M4–O distance actually decreases by 0.02 Å as the average M4–O distance increases by 0.03 Å (Table 5.1). Average distances are expected to increase as the individual distances of a polyhedron become more scattered. The M4–M4 distance increases from 2.60 to 2.79 Å as Ti enters this site. This can be considered as consequence of the increased cation-cation repulsion as a 4+ cation enters this site with face-shared octahedra. The three short M2–O distances related to the triangle of the TBP unit increase from 1.755 to 1.783 Å with the substitution on the M2 site, which is mostly Ti. At the same time the short apical M2–O distance decreases from 2.027 to 1.895 Å. Thus, this TBP site becomes more tetrahedral like.

The distribution of Ni and Ti over the five M sites is far from random with factors other than coordination number playing important roles. Studies of NiAl<sub>2</sub>O<sub>4</sub> with the spinel structure indicate a preference of Ni<sup>2+</sup> for the octahedral sites [67], which would be expected based on the crystal field stabilization of Ni<sup>2+</sup> vs Al<sup>3+</sup> [64]. Disorder with increasing temperature moves much of the Ni to the tetrahedral sites [67]. The preference of Ni<sup>2+</sup> for the tetrahedral M3 site in CaAl<sub>12</sub>O<sub>19</sub> can be attributed to the longer than normal Al–O distances at the M3 site. These long distances cause displacement factors to be high for this site (Table 5.1). The actual displacements are anharmonic, as we have previously shown, because an ellipsoid is not compatible with a tetrahedral site [18]. Small amounts of Ni substitute on all the M1, M2, and M5 sites as expected from our results on Ca<sub>1-x</sub>La<sub>x</sub>Al<sub>12-x</sub>Ni<sub>x</sub>O<sub>19</sub> phases. Substitution of Ti for Al on the tetrahedral site is not expected

because this coordination for Ti is very rare in oxides. Substitution of Ti on the M1 site is unfavorable because Al at this site is significantly overbonded, and the addition of Ti to this site would further aggravate this situation. The location of  $\text{Ti}^{4+}$  is very much influenced by the M–M repulsive interaction that occurs whenever octahedra share faces or edges. Since this M–M distance tends to be shorter for face sharing than for edge sharing, one might expect that Ti would favor the M5 site over the M4 site. But the opposite occurs. There are two reasons for this preference of Ti. Each octahedron based on M5 shares four of its edges with other M5 octahedra, but the M4 based octahedra share only one face. Secondly, the M4–M4 distance is not constrained and can readily expand as Al is replaced by Ti. In fact, this M4–M4 distance across the face expands so much as Ti enters that it becomes essentially the same as the M5–M5 shared edge distance. Thus, the repulsive M–M interaction on the M5 site is about four times stronger than for the M4 site. Therefore, the M4 site is very strongly preferred over the M5 site for  $\text{Ti}^{4+}$ . TBP coordination is well established for  $\text{Ti}^{4+}$  in compounds such as  $\text{YCu}_{0.5}\text{Ti}_{0.5}\text{O}_3$  [68]. Thus, substitution of  $\text{Ti}^{4+}$  into the M2 where there is no M–M interaction can be expected.

The repulsive M4–M4 interaction in the face-shared octahedra causes an overall expansion of the  $\text{O3-M4-O3-M4-O3}$  face-share unit along the  $c$ -axis. Thus, the expansion along the  $c$ -axis is more pronounced in the  $\text{CaAl}_{12-2x}\text{Ni}_x\text{Ti}_x\text{O}_{19}$  series than in the  $\text{Ca}_{1-x}\text{La}_x\text{Al}_{12-x}\text{Ni}_x\text{O}_{19}$  series where no Ti is present (Table 5.1). The  $a$ -axis expansion is also slightly greater in the  $\text{CaAl}_{12-2x}\text{Ni}_x\text{Ti}_x\text{O}_{19}$  series than the  $\text{Ca}_{1-x}\text{La}_x\text{Al}_{12-x}\text{Ni}_x\text{O}_{19}$  series. This can be attributed to the greater concentration of Ni in the M5 site in the  $\text{CaAl}_{12-2x}\text{Ni}_x\text{Ti}_x\text{O}_{19}$  series. The layer associated with M5 cations is under tension, which causes any expansion to be mainly perpendicular to the  $c$ -axis. In the case of  $\text{Ca}_{1-x}\text{La}_x\text{Al}_{12-x}\text{Ni}_x\text{O}_{19}$  series, the large A site where Ca ions locate may provide extra room to accommodate the change upon La substitution and result in an expansion along  $a$ -axis that is smaller than expected.

#### 5.4.3 Optical Properties

The optical spectra of blue hibonite samples are shown in Figure 5.11 for the solid solutions  $\text{CaAl}_{12-2x}\text{Ni}_x\text{Ti}_x\text{O}_{19}$  ( $x = 0-1.2$ ) and  $\text{Ca}_{1-x}\text{La}_x\text{Al}_{12-x}\text{Ni}_x\text{O}_{19}$  ( $x = 0-1$ ). Unlike white  $\text{CaAl}_{12}\text{O}_{19}$  ( $x = 0$ ) powders that exhibit negligible absorption across the entire visible range,

strong absorption centered around 600 nm, in the orange region of the visible spectrum, is detected for all Ni-containing samples. This intense absorption is actually a collection of four peaks arising from d-d transitions of  $\text{Ni}^{2+}$  in tetrahedral coordination. Two of these peaks are spin-allowed. The two weaker peaks are unusually intense considering that they are spin-forbidden [44,47]. The weak peak at  $\sim 710$  nm has been attributed to  $\text{Ni}^{2+}$  in octahedral coordination [47].

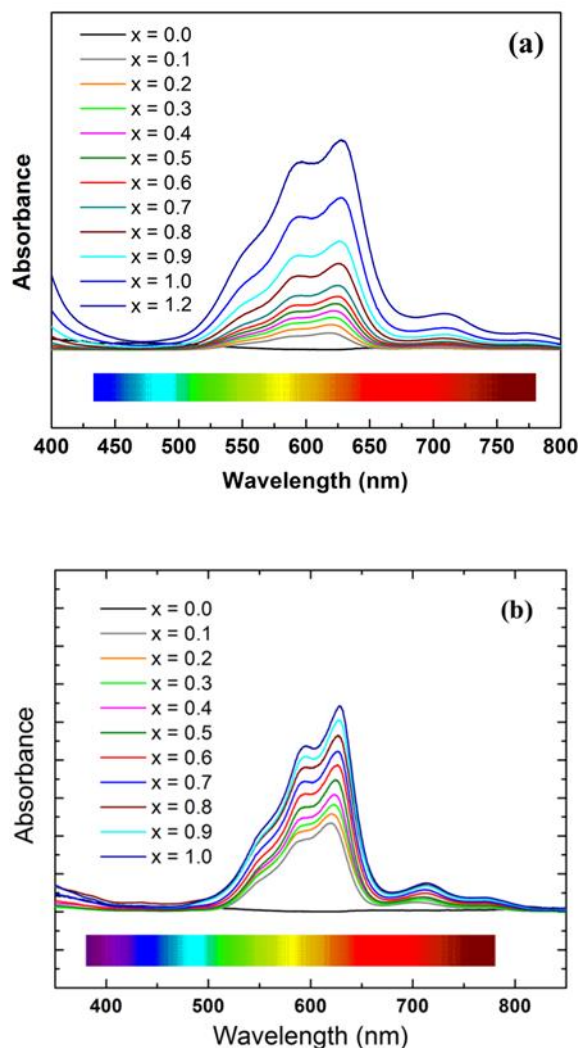
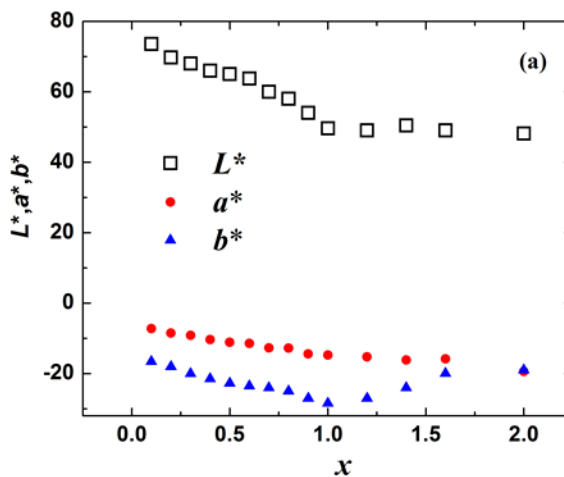


Figure 5.11 Diffuse reflectance spectra of solid solutions (a)  $\text{CaAl}_{12-2x}\text{Ni}_x\text{Ti}_x\text{O}_{19}$  ( $x = 0-1.2$ ) and (b)  $\text{Ca}_{1-x}\text{La}_x\text{Al}_{12-x}\text{Ni}_x\text{O}_{19}$  ( $x = 0-1$ ).

In the case of  $\text{CaAl}_{12-2x}\text{Ni}_x\text{Ti}_x\text{O}_{19}$  (Fig. 5.11(a)), a peak arising from an O-to-Ti charge transfer tails into the visible region, but is too weak to have a significant impact on color.

There is also a small increase in absorption with increasing  $x$  in the low energy region tailing into the infrared range. This feature could be expected if a small amount of the Ti were present as  $\text{Ti}^{3+}$ . These small increases in absorption in the high and low energy regions of the visible spectrum do not occur in the  $\text{Ca}_{1-x}\text{La}_x\text{Al}_{12-x}\text{Ni}_x\text{O}_{19}$  series (Fig. 5.11(b)) because no Ti is present. In both series, the absence of absorption in the 500–430 nm (blue) region of the spectrum is responsible for the observed blue color.

Different shades of color are barely distinguishable when they are visually similar. The subtle alteration in color, however, can be differentiated and quantified using CIE  $L^*a^*b^*$  color space through the hue (color), the chroma (vividness/dull-ness) and the brightness. A unique color can be described precisely by 3-dimensional color coordinates  $L^*$ ,  $a^*$  and  $b^*$ . The vertical axis  $L^*$  gives the brightness from 0 (black) to 100 (white). The value of  $a^*$  shows colors from green to red (- to +) and  $b^*$  from blue to yellow (- to +) with neutral gray values at  $a^* = 0$  and  $b^* = 0$ . Measured chromatic coordinates of two representative solid solutions  $\text{CaAl}_{12-2x}\text{Ni}_x\text{Ti}_x\text{O}_{19}$  ( $x = 0-2$ ) and  $\text{Ca}_{1-x}\text{La}_x\text{Al}_{12-x}\text{Ni}_x\text{O}_{19}$  ( $x = 0-1$ ) are illustrated in Figure 5.12, and those of selected powder samples are given in Table 5.3.



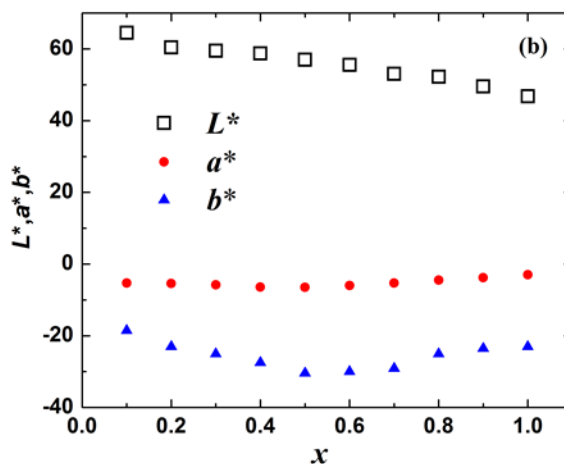


Figure 5.12 The CIE  $L^*a^*b^*$  color coordinates for solid solutions (a)  $\text{CaAl}_{12-2x}\text{Ni}_x\text{Ti}_x\text{O}_{19}$  ( $x = 0-1.2$ ) and (b)  $\text{Ca}_{1-x}\text{La}_x\text{Al}_{12-x}\text{Ni}_x\text{O}_{19}$  ( $x = 0-1$ ). Estimated uncertainties are smaller than the plotted point size.

The blue color of all our samples is clearly indicated by the negative  $b^*$  values range from -16.78 to -30.38. Notice the compositions of  $\text{CaAl}_{12-2x}\text{Ni}_x\text{Ti}_x\text{O}_{19}$  in the range  $x = 1-2$  are not phase pure, and the increasing amount of impurity is accompanied by an undesirable color change from royal blue to dark turquoise. For sake of comparison, the  $L^*$ ,  $a^*$  and  $b^*$  values of commercial Co-blue,  $\text{NiAl}_2\text{O}_4$  spinel and one of our Co-bearing samples are also listed in Table 5.3.

Table 5.3  $L^*$ ,  $a^*$ ,  $b^*$  values of selected hibonite samples with blue colors.

Compositions	$L^*$	$a^*$	$b^*$
$\text{Ca}_{0.5}\text{La}_{0.5}\text{Al}_{11.5}\text{Ni}_{0.5}\text{O}_{19}$	57	-6.5	-30.38
$\text{LaAl}_{11}\text{NiO}_{19}$	46.8	-3	-23
$\text{CaAl}_{11}\text{Ti}_{0.5}\text{Ni}_{0.5}\text{O}_{19}$	65.47	-11.1	-22.76
$\text{CaAl}_{10}\text{TiNiO}_{19}$	49.59	-14.72	-28.44
$\text{SrAl}_{11}\text{Ti}_{0.5}\text{Ni}_{0.5}\text{O}_{19}$	66.07	-10.39	-21.17
$\text{SrAl}_{10}\text{TiNiO}_{19}$	65.12	-11.46	-18.53
$\text{SrAl}_{9.6}\text{Ti}_{1.2}\text{Ni}_{1.2}\text{O}_{19}$	62.94	-12.12	-17.86
$\text{SrAl}_8\text{Ti}_2\text{Ni}_2\text{O}_{19}$	52.31	-17.99	-10.34
$\text{Ca}_{0.5}\text{Ce}_{0.5}\text{Al}_{11.5}\text{Ni}_{0.5}\text{O}_{19}$	57.35	-12.37	-27.43
$\text{Ca}_{0.5}\text{Pr}_{0.5}\text{Al}_{11.5}\text{Ni}_{0.5}\text{O}_{19}$	58.59	-13.03	-22.7
$\text{Ca}_{0.5}\text{Nd}_{0.5}\text{Al}_{11.5}\text{Ni}_{0.5}\text{O}_{19}$	59.87	-12.15	-24.46

La <sub>0.5</sub> Sr <sub>0.5</sub> Al <sub>11.5</sub> Ni <sub>0.5</sub> O <sub>19</sub>	63.51	-10.98	-23.48
CaAl <sub>11</sub> Sn <sub>0.5</sub> Ni <sub>0.5</sub> O <sub>19</sub>	67.51	-9.68	-20.26
CaAl <sub>11</sub> Ge <sub>0.5</sub> Ni <sub>0.5</sub> O <sub>19</sub>	55.19	-13.77	-22.54
CaAl <sub>11.4</sub> Nd <sub>0.2</sub> Ni <sub>0.4</sub> O <sub>19</sub>	57.59	-13.63	-26.83
CaAl <sub>11.4</sub> Sb <sub>0.2</sub> Ni <sub>0.4</sub> O <sub>19</sub>	67.23	-10.49	-18.72
CaAl <sub>11.4</sub> Ta <sub>0.2</sub> Ni <sub>0.4</sub> O <sub>19</sub>	64.83	-12.02	-19.27
Ca <sub>0.5</sub> La <sub>0.5</sub> Al <sub>11</sub> Ga <sub>0.5</sub> Ni <sub>0.5</sub> O <sub>19</sub>	66.28	-10.46	-18.73
Ca <sub>0.5</sub> La <sub>0.5</sub> Al <sub>11</sub> In <sub>0.5</sub> Ni <sub>0.5</sub> O <sub>19</sub>	58.81	-11.73	-26.96
CaAl <sub>10</sub> TiNi <sub>0.5</sub> Zn <sub>0.5</sub> O <sub>19</sub>	54.46	-13.4	-16.78
Ca <sub>0.5</sub> Na <sub>0.5</sub> Al <sub>10.5</sub> TiNi <sub>0.5</sub> O <sub>19</sub>	54.85	-15.91	-24.97
Ca <sub>0.4</sub> Sr <sub>0.6</sub> Al <sub>10.8</sub> Ti <sub>0.6</sub> Ni <sub>0.6</sub> O <sub>19</sub>	66.42	-10.89	-19.85
Ca <sub>0.5</sub> Sr <sub>0.5</sub> Al <sub>10</sub> TiNiO <sub>19</sub>	50.73	-14.17	-25.93
Ca <sub>0.75</sub> La <sub>0.25</sub> Al <sub>11.25</sub> Ti <sub>0.25</sub> Ni <sub>0.5</sub> O <sub>19</sub>	66.69	-11.12	-19.72
Ca <sub>0.5</sub> La <sub>0.5</sub> Al <sub>11</sub> Ti <sub>0.25</sub> Ni <sub>0.75</sub> O <sub>19</sub>	56.22	-10.66	-26.83
CaAl <sub>11.8</sub> Co <sub>0.2</sub> O <sub>19</sub>	64.17	-4.66	-20.22
NiAl <sub>2</sub> O <sub>4</sub>	63.14	-15.72	-16.06
Shepherd Co-Blue	43.51	-4.46	-44.39

As shown in Figure 5.12, both solid solutions demonstrate continuous decrease of  $L^*$ ,  $a^*$  and  $b^*$  values with Ni content till  $x = 0.5$ . Beyond this point, the brightness  $L^*$  keeps dropping till  $x = 1$  for both series, while the trend is reversed for the blue component of the Ca<sub>1-x</sub>La<sub>x</sub>Al<sub>12-x</sub>Ni<sub>x</sub>O<sub>19</sub> series leaving the most negative  $b^*$  value (-30.38) at  $x = 0.5$ . In the case of CaAl<sub>12-2x</sub>Ni<sub>x</sub>Ti<sub>x</sub>O<sub>19</sub>, all three coordinates decline till  $x = 1$ , after that both  $L^*$  and  $a^*$  start to flatten out and  $b^*$  moves towards +b (yellow) direction while the color is shifting from royal blue to dark turquoise. The best blue color therefore is given by  $x = 1$  in the Ti-containing samples ( $b^* = -28.44$ ). Although the values of  $a^*$  associated with red (+)/green (-) hue display the least variation, the overall movement of these data points, in a 2-dimensional color space, is heading towards blue and green region with increasing amount of Ni.

Table 5.3 contains couple of samples discussed in section 5.4.1, and some other compositions that failed to produce decent blue colors such as CaAl<sub>10</sub>TiNi<sub>0.5</sub>Zn<sub>0.5</sub>O<sub>19</sub>. As stated by Bermanec et al. [69] divalent transition metal ions such as Zn<sup>2+</sup> and Mg<sup>2+</sup> exhibit unusual preference for the tetrahedral coordination in hibonite type of structures whereas

$\text{Ni}^{2+}$  show large octahedral crystal field stabilization energy. When substituting  $\text{Ni}^{2+}$  and  $\text{Zn}^{2+}$  simultaneously into the hibonite host lattice, it might be more favorable for  $\text{Zn}^{2+}$  to occupy the tetrahedral site, resulting in less tetrahedral  $\text{Ni}^{2+}$  and hence worse blue color [69]. This also seems to be true for coupled substitution with Ni and Si. In general, Ti-containing samples show better blue colors than their Sn-containing counterparts given the same Ni concentration, and similar conclusion was drawn based on Co-bearing hibonite pigments [51]. For a complex composition like  $\text{Ca}_{0.5}\text{La}_{0.5}\text{Al}_{11}\text{M}_{0.5}\text{Ni}_{0.5}\text{O}_{19}$ , better blue coloration was achieved when the trivalent  $M$  was  $\text{In}^{3+}$  instead of  $\text{Ga}^{3+}$ .

The values of blue component  $b^*$  manifested by our Ni-containing hibonite samples are still not as negative as those exhibited by commercial Co-blue and other Co-bearing pigments [51,52]. The initial evaluation performed by The Shepherd Color Company concluded that our Ni-containing hibonite pigments are likely to provide a cost benefit in the blue color space due to their low cost and high concentration of aluminum trioxide. Additional tests are in progress regarding Acid/Base resistance, weatherability and more.

Besides color, another desired property of pigments is the ability to reflect heat due to rising energy costs. Near infrared (NIR) energy contributes to ~52% of the total solar radiation absorbed by earth as heat. White pigments like  $\text{TiO}_2$  can reflect more than 80% of NIR radiation, leading to less NIR absorption, less heat build-up and hence less cooling expense. However, NIR-reflecting pigments with various colors, including dark colors, are in high demand for “Cool pigment” applications. Our NIR measurements in the range of 700–2500 nm show some peculiar features of reflectance for all hibonite samples prepared in this work (Fig. 5.13). Generally, the total NIR reflectance is inversely proportional to Ni content incorporated in the host material. Despite compositional variation, the spectra of our samples exhibit 3 peaks and 3 valleys over the entire range of measurement, with the peak positions centered near 500 nm, 1000 nm and 1500 nm, respectively. The peak width gradually broadens with wavelength such that the narrowest peak locates in the highest energy end and vice versa. The observed reflectance defined by the valleys and peaks range from 40 to 95% across the NIR region. Although not as good as the YInMn blue, the blue hibonite pigment still reflects more NIR radiation than Co-based pigment especially near 1500 nm as shown in Figure 5.14. Better NIR reflectance and lower cost than Co-blue

make these hibonite-based pigments potential candidates for many applications where solar heat reflection and energy-saving properties are desired.

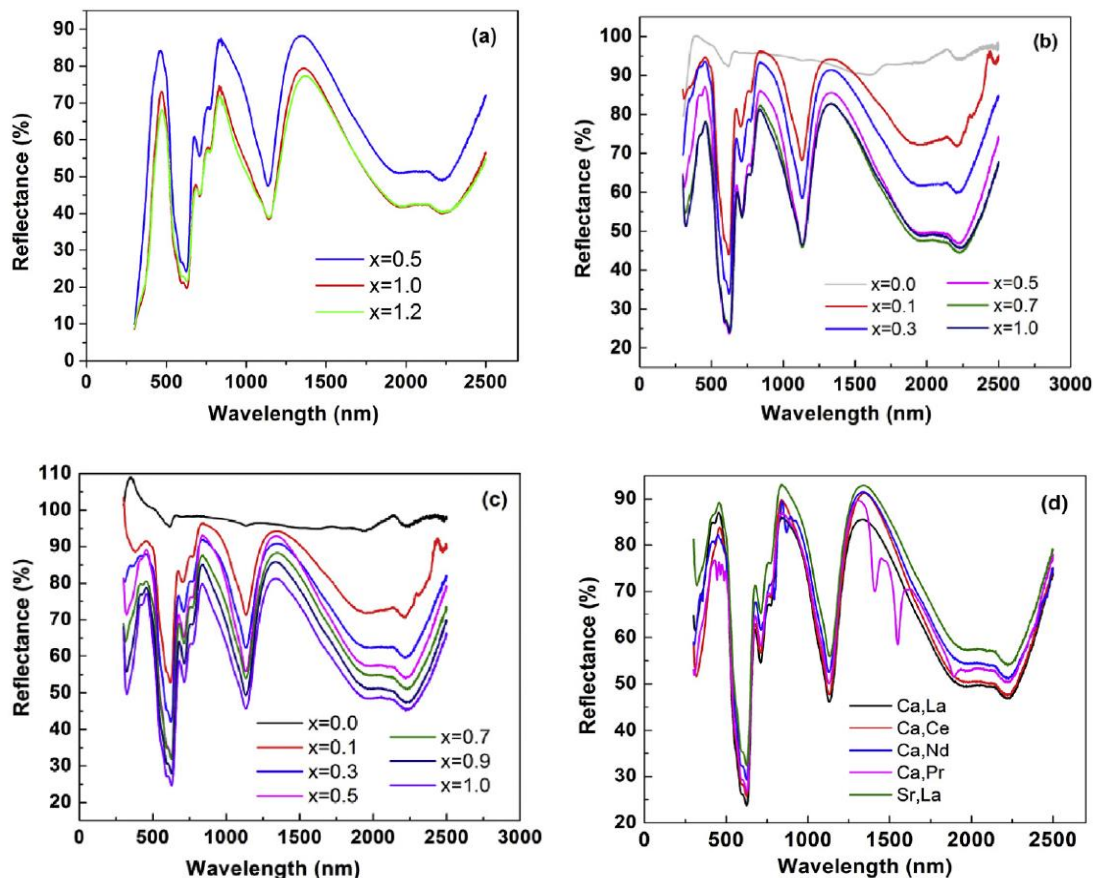


Figure 5.13 NIR reflectance spectra of selected Ni-containing hibonite solid solutions. (a)  $\text{CaAl}_{12-2x}\text{Ni}_x\text{Ti}_x\text{O}_{19}$  ( $x = 0.5, 1.0, 1.2$ ); (b)  $\text{Ca}_{1-x}\text{La}_x\text{Al}_{12-x}\text{Ni}_x\text{O}_{19}$  ( $x = 0.0, 0.1, 0.3, 0.5, 0.7, 1.0$ ); (c)  $\text{Sr}_{1-x}\text{La}_x\text{Al}_{12-x}\text{Ni}_x\text{O}_{19}$  ( $x = 0.0, 0.1, 0.3, 0.5, 0.7, 0.9, 1.0$ ); (d)  $\text{Ca}_{0.5}\text{RE}_{0.5}\text{Al}_{11.5}\text{Ni}_{0.5}\text{O}_{19}$  ( $\text{RE} = \text{La, Ce, Nd, Pr}$ ) and  $\text{Sr}_{0.5}\text{La}_{0.5}\text{Al}_{11.5}\text{Ni}_{0.5}\text{O}_{19}$ .



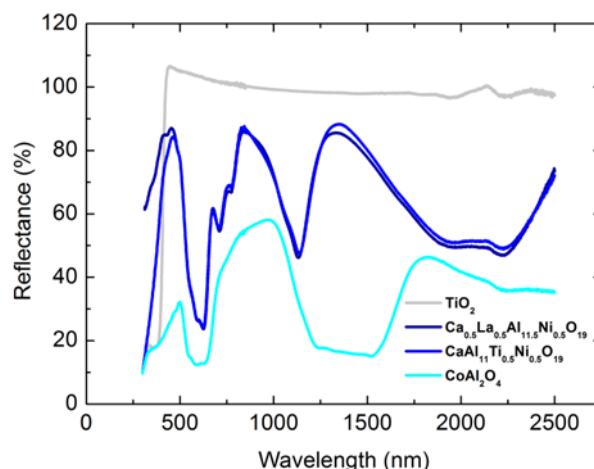


Figure 5.14 NIR reflectance spectra of selected Ni-containing hibonite samples. Commercial Co-blue pigment and  $\text{TiO}_2$  are included for comparison.

#### 5.4.4 Other Properties and Acid/Base Tests

Magnetic susceptibility measurements for  $\text{LaAl}_{11}\text{NiO}_{19}$ ,  $\text{Ca}_{0.5}\text{La}_{0.5}\text{Al}_{11.5}\text{Ni}_{0.5}\text{O}_{19}$  and  $\text{CaAl}_{11}\text{Ti}_{0.5}\text{Ni}_{0.5}\text{O}_{19}$  samples were made to verify the oxidation state of  $\text{Ni}^{2+}$  in the structures. Temperature dependence of magnetic susceptibility ( $\chi$ ) and inverse magnetic susceptibility ( $1/\chi$ ) are shown in Figure 5.15. Curie-Weise law was implemented to determine the effective magnetic moment of nickel. Tetrahedrally coordinated Ni has two unpaired electrons and its spin-only magnetic moment ( $\mu_s$ ) equals  $2.83 \mu_B$ . However, effective magnetic moment ( $\mu_{\text{eff}}$ ) usually observed for  $\text{Ni}^{2+}$  is higher, in a range of  $2.9\text{--}3.9 \mu_B$ , due to an orbital angular momentum contribution, which frequently occurs for 3<sup>rd</sup> row late transition metal cations [70]. This spin–orbit coupling has been observed in Ni-bearing oxides with hibonite structure based on previous optical studies [44,47].

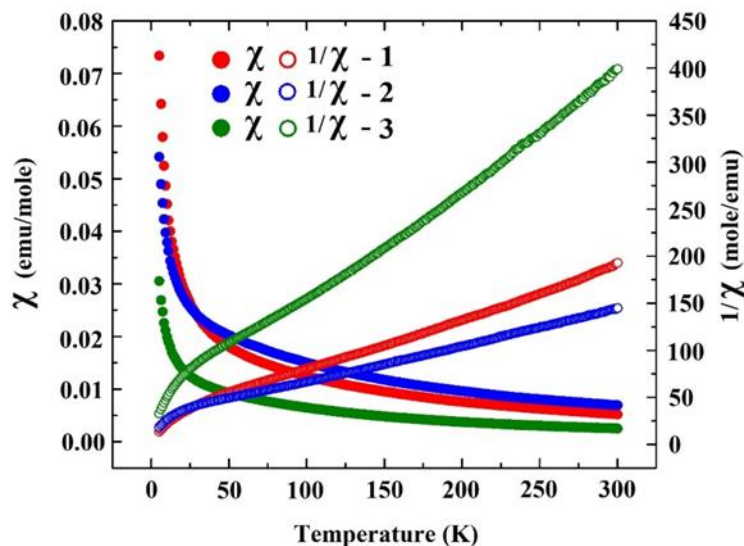


Figure 5.15 Magnetic susceptibility ( $\chi$ ) and inverse magnetic susceptibility ( $1/\chi$ ) vs. temperature of (1)  $\text{LaAl}_{11}\text{NiO}_{19}$ ; (2)  $\text{Ca}_{0.5}\text{La}_{0.5}\text{Al}_{11.5}\text{Ni}_{0.5}\text{O}_{19}$  and (3)  $\text{CaAl}_{11}\text{Ti}_{0.5}\text{Ni}_{0.5}\text{O}_{19}$ . 1 emu (cgs units) =  $10^{-3}$  A m<sup>2</sup> (SI units).

Curie and Weiss constants were calculated from the slope and the intercept of linear region of  $1/\chi$  vs. temperature plot. Effective magnetic moments were derived from experimentally determined Curie constants. Calculated magnetic moments, Curie and Weiss constants of  $\text{LaAl}_{11}\text{NiO}_{19}$ ,  $\text{Ca}_{0.5}\text{La}_{0.5}\text{Al}_{11.5}\text{Ni}_{0.5}\text{O}_{19}$  and  $\text{CaAl}_{11}\text{Ti}_{0.5}\text{Ni}_{0.5}\text{O}_{19}$  are given in Table 5.4.

Table 5.4 Calculated magnetic moments  $\mu_{\text{eff}}$ , Curie and Weiss constants of  $\text{LaAl}_{11}\text{NiO}_{19}$ ,  $\text{Ca}_{0.5}\text{La}_{0.5}\text{Al}_{11.5}\text{Ni}_{0.5}\text{O}_{19}$  and  $\text{CaAl}_{11}\text{Ti}_{0.5}\text{Ni}_{0.5}\text{O}_{19}$  samples.

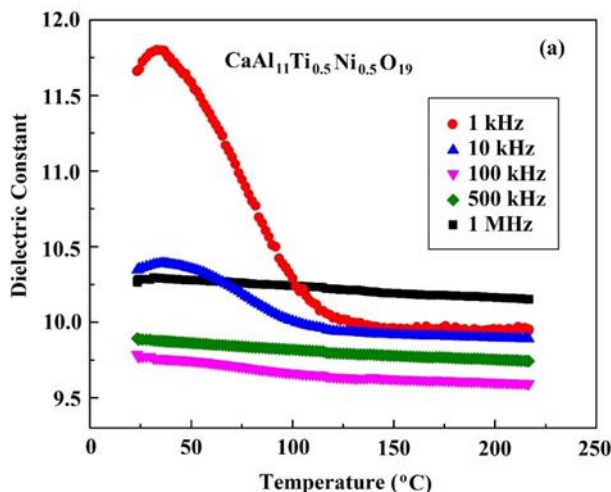
Compound	T range (K)	Curie constant	Weiss constant (K)	$\mu_{\text{eff}}$ (without diamagnetic correction)	$\mu_{\text{eff}}$ (with diamagnetic correction)
<b><math>\text{LaAl}_{11}\text{NiO}_{19}</math></b>	250–300	1.70	-8.78	3.53	3.70
<b><math>\text{Ca}_{0.5}\text{La}_{0.5}\text{Al}_{11.5}\text{Ni}_{0.5}\text{O}_{19}</math></b>	250–300	1.64	-5.19	3.47	3.64
<b><math>\text{CaAl}_{11}\text{Ti}_{0.5}\text{Ni}_{0.5}\text{O}_{19}</math></b>	250–300	1.59	-4.10	3.41	3.58

Diamagnetic correction for  $\mu_{\text{eff}}$  was applied [71]. As we can see, all samples show paramagnetic behavior in the measured temperature region (5–300 K). Weiss constants of all compounds are not significantly different from zero and they are negative, suggesting a weak antiferromagnetic interaction. The experimental moments are in reasonable agreement with the moments expected from high-spin  $\text{Ni}^{2+}$ , hence +2 oxidation state for

nickel is confirmed.  $\text{LaAl}_{11}\text{NiO}_{19}$  has higher concentration of  $\text{Ni}^{2+}$  and more negative Weiss constant value comparing to  $\text{Ca}_{0.5}\text{La}_{0.5}\text{Al}_{11.5}\text{Ni}_{0.5}\text{O}_{19}$  and  $\text{CaAl}_{11}\text{Ti}_{0.5}\text{Ni}_{0.5}\text{O}_{19}$  due to stronger nickel-nickel interactions.

Dielectric properties have been widely investigated for hexaferrites with the magnetoplumbite structure. Arora and co-authors studied dielectric properties of co-substituted M-type barium hexaferrites  $\text{Ba}_{1-2x}\text{La}_x\text{Na}_x\text{Fe}_{10}\text{CoZnO}_{19}$ , showing that dielectric constant ( $\kappa$ ) decreases and dielectric loss ( $\tan \delta$ ) increases with increasing La-Na content [72]. Dielectric properties of Ni-containing hibonite materials however have never been reported.

Dielectric measurements were made for  $\text{CaAl}_{11}\text{Ti}_{0.5}\text{Ni}_{0.5}\text{O}_{19}$  and  $\text{CaAl}_{10}\text{TiNiO}_{19}$  compounds at frequencies of 1, 10, 100, 500, 750 kHz and 1 MHz and in the temperature range 25–250°C. Temperature dependence curves of  $\kappa$  and  $\tan \delta$  for  $\text{CaAl}_{11}\text{Ti}_{0.5}\text{Ni}_{0.5}\text{O}_{19}$  and  $\text{CaAl}_{11}\text{Ti}_{0.5}\text{Ni}_{0.5}\text{O}_{19}$  are illustrated in Figure 5.16 and Figure 5.17, respectively. Frequency dependence values of  $\kappa$  and  $\tan \delta$  are given in Figure 5.18.



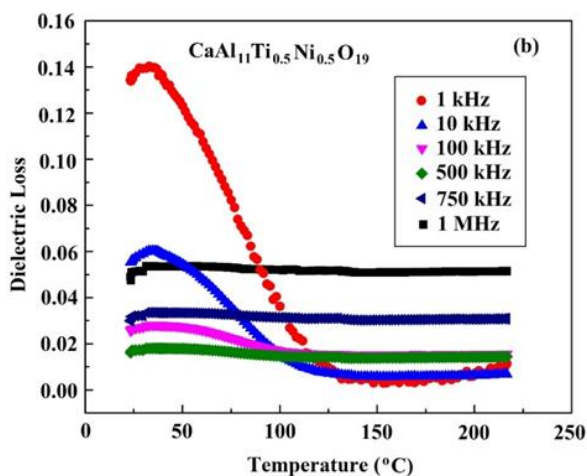


Figure 5.16 (a) Temperature dependence of (a) dielectric constant  $\kappa$  and (b) dielectric loss  $\tan \delta$  for  $\text{CaAl}_{11}\text{Ti}_{0.5}\text{Ni}_{0.5}\text{O}_{19}$  hibonite sample.

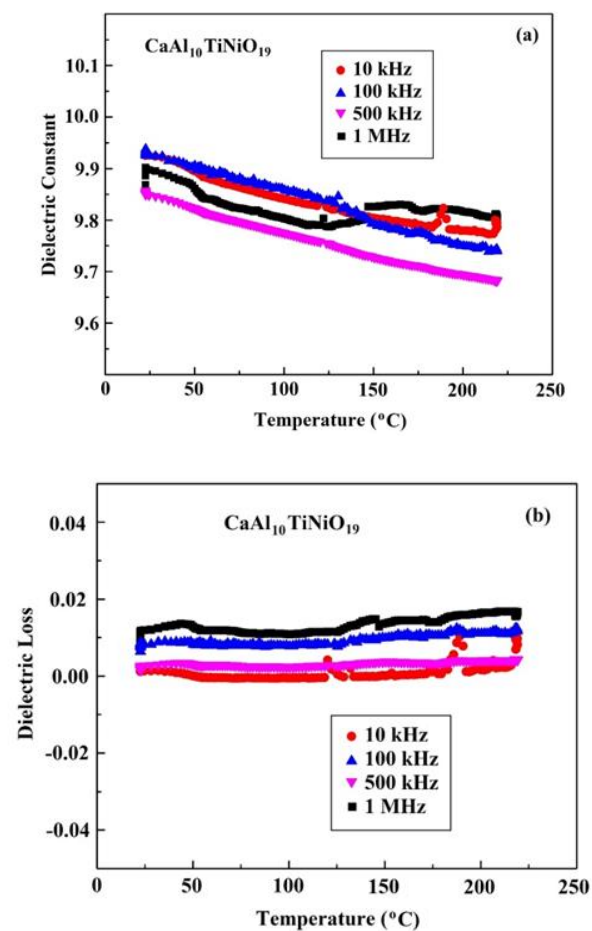


Figure 5.17 (a) Temperature dependence of (a) dielectric constant  $\kappa$  and (b) dielectric loss ( $\tan \delta$ ) for  $\text{CaAl}_{10}\text{TiNiO}_{19}$  hibonite sample.

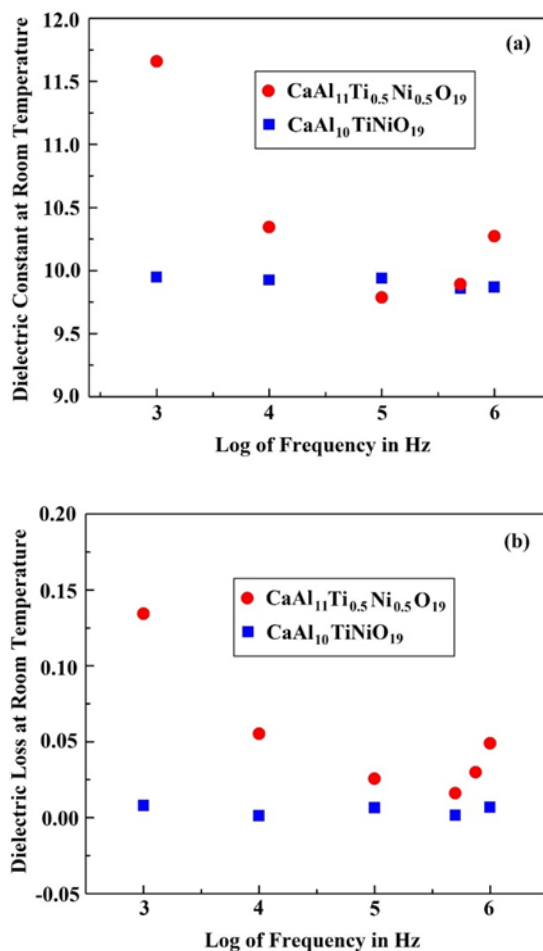


Figure 5.18 (a) Frequency dependence of (a) dielectric constant  $\kappa$  and (b) dielectric loss ( $\tan \delta$ ) for  $\text{CaAl}_{11}\text{Ti}_{0.5}\text{Ni}_{0.5}\text{O}_{19}$  and  $\text{CaAl}_{10}\text{TiNiO}_{19}$  hibonite samples.

The compositions are insulators and dielectric measurements reveal relatively low dielectric constants. The  $\kappa$  values decrease with the increase of applied temperature and frequency for both samples. In the case of  $\text{CaAl}_{11}\text{Ti}_{0.5}\text{Ni}_{0.5}\text{O}_{19}$   $\tan \delta$  decreases with increasing temperature and frequency, while  $\tan \delta$  for  $\text{CaAl}_{10}\text{TiNiO}_{19}$  is relatively constant at all studied temperatures and frequencies. Theoretical values of  $\kappa$  ( $\kappa_{\text{th}}$ ) were calculated according to Subramanian et al. [73] and compared with experimentally determined values. The  $\kappa_{\text{th}}$  of  $\text{CaAl}_{10}\text{TiNiO}_{19}$  equals 9.70, which is in good agreement with the experimental values. The  $\kappa_{\text{th}} = 9.33$  for  $\text{CaAl}_{11}\text{Ti}_{0.5}\text{Ni}_{0.5}\text{O}_{19}$  and it is somewhat smaller than the experimentally measured values.

To check stability of blue hibonite samples under rigid basic and acidic conditions, a series of experiments were performed. The lab tests were carried out using the following acids and base: HCl, HNO<sub>3</sub>, CH<sub>3</sub>COOH and NaOH, for selected samples like CaAl<sub>10</sub>TiNiO<sub>19</sub> and LaAl<sub>11</sub>NiO<sub>19</sub>. We weighed powders of our samples and mixed them with small amount of 50–60% diluted acid/base. The powders were then stirred for ~12 h, washed with DI water to remove residue acid/base from the solid, and dried in the oven overnight. XRD was performed to check the phase purity after acid/base exposure. For all our blue hibonite samples, no significant change was found based on XRD patterns and sample colors before and after the experiment. Powder XRD patterns of CaAl<sub>11</sub>TiNiO<sub>19</sub> and LaAl<sub>11</sub>NiO<sub>19</sub> before and after acid/base treatment are shown in Figure 5.19.

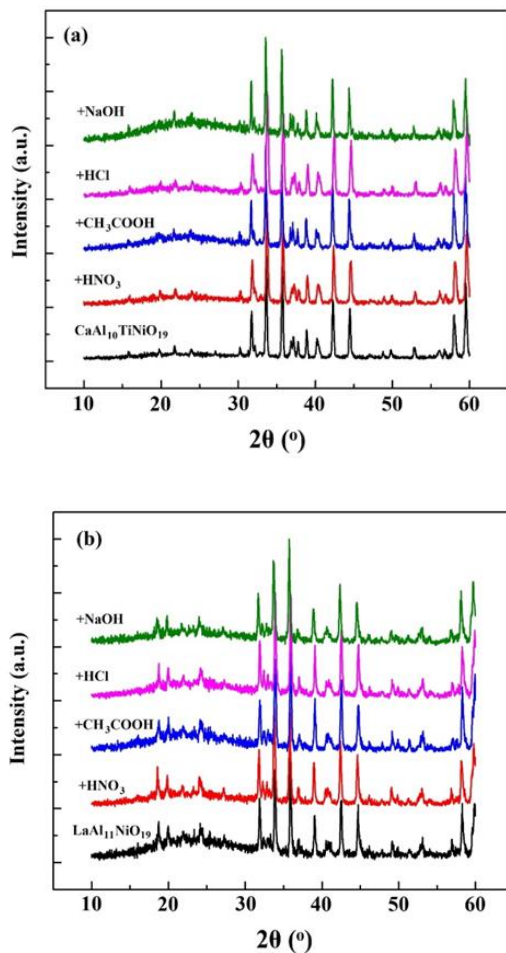


Figure 5.19 XRD patterns of (a) CaAl<sub>11</sub>TiNiO<sub>19</sub> (a) and (b) LaAl<sub>11</sub>NiO<sub>19</sub> hibonite compounds before and after exposure of various acids (HNO<sub>3</sub>, CH<sub>3</sub>COOH, HCl) and base (NaOH).

Stability with respect to temperature, acid and base is very crucial for pigment performance. Commercial blue pigments like ultramarine ( $\text{Na}_7\text{Al}_6\text{Si}_6\text{O}_{24}\text{S}_3$ ), Prussian blue ( $\text{Fe}_4[\text{Fe}(\text{CN})_6]_3$ ) and azurite [ $\text{Cu}_3(\text{CO}_3)_2(\text{OH})_2$ ] are not stable under acidic conditions [53]. Our Ni-containing hibonites are promising for applications like highly durable and cost-effective blue pigments.

## 5.5 Conclusion

In this work, a range of blue colors including sky-blue and bright royal-blue are successfully produced by cation substitution on both A and M sites in hibonite-based oxides  $AM_{12}\text{O}_{19}$  in presence of  $\text{Ni}^{2+}$  ions. A is one or two of the following elements: Ca, Sr, Ba, Y, La, Ce, Pr, Nd, Sm, Eu, Gd, Tb, Dy, Ho, Er, Tm, Yb and Lu, Na; and M is one or more of the following elements: Al, Ni, Ga, In, Ge, Si, Ti, Sn, Zr, Nb, Ta, Sb, Te. Detailed synthesis and structural, optical, magnetic, dielectric characterization are presented for two representative solid solutions:  $\text{CaAl}_{12-2x}\text{Ni}_x\text{Ti}_x\text{O}_{19}$  ( $x = 0-1$ ) and  $\text{Ca}_{1-x}\text{La}_x\text{Al}_{12-x}\text{Ni}_x\text{O}_{19}$  ( $x = 0-1$ ).

Due to big difference in neutron scattering lengths, incorporated  $\text{Ni}^{2+}$  and  $\text{Ti}^{4+}$  ions are successfully located in the hibonite lattice through Reitveld refinements. Optical spectra reveal an intense absorption band that broadens with increasing Ni content. Origin of the observed blue color is attributed to the allowed d-d transition of  $\text{Ni}^{2+}$  on tetrahedral sites. Recorded CIE  $L^*a^*b^*$  color parameters of our blue samples manifest exclusively large negative values for blue component  $b^*$ . Ni-containing blue hibonites in this work show better reflectance than Co-blue in the near-infrared region suggesting potential “Cool Pigments” applications.

In this chapter, we also provide a brief review on synthesis and characterization of hibonite related oxides with colors, especially those with blue colors.

## 5.6 Acknowledgements

Text and figures within this chapter have been used in part or whole from the publication:

Li, J., **Medina, E.A.**, Stalick, J.K., Sleight A.W., Subramanian, M.A. Colored oxides with hibonite structure: A potential route to non-cobalt blue pigments *Progress in Solid State Chemistry* **2016**, 44, 107-122.

This research was supported by National science Foundation (DMR - 1508527). We thank Dr. Andrew Smith of the Shepherd Color Company for running the initial tests on our pigment samples. The identification of any commercial product or trade name does not imply endorsement or recommendation by the National Institute of Standard and Technology.

## 5.7 References

- [1] Hibonite: Hibonite Mineral Information and Data. Hudson Institute of Mineralogy. [www.mindat.org](http://www.mindat.org) (accessed 11/01/2016).
- [2] Curien, H., Guillemin, C., Orcel, J., Stenberg, M., C R Hebd. Acad. Sci. 242 (1956) 2845.
- [3] Keil, K., Fuchs, L.H., Earth Planet Sci. Lett. 12 (1971) 184.
- [4] Ulianov, A., Kalt, A., Pettke, T., Eur. J. Mineral. 17 (2005) 357.
- [5] Burns, R.G., Burns, V.M., J. Geophys. Res. 89 (Suppl.) (1984) C313.
- [6] Rakotondrazafy, M.A.F., Moine, B., Cuney, M., Contrib. Mineral. Petrol. 123 (2) (1996) 190.
- [7] Simon, S.B., Grossman, L., Hutcheon, I.D., Phinney, D.L., Weber, P.K., Fallon, S.J., Am. Mineral. 91(10) (2006) 1675.
- [8] Nagashima, M., Armbruster, T., Hainschwang, T., Mineral. Mag. 74(5) (2010) 871.
- [9] Beckett, J.R., Stolper, E., Meteorit. Planet Sci. 29(1) (1994) 41.
- [10] Wagner, T.R., O'Keeffe, M., J. Solid State Chem. 73 (1988) 211.
- [11] Utsunomiya, A., Tanaka, K., Morikawa, H., Marumo, F., Kojima, H., J. Solid State Chem. 75 (1988) 197.
- [12] Iyi, N., Inoue, Z., Takekawa, S., Kimura, S., J. Solid State Chem. 54(1) (1984) 70.
- [13] Abrahams, S.C., Marsh, P., Brandle, C.D., J. Chem. Phys. 86(7) (1987) 4221.
- [14] Comer, J.J., Croft, W.J., Kestigian, M., Carter, J.R., Mater. Res. Bull. 2(3) (1967) 293.
- [15] Wagner, T.R., J. Solid State Chem. 136(1) (1998) 120.
- [16] Kimura, K., Ohgaki, M., Tanaka, K., Morikawa, H., Marumo, F., J. Solid State Chem. 87(1) (1990) 186.
- [17] Gasperin, M., Saine, M.C., Kahn, A., Laville, F., Lejus, A.M., J. Solid State Chem. 54(1) (1984) 61.
- [18] Li, J., Medina, E.A., Stalick, J.K., Sleight, A.W., Subramanian, M.A., Z. Naturforsch. B Chem. Sci. 71(5) (2016) 475.
- [19] Du, L.S., Stebbins, J.F., J. Phys. Chem. B 108(12) (2004) 3681.
- [20] Obradors, X., Collomb, A., Pernet, M., Samaras, D., Joubert, J.C., J. Solid State Chem. 56(2) (1985) 171.



- [21] Bergstein, A., White, W.B., *J. Electrochem. Soc.* 118(7) (1971) 1166.
- [22] Verstegen, J.M.P.J., Sommerdijk, J.L., Verriet, J.G., *J. Lumin.* 6(5) (1973) 425.
- [23] Kahn, A., Lejus, A.M., Madsac, M., Thery, J., Vivien, D., Bernier, J.C., *J. Appl. Phys.* 52(11) (1981) 6864.
- [24] Li, Y.J., Ma, Y.Y., Ye, S., Hu, G.P., Zhang, Q.Y., *Mater. Res. Bull.* 51 (2014) 1.
- [25] Collongues, R., Gourier, D., Kahn-Harari, A., Lejus, A.M., Thery, J., Vivien, D., *Annu. Rev. Mater. Sci.* 20 (1990) 51.
- [26] Saber, D., Lejus, A.M., *Mater. Res. Bull.* 16(10) (1981) 1325.
- [27] Armstrong, J.T., Meeker, G.P., Huneke, J.C., Wasserburg, G.J., *Geochim. Cosmochim. Acta* 46(4) (1982) 575.
- [28] Ihinger, P.D., Stolper, E., *Earth Planet Sci. Lett.* 78(1) (1986) 67.
- [29] Burns, R.G., *NATO ASI Series, Series C: Math. Phys. Sci.* 343 (1991) 175.
- [30] Graetsch, H., Gerbert, W., *Z. Kristallogr.* 211(1) (1996) 25.
- [31] Simon, S.B., Davis, A.M., Grossman, L., *Meteorit. Planet Sci.* 36(3) (2001) 331.
- [32] Hainschwang, T., Notari, F., Massi, L., Armbruster, T., Rondeau, B., Fritsch, E., Nagashima, M., *Gems Gemol.* 46(2) (2010) 135.
- [33] Beckett, J.R., Live, D., Tsay, F.D., Lawrence, G., Stolper, E., *Geochim. Cosmochim. Acta* 52(6) (1988) 1479.
- [34] Doyle, P.M., Berry, A.J., Schofield, P.F., Mosselmans, J.F.W., *Geochim. Cosmochim. Acta* 187 (2016) 294.
- [35] Giannini, M., Ballaran, T.B., Langenhorst, F., *Am. Mineral.* 99 (2014) 2060.
- [36] Doyle, P.M., Schofield, P.F., Berry, A.J., Walker, A.M., Knight, K.S., *Am. Mineral.* 99 (2014) 1369.
- [37] Laville, F., Lejus, A.M., *J. Cryst. Growth* 63(2) (1983) 426.
- [38] Thuery, P., Laville, F., Tronc, E., Lejus, A.M., Vivien, D., *Rev. Chim. Mineral.* 22(2) (1985) 216.
- [39] Laville, F., Perrin, M., Lejus, A.M., Gasperin, M., Moncorge, R., Vivien, D., *J. Solid State Chem.* 65(3) (1986) 301.
- [40] Lejus, A.M., Laville, F., Thery, J., *Mater. Res. Bull.* 23(6) (1988) 913.
- [41] Slagtern, A., Fjellvaag, H., *Eur. J. Solid State Inorg. Chem.* 33(11) (1996) 1241.
- [42] Cinibulk, M.K., *J. Am. Ceram. Soc.* 81(12) (1998) 3157.
- [43] Batista, J.A.L., Ribeiro, M.J.P.M., Cordeiro da Costa M.G.C., *US Patent PT103889, A20090521*, 2009.
- [44] Costa, G., Ribeiro, M.J., Hajjaji, W., Seabra, M.P., Labrincha, J.A., Dondi, M., Cruciani, G., *J. Eur. Ceram. Soc.* 29 (2009) 2671.
- [45] Hajjaji, W., Costa, G., Zanelli, C., Ribeiro, M.J., Seabra, M.P., Dondi, M., Labrincha, J.A., *J. Eur. Ceram. Soc.* 32(4) (2012) 753.
- [46] Kim, G., Lee, B.-H., *Korean J. Mater. Res.* 24(1) (2014) 43.
- [47] Ardit, M., Borcanescu, S., Cruciani, G., Dondi, M., Lazau, I., Pacurariu, C., Zanelli, C., *J. Am. Ceram. Soc.* 99(5) (2016) 1749.
- [48] Doynov, M.I., Bozadjiev, R.L., Dimitrov, T.I., Bozadjiev, L.S., *Oxid. Commun.* 34(3) (2011) 726.
- [49] Dondi, M., Cruciani, G., Guarini, G., Matteucci, F., Raimondo, M., *Ceram. Int.* 32(4) (2006) 393.

- [50] Subramanian, M.A., Li, J., Sleight, A.W., UC Patent WO2015131036, A120150903, 2015.
- [51] Hajjaji, W., Seabra, M.P., Labrincha, J.A., *Dyes Pigments* 83 (2009) 385.
- [52] Leite, A., Costa, G., Hajjaji, W., Ribeiro, M.J., Seabra, M.P., Labrincha, J.A., *Dyes Pigments* 81 (2009) 211.
- [53] Smith, A.E., Mizoguchi, H., Delaney, K., Spaldin, N.A., Sleight, A.W., Subramanian, M.A., *J. Am. Chem. Soc.* 131 (2009) 17084.
- [54] Han, J., Brearley, A.J., Keller, L.P., *Meteorit. Planet. Sci.* 50(12) (2015) 2121.
- [55] Mao, H.H., Hillert, M., Selleby, M., Sundman, B., *J. Am. Ceram. Soc.* 89 (2006) 298.
- [56] Altay, A., Carter, C.B., Rulis, P., Ching, W.-Y., Arslan, I., Guelguen, M.A., *J. Solid State Chem.* 183(8) (2010) 1776.
- [57] Giannini, M., Ballaran, T.B., Langenhorst, F., Bischoff, A., *Meteoritics & Planetary Sci.* 46 (2011) A77.
- [58] Kadyrova, Z.R., Sirazhiddinov, N.A., Tuganova, S.K., *Inorg. Mater.* 33(3) (1997) 300.
- [59] Larson, A.C., Von Dreele, R.B., General Structure Analysis System (GSAS), Los Alamos National Laboratory Report LAUR (1994) 86.
- [60] EXPGUI, a graphical user interface for GSAS: Toby, B.H., *J. Appl. Crystallogr.* 34 (2001) 210.
- [61] Hormillosa, C., Healy, S., Stephen, T., Brown, I.D., Bond Valence Calculator, Version 2.0 (1993) <http://www.ccp14.ac.uk> (accessed 07/15/2016).
- [62] Kubelka, P., Munk, F.Z., *Tech. Phys.* 12 (1931) 593.
- [63] Bain, G.A., Berry, J.F., *J. Chem. Educ.* 85 (2008) 532.
- [64] Shannon, R.D., *Acta Crystallogr.* A32 (1976) 751.
- [65] O'Keeffe, M., Eutax; <http://www.iucr.org/sincris-top/logiciel/prg-eutax.html> (accessed 02/17/2016).
- [66] Iyi, N., Göbbels, M., *J. Solid State Chem.* 122 (1996) 46.
- [67] O'Neill, H.S.C., Dollase, W.A., Rose II C.R., *Phys. Chem. Minerals* 18 (1991) 302.
- [68] Smith, A.E., Sleight, A.W., Subramanian, M.A., *Mater. Res. Bull.* 46 (2011) 1.
- [69] Bermanec, V., Holtstam, D., Sturman, D., Criddle, A.J., Black, M.E., Nezilovite Scavnicar S., *Can. Mineral* 34 (1996) 1287.
- [70] Figgis, B.N., Lewis, J., *Prog. Inorg. Chem.*, Eds. Cotton FA 6 (1964) 37.
- [71] Bain, G.A., Berry, J.F., *J. Chem. Educ.* 85 (2008) 532.
- [72] Arora, A., Narang, S.B., *J. Mater. Sci.: Mater. Electron.* 27 (2016) 10157.
- [73] Subramanian, M.A., Shannon, R.D., *Mat. Res. Bull.* 24 (1989) 1477.

## CHAPTER 6

### **Color Pigments with Hibonite-type Structure: $\text{CaAl}_{12}\text{O}_{19}$ -based pigments with Fe, Mn, Cr and Cu as chromophores**

#### **Abstract**

Colored hibonite-type oxides with a general formula  $\text{CaAl}_{12-x}\text{M}_x\text{O}_{19}$  were prepared by solid state reactions through M-site substitution of aluminum with various di-, tri- and tetravalent cations ( $M = \text{Fe}, \text{Mn}, \text{Cr}, \text{Cu}, \text{Ga}, \text{In}, \text{Ti}, \text{Ge}, \text{Sn}$  or any combination thereof), where Fe, Mn, Cr and Cu are chromophore ions. Neutron Rietveld refinement of  $\text{CaAl}_{9.5}\text{Fe}_{2.5}\text{O}_{19}$ ,  $\text{CaAl}_{11.5}\text{Mn}_{0.5}\text{O}_{19}$  and  $\text{CaAl}_{10}\text{SnMnO}_{19}$  compounds shows that  $\text{Fe}^{3+}$  and  $\text{Mn}^{2+}$  prefer to occupy the tetrahedral site, while  $\text{Mn}^{3+}$  has an evident preference for both tetrahedral and octahedral sites and  $\text{Sn}^{4+}$  for octahedral site in the hibonite structure. No oxygen vacancies are found by structural refinements, and magnetic measurements confirm divalent Mn for  $\text{CaAl}_{11}\text{Ti}_{0.5}\text{Mn}_{0.5}\text{O}_{19}$  and trivalent Mn for  $\text{CaAl}_{11.5}\text{Mn}_{0.5}\text{O}_{19}$ . Diffuse reflectance spectra reveal that the d-d transitions occurring in transition metal chromophores are mainly responsible for the observed colors. The colored powders exhibit fairly high reflectance in near-infrared region (750–2500 nm) which makes them potential candidates for “Cool pigment” applications. Synthesis and characterization methods are briefly reviewed for hibonite type oxides, especially those containing Fe, Mn, Cr and Cu.

Publication based on this chapter:

- 1) **Medina, E.A.**, Li, J., Subramanian, M.A. Colored oxides with hibonite structure II: Structural and optical properties of  $\text{CaAl}_{12}\text{O}_{19}$ -type pigments with chromophores based on Fe, Mn, Cr and Cu *Progress in Solid State Chemistry* **2017** (submitted).

## 6.1 Introduction

Hibonite is a family of metal oxides isostructural to magnetoplumbite [1-4]. Mineral hibonite is more often found in meteorites than on earth [5]. The natural and synthetic hibonites have been widely studied for their structural and magnetic properties and applications as phosphor and laser materials [6-10].

The ideal hibonite  $\text{CaAl}_{12}\text{O}_{19}$  has a hexagonal unit cell and crystallizes in  $P6_3/mmc$  space group,  $a = 5.5587(1) \text{ \AA}$ ,  $c = 21.8929(3) \text{ \AA}$ ,  $V = 585.84 \text{ \AA}^3$  [11,12]. The crystal structure consists of two building blocks alternating along the  $c$ -axis (Fig. 6.1): the spinel layer (S-block) and the trigonal bipyramidal layer (R-block) [13-15]. Calcium ions occupy the 12-fold coordinated sites. There are five different crystallographic positions for  $\text{Al}^{3+}$  ions in this hexagonal crystal structure: Al1: trigonal antiprism (CN=6); Al2: trigonal bipyramid (TBP, CN=5); Al3: tetrahedra (CN=4); Al4: face-shared octahedra (CN=6); and Al5: edge-shared octahedra (CN=6). This unique structural feature, in addition to the low cost of its chemical constituents, makes  $\text{CaAl}_{12}\text{O}_{19}$  an attractive oxide host in search for new materials with interesting and applicable properties.

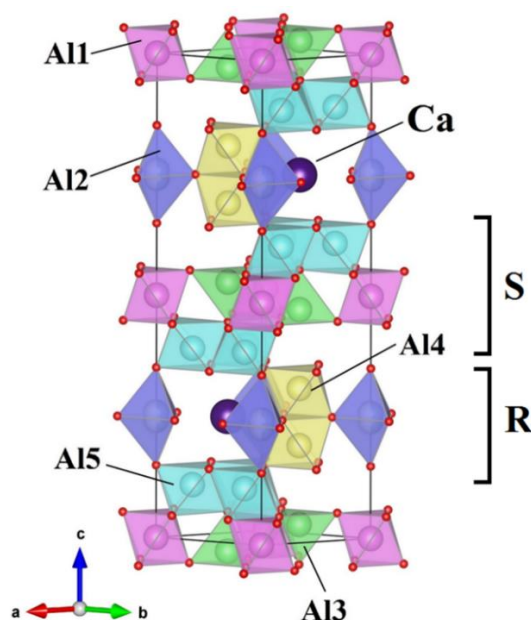


Figure 6.1 Hexagonal structure of hibonite  $\text{CaAl}_{12}\text{O}_{19}$  with five different crystallographic positions of aluminum. The crystal structure consists of two blocks alternating along the  $c$ -axis: the spinel layer (S-block) and the trigonal bipyramidal layer (R-block).

Hibonite-type compounds containing Fe, Mn, Cr and Cu have been reported mostly for their crystal structures and magnetic properties, their optical properties however are rarely investigated.  $\text{CaFe}_6\text{Al}_6\text{O}_{19}$  [16],  $\text{SrAl}_x\text{Fe}_{12-x}\text{O}_{19}$  [17,18] and  $\text{BaFe}_{12-x}\text{Mn}_x\text{O}_{19}$  [19] phases were prepared and their structures were refined by X-ray [16-18] and neutron diffraction [19] methods. Mn and Fe ions distribution of  $\text{BaFe}_{12-x}\text{Mn}_x\text{O}_{19}$  [20], Cr-site preference of  $\text{BaFe}_{12-x}\text{Cr}_x\text{O}_{19}$  [21], Ti and Mn cations arrangement of  $\text{BaTiMnFe}_{10}\text{O}_{19}$  [22] and Fe-sites occupancies of  $\text{SrAl}_x\text{Fe}_{12-x}\text{O}_{19}$  [23] compounds were investigated. Structural, electrical and magnetic properties of  $\text{CaCr}_x\text{Fe}_{12-x}\text{O}_{19}$  ( $x = 3, 4, 8, 9$ ) [24] and  $\text{CaFe}_{12-x}\text{Al}_x\text{O}_{19}$  ( $x = 3, x = 4$ ) [25] series were reported. Relaxor-like improper ferroelectricity in  $\text{PbFe}_6\text{Ga}_6\text{O}_{19}$  was studied [26]. Mn-doped  $\text{CaAl}_{12}\text{O}_{19}$  is used as phosphor material in white organic light-emitting devices [27]. Iron-containing hibonites were widely explored as magnetic materials for permanent magnets, microwave and high-density magnetic recording devices [28]. Single crystals with composition  $\text{BaAl}_x\text{Fe}_{12-x}\text{O}_{19}$  were studied and magnetic properties of the series were reported [29]. Structural and spectroscopic investigations of  $\text{LaAlFe}_{11}\text{O}_{19}$ ,  $\text{SmFe}_4\text{Al}_8\text{O}_{19}$  and  $\text{Eu}_{0.83}\text{Fe}_2\text{Al}_{10}\text{O}_{19}$  were performed and summarized [30,31]. An effect of La doping on structural, magnetic and microstructural properties of  $\text{Ba}_{1-x}\text{La}_x\text{Fe}_{12}\text{O}_{19}$  ceramics was explored [32]. Physical and magnetic properties of  $\text{SrFe}_{12-x}\text{Al}_x\text{O}_{19}$  nanoparticles were investigated [33].

Although the color of ideal hibonite  $\text{CaAl}_{12}\text{O}_{19}$  is white, it rarely forms without impurities in nature. A variety of colors have been discovered for hibonite-bearing minerals [34-38]. Murchison meteorite found in 1969 in Australia contains “Blue Angel”, a relatively large ( $\sim 1.5$  mm) hibonite-containing inclusion, and the brilliant blue color of which was ascribed to the presence of  $\text{V}^{3+}$  [39]. The Fe-containing hibonite  $(\text{Fe,Mg})\text{Al}_{12}\text{O}_{19}$  was discovered in inclusion from the Allende meteorite [40]. Burns [41] proposed three mechanisms responsible for the blue color in natural meteoritic hibonite: 1) crystal field transitions within  $\text{V}^{3+}$  and  $\text{Ti}^{3+}$  located in the TBP sites; 2) charge transfer transitions from  $\text{Fe}^{2+}$  to  $\text{Ti}^{4+}$  in face-shared octahedra similar to that in sapphire; 3) color centers introduced when  $\text{Al}^{26}$  decays to  $\text{Mg}^{26}$  or trapped electrons in the lattice as a result of nonstoichiometry and structural defects. Also spectroscopic study of iron in natural hibonite from Madagascar was performed [42]. Synthetic hibonite-type oxides also show

interesting colors upon various substitutions in different M sites of  $AM_{12}O_{19}$  and the origin of the coloration has been explored experimentally.  $LnMgAl_{11}O_{19}$  single crystals [43] were prepared and characterized:  $LaMgAl_{11}O_{19}$  and  $GdMgAl_{11}O_{19}$  are colorless,  $La_{1-x}Nd_xMgAl_{11}O_{19}$  is slightly mauve colored,  $PrMgAl_{11}O_{19}$  is green,  $NdMgAl_{11}O_{19}$  is purple,  $SmMgAl_{11}O_{19}$  is ochre,  $EuMgAl_{11}O_{19}$  is slightly blue. The correlation between observed blue color and the amount of  $Ti^{3+}$  in the  $CaAl_{12}O_{19}$  structure was investigated and the concentration of  $Ti^{3+}$  was found to be associated with oxygen fugacity [44]. It was shown that depending on the amount and ratio of  $Ti^{3+}$  and  $Ti^{4+}$  ions,  $CaAl_{12}O_{19}$ -based crystals might be colorless, blue, greenish or orange [45]. Study of  $LaM_xAl_{11}O_{18+x}$  ( $M = Mn, Co, Cu$ ) series [46] concluded that the green color of  $LaMn_xAl_{11}O_{18+x}$  single crystals is due to  $Mn^{2+}$  ions, Co-containing crystals are blue and  $LaCu_xAl_{11}O_{19}$  is colorless.  $LaMAl_{11}O_{19}$  ( $M = Ni, Co, Fe, Mn$ ) compounds [47] were found to be blue with Ni substitution on the Al site, dark blue with Co, pink with Fe, and green with Mn. Originally colorless  $La(Mg_{1-y}Mn_y)Al_{11}O_{18+x}$  ( $x, y \leq 1$ ) crystals show brownish coloration under UV and X-ray radiation exposure; defect centers were responsible for the color change [48].  $SrCr_9Ga_3O_{19}$  single crystals have dark green color due to the presence of  $Cr^{3+}$  ions [49].

Recently colored oxides with hibonite structure has attracted attention as an appealing host for inorganic pigment design. There were several papers on turquoise pigments with  $Ni^{2+}$  as a chromophore in tetrahedral coordination of  $CaAl_{12}O_{19}$  [50-52]. We have prepared a series of hibonite-type pigments with intense royal blue colors [53] as well as many hibonite compositions with a variety of colors other than blue [54]. Blue hibonite type compounds based on tetrahedrally coordinated  $Co^{2+}$  were investigated [55]. Hajjaji et al. [56,57] proposed to use solid wastes for making inorganic pigments based on hibonite with cobalt and nickel chromophores. In this work we are mainly focused on syntheses and characterization of colored hibonite solid solutions and compositions with Fe, Mn, Cr and Cu as chromophores.

We report here crystal structures (by neutron powder diffraction) and optical properties of three solid solutions  $CaAl_{12-x}Mn_xO_{19}$ ,  $CaAl_{12-x}Fe_xO_{19}$  and  $CaAl_{12-2x}Mn_xSn_xO_{19}$  along with some new hibonite compositions that exhibit colors other than blue. Magnetic and dielectric data are also measured and analyzed. Most of the hibonite compositions

show relatively high near-infrared (NIR) reflectance that makes them potential candidates for “Cool pigment” applications.

## 6.2 Materials and Synthesis

### 6.2.1 Conventional Solid State Method

Conventional solid state synthesis is the most common way to prepare inorganic metal oxides, particularly in this work, colored oxides based on hibonite structure. Reaction of starting materials occurs at high temperature. All our samples were made using this method. Stoichiometric amounts of  $\text{CaCO}_3$  (Sigma-Aldrich, 99.0%),  $\text{Al}_2\text{O}_3$  (Cerac, 99.99%),  $\text{Fe}_2\text{O}_3$  (Alfa Aesar, 99.945%),  $\text{In}_2\text{O}_3$  (Aldrich, 99.99%),  $\text{Cr}_2\text{O}_3$  (Alfa Aesar, 99.997%),  $\text{Mn}_2\text{O}_3$  (Alfa Products, 98%),  $\text{Ga}_2\text{O}_3$  (Aldrich, 99.99%),  $\text{MnO}$  (JMC, 99.5%),  $\text{FeO}$  (Alfa Aesar, 99.5%),  $\text{TiO}_2$  (Aldrich, 99.9%),  $\text{SnO}_2$  (JMC, 99.9%),  $\text{GeO}_2$  (Cerac, 99.999%),  $\text{CuO}$  (Alfa Aesar, 99.0%) were mixed and grounded using agate mortar with pestle. The mixture was pelletized and heated in an alumina crucible at 1400 °C for 12 h in air; then the mixture was grounded again, pelletized and reheated at 1450 °C for 12 h.

### 6.2.2 Other Preparation Methods

In addition to standard solid state synthesis [2,7,8,20,23,24,38,44,49,51-53] other preparation methods were also applied to obtain hibonite-type oxides. Solution combustion synthesis using metal nitrates was performed [25,32,50]. Powder samples have been made through wet techniques: sol-gel [8,21] and hydrolysis of alkoxydes followed by thermal decomposition and reaction [8]. However, low temperature synthesis techniques are not always applicable for synthesis of hibonites phases because most of them require fairly high synthetic temperatures (above 1200 °C).

Single crystals have been obtained by flux method [8,29,58] or by various high temperature techniques: flame fusion or Verneuil method [6,8,9,43,46,47], floating zone method [6,8,12,43,47] and Czochralski method [6,8,18,49,59,60].



## 6.3 Characterization

### 6.3.1 Techniques Applied for Hibonites

X-ray diffraction (XRD) structure refinement is the most common technique applied for hibonite-type single crystals and powder samples [1,3-6,8,12,14,16,18,23,37,44,49,50,51]. In some cases neutron data Rietveld refinement was performed [2,3,19,20,22,44,53]. Chemical composition and surface topography of natural and prepared hibonite-type single crystals were analyzed by scanning electron microscope method (SEM) [14,25,32,33,37,39,40,44,51,55,57]. Elemental distribution was studied by electron microprobe analysis (EMP) [3-5,40]. Spectroscopic investigations (absorbance and fluorescence spectra) [4,6,7,34,42,57], near-infrared (IR) spectra [7,37], emission spectra [9], luminescence [10], color description by  $L^*a^*b^*$  parameters [53-55] and other optical properties characterization [34,35,40,43,50,51,55-57] were made. Additional information of the hibonite-based oxides was collected using Mössbauer technique [4,35,38,41-43], magnetic susceptibility measurements [6,21,53] along with magnetic structure refinement [19,29,33,47], electrical properties [24,25], electron paramagnetic resonance (EPR) [7], chemical reactivity [43], microhardness measurements [43,47], dielectric properties [53], thermal analysis [33,57].

### 6.3.2 For Hibonites in This Work

XRD data were collected using a Rigaku MiniFlex II diffractometer with  $\text{CuK}\alpha$  radiation ( $\lambda = 1.5418\text{\AA}$ ) and a graphite monochromator at room temperature. For phase identification the measurements were carried out at  $0.5^\circ/\text{min}$  within  $15^\circ$  to  $70^\circ$   $2\theta$  range. Powder neutron diffraction data were collected on the 32-counter high-resolution diffractometer BT-1 at the Center for Neutron Research at the National Institute of Standards and Technology. A Cu (311) monochromator, yielding a wavelength of  $1.5403(2)\text{\AA}$ , was employed. Collimation of  $15'$  of arc was used before the monochromator,  $20'$  before the sample, and  $7'$  before the detectors. The samples were loaded into vanadium containers of 15.6 mm diameter and 50 mm length. Data were collected at room temperature over a  $2\theta$  range of  $3^\circ$  to  $167^\circ$  for 5.5 hr. XRD and neutron data were refined

using the Rietveld method, as implemented in GSAS-EXPGUI software [61,62]. Bond-valence analysis of the neutron structures made use of the bond-valence calculator [63].

Konica Minolta CM-700d Spectrophotometer (Standard illuminant D<sub>65</sub>) was used to measure  $L^*$ ,  $a^*$ ,  $b^*$  color coordinates. Diffuse reflectance data in the visible range were measured using a homemade UV-VIS spectrophotometer (MgO as the reference) and converted to absorbance using the Kubelka-Munk equation [64]. NIR reflectance data (up to 2500 nm) were collected using a Jasco V-670 Spectrophotometer.

Magnetic properties measurements were made using a Quantum Design Physical Property Measurement System (QD-PPMS) at temperature range of 5 K to 300 K (zero-field cooling, applied magnetic field 0.5 T). Inverse magnetic susceptibility data was used to fit for Curie-Weiss law. Diamagnetic corrections were made for calculations of experimental  $\mu_B$  [65].

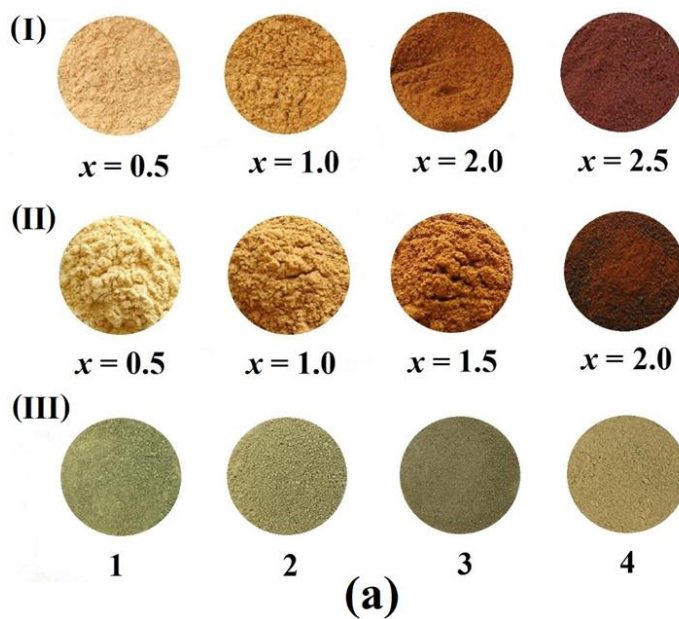
Dielectric properties measurements were performed on Dielectric instrument HP Precision LCR Meter 4284A (20 Hz – 1 MHz) in 25–250 °C temperature range. Samples were pelletized and quenched at temperature of synthesis to obtain the percent theoretical density is above 75%. Pellet's faces were sand to produce an even thickness, then faces were painted with silver coating and dried. Before the experiment the resistivity of the samples were measured, the samples were completely insulating in order to accurate measurements to take place.

## 6.4 Results and Discussion

### 6.4.1 Colors and Phase Analysis

In the present work we mainly focused on M-site substitutions in  $\text{CaAl}_{12}\text{O}_{19}$  hibonite lattice; four transition metals (Fe, Mn, Cr, Cu) were used as chromophore elements. When  $\text{Fe}^{3+}$  is a chromophore in  $\text{CaAl}_{12-x}\text{Fe}_x\text{O}_{19}$  ( $x = 0.5\text{--}4.5$ ) series (Fig. 6.2-a (I)) the color of the samples changes from yellow ( $x = 0.5$ ) to orange brown ( $x = 1.0$ ), red brown ( $x = 2.5$ ), reddish chocolate ( $x = 3.0$ ) and dark chocolate ( $x = 3.5$ ) with increasing  $x$ .  $\text{CaAl}_{11-x}\text{GaFe}_x\text{O}_{19}$  ( $x = 0.5\text{--}2.5$ ) compounds (Fig. 6.2-a (II)) have similar but darker colors than  $\text{CaAl}_{12-x}\text{Fe}_x\text{O}_{19}$  series; when  $x = 2.0$   $\text{CaAl}_{10}\text{Fe}_2\text{O}_{19}$  is dark orange brown and

$\text{CaAl}_9\text{GaFe}_2\text{O}_{19}$  is dark brick red. When different di-, tri- and tetravalent ions were added to achieve charge compensation, iron-containing hibonites show slightly different colors (Fig. 6.2-a (III)) and  $\text{Fe}^{2+}$  is a chromophore atom in this case. Addition of Ti, Ge, Sn to  $\text{CaAl}_{11.5}\text{Fe}_{0.5}\text{O}_{19}$  sample gives change from sandy brown to greenish white, light olive and light bright olive colors. Add  $\text{Cu}^{2+}$  as a second chromophore to  $\text{CaAl}_{11}\text{Fe}_{0.5}(\text{Ti,Ge,Sn})_{0.5}\text{O}_{19}$  gives slightly darker colors. Doping of In to  $\text{CaAl}_{10.5}\text{Fe}_{0.5}\text{Cu}_{0.5}(\text{Sn,Ti})_{0.5}\text{O}_{19}$  results in more darker color;  $\text{CaAl}_{9.5}\text{InSn}_{0.5}\text{Cu}_{0.5}\text{Fe}_{0.5}\text{O}_{19}$  shows the most green olive color. After addition of Ga to  $\text{CaAl}_{10.5}\text{Fe}_{0.5}\text{Cu}_{0.5}(\text{Sn,Ti})_{0.5}\text{O}_{19}$  color gets darker and more green for Sn, but it is yellowish olive for Ti. In general,  $\text{Fe}^{3+}$  gives yellowish and brownish colors while  $\text{Fe}^{2+}$ -containing samples have greenish hue.



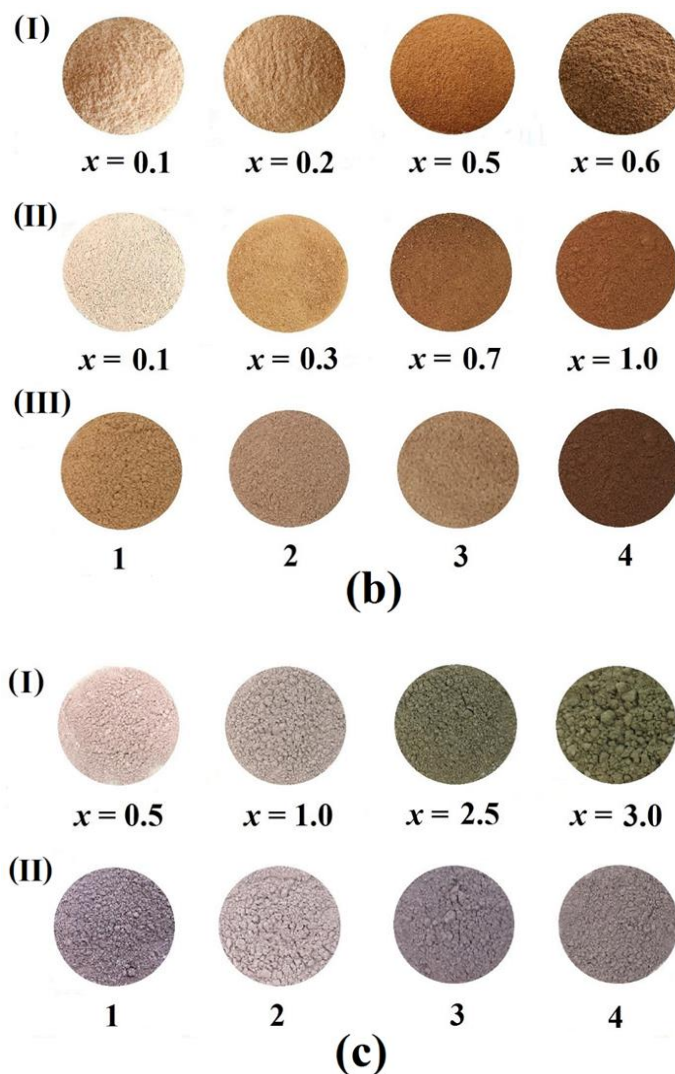


Figure 6.2 (a) Colors resulted from iron substitutions for the hibonite host with an ideal formula  $\text{CaAl}_{12}\text{O}_{19}$ . (I)  $\text{CaAl}_{12-x}\text{Fe}_x\text{O}_{19}$ ; (II)  $\text{CaAl}_{11-x}\text{GaFe}_x\text{O}_{19}$ ; (III) 1:  $\text{CaAl}_{9.5}\text{InSn}_{0.5}\text{Cu}_{0.5}\text{Fe}_{0.5}\text{O}_{19}$ , 2:  $\text{CaAl}_{9.5}\text{GaSn}_{0.5}\text{Cu}_{0.5}\text{Fe}_{0.5}\text{O}_{19}$ , 3:  $\text{CaAl}_{9.5}\text{InTi}_{0.5}\text{Cu}_{0.5}\text{Fe}_{0.5}\text{O}_{19}$ , 4:  $\text{CaAl}_{9.5}\text{GaTi}_{0.5}\text{Cu}_{0.5}\text{Fe}_{0.5}\text{O}_{19}$ . (b) Colors resulted from manganese substitutions for the hibonite host with an ideal formula  $\text{CaAl}_{12}\text{O}_{19}$ . (I)  $\text{CaAl}_{12-x}\text{Mn}_x\text{O}_{19}$ ; (II)  $\text{CaAl}_{12-2x}\text{Sn}_x\text{Mn}_x\text{O}_{19}$ ; (III) 1:  $\text{CaAl}_{10.5}\text{Ti}_{0.5}\text{Cu}_{0.5}\text{Mn}_{0.5}\text{O}_{19}$ , 2:  $\text{CaAl}_{10.5}\text{Sn}_{0.5}\text{Cu}_{0.5}\text{Mn}_{0.5}\text{O}_{19}$ , 3:  $\text{CaAl}_{9.5}\text{InTi}_{0.5}\text{Cu}_{0.5}\text{Mn}_{0.5}\text{O}_{19}$ , 4:  $\text{CaAl}_{9.5}\text{InSn}_{0.5}\text{Cu}_{0.5}\text{Mn}_{0.5}\text{O}_{19}$ . (c) Colors resulted from chromium substitutions for the hibonite host with an ideal formula  $\text{CaAl}_{12}\text{O}_{19}$ . (I)  $\text{CaAl}_{12-x}\text{Cr}_x\text{O}_{19}$ ; (II) 1:  $\text{CaAl}_{10.5}\text{Sn}_{0.5}\text{Cu}_{0.5}\text{Cr}_{0.5}\text{O}_{19}$ , 2:  $\text{CaAl}_{10.5}\text{GaCr}_{0.5}\text{O}_{19}$ , 3:  $\text{CaAl}_{10.5}\text{Ge}_{0.5}\text{Cu}_{0.5}\text{Cr}_{0.5}\text{O}_{19}$ , 4:  $\text{CaAl}_{10.5}\text{Ti}_{0.5}\text{Cu}_{0.5}\text{Cr}_{0.5}\text{O}_{19}$ .

When Mn plays a role of chromophore color of  $\text{CaAl}_{12-x}\text{Mn}_x\text{O}_{19}$  ( $x = 0.1-0.6$ ) series varies from burlywood ( $x = 0.1$ ) to saddle brown ( $x = 0.5$ ) and light brown ( $x = 0.6$ ) (Fig. 6.2-b (I)).  $\text{CaAl}_{12-x}\text{Sn}_x\text{Mn}_x\text{O}_{19}$  ( $x = 0.1-1.0$ ) (Fig. 6.2-b (II)) has lighter colors,  $\text{CaAl}_{12-}$

$x\text{Ti}_x\text{Mn}_x\text{O}_{19}$  ( $x = 0.5; 1.0$ ) series colors are similar to  $\text{CaAl}_{12-x}\text{Sn}_x\text{Mn}_x\text{O}_{19}$  solid solution, but brighter. Addition of  $\text{Cu}^{2+}$  to  $\text{CaAl}_{11}\text{Mn}_{0.5}\text{Sn}_{0.5}\text{O}_{19}$  sample results in almost the same, slightly darker color (Fig. 6.2-b (III)); Ga makes the sample color even darker. Doping of In to  $\text{CaAl}_{10.5}\text{Mn}_{0.5}\text{Cu}_{0.5}\text{Sn}_{0.5}\text{O}_{19}$  compound gives dark saddle brown color darker than  $\text{CaAl}_{11.5}\text{Mn}_{0.5}\text{O}_{19}$ . Combination of Cu and Ge shows more dull hue comparing to color of  $\text{CaAl}_{12-x}\text{Mn}_x\text{O}_{19}$ . Add Cu, Cu and In, Cu and Ga to  $\text{CaAl}_{11}\text{Ti}_{0.5}\text{Mn}_{0.5}\text{O}_{19}$  and color gets darker (milk chocolate brown) than in case of  $\text{CaAl}_{12-x}\text{Mn}_x\text{O}_{19}$  series.

The colors of  $\text{CaAl}_{12-x}\text{Cr}_x\text{O}_{19}$  ( $x = 0.5-3.5$ ) series is shown in Figure 6.2-c (I); Cr is a chromophore in this case. Color changes from light rosy brown ( $x = 0.5$ ) to light gray ( $x = 1.5$ ) and becomes grayish green when  $x = 3.0$  and  $3.5$ . Color of  $\text{CaAl}_{11-x}\text{GaCr}_x\text{O}_{19}$  ( $x = 0.5; 1.0$ ) series varies from light rosy brown for  $x = 0.5$  (Fig. 6.2-c (II)) to light gray when  $x = 1.0$ .  $\text{CaAl}_{10.5}\text{Ti}_{0.5}\text{Cu}_{0.5}\text{Cr}_{0.5}\text{O}_{19}$  is rosy brown, addition of Ga and In results in dark rosy brown hue in the first case and more brownish light chocolate color in the second case.  $\text{CaAl}_{10.5}\text{InCr}_{0.5}\text{O}_{19}$  is burly wood and  $\text{CaAl}_{10}\text{InCrO}_{19}$  is more dark (grayish brown). With addition of Cu and Sn  $\text{CaAl}_{11.5}\text{Cr}_{0.5}\text{O}_{19}$  becomes tan; with In  $\text{CaAl}_{9.5}\text{InSn}_{0.5}\text{Cu}_{0.5}\text{Cr}_{0.5}\text{O}_{19}$  has more brownish color comparing to  $\text{CaAl}_{10.5}\text{Sn}_{0.5}\text{Cu}_{0.5}\text{Cr}_{0.5}\text{O}_{19}$ .  $\text{CaAl}_{10.5}\text{Ge}_{0.5}\text{Cu}_{0.5}\text{Cr}_{0.5}\text{O}_{19}$  and  $\text{CaAl}_{9.5}\text{GaSn}_{0.5}\text{Cu}_{0.5}\text{Cr}_{0.5}\text{O}_{19}$  are rosy brown. In general, Sn-containing hibonites give lighter colors than Ti; In gives more brownish shades comparing to Ga, Ga-containing samples have rosy brown hue.

When Cu is a chromophore the combination with Ti gives creamy color for  $\text{CaAl}_{11}\text{Cu}_{0.5}\text{Ti}_{0.5}\text{O}_{19}$  and golden brown for  $\text{CaAl}_{10}\text{CuTiO}_{19}$ .  $\text{CaAl}_{11}\text{Ge}_{0.5}\text{Cu}_{0.5}\text{O}_{19}$  have light turquoise color very close to white and  $\text{CaAl}_{11}\text{Sn}_{0.5}\text{Cu}_{0.5}\text{O}_{19}$  is light blue.

#### 6.4.2 Crystal Structures: X-ray and Neutron Diffraction

Compounds with hibonite-type structure containing di-, tri- and tetravalent cations were prepared using standard solid state synthesis method (Table 6.1). To guarantee the charge neutrality of the system  $\text{Al}^{3+}$  ion can be substituted for divalent ions ( $M = \text{Fe}, \text{Mn}, \text{Cu}$ ) with tetravalent ions ( $M = \text{Ti}, \text{Sn}, \text{Ge}$ ) such that  $M^{2+} + M^{4+} \rightarrow 2\text{Al}^{3+}$ .

Table 6.1 List of synthesized compounds.

Formula of compounds	Range of $x$ or $M$ atoms	XRD powder patterns
$\text{CaAl}_{12-x}\text{Fe}_x\text{O}_{19}$	$x = 0.5 - 4.5$	Figure 6.3
$\text{CaAl}_{11-x}\text{GaFe}_x\text{O}_{19}$	$x = 0.5 - 2.5$	Figure 6.4(a)
$\text{CaAl}_{12-2x}\text{Sn}_x\text{Fe}_x\text{O}_{19}$	$x = 0.5 - 1.5$	Figure 6.4(b)
$\text{CaAl}_{12-2x}\text{Ti}_x\text{Fe}_x\text{O}_{19}$	$x = 0.5; 1.0$	Figure 6.4(b)
$\text{CaAl}_{12-x}\text{Mn}_x\text{O}_{19}$	$x = 0.1 - 0.6$	Figure 6.5
$\text{CaAl}_{12-2x}\text{Sn}_x\text{Mn}_x\text{O}_{19}$	$x = 0.1 - 1.0$	Figure 6.6
$\text{CaAl}_{12-2x}\text{Ti}_x\text{Mn}_x\text{O}_{19}$	$x = 0.5; 1.0$	Figure 6.4(b)
$\text{CaAl}_{11-x}\text{Ti}_{0.5}\text{Cu}_{0.5}\text{Mn}_x\text{O}_{19}$	$x = 0.5; 1.0$	Figure 6.8(a)
$\text{CaAl}_{10}\text{GeMO}_{19}$	$M(\text{II}) = \text{Fe}, \text{Mn}$	Figure 6.4(b)
$\text{CaAl}_{12-x}\text{Cr}_x\text{O}_{19}$	$x = 0.5 - 3.5$	Figure 6.7
$\text{CaAl}_{11-x}\text{GaCr}_x\text{O}_{19}$	$x = 0.5; 1.0$	Figure 6.4(a)
$\text{CaAl}_{11-x}\text{InCr}_x\text{O}_{19}$	$x = 0.5; 1.0$	Figure 6.4(c)
$\text{CaAl}_{12-2x}\text{Ti}_x\text{Cu}_x\text{O}_{19}$	$x = 0.5 - 1.5$	Figure 6.8(b)
$\text{CaAl}_{11}M_{0.5}\text{Cu}_{0.5}\text{O}_{19}$	$M(\text{IV}) = \text{Ge}, \text{Sn}$	Figure 6.8(b)
$\text{CaAl}_{9.5}\text{Ga}M'_{0.5}\text{Cu}_{0.5}M''_{0.5}\text{O}_{19}$	$M'(\text{IV}) = \text{Ti}, \text{Sn}; M''(\text{III}) = \text{Fe}, \text{Mn}, \text{Cr}$	Figure 6.9(a)
$\text{CaAl}_{9.5}\text{In}M'_{0.5}\text{Cu}_{0.5}M''_{0.5}\text{O}_{19}$	$M'(\text{IV}) = \text{Ti}, \text{Sn}; M''(\text{III}) = \text{Fe}, \text{Mn}, \text{Cr}$	Figure 6.9(b)
$\text{CaAl}_{10.5}M'_{0.5}\text{Cu}_{0.5}M''_{0.5}\text{O}_{19}$	$M'(\text{IV}) = \text{Ge}, \text{Sn}; M''(\text{III}) = \text{Fe}, \text{Mn}, \text{Cr}$	Figure 6.9(c)
$\text{CaAl}_{11-x}\text{Ti}_{0.5}\text{Cu}_{0.5}M_{0.5}\text{O}_{19}$	$M(\text{III}) = \text{Fe}, \text{Cr}$	Figure 6.8(a)
$\text{CaAl}_{10.5}\text{Ti}_{0.5}\text{Cu}_{0.5}\text{Mn}_{0.25}\text{Fe}_{0.25}\text{O}_{19}$		Figure 6.8(a)
$\text{CaAl}_{10.5}\text{Sn}_{0.5}\text{Cu}_{0.5}\text{Mn}_{0.25}\text{Fe}_{0.25}\text{O}_{19}$		Figure 6.9(c)
$\text{CaAl}_{11}M'_{0.5}M''_{0.5}\text{O}_{19}$	$M' = \text{Fe}, \text{Cr}; M'' = \text{Fe}, \text{Mn}$	Figure 6.4(d)

All compounds except  $\text{CaAl}_{12-x}\text{Fe}_x\text{O}_{19}$  ( $x = 0.5-4.5$ ) series [66] are reported in the present work for the first time.

GSAS software was used to perform unit cell refinement for X-ray (Le Bail method: cell edges and volumes) and neutron data (Rietveld method: atomic positions, thermal displacements and occupancies). There is a good agreement between Rietveld and Le Bail refinement results.

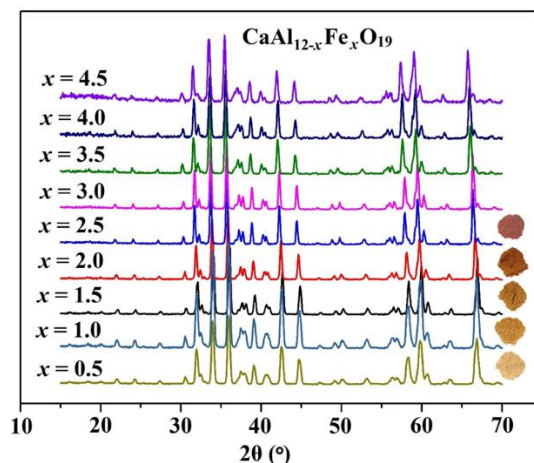


Figure 6.3 XRD patterns of  $\text{CaAl}_{12-x}\text{Fe}_x\text{O}_{19}$  ( $x = 0.5\text{--}4.5$ ) series.

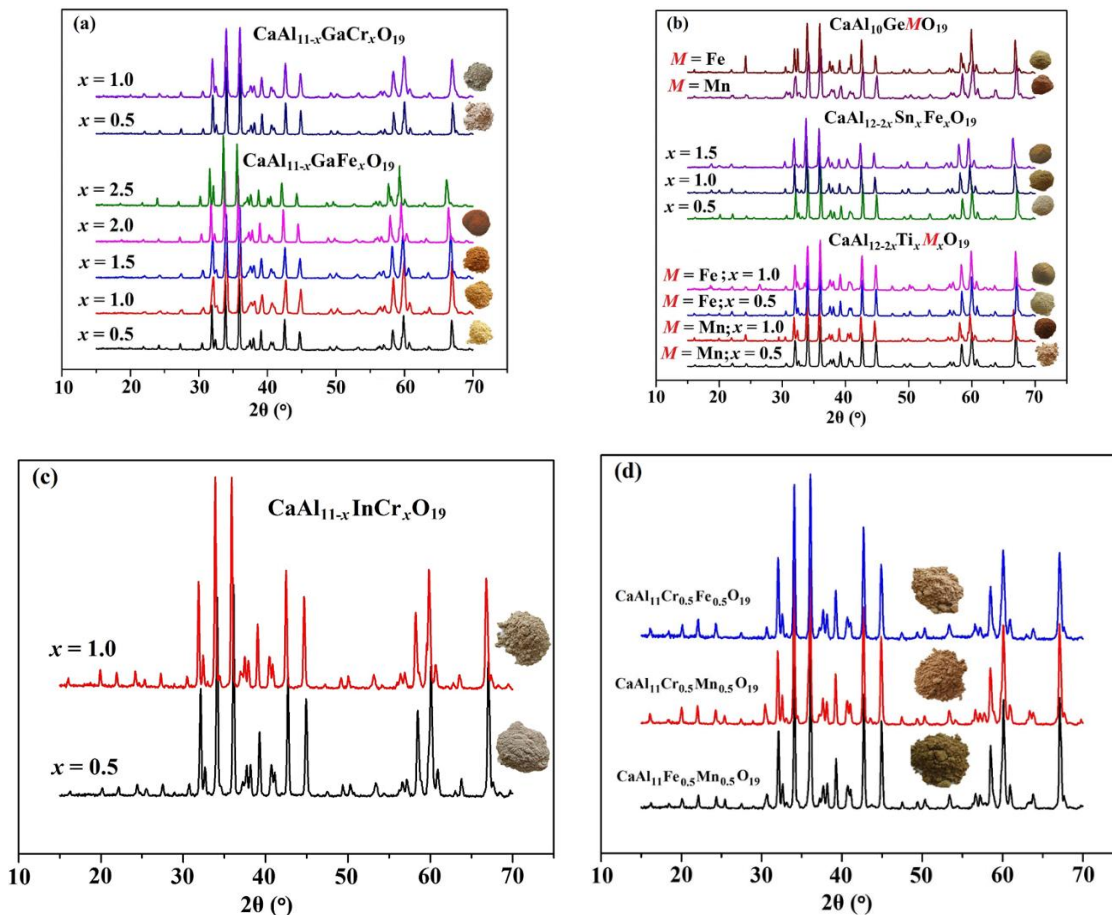


Figure 6.4 XRD patterns of (a)  $\text{CaAl}_{11-x}\text{GaM}^{\text{III}}_x\text{O}_{19}$  ( $M^{\text{III}} = \text{Cr}$  ( $x = 0.5; 1.0$ ) and  $\text{Fe}$  ( $x = 0.5 - 2.5$ )) series; (b)  $\text{CaAl}_{10}\text{GeM}^{\text{II}}_x\text{O}_{19}$  ( $M^{\text{II}} = \text{Mn}, \text{Fe}$ ),  $\text{CaAl}_{12-2x}\text{Sn}_x\text{Fe}_x\text{O}_{19}$  ( $x = 0.5\text{--}1.5$ ) and  $\text{CaAl}_{12-2x}\text{Ti}_x\text{M}^{\text{II}}_x\text{O}_{19}$  ( $M^{\text{II}} = \text{Mn}, \text{Fe}$  ( $x = 0.5; 1.0$ )) series; (c)  $\text{CaAl}_{11-x}\text{InCr}_x\text{O}_{19}$  ( $x = 0.5; 1.0$ ) solid solution; (d)  $\text{CaAl}_{11}\text{Cr}_{0.5}\text{Fe}_{0.5}\text{O}_{19}$ ,  $\text{CaAl}_{11}\text{Cr}_{0.5}\text{Mn}_{0.5}\text{O}_{19}$  and  $\text{CaAl}_{11}\text{Fe}_{0.5}\text{Mn}_{0.5}\text{O}_{19}$  compounds.

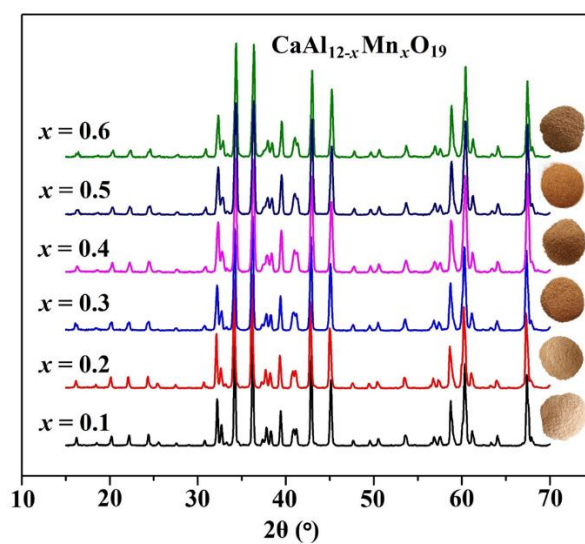


Figure 6.5 XRD patterns of  $\text{CaAl}_{12-x}\text{Mn}_x\text{O}_{19}$  ( $x = 0.1$ – $0.6$ ) solid solution.

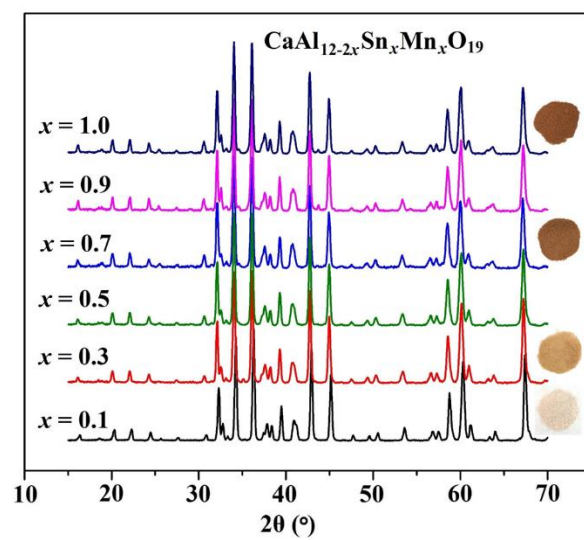


Figure 6.6 XRD patterns of  $\text{CaAl}_{12-2x}\text{Sn}_x\text{Mn}_x\text{O}_{19}$  ( $x = 0.1$ – $1.0$ ) solid solution.



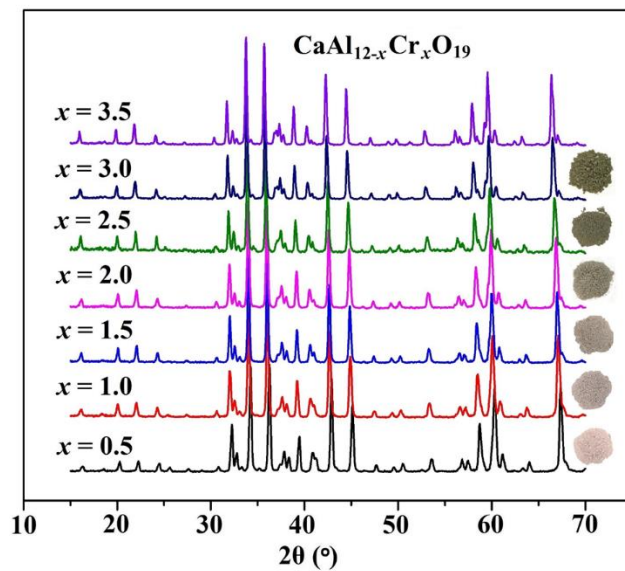


Figure 6.7 XRD patterns of  $\text{CaAl}_{12-x}\text{Cr}_x\text{O}_{19}$  ( $x = 0.5\text{--}3.5$ ) series.

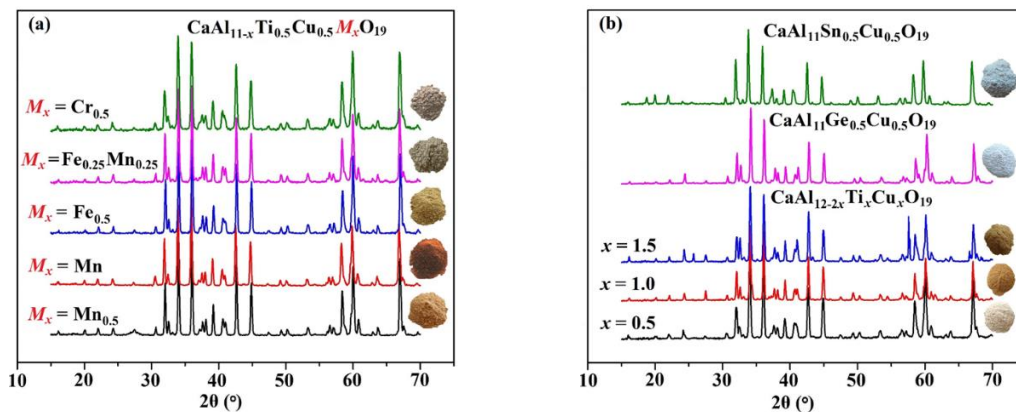


Figure 6.8 XRD patterns of (a)  $\text{CaAl}_{11-x}\text{Ti}_{0.5}\text{Cu}_{0.5}M_x\text{O}_{19}$  ( $M_x = \text{Cr}_{0.5}, \text{Mn}_{0.25}\text{Fe}_{0.25}, \text{Mn}_{0.5}, \text{Mn}, \text{Fe}_{0.5}$ ) compounds and (b)  $\text{CaAl}_{11}M_{\text{IV}}^{0.5}\text{Cu}_{0.5}\text{O}_{19}$  ( $M_{\text{IV}} = \text{Ge}, \text{Sn}$ ) and  $\text{CaAl}_{12-2x}\text{Ti}_x\text{Cu}_x\text{O}_{19}$  ( $x = 0.5\text{--}1.5$ ) solid solutions.

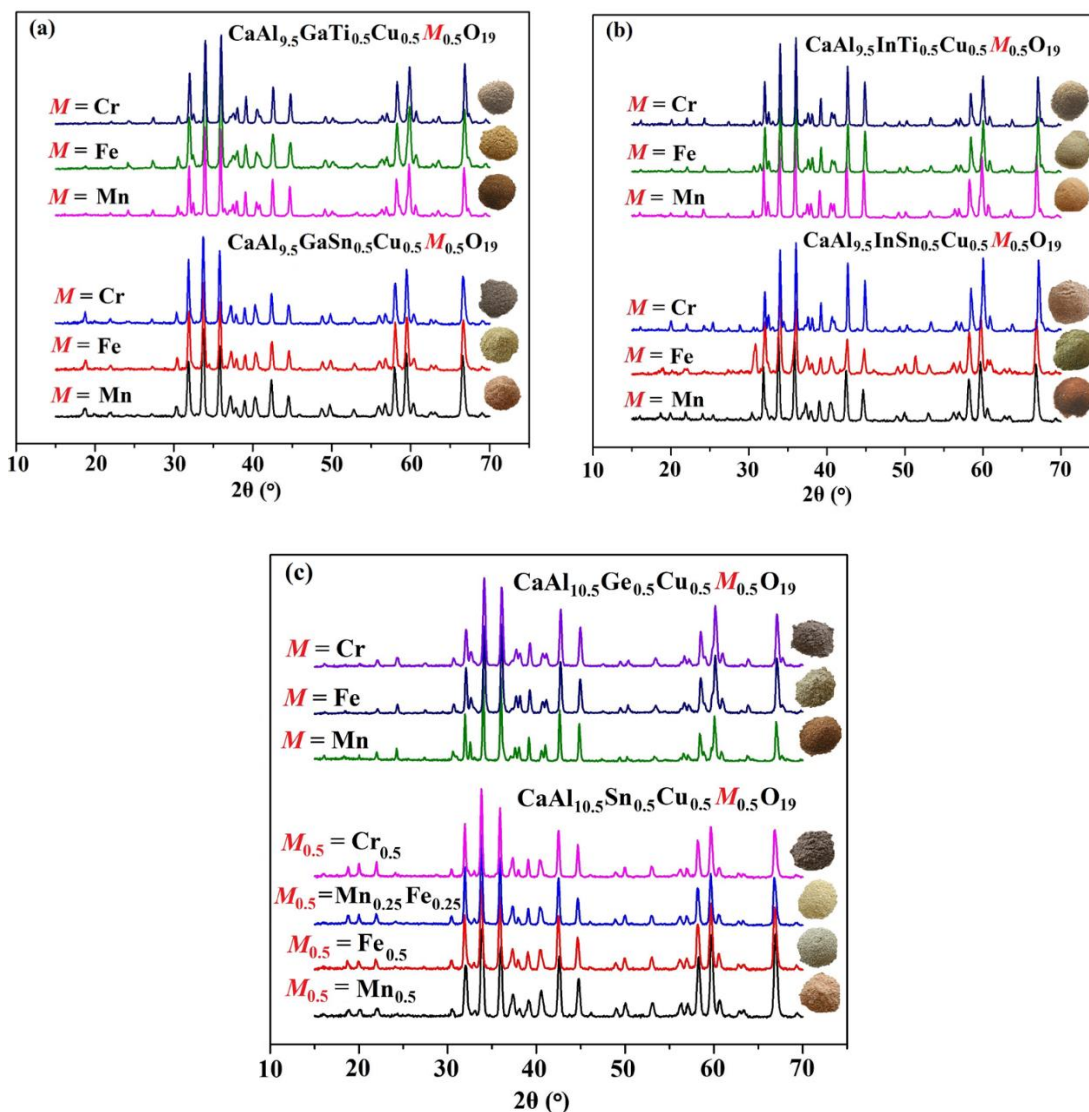


Figure 6.9 XRD patterns of (a)  $\text{CaAl}_{9.5}\text{GaTi}_{0.5}\text{Cu}_{0.5}M_{0.5}\text{O}_{19}$  and  $\text{CaAl}_{9.5}\text{GaSn}_{0.5}\text{Cu}_{0.5}M_{0.5}\text{O}_{19}$  ( $M^{\text{III}} = \text{Cr, Mn, Fe}$ ) compounds; (b)  $\text{CaAl}_{9.5}\text{InTi}_{0.5}\text{Cu}_{0.5}M_{0.5}\text{O}_{19}$  and  $\text{CaAl}_{9.5}\text{InSn}_{0.5}\text{Cu}_{0.5}M_{0.5}\text{O}_{19}$  ( $M^{\text{III}} = \text{Cr, Mn, Fe}$ ) solid solutions and (c)  $\text{CaAl}_{10.5}\text{Ge}_{0.5}\text{Cu}_{0.5}M_{0.5}\text{O}_{19}$  ( $M^{\text{III}} = \text{Cr, Mn, Fe}$ ) and  $\text{CaAl}_{10.5}\text{Sn}_{0.5}\text{Cu}_{0.5}M_{0.5}\text{O}_{19}$  ( $M_{0.5}^{\text{III}} = \text{Cr}_{0.5}, \text{Mn}_{0.25}\text{Fe}_{0.25}, \text{Fe}_{0.5}, \text{Mn}_{0.5}$ ) compounds.

All samples are pure and isostructural, they crystallize in  $P6_3/mmc$  space group. Lattice parameters of  $\text{CaAl}_{12-x}\text{Fe}_x\text{O}_{19}$  ( $x = 0.5-4.5$ ) and  $\text{CaAl}_{12-x}\text{Cr}_x\text{O}_{19}$  ( $x = 0.5-3.5$ ) series are shown in Figure 6.10. Shannon ionic radii of  $\text{Fe}^{3+}$  (CN = 6, high spin) and  $\text{Cr}^{3+}$  (CN = 6) equal  $0.78\text{\AA}$  and  $0.615\text{\AA}$  correspondingly [67], these values are larger than ionic radius of  $\text{Al}^{3+}$ , thus as the Fe/Cr content increases  $a$ ,  $c$  and  $V$  parameters also increase. The  $c$  parameter increases faster than the  $a$  with increasing of  $x$  due to the fact that hibonite

structure is more susceptible to the changes (expansion or construction) in the direction of  $c$ -axis.

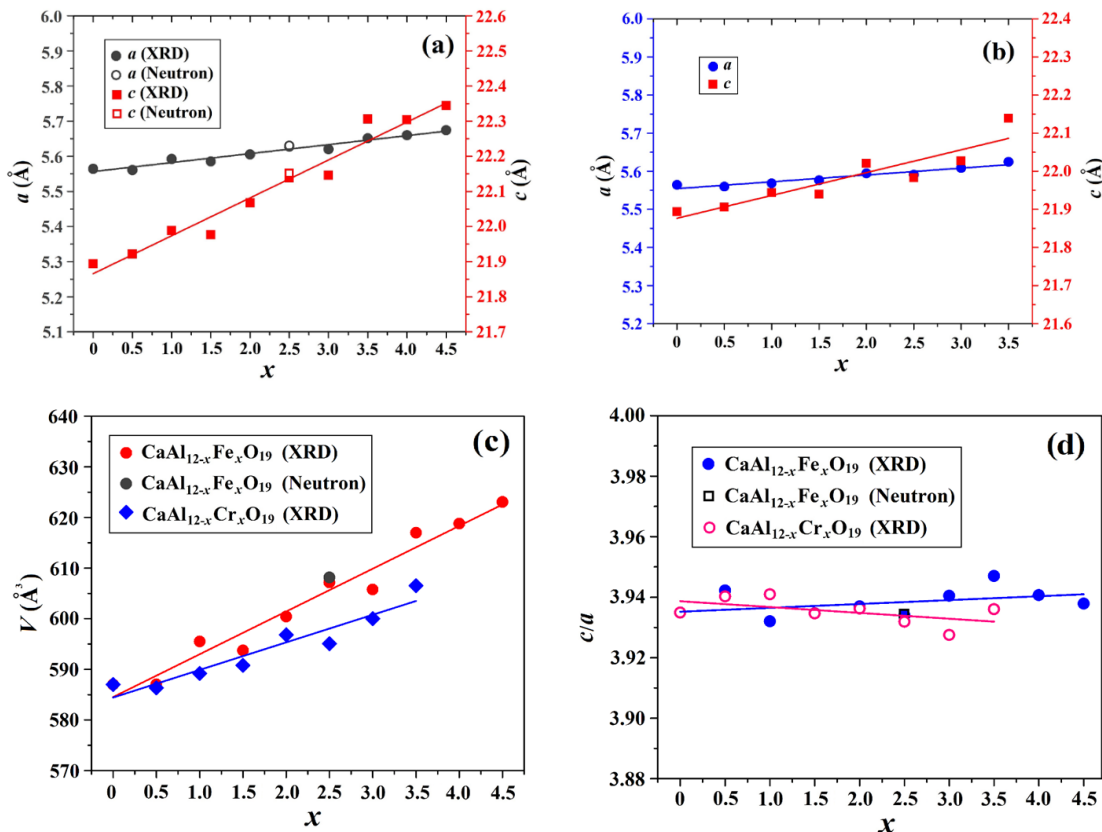


Figure 6.10 Lattice parameters of  $\text{CaAl}_{12-x}\text{Fe}_x\text{O}_{19}$  ( $x = 0.5 - 4.5$ ) and  $\text{CaAl}_{12-x}\text{Cr}_x\text{O}_{19}$  ( $x = 0.5 - 3.5$ ) solid solutions: (a) unit cell edges  $a$  and  $c$  of  $\text{CaAl}_{12-x}\text{Fe}_x\text{O}_{19}$  ( $x = 0.5 - 4.5$ ), (b) unit cell edges  $a$  and  $c$  of  $\text{CaAl}_{12-x}\text{Cr}_x\text{O}_{19}$  ( $x = 0.5 - 3.5$ ), (c) unit cell volumes  $V$  and (d)  $c/a$  ratio as a function of  $x$ . The estimated errors for  $a$ ,  $c$  and  $V$  are less than the size of the points in the figure.

Lattice parameters of  $\text{CaAl}_{12-x}\text{Mn}_x\text{O}_{19}$  ( $x = 0.1 - 0.6$ ) series are shown in Figure 6.11. Unit cell parameters  $a$ ,  $c$ ,  $V$  and  $c/a$  ratio are relatively constant for  $x$  values from 0.1 to 0.6. This result was expected, with substitution of  $\text{Al}^{3+}$  for  $\text{Mn}^{3+}$  there is no dramatic change in lattice parameters because these cations have similar ionic radii (ionic radius of  $\text{Mn}^{3+}$  (CN = 6) equals 0.58 Å and ionic radius of  $\text{Al}^{3+}$  (CN = 6) equals 0.535 Å).

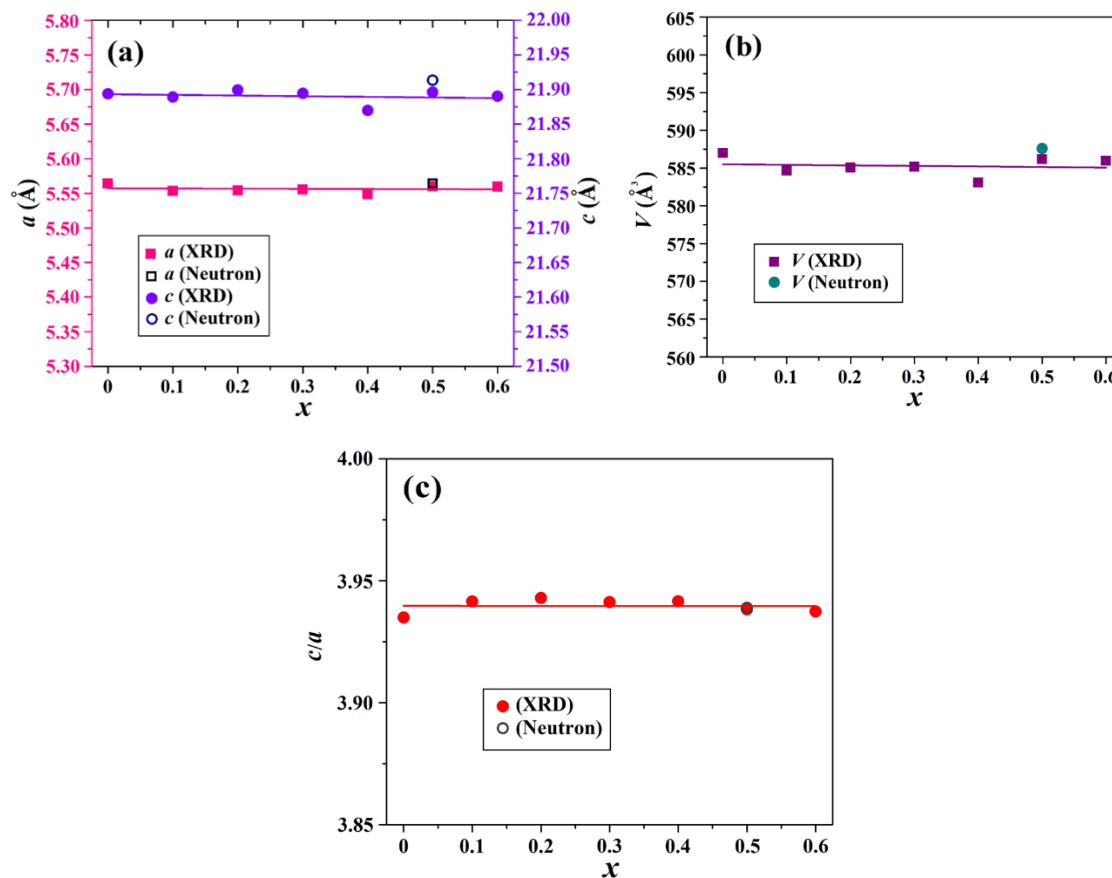


Figure 6.11 Lattice parameters of  $\text{CaAl}_{12-x}\text{Mn}_x\text{O}_{19}$  ( $x = 0.1$ – $0.6$ ): (a) unit cell edges  $a$  and  $c$ , (b) unit cell volumes  $V$  and (c)  $c/a$  ratio as a function of  $x$ . The estimated errors for  $a$ ,  $c$  and  $V$  are less than the size of the points in the figure.

Unit cell parameters of  $\text{CaAl}_{12-2x}\text{Sn}_x\text{Mn}_x\text{O}_{19}$  ( $x = 0.1$ – $1.0$ ) series are given in Figure 6.12:  $a$ ,  $c$ , and  $V$  values increase with  $x$ . The  $c/a$  ratio indicates a small structural change,  $c/a$  increases with the addition of  $\text{Sn}^{4+}$  and  $\text{Mn}^{2+}$ . This trend conforms to the change in ionic radii (ionic radii of  $\text{Sn}^{4+}$  (CN = 6) and  $\text{Mn}^{2+}$  (CN = 4) are 0.690 Å and 0.66 Å respectively).

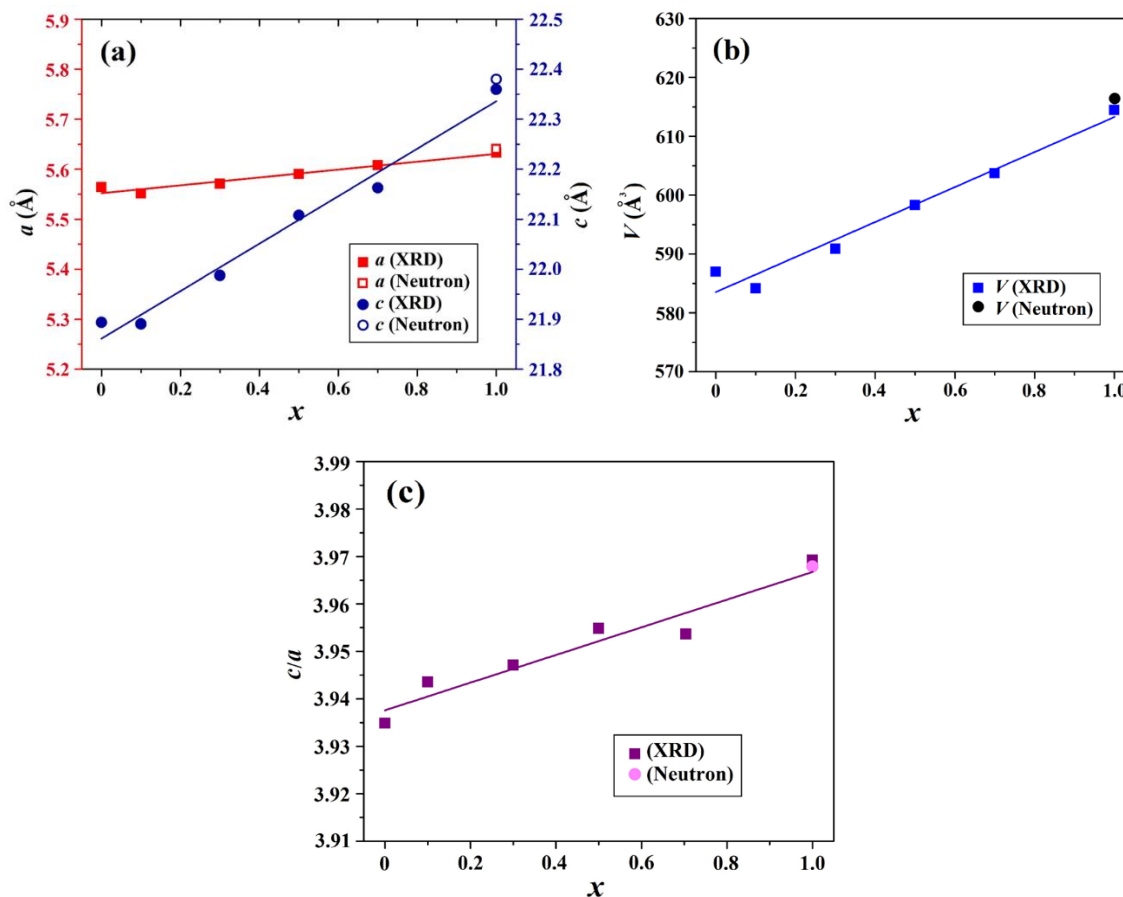


Figure 6.12 Lattice parameters of  $\text{CaAl}_{12-2x}\text{Sn}_x\text{Mn}_x\text{O}_{19}$  ( $x = 0.1$ – $1.0$ ): (a) unit cell edges  $a$  and  $c$ , (b) unit cell volumes  $V$  and (c)  $c/a$  ratio as a function of  $x$ . The estimated errors for  $a$ ,  $c$  and  $V$  are less than the size of the points in the figure.

Rietveld refinement of neutron data were performed for  $\text{CaAl}_{9.5}\text{Fe}_{2.5}\text{O}_{19}$ ,  $\text{CaAl}_{11.5}\text{Mn}_{0.5}\text{O}_{19}$ , and  $\text{CaAl}_{10}\text{SnMnO}_{19}$  samples. Neutron data of  $\text{CaAl}_{9.5}\text{Fe}_{2.5}\text{O}_{19}$  phase with a Rietveld fit is shown in Figure 6.13, similar plots of  $\text{CaAl}_{11.5}\text{Mn}_{0.5}\text{O}_{19}$  (impurities of  $\text{CaAl}_4\text{O}_7$ , ~7% by mass and  $\text{MnAl}_2\text{O}_4$ , ~2% by mass) and  $\text{CaAl}_{10}\text{SnMnO}_{19}$  samples might be found in Figure 6.14 and Figure 6.15 respectively. Refinement results are given in Table 6.2. Atoms coordinates and anisotropic displacements of ions for  $\text{CaAl}_{9.5}\text{Fe}_{2.5}\text{O}_{19}$  phase are summarized in Table 6.3,  $\text{CaAl}_{11.5}\text{Mn}_{0.5}\text{O}_{19}$ : Table 6.4 and  $\text{CaAl}_{10}\text{SnMnO}_{19}$ : Table 6.5. Thermal displacement parameters are given in Table 6.6. Al, Mn, Fe and Sn have well distinguished values of neutron bound coherent scattering lengths (Al (3.449 fm), Mn (-3.73 fm), Fe (9.94 fm), Sn (5.93 fm) – [68]), thus cation occupancies could be refined accurately and neutron data refinement were performed successfully.

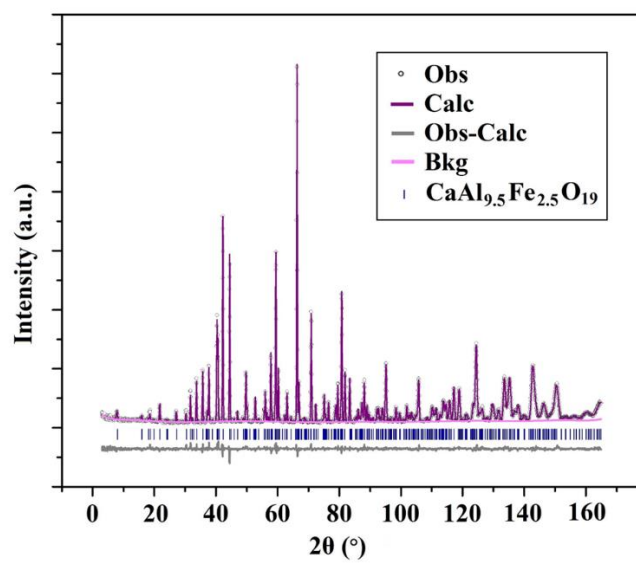


Figure 6.13 Neutron data of  $\text{CaAl}_{9.5}\text{Fe}_{2.5}\text{O}_{19}$  phase shown with a Rietveld fit.

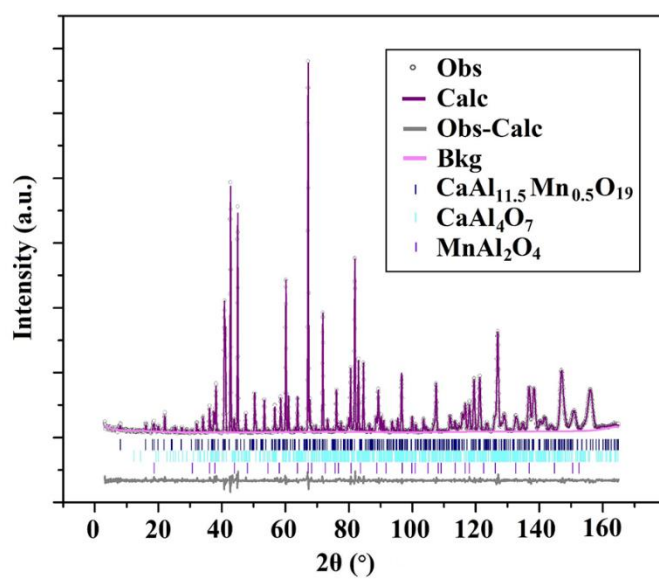


Figure 6.14 Neutron data of  $\text{CaAl}_{11.5}\text{Mn}_{0.5}\text{O}_{19}$  phase shown with a Rietveld fit.

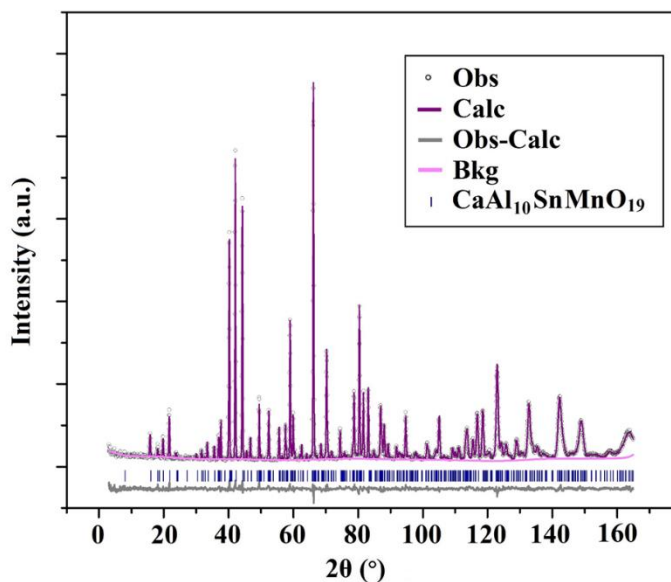


Figure 6.15 Neutron data of  $\text{CaAl}_{10}\text{SnMnO}_{19}$  phase shown with a Rietveld fit.

Table 6.2 Cell parameters by Rietveld refinement of  $\text{CaAl}_{9.5}\text{Fe}_{2.5}\text{O}_{19}$ ,  $\text{CaAl}_{11.5}\text{Mn}_{0.5}\text{O}_{19}$  and  $\text{CaAl}_{10}\text{SnMnO}_{19}$  samples.

Compound	$\text{CaAl}_{9.5}\text{Fe}_{2.5}\text{O}_{19}$	$\text{CaAl}_{11.5}\text{Mn}_{0.5}\text{O}_{19}$	$\text{CaAl}_{10}\text{SnMnO}_{19}$
$a$ (Å)	5.6302(5)	5.5640(2)	5.6402(6)
$c$ (Å)	22.151(5)	21.915(7)	22.379(9)
$V$ (Å <sup>3</sup> )	608.12(2)	587.57(4)	616.57(9)
$R_{\text{wp}}$ (%)	5.16	6.00	5.96
$R_{\text{p}}$ (%)	4.22	4.54	4.61
$\chi^2$	1.45	1.76	1.59

Table 6.3 Neutron structural refinement of  $\text{CaAl}_{9.50}\text{Fe}_{2.50}\text{O}_{19}$ . The refined chemical formula of the compound is  $\text{CaAl}_{9.47}\text{Fe}_{2.53}\text{O}_{19}$ .

Atoms	Wyckoff position	$x$	$y$	$z$	Occupancy	$U_{\text{iso}}$ (Å <sup>2</sup> )
Ca	2d	2/3	1/3	1/4	1.00	0.013(2)
Al1	2a	0	0	0	0.902(8)	0.006(1)
Al2	4e	0	0	0.2522(4)	0.321(9)	0.003(2)
Al3	4f	1/3	2/3	0.0285(7)	0.626(4)	0.009(4)
Al4	4f	1/3	2/3	0.1895(8)	0.734(5)	0.007(0)
Al5	12k	0.1683(2)	0.3366(4)	-0.1092(2)	0.867(7)	0.003(1)
Fe1	2a	0	0	0	0.098(8)	0.007(1)
Fe2	4e	0	0	0.2522(4)	0.178(1)	0.003(2)
Fe3	4f	1/3	2/3	0.0285(7)	0.374(4)	0.009(4)

<b>Fe4</b>	4 <i>f</i>	1/3	2/3	0.1895(8)	0.266(5)	0.007(0)
<b>Fe5</b>	12 <i>k</i>	0.1683(2)	0.3366(4)	-0.1092(2)	0.132(3)	0.003(1)
<b>O1</b>	4 <i>e</i>	0	0	0.1481(9)	1.00	0.009(1)
<b>O2</b>	4 <i>f</i>	1/3	2/3	-0.0556(1)	1.00	0.006(4)
<b>O3</b>	6 <i>h</i>	0.1842(6)	0.3685(2)	1/4	1.00	0.005(4)
<b>O4</b>	12 <i>k</i>	0.1526(8)	0.3053(7)	0.0522(1)	1.00	0.008(5)
<b>O5</b>	12 <i>k</i>	0.5050(7)	1.0101(5)	0.1486(9)	1.00	0.006(3)

Table 6.4 Neutron structural refinement of  $\text{CaAl}_{11.50}\text{Mn}_{0.50}\text{O}_{19}$ . The refined chemical formula of the compound is  $\text{CaAl}_{11.62}\text{Mn}_{0.38}\text{O}_{19}$ .

Atoms	Wyckoff position	<i>x</i>	<i>y</i>	<i>z</i>	Occupancy	$U_{\text{iso}} (\text{\AA}^2)$
<b>Ca</b>	2 <i>d</i>	2/3	1/3	1/4	1.00	0.015(5)
<b>Al1</b>	2 <i>a</i>	0	0	0	0.983(6)	0.003(1)
<b>Al2</b>	4 <i>e</i>	0	0	0.2590(7)	0.5	0.005(1)
<b>Al3</b>	4 <i>f</i>	1/3	2/3	0.0276(2)	0.955(4)	0.004(2)
<b>Al4</b>	4 <i>f</i>	1/3	2/3	0.1906(5)	0.955(5)	0.004(1)
<b>Al5</b>	12 <i>k</i>	0.1692(8)	0.3385(6)	-0.1091(6)	0.968(9)	0.006(4)
<b>Mn1</b>	2 <i>a</i>	0	0	0	0.017(6)	0.003(1)
<b>Mn3</b>	4 <i>f</i>	1/3	2/3	0.0276(2)	0.045(4)	0.004(2)
<b>Mn4</b>	4 <i>f</i>	1/3	2/3	0.1906(5)	0.045(5)	0.004(1)
<b>Mn5</b>	12 <i>k</i>	0.1692(8)	0.3385(6)	-0.1091(6)	0.031(1)	0.006(4)
<b>O1</b>	4 <i>e</i>	0	0	0.1494(3)	1.00	0.004(2)
<b>O2</b>	4 <i>f</i>	1/3	2/3	-0.0553(3)	1.00	0.004(1)
<b>O3</b>	6 <i>h</i>	0.1812(6)	0.3625(1)	1/4	1.00	0.003(2)
<b>O4</b>	12 <i>k</i>	0.1547(2)	0.3094(3)	0.0521(3)	1.00	0.003(1)
<b>O5</b>	12 <i>k</i>	0.5035(4)	1.0070(8)	0.1494(6)	1.00	0.003(1)

Table 6.5 Neutron structural refinement of  $\text{CaAl}_{10}\text{Sn}_{1.0}\text{Mn}_{1.0}\text{O}_{19}$ . The refined chemical formula of the compound is  $\text{CaAl}_{10.01}\text{Sn}_{0.98}\text{Mn}_{1.00}\text{O}_{19.00}$ .

Atoms	Wyckoff position	<i>x</i>	<i>y</i>	<i>z</i>	Occupancy	$U_{\text{iso}} (\text{\AA}^2)$
<b>Ca</b>	2 <i>d</i>	2/3	1/3	1/4	1.00	0.0377(17)
<b>Al1</b>	2 <i>a</i>	0	0	0	0.973(11)	0.0048(17)
<b>Al2</b>	4 <i>e</i>	0	0	0.2627(1)	0.456(6)	0.0058(24)
<b>Al3</b>	4 <i>f</i>	1/3	2/3	0.0223(8)	0.607(4)	0.002(1)
<b>Al4</b>	4 <i>f</i>	1/3	2/3	0.1888(1)	0.608(21)	0.0034(2)
<b>Al5</b>	12 <i>k</i>	0.1664(8)	0.3329(6)	-0.1069(9)	0.950(4)	0.0058(5)
<b>Mn1</b>	2 <i>a</i>	0	0	0	0.027(11)	0.0048(17)
<b>Mn2</b>	4 <i>e</i>	0	0	0.2627(1)	0.026(6)	0.0058(24)



<b>Mn3</b>	4 <i>f</i>	1/3	2/3	0.0223(8)	0.393(4)	0.002(1)
<b>Mn5</b>	12 <i>k</i>	0.1664(8)	0.3329(6)	-0.1069(9)	0.023(4)	0.0255(5)
<b>Sn2</b>	4 <i>e</i>	0	0	0.2627(1)	0.0179(6)	0.02351(2)
<b>Sn4</b>	4 <i>f</i>	1/3	2/3	0.1888(1)	0.392(21)	0.0034(2)
<b>Sn5</b>	12 <i>k</i>	0.1664(8)	0.3329(6)	-0.1069(9)	0.027(4)	0.0058(5)
<b>O1</b>	4 <i>e</i>	0	0	0.1488(7)	1.00	0.00475(2)
<b>O2</b>	4 <i>f</i>	1/3	2/3	-0.0586(4)	1.00	0.00788(4)
<b>O3</b>	6 <i>h</i>	0.1802(0)	0.3600(1)	1/4	1.00	0.0062(1)
<b>O4</b>	12 <i>k</i>	0.1506(9)	0.3012(8)	0.0525(5)	1.00	0.00879(1)
<b>O5</b>	12 <i>k</i>	0.5077(0)	1.0153(0)	0.14864(8)	1.00	0.00578(1)

Table 6.6 Thermal displacement parameters.

	$U_{11} (\text{\AA}^2)$	$U_{22} (\text{\AA}^2)$	$U_{33} (\text{\AA}^2)$	$U_{12} (\text{\AA}^2)$	$U_{13} (\text{\AA}^2)$	$U_{23} (\text{\AA}^2)$
<b>CaAl<sub>9.5</sub>Fe<sub>2.5</sub>O<sub>19</sub></b>						
<b>Ca</b>	0.011(9)	0.011(9)	0.015(7)	0.005(9)	0.0	0.0
<b>O1</b>	0.002(2)	0.002(2)	0.009(8)	0.001(8)	0.0	0.0
<b>O2</b>	0.002(2)	0.002(2)	0.007(3)	0.001(0)	0.0	0.0
<b>O3</b>	0.004(4)	0.004(4)	0.004(9)	-0.001(0)	0.0	0.0
<b>O4</b>	0.005(0)	0.008(5)	0.004(9)	0.004(3)	0.000(3)	0.000(6)
<b>O5</b>	0.004(5)	0.005(3)	0.008(7)	0.002(7)	0.000(9)	0.001(8)
<b>CaAl<sub>11.5</sub>Mn<sub>0.5</sub>O<sub>19</sub></b>						
<b>Ca</b>	0.009(7)	0.009(7)	0.026(5)	0.004(9)	0.0	0.0
<b>O1</b>	0.002(1)	0.002(1)	0.010(6)	0.001(0)	0.0	0.0
<b>O2</b>	0.005(9)	0.005(9)	0.007(3)	0.001(0)	0.0	0.0
<b>O3</b>	0.006(7)	0.001(4)	0.004(2)	-0.000(9)	0.0	0.0
<b>O4</b>	0.004(2)	0.001(9)	0.004(6)	0.001(0)	0.000(7)	0.001(5)
<b>O5</b>	0.003(9)	0.003(4)	0.003(4)	0.001(7)	0.000(4)	0.000(8)
<b>CaAl<sub>10</sub>SnMnO<sub>19</sub></b>						
<b>Ca</b>	0.018(0)	0.018(0)	0.069(4)	0.009(0)	0.0	0.0
<b>O1</b>	0.001(9)	0.001(9)	0.002(2)	0.000(9)	0.0	0.0
<b>O2</b>	0.004(4)	0.004(4)	0.007(0)	0.002(2)	0.0	0.0
<b>O3</b>	0.006(9)	0.001(1)	0.004(5)	-0.000(9)	0.0	0.0
<b>O4</b>	0.004(8)	0.001(7)	0.004(7)	0.001(0)	0.000(7)	0.001(9)
<b>O5</b>	0.003(7)	0.007(4)	0.003(4)	0.003(7)	0.000(8)	0.001(5)

Refinement for all samples were made using  $P6_3/mmc$  space group. The common feature of hibonite-type compounds is underbonded  $\text{Ca}^{2+}$  and some  $\text{Al}^{3+}$  sites [69]. Calcium shows a big difference in displacement parameters at low and high temperature, its vibrational movements larger than coordinating oxygen atoms. Ca is a “rattling ion” in the structure [14]. All calcium and oxygen sites are fully occupied.

TBP site (M2) is splitted along *c*-axis into two equivalent sites and each site is half occupied. They are located on the equal distances above and below the TBP equatorial plane [70]. Splitted sites are common for ions which don't like to sit in the middle of polyhedra. The distance between splitted M2 sites in  $\text{CaAl}_{11.5}\text{Mn}_{0.5}\text{O}_{19}$  is 0.39755 Å and in  $\text{CaAl}_{10}\text{SnMnO}_{19}$  is 0.40776 Å. In  $\text{CaAl}_{9.5}\text{Fe}_{2.5}\text{O}_{19}$  the same distance decreases and equals 0.09924 Å; in  $\text{CaAl}_6\text{Fe}_6\text{O}_{19}$  [16] splitted M2 site disappears. Introducing iron into M2 position gradually removes the local strain field around this site and with increasing of Fe concentration M2 site ceases to be splitted. Al2 cation is more underbonded in compounds with larger site splitting: BVS (Al2) = 2.54 ( $\text{CaAl}_{11.5}\text{Mn}_{0.5}\text{O}_{19}$ ) and BVS (Al2) = 2.47 ( $\text{CaAl}_{10}\text{SnMnO}_{19}$ ).  $\text{CaAl}_{9.5}\text{Fe}_{2.5}\text{O}_{19}$  hibonite has shorter Al2-O1' apical distances comparing to  $\text{CaAl}_{11.5}\text{Mn}_{0.5}\text{O}_{19}$  and  $\text{CaAl}_{10}\text{SnMnO}_{19}$  compounds as a result BVS (Al2) increases; BVS (Al2) = 2.73 ( $\text{CaAl}_{9.5}\text{Fe}_{2.5}\text{O}_{19}$ ).  $\text{CaAl}_6\text{Fe}_6\text{O}_{19}$  has BVS (Al2) ~ 3 when splitting vanishes, the compound has the shortest Al2-O1' bond distance equals 2.2301 Å. Selected bond lengths (Å) of  $\text{CaAl}_{9.5}\text{Fe}_{2.5}\text{O}_{19}$ ,  $\text{CaAl}_{11.5}\text{Mn}_{0.5}\text{O}_{19}$  and  $\text{CaAl}_{10}\text{SnMnO}_{19}$  phases are given in Table 6.7.

Table 6.7 Selected bond lengths (Å) of  $\text{CaAl}_{9.5}\text{Fe}_{2.5}\text{O}_{19}$ ,  $\text{CaAl}_{11.5}\text{Mn}_{0.5}\text{O}_{19}$  and  $\text{CaAl}_{10}\text{SnMnO}_{19}$  phases.

Bond (Å)	$\text{CaAl}_{9.5}\text{Fe}_{2.5}\text{O}_{19}$	$\text{CaAl}_{11.5}\text{Mn}_{0.5}\text{O}_{19}$	$\text{CaAl}_{10}\text{SnMnO}_{19}$
<b>6 × M1—O4</b>	<b>1.8853(6)</b>	<b>1.8783(9)</b>	<b>1.8795(0)</b>
<b>3 × M2—O3</b>	1.7975(7)	1.7580(6)	1.7741(7)
<b>M2—O1</b>	2.2056(3)	2.0052(8)	2.0683(6)
<b>M2—O1'</b>	2.3048(7)	2.4028(4)	2.4761(2)
<b>M2—O (average)</b>	<b>1.981</b>	<b>1.936</b>	<b>1.973</b>
<b>3 × M3—O4</b>	1.8378(4)	1.8032(4)	1.8806(9)
<b>M3—O2</b>	1.8647(2)	1.8179(1)	1.9094(6)
<b>M3—O (average)</b>	<b>1.844</b>	<b>1.807</b>	<b>1.888</b>
<b>M4—M4</b>	<b>2.6768(0)</b>	<b>2.6013(9)</b>	<b>2.7701(9)</b>
<b>3 × M4—O5</b>	1.9040(5)	1.8723(0)	1.9182(7)
<b>3 × M4—O3</b>	1.9760(3)	1.9595(4)	2.0372(8)
<b>M4—O (average)</b>	<b>1.940</b>	<b>1.916</b>	<b>1.978</b>
<b>2 × M5—O5</b>	1.8169(4)	1.8071(0)	1.8443(2)
<b>M5—O1</b>	1.8545(9)	1.8548(0)	1.8805(7)
<b>M5—O2</b>	1.9999(4)	1.9726(5)	1.9499(9)
<b>2 × M5—O4</b>	2.0154(5)	2.0035(4)	1.9758(2)
<b>M5—O (average)</b>	<b>1.920</b>	<b>1.907</b>	<b>1.912</b>

As we mentioned above hibonite structure is built of two blocks (spinel and trigonal bipyramidal layer).  $A^{2+}B^{3+}_2O_4$  is a spinel structure, it is a cubic closed-packed array of oxygen atoms with 1/2 of  $O_h$  and 1/8 of  $T_d$  holes filled by  $A^{2+}$  and  $B^{3+}$  transition metal cations. In normal spinel  $A^{2+}$  sits in  $T_d$  holes and  $B^{3+}$  occupies  $O_h$  holes. In inverse spinel  $A^{2+}$  has a tendency to sit in  $O_h$  sites and  $B^{3+}$  fully occupies  $T_d$  holes and 1/2 of  $O_h$  holes. Crystal field stabilization energy value helps to understand the transition metals preferences to occupy one or the other site in spinel/inverse spinel structure.  $Mn^{2+}$  ( $d^5$ ) and its isostructural  $Fe^{3+}$  ( $d^5$ ) have zero  $O_h$  and  $T_d$  stabilization energies, they don't have preference for  $O_h$  or  $T_d$  site.  $Mn^{3+}$  ( $d^4$ ) cation has  $O_h$  stabilization energy equals 135.4 kJ/mol,  $T_d$  stabilization energy is 40.1 kJ/mol, and excess of  $O_h$  stabilization energy is 95.3 kJ/mol; it shows that  $Mn^{3+}$  has the preference for  $O_h$  sites [71].

Moving from spinel to hibonite one can notice similar trends. In  $CaAl_{10}SnMnO_{19}$  and  $CaAl_{9.5}Fe_{2.5}O_{19}$  structures  $Mn^{2+}$  and  $Fe^{3+}$  have a tendency to occupy tetrahedral site (Al3) (Table 6.8). As shown before [72]  $Al^{3+}$  ( $2p^6$ ) prefers to occupy high symmetry octahedral sites (Al1, Al4 and Al5) due to its higher ionic character than  $Mn^{2+}$  and  $Fe^{3+}$   $3d^5$  - ions. These 3d-transition metal cations have no crystal field stabilization energy, tend to form hybrid bonds with 2p orbitals of oxygen therefore they favor to occupy tetrahedral sites. As in spinel case,  $Mn^{3+}$  behaves differently due to its non-zero  $O_h$  stabilization energy. It has a tendency to occupy  $T_d$  and face-shared octahedral  $O_h$  (M4) positions in the hibonite structure as a result M3 and M4 sites have an identical percentage of occupation.

Table 6.8 Percent of site preferences in  $CaAl_{9.5}Fe_{2.5}O_{19}$ ,  $CaAl_{11.5}Mn_{0.5}O_{19}$ , and  $CaAl_{10}SnMnO_{19}$  compounds (without site multiplicities consideration).

Site	$CaAl_{9.5}Fe_{2.5}O_{19}$ (Fe%)	$CaAl_{11.5}Mn_{0.5}O_{19}$ (Mn%)	$CaAl_{10}SnMnO_{19}$ (Sn% and Mn%)
<b>M1: trigonal antiprism</b>	9.34	12.31	5.76 (Mn)
<b>M2: trigonal bipyramid</b>	16.97	0	5.54 (Mn), 4.10 (Sn)
<b>M3: tetrahedral</b>	35.62	32.59	83.80 (Mn)
<b>M4: face-shared octahedra</b>	25.34	32.58	89.72 (Sn)
<b>M5: edge-shared octahedra</b>	12.60	22.52	4.90 (Mn), 6.18 (Sn)

B-site cation distribution in  $\text{CaAl}_{10}\text{SnMnO}_{19}$  can be compared with similar hibonite-type  $\text{BaFe}_{12-x}\text{Co}_x\text{Sn}_x\text{O}_{19}$  compounds [73]. In both structures  $\text{Sn}^{4+}$  has a preference to enter face-shared octahedral (Al4) sites and in less degree edge-shared octahedral (Al5) sites and they don't occupy trigonal-antiprism (Al1) sites. As a result in  $\text{CaAl}_{10}\text{SnMnO}_{19}$  M4—M4 distance is larger than in  $\text{CaAl}_{11.5}\text{Mn}_{0.5}\text{O}_{19}$  and  $\text{CaAl}_{9.5}\text{Fe}_{2.5}\text{O}_{19}$  phases (Table 6.7) because high concentration of  $\text{Sn}^{4+}$  in M4 sites creates big repulsion between two neighboring Sn4 positions and they move away from each other along the *c*-axis.  $\text{M}^{2+}$  cations are distributed between octahedral (Al1: trigonal antiprism and Al2: trigonal bipyramid) and tetrahedral (Al3) sites, tend to sit in Al3 sites.

$\text{Mn}^{2+}$ ,  $\text{Mn}^{3+}$ , and  $\text{Fe}^{3+}$  transition metal cations are mainly responsible for the color in studied compounds (d-d transitions take place in these atoms), thus their environment is very important because it defines the value of field splitting energy ( $\Delta$ ) – difference in energy between splitted d-orbitals. Thus even small deviations of polyhedral geometry from the ideal affect the color of compounds.

$\text{CaAl}_{11.5}\text{Mn}_{0.5}\text{O}_{19}$ ,  $\text{CaAl}_{9.5}\text{Fe}_{2.5}\text{O}_{19}$ ,  $\text{CaAl}_{10}\text{SnMnO}_{19}$  (present work),  $\text{CaAl}_{12}\text{O}_{19}$  [12],  $\text{CaAl}_{12-2x}\text{Ti}_x\text{Ni}_x\text{O}_{19}$  ( $x = 0.5$  and  $1.0$ ) [53,69] and  $\text{CaAl}_6\text{Fe}_6\text{O}_{19}$  [16] structures were analyzed and special attention was paid to  $\text{M}_3\text{O}_4$  tetrahedra geometry because in all considered compounds transition metal cations which are responsible for the color mainly occupy  $T_d$  sites. Average M3—O bond length and average  $T_d$  bond angle of the structures were compared to analyze structure-property relationships (Fig. 6.16). M3—O bond length increases as larger transition metal cation ( $\text{Mn}^{3+}$ ,  $\text{Fe}^{3+}$ ,  $\text{Mn}^{2+}$ ,  $\text{Ni}^{2+}$ ) substitutes for  $\text{Al}^{3+}$ . With increasing of bond length the overlap between 3d transition metal orbitals and 2p O orbitals decreases, the bond becomes weaker. Lowering in energy occurs and there is an increasing of crystal field splitting energy. As a result samples with larger M3—O length show lighter colors (when *x* value is fixed). Introducing of larger than  $\text{Al}^{3+}$  cations in  $T_d$  site decrease structural strain around M3 position in hibonite structure. The overlap between orbitals also is defined by the magnitude of bond angle. The average  $T_d$  angle stays comparatively unchanged showing that M3—O bond distance provide the biggest effect on the orbital overlap.

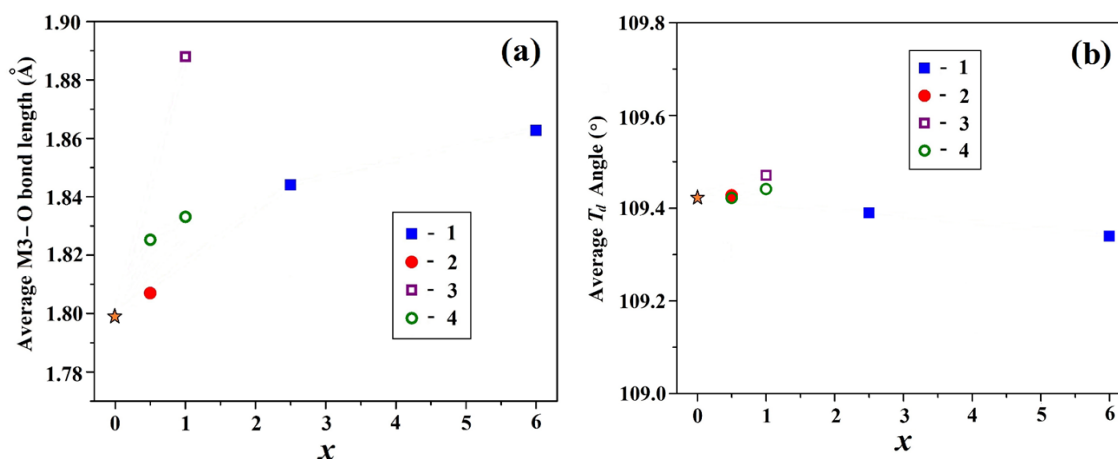
















Figure 6.16 (a) Average M3—O bond length, and (b) average  $T_d$  bond angle of  $\text{CaAl}_{12-x}\text{Fe}_x\text{O}_{19}$  (1)  $\text{CaAl}_6\text{Fe}_6\text{O}_{19}$  [40],  $\text{CaAl}_{11.5}\text{Mn}_{0.5}\text{O}_{19}$  (2),  $\text{CaAl}_{10}\text{SnMnO}_{19}$  (3), and  $\text{CaAl}_{12-2x}\text{Ti}_x\text{Ni}_x\text{O}_{19}$  [35,66] (4) as a function of  $x$  as determined by Rietveld refinement ( $\text{CaAl}_{12}\text{O}_{19}$  – small orange star [12]). The estimated error bars are less than the size of the points in the figure.














#### 6.4.3 Optical Properties: $L^*a^*b^*$ values, Diffuse Reflectance, NIR Reflectance















To describe the color of each compound  $L^*a^*b^*$  parameters were measured; all  $L^*a^*b^*$  values and pictures of compounds and given in Table 6.9.  $L^*$  represents a black ( $L^*=0$ )/white ( $L^*=100$ ) component of color,  $a^*$  is responsible for a red ( $a^*>0$ )/green ( $a^*<0$ ) component and  $b^*$  represents a yellow ( $b^*>0$ )/blue ( $b^*<0$ ) component.

Table 6.9  $L^*a^*b^*$  values and pictures of compounds.














Formula	$L^*$	$a^*$	$b^*$	Picture
<b><math>\text{CaAl}_{12-x}\text{Fe}_x\text{O}_{19}</math></b>				
$\text{CaAl}_{11.5}\text{Fe}_{0.5}\text{O}_{19}$	67.22	5.87	22.33	
$\text{CaAl}_{11}\text{FeO}_{19}$	52.47	11.35	30.15	
$\text{CaAl}_{10.5}\text{Fe}_{1.5}\text{O}_{19}$	45.26	13.28	30.83	
$\text{CaAl}_{10}\text{Fe}_2\text{O}_{19}$	37.18	15.48	28.35	
$\text{CaAl}_{9.5}\text{Fe}_{2.5}\text{O}_{19}$	20.74	10.95	11.37	













$\text{CaAl}_9\text{Fe}_3\text{O}_{19}$	20.56	9.54	8.46	
<b><math>\text{CaAl}_{11-x}\text{GaFe}_x\text{O}_{19}</math></b>				
$\text{CaAl}_{10.5}\text{GaFe}_{0.5}\text{O}_{19}$	62.27	5.92	24.32	
$\text{CaAl}_{10}\text{GaFeO}_{19}$	54.93	10.88	32.08	
$\text{CaAl}_{9.5}\text{GaFe}_{1.5}\text{O}_{19}$	41.83	13.96	32.54	
$\text{CaAl}_9\text{GaFe}_2\text{O}_{19}$	25.58	12.28	16.31	
<b><math>\text{CaAl}_{12-2x}\text{Sn}_x\text{Fe}_x\text{O}_{19}</math></b>				
$\text{CaAl}_{11}\text{Sn}_{0.5}\text{Fe}_{0.5}\text{O}_{19}$	64.69	0.97	14.05	
$\text{CaAl}_{10}\text{SnFeO}_{19}$	48.89	3.27	22.72	
$\text{CaAl}_9\text{Sn}_{1.5}\text{Fe}_{1.5}\text{O}_{19}$	32.00	5.79	19.98	
<b><math>\text{CaAl}_{12-2x}\text{Ti}_x\text{Fe}_x\text{O}_{19}</math></b>				
$\text{CaAl}_{11}\text{Ti}_{0.5}\text{Fe}_{0.5}\text{O}_{19}$	56.87	2.62	22.13	
$\text{CaAl}_{10}\text{TiFeO}_{19}$	34.87	4.08	19.74	
<b><math>\text{CaAl}_{12-x}\text{Mn}_x\text{O}_{19}</math></b>				
$\text{CaAl}_{11.9}\text{Mn}_{0.1}\text{O}_{19}$	66.92	8.50	18.46	
$\text{CaAl}_{11.8}\text{Mn}_{0.2}\text{O}_{19}$	56.89	11.49	22.90	
$\text{CaAl}_{11.7}\text{Mn}_{0.3}\text{O}_{19}$	41.27	13.60	23.83	
$\text{CaAl}_{11.6}\text{Mn}_{0.4}\text{O}_{19}$	38.29	11.53	19.24	

$\text{CaAl}_{11.5}\text{Mn}_{0.5}\text{O}_{19}$	37.04	13.48	22.58	
$\text{CaAl}_{11.4}\text{Mn}_{0.6}\text{O}_{19}$	32.90	12.71	20.39	
<b><math>\text{CaAl}_{12-2x}\text{Sn}_x\text{Mn}_x\text{O}_{19}</math></b>				
$\text{CaAl}_{11.8}\text{Sn}_{0.1}\text{Mn}_{0.1}\text{O}_{19}$	73.42	3.74	11.78	
$\text{CaAl}_{11.6}\text{Sn}_{0.3}\text{Mn}_{0.3}\text{O}_{19}$	64.83	7.81	13.87	
$\text{CaAl}_{11}\text{Sn}_{0.5}\text{Mn}_{0.5}\text{O}_{19}$	50.66	9.90	20.18	
$\text{CaAl}_{10.6}\text{Sn}_{0.7}\text{Mn}_{0.7}\text{O}_{19}$	42.34	13.17	17.87	
$\text{CaAl}_{10}\text{SnMnO}_{19}$	36.53	11.49	18.35	
<b><math>\text{CaAl}_{12-2x}\text{Ti}_x\text{Mn}_x\text{O}_{19}</math></b>				
$\text{CaAl}_{11}\text{Ti}_{0.5}\text{Mn}_{0.5}\text{O}_{19}$	64.86	8.31	18.26	
$\text{CaAl}_{10}\text{TiMnO}_{19}$	34.99	11.84	18.71	
<b><math>\text{CaAl}_{11-x}\text{Ti}_{0.5}\text{Cu}_{0.5}\text{Mn}_x\text{O}_{19}</math></b>				
$\text{CaAl}_{10.5}\text{Ti}_{0.5}\text{Cu}_{0.5}\text{Mn}_{0.5}\text{O}_{19}$	57.47	10.26	23.09	
$\text{CaAl}_{10}\text{Ti}_{0.5}\text{Cu}_{0.5}\text{MnO}_{19}$	31.96	12.18	16.88	
<b><math>\text{CaAl}_{10}\text{GeMO}_{19}</math></b>				
$\text{CaAl}_{10}\text{GeFeO}_{19}$	43.16	5.21	27.35	
$\text{CaAl}_{10}\text{GeMnO}_{19}$	38.39	11.18	16.55	
<b><math>\text{CaAl}_{12-x}\text{Cr}_x\text{O}_{19}</math></b>				
$\text{CaAl}_{11.5}\text{Cr}_{0.5}\text{O}_{19}$	62.77	2.20	8.30	

$\text{CaAl}_{11}\text{CrO}_{19}$	55.88	1.35	10.52	
$\text{CaAl}_{10.5}\text{Cr}_{1.5}\text{O}_{19}$	55.33	0.29	12.52	
$\text{CaAl}_{10}\text{Cr}_2\text{O}_{19}$	48.73	-0.32	13.66	
$\text{CaAl}_{9.5}\text{Cr}_{2.5}\text{O}_{19}$	46.29	-0.67	14.74	
$\text{CaAl}_9\text{Cr}_3\text{O}_{19}$	37.48	-0.42	16.12	
$\text{CaAl}_{8.5}\text{Cr}_{3.5}\text{O}_{19}$	31.97	0.13	15.15	
<b><math>\text{CaAl}_{11-x}\text{GaCr}_x\text{O}_{19}</math></b>				
$\text{CaAl}_{10.5}\text{GaCr}_{0.5}\text{O}_{19}$	58.58	1.95	9.00	
$\text{CaAl}_{10}\text{GaCrO}_{19}$	55.62	0.53	10.97	
<b><math>\text{CaAl}_{11-x}\text{InCr}_x\text{O}_{19}</math></b>				
$\text{CaAl}_{10.5}\text{InCr}_{0.5}\text{O}_{19}$	47.66	2.38	11.50	
$\text{CaAl}_{10}\text{InCrO}_{19}$	43.83	1.40	13.51	
<b><math>\text{CaAl}_{12-2x}\text{Ti}_x\text{Cu}_x\text{O}_{19}</math></b>				
$\text{CaAl}_{11}\text{Ti}_{0.5}\text{Cu}_{0.5}\text{O}_{19}$	72.85	2.83	9.60	
$\text{CaAl}_{10}\text{TiCuO}_{19}$	42.87	9.10	20.81	
$\text{CaAl}_9\text{Ti}_{1.5}\text{Cu}_{1.5}\text{O}_{19}$	55.29	6.27	22.25	
<b><math>\text{CaAl}_{11}\text{M}_{0.5}\text{Cu}_{0.5}\text{O}_{19}</math></b>				
$\text{CaAl}_{11}\text{Sn}_{0.5}\text{Cu}_{0.5}\text{O}_{19}$	78.11	-1.52	-0.93	
$\text{CaAl}_{11}\text{Ge}_{0.5}\text{Cu}_{0.5}\text{O}_{19}$	67.72	-1.51	2.77	
<b><math>\text{CaAl}_{9.5}\text{GaM}'_{0.5}\text{Cu}_{0.5}\text{M}''_{0.5}\text{O}_{19}</math></b>				



$\text{CaAl}_{9.5}\text{GaSn}_{0.5}\text{Cu}_{0.5}\text{Mn}_{0.5}\text{O}_{19}$	55.60	10.06	16.13	
$\text{CaAl}_{9.5}\text{GaSn}_{0.5}\text{Cu}_{0.5}\text{Fe}_{0.5}\text{O}_{19}$	58.79	1.00	20.58	
$\text{CaAl}_{9.5}\text{GaSn}_{0.5}\text{Cu}_{0.5}\text{Cr}_{0.5}\text{O}_{19}$	47.93	3.04	6.51	
$\text{CaAl}_{9.5}\text{GaTi}_{0.5}\text{Cu}_{0.5}\text{Mn}_{0.5}\text{O}_{19}$	36.53	7.68	14.24	
$\text{CaAl}_{9.5}\text{GaTi}_{0.5}\text{Cu}_{0.5}\text{Fe}_{0.5}\text{O}_{19}$	60.86	5.96	24.98	
$\text{CaAl}_{9.5}\text{GaTi}_{0.5}\text{Cu}_{0.5}\text{Cr}_{0.5}\text{O}_{19}$	33.66	2.41	6.87	
<b><math>\text{CaAl}_{9.5}\text{In}M'_{0.5}\text{Cu}_{0.5}M''_{0.5}\text{O}_{19}</math></b>				
$\text{CaAl}_{9.5}\text{InSn}_{0.5}\text{Cu}_{0.5}\text{Mn}_{0.5}\text{O}_{19}$	31.94	10.56	13.11	
$\text{CaAl}_{9.5}\text{InSn}_{0.5}\text{Cu}_{0.5}\text{Fe}_{0.5}\text{O}_{19}$	47.24	1.49	22.00	
$\text{CaAl}_{9.5}\text{InSn}_{0.5}\text{Cu}_{0.5}\text{Cr}_{0.5}\text{O}_{19}$	46.22	3.17	10.21	
$\text{CaAl}_{9.5}\text{InTi}_{0.5}\text{Cu}_{0.5}\text{Mn}_{0.5}\text{O}_{19}$	55.74	9.39	20.14	
$\text{CaAl}_{9.5}\text{InTi}_{0.5}\text{Cu}_{0.5}\text{Fe}_{0.5}\text{O}_{19}$	53.32	1.90	19.39	
$\text{CaAl}_{9.5}\text{InTi}_{0.5}\text{Cu}_{0.5}\text{Cr}_{0.5}\text{O}_{19}$	37.96	1.62	9.50	
<b><math>\text{CaAl}_{10.5}M'_{0.5}\text{Cu}_{0.5}M''_{0.5}\text{O}_{19}</math></b>				
$\text{CaAl}_{10.5}\text{Sn}_{0.5}\text{Cu}_{0.5}\text{Mn}_{0.5}\text{O}_{19}$	59.83	9.57	17.47	

$\text{CaAl}_{10.5}\text{Sn}_{0.5}\text{Cu}_{0.5}\text{Fe}_{0.5}\text{O}_{19}$	62.20	1.17	16.26	
$\text{CaAl}_{10.5}\text{Sn}_{0.5}\text{Cu}_{0.5}\text{Cr}_{0.5}\text{O}_{19}$	50.03	3.78	6.02	
$\text{CaAl}_{10.5}\text{Ge}_{0.5}\text{Cu}_{0.5}\text{Mn}_{0.5}\text{O}_{19}$	44.99	9.19	17.57	
$\text{CaAl}_{10.5}\text{Ge}_{0.5}\text{Cu}_{0.5}\text{Fe}_{0.5}\text{O}_{19}$	56.79	3.18	17.22	
$\text{CaAl}_{10.5}\text{Ge}_{0.5}\text{Cu}_{0.5}\text{Cr}_{0.5}\text{O}_{19}$	48.25	4.29	5.70	
<b><math>\text{CaAl}_{11-x}\text{Ti}_{0.5}\text{Cu}_{0.5}\text{M}_{0.5}\text{O}_{19}</math></b>				
$\text{CaAl}_{10.5}\text{Ti}_{0.5}\text{Cu}_{0.5}\text{Fe}_{0.5}\text{O}_{19}$	54.53	3.47	23.43	
$\text{CaAl}_{10.5}\text{Ti}_{0.5}\text{Cu}_{0.5}\text{Cr}_{0.5}\text{O}_{19}$	46.96	3.22	6.58	
$\text{CaAl}_{10.5}\text{Ti}_{0.5}\text{Cu}_{0.5}\text{Mn}_{0.25}\text{Fe}_{0.25}\text{O}_{19}$	55.79	3.72	15.56	
$\text{CaAl}_{10.5}\text{Sn}_{0.5}\text{Cu}_{0.5}\text{Mn}_{0.25}\text{Fe}_{0.25}\text{O}_{19}$	69.95	0.78	20.57	
<b><math>\text{CaAl}_{11}\text{M}'_{0.5}\text{M}''_{0.5}\text{O}_{19}</math></b>				
$\text{CaAl}_{11}\text{Cr}_{0.5}\text{Fe}_{0.5}\text{O}_{19}$	51.47	5.12	15.47	
$\text{CaAl}_{11}\text{Cr}_{0.5}\text{Mn}_{0.5}\text{O}_{19}$	43.43	8.11	16.58	
$\text{CaAl}_{11}\text{Fe}_{0.5}\text{Mn}_{0.5}\text{O}_{19}$	41.47	6.65	17.88	

UV-VIS measurements were performed to estimate the crystal field splitting of compounds and illustrating the structure/property changes through the solid solutions. The UV-VIS diffuse reflectance spectra were measured for four solid solutions:  $\text{CaAl}_{12-x}\text{Fe}_x\text{O}_{19}$  ( $x = 0.5 - 3.0$ ) (Fig. 6.17(a)),  $\text{CaAl}_{12-x}\text{Mn}_x\text{O}_{19}$  ( $x = 0.1-0.6$ ) (Fig. 6.17(b)),  $\text{CaAl}_{12-x}$

$_{2x}\text{Sn}_x\text{Mn}_x\text{O}_{19}$  ( $x = 0.1\text{--}1.0$ ) (Fig. 6.17(c)) and  $\text{CaAl}_{12-x}\text{Cr}_x\text{O}_{19}$  ( $x = 0.5\text{--}3.5$ ) (Fig. 6.17(d)); measured reflectance was transformed to absorbance using the Kubelka-Munk equation.

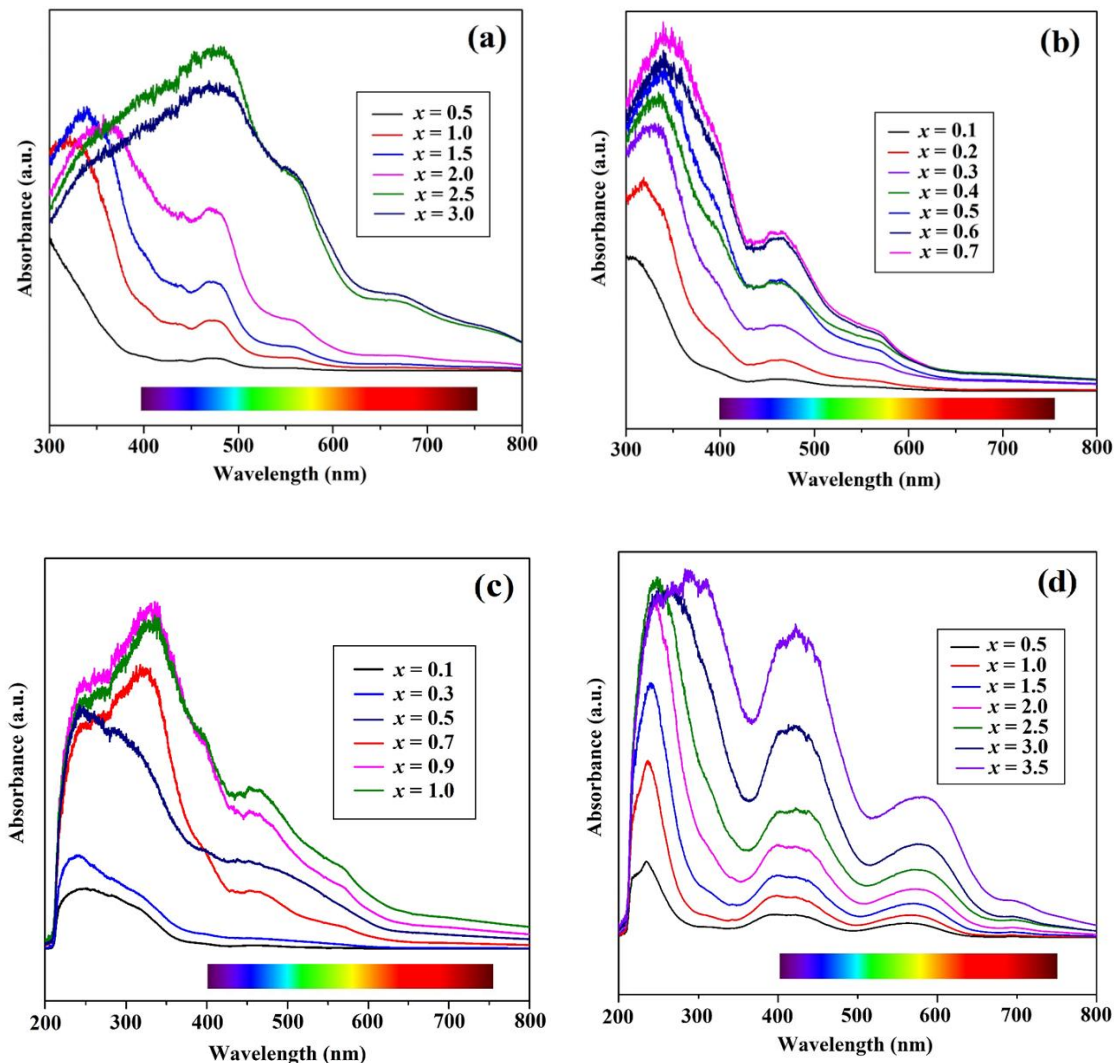


Figure 6.17 Diffuse-reflectance spectra of (a)  $\text{CaAl}_{12-x}\text{Fe}_x\text{O}_{19}$  ( $x = 0.5\text{--}3.0$ ); (b)  $\text{CaAl}_{12-x}\text{Mn}_x\text{O}_{19}$  ( $x = 0.1\text{--}0.6$ ); (c)  $\text{CaAl}_{12-2x}\text{Sn}_x\text{Mn}_x\text{O}_{19}$  ( $x = 0.1\text{--}1.0$ ) and (d)  $\text{CaAl}_{12-x}\text{Cr}_x\text{O}_{19}$  ( $x = 0.5\text{--}3.5$ ) series.

Diffuse reflectance spectra of  $\text{CaAl}_{10}\text{Fe}_2\text{O}_{19}$ ,  $\text{CaAl}_{11.5}\text{Mn}_{0.5}\text{O}_{19}$ ,  $\text{CaAl}_{10}\text{SnMnO}_{19}$  and  $\text{CaAl}_{10}\text{Cr}_2\text{O}_{19}$  compounds are shown in Figure 6.18. Absorption in the visible region of spectrum interprets the color of the sample which human eye can see.  $\text{CaAl}_{10}\text{Fe}_2\text{O}_{19}$ ,  $\text{CaAl}_{11.5}\text{Mn}_{0.5}\text{O}_{19}$  and  $\text{CaAl}_{10}\text{SnMnO}_{19}$  have one peak and one shoulder in visible region. Low energy peaks (2.50–2.75 eV) are due to d-d transitions, for samples with higher

concentration of transition metal in the structure d-d transitions become more significant, the intensity of these peaks go up. Also the color of samples become darker with addition of transition metal because intensity of interatomic excitations increases. High energy shoulder ( $\sim 3$  eV) in visible region and the peak in UV-region are due to transition metal –  $O^{2-}$  charge transfer. When amount of transition metal in structure is small charge transfer excitations are mainly liable for the color and minimum of absorbance became less sharp because transition metal –  $O^{2-}$  charge transfer intensity increases. Strong absorption in the green and blue regions and low or absence of absorption in the red-orange region is responsible for the observed tan/brown colors of  $CaAl_{10}Fe_2O_{19}$ ,  $CaAl_{11.5}Mn_{0.5}O_{19}$  and  $CaAl_{10}SnMnO_{19}$  samples.  $CaAl_{10}Cr_2O_{19}$  sample has two bands ( $\sim 2.12$  eV and  $\sim 3.12$  eV) for one single transition  $t^3_{2g} \rightarrow t^2_{2g}e^1_g$  due to electron-electron repulsion and this compound has olive color in contrast to the compounds described above. It is a known characteristic of  $Cr^{3+}$  ( $O_h$ ) complexes [74]. Estimated crystal field splitting in eV for selected compounds are summarized in Table 6.10. The crystal field splitting for each sample was estimated using extrapolation of the linear portion of the absorption onset in absorption vs. energy (eV) plot.

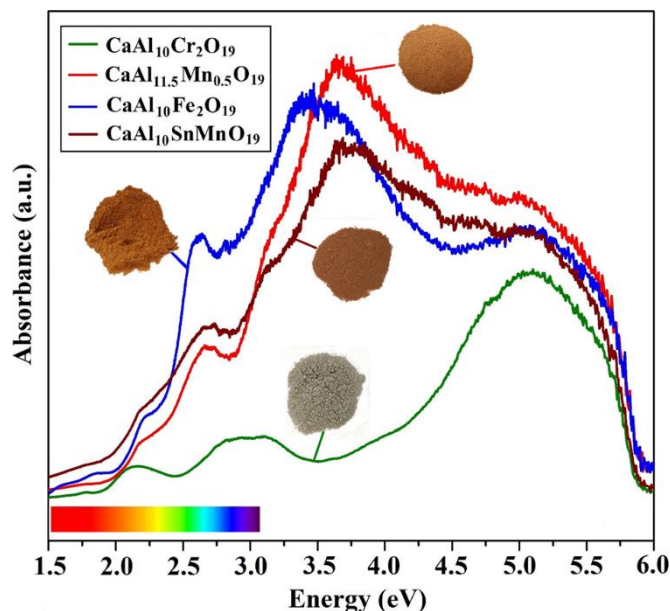
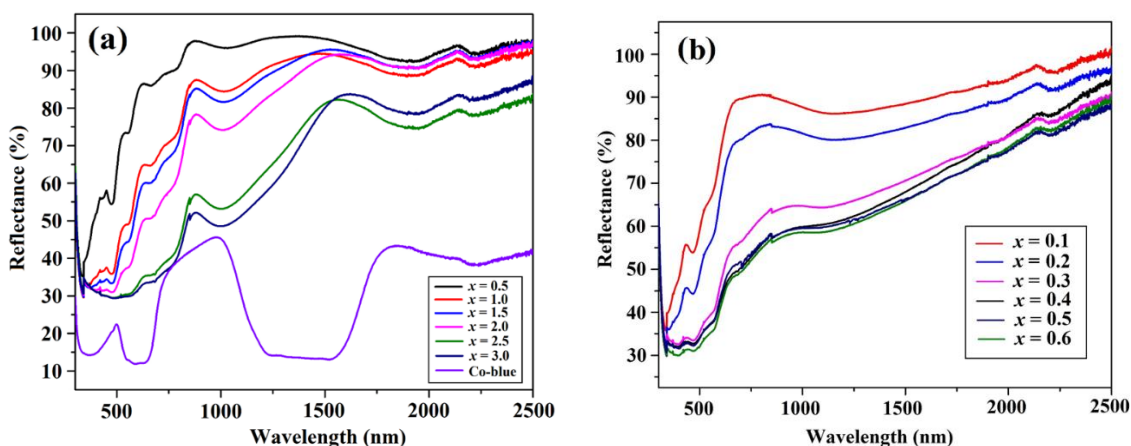


Figure 6.18 Diffuse-reflectance spectra of  $CaAl_{10}Fe_2O_{19}$ ,  $CaAl_{11.5}Mn_{0.5}O_{19}$ ,  $CaAl_{10}SnMnO_{19}$  and  $CaAl_{10}Cr_2O_{19}$ .

Table 6.10 Estimated crystal field splitting (eV) of selected compounds.

Compound	Estimated crystal field splitting (eV)
$\text{CaAl}_{11.5}\text{Fe}_{0.5}\text{O}_{19}$	2.61
$\text{CaAl}_{10.5}\text{Fe}_{1.5}\text{O}_{19}$	2.58
$\text{CaAl}_9\text{Fe}_3\text{O}_{19}$	2.25
$\text{CaAl}_{11.9}\text{Mn}_{0.1}\text{O}_{19}$	2.64
$\text{CaAl}_{11.5}\text{Mn}_{0.5}\text{O}_{19}$	2.58
$\text{CaAl}_{11.8}\text{Sn}_{0.1}\text{Mn}_{0.1}\text{O}_{19}$	2.76
$\text{CaAl}_{11}\text{Sn}_{0.5}\text{Mn}_{0.5}\text{O}_{19}$	2.61
$\text{CaAl}_{10}\text{SnMnO}_{19}$	2.57
$\text{CaAl}_{11.5}\text{Cr}_{0.5}\text{O}_{19}$	2.95
$\text{CaAl}_{9.5}\text{Cr}_{2.5}\text{O}_{19}$	2.82
$\text{CaAl}_{8.5}\text{Cr}_{3.5}\text{O}_{19}$	2.76

Reflectance of  $\text{CaAl}_{12-x}\text{Fe}_x\text{O}_{19}$  ( $x = 0.5\text{--}3.0$ ) (Fig. 6.19(a)),  $\text{CaAl}_{12-x}\text{Mn}_x\text{O}_{19}$  ( $x = 0.1\text{--}0.6$ ) (Fig. 6.19(b)),  $\text{CaAl}_{12-2x}\text{Sn}_x\text{Mn}_x\text{O}_{19}$  ( $x = 0.1\text{--}1.0$ ) (Fig. 6.19(c)) and  $\text{CaAl}_{12-x}\text{Cr}_x\text{O}_{19}$  ( $x = 0.5\text{--}3.5$ ) (Fig. 6.19(d)) samples in NIR region was measured. High reflectance in this region is an essential property of “Cool pigments”, pigments which reflect heat and stay cool under sun light. All synthesized compounds show relatively high reflectance (70 ~ - 80%) in NIR region. Our compounds might be promising candidates for “Cool pigments” application. Many commercially used pigments (Co-blue, for example, Figure 6.19(a)) reflect very poorly in NIR and their properties need to be improved.



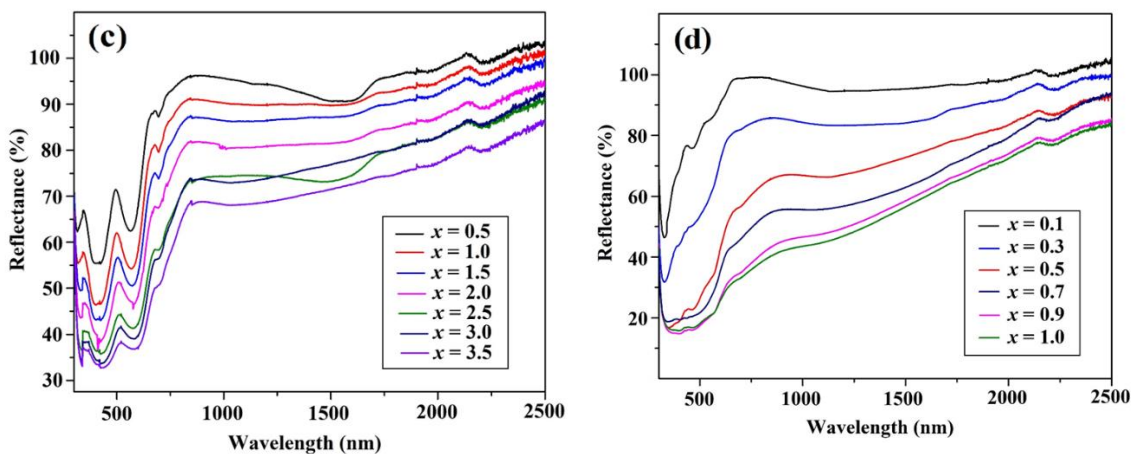


Figure 6.19 UV-VIS and NIR reflectance (%) of (a)  $\text{CaAl}_{12-x}\text{Fe}_x\text{O}_{19}$  ( $x = 0.5\text{--}3.0$ ) series and Co-blue pigment; (b)  $\text{CaAl}_{12-x}\text{Mn}_x\text{O}_{19}$  ( $x = 0.1\text{--}0.6$ ); (c)  $\text{CaAl}_{12-2x}\text{Sn}_x\text{Mn}_x\text{O}_{19}$  ( $x = 0.1\text{--}1.0$ ) and (d)  $\text{CaAl}_{12-x}\text{Cr}_x\text{O}_{19}$  ( $x = 0.5\text{--}3.5$ ) samples as a function of wavelength (nm).

#### 6.4.4 Magnetism

Magnetic properties measurements (magnetic susceptibility vs. temperature) were performed for  $\text{CaAl}_{11.5}\text{Mn}_{0.5}\text{O}_{19}$  and  $\text{CaAl}_{11}\text{Ti}_{0.5}\text{Mn}_{0.5}\text{O}_{19}$  samples to verify the oxidation states of manganese +3 and +2 respectively. Using inverse magnetic susceptibility vs. temperature plots (Fig. 6.20) and Curie-Weiss law Curie constants ( $C$ ), Weiss constants ( $\theta_w$ ) and effective magnetic moments ( $\mu_{\text{eff}}$ ) were calculated (Table 6.11). Diamagnetic correction was made. The compounds show paramagnetic behavior in 5-300 K temperature region. Received effective magnetic moments values are similar to the theoretical magnetic moments of high spin tetrahedral complexes of  $\text{Mn}^{3+}(3d^4, \mu_{\text{th}} = 4.89 \mu_B)$  in case of  $\text{CaAl}_{11.5}\text{Mn}_{0.5}\text{O}_{19}$  and  $\text{Mn}^{2+}(3d^5, \mu_{\text{th}} = 5.92 \mu_B)$  in case of  $\text{CaAl}_{11}\text{Ti}_{0.5}\text{Mn}_{0.5}\text{O}_{19}$ . This demonstrates the existence of  $\text{Mn}^{3+}$  and  $\text{Mn}^{2+}$  in the structures.



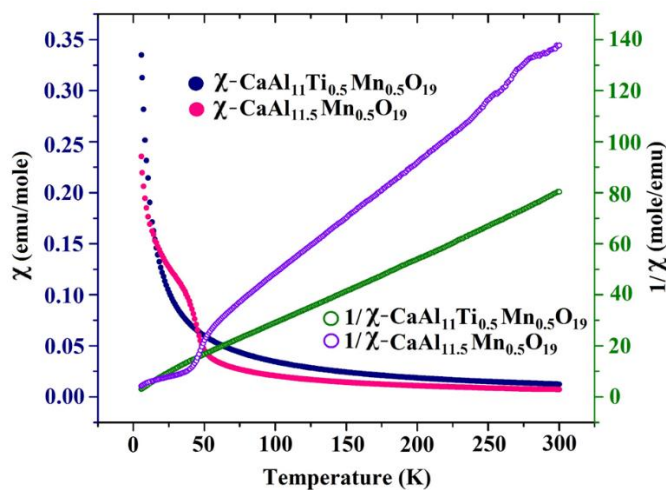


Figure 6.20 Magnetic susceptibility and inverse magnetic susceptibility of  $\text{CaAl}_{11.5}\text{Mn}_{0.5}\text{O}_{19}$  and  $\text{CaAl}_{11}\text{Ti}_{0.5}\text{Mn}_{0.5}\text{O}_{19}$  as a function of temperature; 1 emu (cgs units) =  $10^{-3}$  A m<sup>2</sup> (SI units).

Table 6.11 Calculated magnetic moments, Curie and Weiss constants of  $\text{CaAl}_{11.5}\text{Mn}_{0.5}\text{O}_{19}$  and  $\text{CaAl}_{11}\text{Ti}_{0.5}\text{Mn}_{0.5}\text{O}_{19}$  samples.

Compound	T region (K)	C	$\theta$ (K)	$\mu_{\text{eff}}$ ( $\mu_B$ )
<b><math>\text{CaAl}_{11.5}\text{Mn}_{0.5}\text{O}_{19}</math></b>	250–300	2.4307	-28.10	4.43
<b><math>\text{CaAl}_{11}\text{Ti}_{0.5}\text{Mn}_{0.5}\text{O}_{19}</math></b>	250–300	3.8270	-1.050	5.56

#### 6.4.5 Dielectric Properties

Dielectric properties of hibonite materials are not well studied. Arora A. and coauthors [75] investigated dielectric properties of co-substituted M-type barium hexaferrite, compounds with similar to hibonite structure. Recently we reported dielectric properties of  $\text{CaAl}_{11}\text{Ti}_{0.5}\text{Ni}_{0.5}\text{O}_{19}$  and  $\text{CaAl}_{10}\text{TiNiO}_{19}$  Ni-containing hibonite-type samples [53].

Dielectric measurements were made for compounds at frequencies of 1, 10, 100, 500, 750 kHz and 1 MHz and in the temperature range 25–250°C. Dielectric properties measurements were performed for  $\text{CaAl}_{11.5}\text{Fe}_{0.5}\text{O}_{19}$  and  $\text{CaAl}_{11.4}\text{Sn}_{0.3}\text{Mn}_{0.3}\text{O}_{19}$  compounds. Dielectric constant ( $\kappa$ ) and dielectric loss ( $\delta$ ) (at different applied frequencies) of  $\text{CaAl}_{11.5}\text{Fe}_{0.5}\text{O}_{19}$  and  $\text{CaAl}_{11.4}\text{Sn}_{0.3}\text{Mn}_{0.3}\text{O}_{19}$  as a function of temperature (°C) are shown in Fig. 6.21(a,b) and Fig. 6.21(c,d) correspondingly. Frequency dependence of dielectric constant and dielectric loss of  $\text{CaAl}_{11.5}\text{Fe}_{0.5}\text{O}_{19}$  and  $\text{CaAl}_{11.4}\text{Sn}_{0.3}\text{Mn}_{0.3}\text{O}_{19}$  at room temperature are given in Fig. 6.22. Studied samples are insulators.

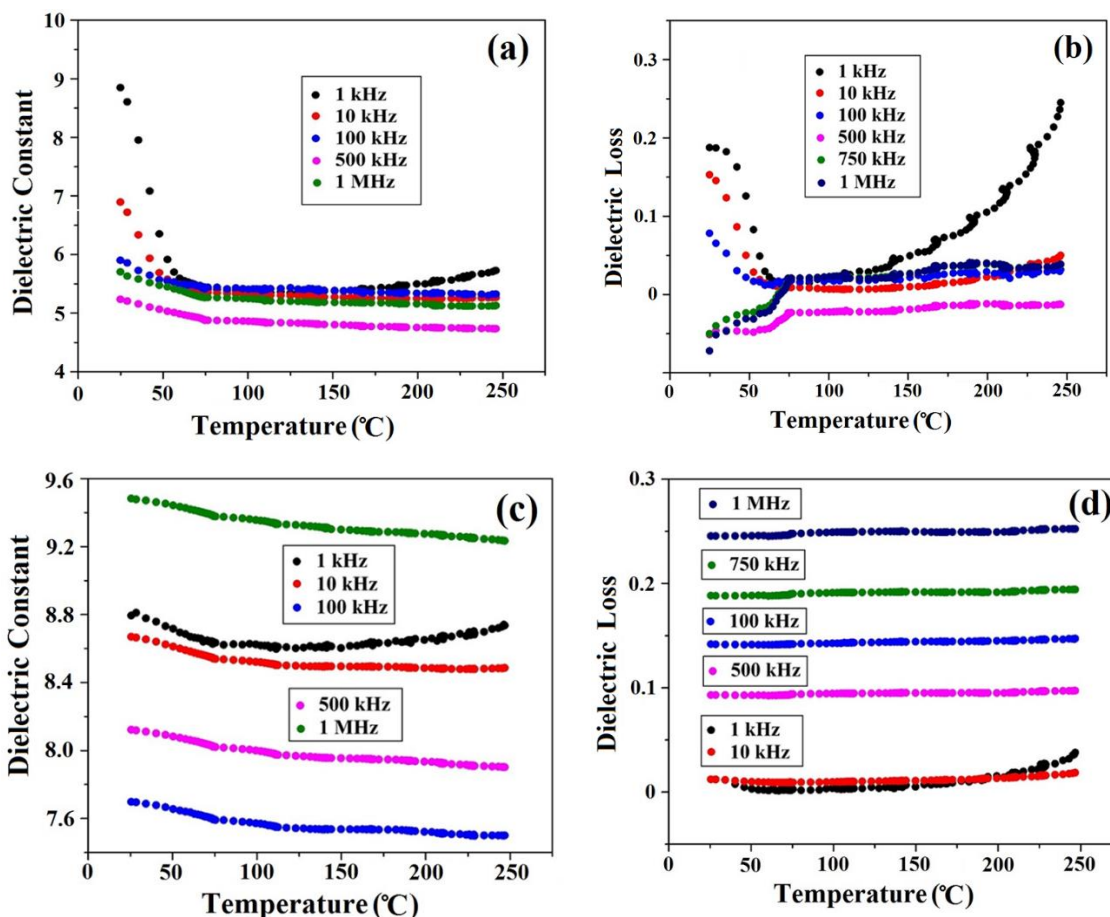


Figure 6.21 Dielectric constant (a) and dielectric loss (b) of  $\text{CaAl}_{11.5}\text{Fe}_{0.5}\text{O}_{19}$  as a function of temperature (°C); dielectric constant (c) and dielectric loss (d) of  $\text{CaAl}_{11.4}\text{Sn}_{0.3}\text{Mn}_{0.3}\text{O}_{19}$  as a function of temperature (°C).

Theoretical values of dielectric constants ( $\kappa_{\text{th}}$ ) for both compounds were calculated.  $\kappa_{\text{th}} = 9.37$  ( $\text{CaAl}_{11.5}\text{Fe}_{0.5}\text{O}_{19}$ ) and  $\kappa_{\text{th}} = 9.42$  ( $\text{CaAl}_{11.4}\text{Sn}_{0.3}\text{Mn}_{0.3}\text{O}_{19}$ ), these values were compared with experimental  $\kappa$  values for both compounds.  $\text{CaAl}_{11.5}\text{Fe}_{0.5}\text{O}_{19}$  shows smaller experimental  $\kappa$ ;  $\text{CaAl}_{11.4}\text{Sn}_{0.3}\text{Mn}_{0.3}\text{O}_{19}$  experimental  $\kappa$  values are smaller than  $\kappa_{\text{th}}$  at all frequencies except 1 MHz. For  $\text{CaAl}_{11.5}\text{Fe}_{0.5}\text{O}_{19}$  dielectric constant and dielectric loss go down with the increase of temperature and frequency. For  $\text{CaAl}_{11.4}\text{Sn}_{0.3}\text{Mn}_{0.3}\text{O}_{19}$  dielectric constant slightly decreases with increasing temperature and increases with increase of applied frequency; dielectric loss is relatively constant in 25-250 °C region and increases with frequency.



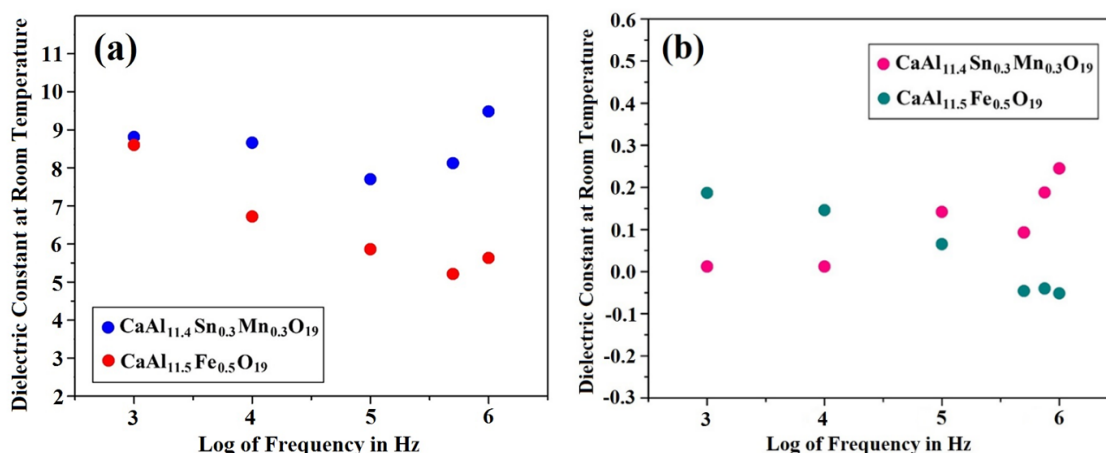


Figure 6.22 Frequency dependence of dielectric constants (a) and dielectric losses (b) of  $\text{CaAl}_{11.5}\text{Fe}_{0.5}\text{O}_{19}$  and  $\text{CaAl}_{11.4}\text{Sn}_{0.3}\text{Mn}_{0.3}\text{O}_{19}$  at room temperature.

## 6.5 Conclusion

We demonstrate in the present work that various colors can be induced in hibonite host  $\text{CaAl}_{12}\text{O}_{19}$  by tuning the crystal structure through M-site substitution using standard solid state synthesis method. Majority of phases are reported for the first time. Using neutron data of  $\text{CaAl}_{9.5}\text{Fe}_{2.5}\text{O}_{19}$ ,  $\text{CaAl}_{11.5}\text{Mn}_{0.5}\text{O}_{19}$  and  $\text{CaAl}_{10}\text{SnMnO}_{19}$  samples their structures were refined. Shades of all samples were characterized using  $L^*a^*b^*$  parameters and diffuse reflectance measurements. Magnetic measurements proved existence of  $\text{Mn}^{3+}$  and  $\text{Mn}^{2+}$  in  $\text{CaAl}_{11.5}\text{Mn}_{0.5}\text{O}_{19}$  and  $\text{CaAl}_{11}\text{Ti}_{0.5}\text{Mn}_{0.5}\text{O}_{19}$  accordingly. Synthesized compounds are cheap, nontoxic and stable, they might be promising candidates for “Cool pigments” application due to their relatively high reflectance in NIR region.

## 6.6 Acknowledgements

Text and figures within this chapter have been used in part or whole from the publication:

**Medina, E.A.**, Li, J., Subramanian, M.A. Colored oxides with hibonite structure II: Structural and optical properties of  $\text{CaAl}_{12}\text{O}_{19}$ -type pigments with chromophores based on Fe, Mn, Cr and Cu *Progress in Solid State Chemistry* **2017** (submitted).

This research was supported by National Science Foundation (DMR-1508527). The identification of any commercial product or trade name does not imply endorsement or recommendation by the National Institute of Standards and Technology.

## 6.7 References

- [1] Townes, W.D., Fang, J.H., Perrotta, A.J., *Z. Kristallogr.* 125 (1967) 437.
- [2] Aleshko-Ozhevskii, O.P., Faek, M.K., Yamzin, I.I., *Sov. Phys. Crystallogr.* 14(3) (1969) 367.
- [3] Grey, I.E., Madsen, I.C., Haggerty, S.E., *Am. Mineral.* 72 (1987) 633.
- [4] Bermanec, V., Sturman, D., Criddle, A.J. et al., *Can. Mineral.* 34 (1996) 1287.
- [5] Keil, K., Fuchs, L.H., *Earth Planet Sci. Lett.* 12 (1971) 184.
- [6] Kahl, A., Lejus, A.M., Madsac, M., Thery, J., Vivien, D., *J. Appl. Phys.* 52(11) (1981) 6864.
- [7] Li, Y.J., Ma, Y.Y., Ye, S., Hu, G.P., Zhang, Q.Y., *Mater. Res. Bull.* 51 (2014) 1.
- [8] Collongues, R., Gourier, D., Kahn-Harari, A. et al., *Annu. Rev. Mater. Sci.* 20 (1990) 51.
- [9] Bergstein, A., White, W.D., *J. Electrochem. Soc.* 118(7) (1971) 1166.
- [10] Verstegen, J.M.P.J., Sommerdijk, J.L., Verriet, J.G., *J. Lumin.* 6 (1973) 425.
- [11] Curien, H., Guillemin, C., Orcel, J. et al., *Comptes Rendus de l'Academie des Sciences, Paris* (1956) 2845.
- [12] Utsunomiya, A., Tanaka, K., Morikawa, H., Marumo, F., Kojima, H., *J. Solid State Chem.* 75 (1988) 197.
- [13] Wagner, T.R., O'Keeffe, M., *J. Solid State Chem.* 73(1) (1988) 211.
- [14] Nagashima, M., Armbruster, T., Hainschwang, T., *Mineral. Mag.* 74 (2010) 871.
- [15] Kohn, J.A., Eckart, D.W., *J. Appl. Phys.* 35 (1964) 968.
- [16] Harder, M., Muller-Buschbaum, H., *Z. Naturforsch B Chem. Sci.* 32(7) (1977) 833 (in German).
- [17] Pausch, H., Mueller-Buschbaum, H., *Z. Naturforsch B Chem. Sci.* 31(8) (1976) 1148 (in German).
- [18] Kimura, K., Ohgaki, M., Tanaka, K. et al., *J. Solid State Chem.* 87 (1990) 186.
- [19] Collomb, A., Obradors, X., Isalgue, A., Fruchart, D., *J. Magn. Magn. Mater.* 69(3) (1987) 317.
- [20] Jirak, D.Z., Krupka, M., Pollert, E., *Cryst. Res. Technol.* 22(4) (1987) K71.
- [21] Ounnunkad, S., Phanichphant, S., Winotai, P., Tang, I.-M., *Phys. Stat. Sol. (b)* 244(6) (2007) 2190.
- [22] Okube, M., Yoshizaki, J., Toyoda, T., Sasaki, S., *J. Appl. Cryst.* 49 (2016) 1433.
- [23] Sandiumenge, F., Gali, S., Rodriguez, J., *Mat. Res. Bull.* 23 (1988) 685.
- [24] Prakash, C.S., Kulkarni, D.K., *Indian J. Pure Appl. Phys.* 32 (1994) 361.
- [25] Mamatha, C., Krishnaiah, M., Prakash, C.S., Rewetkar, K.G., *Procedia Mat. Sci.* 5 (2014) 780.
- [26] Na, E.H., Song, S., Koo, Y.-M., Jang, H.M., *Acta Mater.* 61 (2013) 7705.
- [27] Ahn, S.D., Jung, H.S., Choo, D.C. et al., *J. Electrochem. Soc.* 157(6) (2010) J238.

- [28] Kojima, H., Sugimoto, M., *Ferromagnetic Materials*, Eds. Wolfarth E.P., North-Holland, Amsterdam 3 (1982) 305.
- [29] Vinnik, D.A., Zharebtsov, D.A., Mashkovtseva, L.S. et al., *J. Alloys Compd.* 615 (2014) 1043.
- [30] Tronc, E., Laville, F., Gasperin, M., Lejus, A.M., Vivien, D., *J. Solid State Chem.* 81(2) (1989) 192.
- [31] Schwanitz, S.U., Buschbaum, H.M., *Monatsh. Chem.* 113 (1982) 1079 (in German).
- [32] Ounnunkad, S., Winotai, P., Phanichphant, S., *J. Electroceram.* 16 (2006) 357.
- [33] Luo, H., Rai, B.K., Mishra, S.R., Nguyen, V.V., Liu, J.P., *J. Magn. Magn. Mater.* 324 (2012) 2602.
- [34] Ihinger, P.D., Stolper, E., *Earth Planet Sci. Lett.* 78 (1986) 67.
- [35] Burns, R.G., *Mixed Valency Syst.: Appl. Chem. Phys. Biol.* 343 (1991) 175.
- [36] Simon, S.B., Davis, A.M., Grossman, L., *Meteorit. Planet Sci.* 36 (2001) 331.
- [37] Hainschwang, T., Notari, F., Massi, L., Armbruster, T., Rondeau, B., Fritsch, E., Nagashima, M., *Gems Gemol.* 46(2) (2010) 135.
- [38] Dyar, M.D., Solberg, T.C., Burns, R.G., *Lunar Planet Sci. XVII* (1986) 194.
- [39] Armstrong, J.T., Meeker, G.P., Huneke, J.C., Wasserburg, G.J., *Geochimica et Cosmochimica Acta* 46 (1982) 575.
- [40] Ma, C., *Am. Mineral* 95 (2010) 188.
- [41] Burns, R.G., Burns, V.M., *J. Geophys. Res.* 89 (1984) C313.
- [42] Holtsman, D., *Phys. Chem. Miner.* 23(7) (1996) 452.
- [43] Saber, D., Lejus, A.M., *Mat. Res. Bull.* 16 (1981) 1325.
- [44] Doyle, P.M., Schofield, P.F., Berry, A.J. et al., *Am. Mineral.* 99 (2014) 1369.
- [45] Rout, S.S., Bischoff, A., *Meteorit. Planet Sci.* 43(7) (2008) A134.
- [46] Gasperin, M., Saine, M.C., Kahn, A. et al., *J. Solid State Chem.* 54 (1984) 61.
- [47] Laville, F., Lejus, A.M., *J. Cryst. Growth* 63 (1983) 426.
- [48] Gourier, D., Laville, F., Vivien, D., *J. Solid State Chem.* 61 (1986) 67.
- [49] Graetsch, H., Gebert, W., *Z. Kristallogr.* 211 (1996) 25.
- [50] Ardit, M., Borcanescu, S., Cruciani, G. et al., *J. Am. Ceram. Soc.* 99 (2016) 1749.
- [51] Costa, G., Ribeiro, M.J., Hajjaji, W. et al., *J. Eur. Ceram. Soc.* 29 (2009) 2671.
- [52] Kim, G., Lee, B.-H., *Kor. J. Mater. Res.* 24(1) (2014) 43 (in Korean).
- [53] Li, J., Medina, E.A., Stalick, J.K., Sleight, A.W., Subramanian, M.A., *Prog. Solid State Chem.* (2016) 1.
- [54] Subramanian, M.A., Li, J., Sleight, A.W., UC Patent WO2015131036, A120150903, 2015.
- [55] Leite, A., Costa, G., Hajjaji, W. et al., *Dyes Pigm.* 81 (2009) 211.
- [56] Hajjaji, W., Costa, G., Zanelli, C. et al., *J. Eur. Ceram. Soc.* 32 (2012) 753.
- [57] Hajjaji, W., Seabra, M.P., Labrincha, J.A., *Dyes Pigm.* 83 (2009) 385.
- [58] Haberey, F., Leckebusch, R., Rosenberg, M., Sahl, K., *J. Cryst. Growth* 61 (1983) 284.
- [59] Mateika, D., Laudan, M., *J. Cryst. Growth* 46(1) (1979) 85.
- [60] Vivien, D., Lejus, A.M., Thery, J., Collongues, R., Aubert, J.J. et al., *C. R. Acad. Sci. Paris (II)* 298(6) (1984) 195.
- [61] Larson, A.C., Von Dreele, R.B., *General Structure Analysis System (GSAS)*, Los Alamos National Laboratory Report LAUR (1994) 86.

- [62] EXPGUI, a graphical user interface for GSAS: Toby, B.H., J. Appl. Crystallogr. 34 (2001) 210.
- [63] Hormillosa, C., Healy, S., Stephen, T., Brown, I.D., Bond Valence Calculator, Version 2.0 (1993) <http://www.ccp14.ac.uk> (accessed 09/09/2016).
- [64] Sherif, M.E., Bayoumi, O.A., Sokkar, T.Z.N., Color Res. Appl. 22(1) (1997) 32.
- [65] Bain, G.A., Berry, J.F., J. Chem. Educ. 85 (2008) 532.

## CHAPTER 7

### Pigments Forming in $\text{Li}_2\text{Mn}_{1-x}\text{Ti}_x\text{O}_3$ ( $x = 0 - 1.0$ ) System

#### Abstract

Colored oxides forming in  $\text{Li}_2\text{Mn}_{1-x}\text{Ti}_x\text{O}_3$  ( $x = 0 - 1.0$ ) system were prepared using standard solid state synthesis method. All Mn-containing samples show bright orange color varying from dark brick red ( $x = 0$ ) to orange ( $x = 0.5$ ) and light orange ( $x = 0.8$ );  $\text{Li}_2\text{TiO}_3$  is white. Octahedrally coordinated  $\text{Mn}^{4+}$  is a chromophore element and responsible for the color of the  $\text{Li}_2\text{Mn}_{1-x}\text{Ti}_x\text{O}_3$  series. Optical properties measurements reveal the color origin; the color is due to combination of d-d interatomic transitions of d electrons in octahedral  $\text{Mn}^{4+}$  and  $M(\text{IV})-\text{O}^{2-}$  charge transfer. The synthesized samples show relatively high reflectance in near-IR region and might be promising candidates for “Cool pigments” application.

## 7.1 Introduction

Layered Li-containing inorganic oxides play an important role in batteries field. In such structures lithium ions can easily move; due to this property the compounds are widely used as cathodes for lithium ion batteries [1,2]. For example,  $\text{Li}_x\text{CoO}_2$  is the most popular and effective intercalation cathode material which is used nowadays [3,4]. Also  $\text{Li}_2\text{MnO}_3$  compound is of interest because of its high discharge capacity and working voltage [5-7]. Doped  $\text{Li}_2\text{MnO}_3$  was investigated as potential cathode material with improved properties. Zirconium and nickel modified  $\text{Li}_2\text{MnO}_3$  [8],  $\text{LiCoO}_2$ - $\text{Li}_2\text{MnO}_3$  solid solution [9],  $\text{Li}_2\text{MnO}_3$ - $\text{LiMO}_2$  ( $M = \text{Mn, Ni, Co, Fe, Cr, etc.}$ ) series [10] and coaxial  $\text{LiCoO}_2 \cdot \text{Li}_2\text{MnO}_3$  nanoribbon [11] were studied and have found their applications in Li-ion battery field.

However,  $\text{Li}_2\text{MnO}_3$  is also interesting as perspective material for pigments application. The compound has dark brick red color [12]; it is very unusual hue for manganese (IV) oxides. The color might be tuned by creating solid solutions through manganese site substitution.  $\text{Li}_2\text{MnO}_3$  is a particular compound having a layered honeycomb rock salt structure and containing octahedral  $\text{Mn}^{4+}$  as a chromophore. Red emitting phosphors containing  $\text{Mn}^{4+}$  ion were investigated and are used for white LEDs (light-emitting diodes) [13-16].

In the  $\text{Li}_2\text{MnO}_3$  structure manganese and lithium are octahedrally coordinated by oxygen (Fig. 7.1).

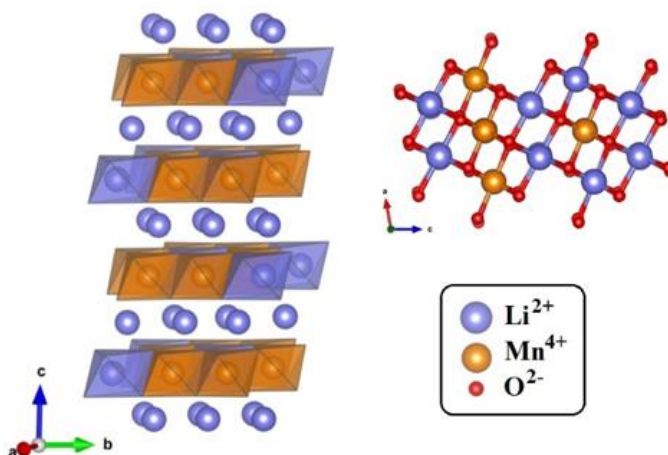


Figure 7.1 Crystal structure of  $\text{Li}_2\text{MnO}_3$ .

$\text{LiO}_6$  octahedra are surrounded by six  $\text{MnO}_6$  edge-sharing octahedra and form  $\text{LiMn}_2$  layers;  $\text{Li}_2\text{MnO}_3$  has a layered honeycomb rock salt structure (Fig. 7.2). The rest of the  $\text{Li}^+$  ions are intercalated between  $\text{LiMn}_2$  slabs and occupy octahedral sites.

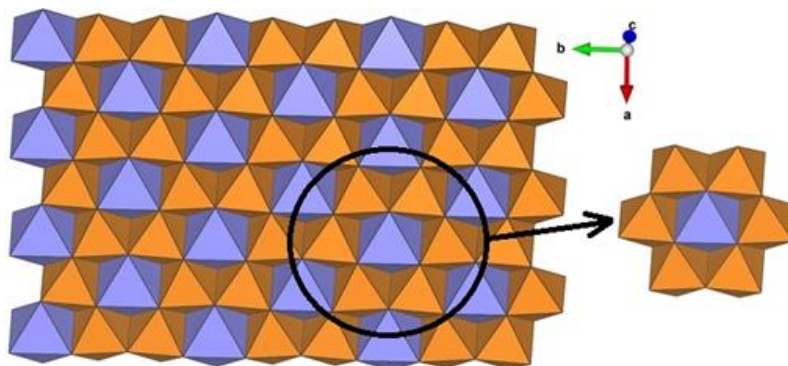


Figure 7.2  $\text{LiMn}_2$  sheet in the honeycomb lattice of  $\text{Li}_2\text{MnO}_3$ .

There are two possible space groups reported for  $\text{Li}_2\text{MnO}_3$ :  $C2/m$  and  $C2/c$ . The first polytype of  $\text{Li}_2\text{MnO}_3$  crystallizes in  $C2/m$  space group:  $a = 4.937 \text{ \AA}$ ,  $b = 8.532 \text{ \AA}$ ,  $c = 5.030 \text{ \AA}$ ,  $\alpha = \gamma = 90^\circ$ ,  $\beta = 109.5^\circ$ ,  $Z = 4$  [17]. The second polytype of  $\text{Li}_2\text{MnO}_3$  has monoclinic unit cell and crystallizes in  $C2/c$  space group:  $a = 4.921 \text{ \AA}$ ,  $b = 8.526 \text{ \AA}$ ,  $c = 9.606 \text{ \AA}$ ,  $\alpha = \gamma = 90^\circ$ ,  $\beta = 99.5^\circ$ ,  $Z = 8$  [18,19].  $C2/m$  space group has higher symmetry. The main difference between two polytypes is distinction in  $\text{LiMn}_2$  layers stacking along the  $c$ -axis [20]. Like most of the honeycomb layered oxides  $\text{Li}_2\text{MnO}_3$  rare exhibits an ideal structure [21,22] and might have different percent of disorder present. The most common type of disorder is stacking faults [23].

The  $\text{Li}_2\text{Mn}_{1-x}\text{Ti}_x\text{O}_3$  solid solution was prepared and magnetic properties of the series were studied before [24,25] as well as electric and magnetic properties of  $\text{Li}_2\text{MnO}_3$  parent compound [26,27]. Also structure of  $\text{Li}_2\text{TiO}_3$  was reported [28]. Systematic investigation of optical properties of  $\text{Li}_2\text{Mn}_{1-x}\text{Ti}_x\text{O}_3$  series were not performed. We synthesized  $\text{Li}_2\text{Mn}_{1-x}\text{Ti}_x\text{O}_3$  ( $x = 0 - 1.0$ ) full solid solution, refined unit cell parameters, characterized the colors of the compounds and investigated optical properties of the series.

## 7.2 Results and Discussion

$\text{Li}_2\text{Mn}_{1-x}\text{Ti}_x\text{O}_3$  ( $x = 0 - 1.0$ ) solid solution was synthesized using solid state synthesis. XRD patterns of all samples are shown in Fig. 7.3. All synthesized compounds are pure.

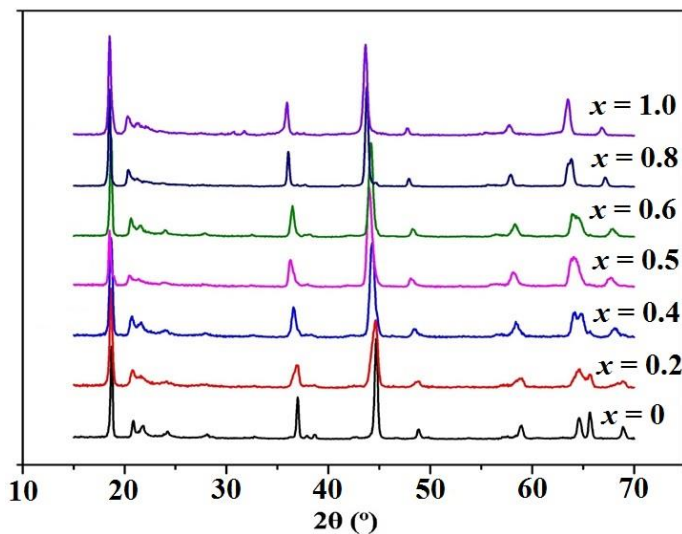


Figure 7.3 XRD patterns of  $\text{Li}_2\text{Mn}_{1-x}\text{Ti}_x\text{O}_3$  solid solution.

Using GSAS software and LeBail fitting method unit cell parameters ( $a$ ,  $b$ ,  $c$ ) were refined. All samples are isostructural and crystallize in  $C2/c$  space group. Manganese and titanium occupy the same sites in the structure. There is a gradual increase of the cell parameters with substitution of smaller  $\text{Mn}^{4+}$  by larger  $\text{Ti}^{4+}$  (Shannon ionic radii:  $\text{Mn}^{4+}$  (CN = 6) = 0.530 Å and  $\text{Ti}^{4+}$  (CN = 6) = 0.605 Å [29]) (Fig. 7.4). Unit cell edge  $b$  changes faster than  $a$  and  $c$ ; it is an evidence that the structure is more susceptible to changes (compression and expansion) along this direction.



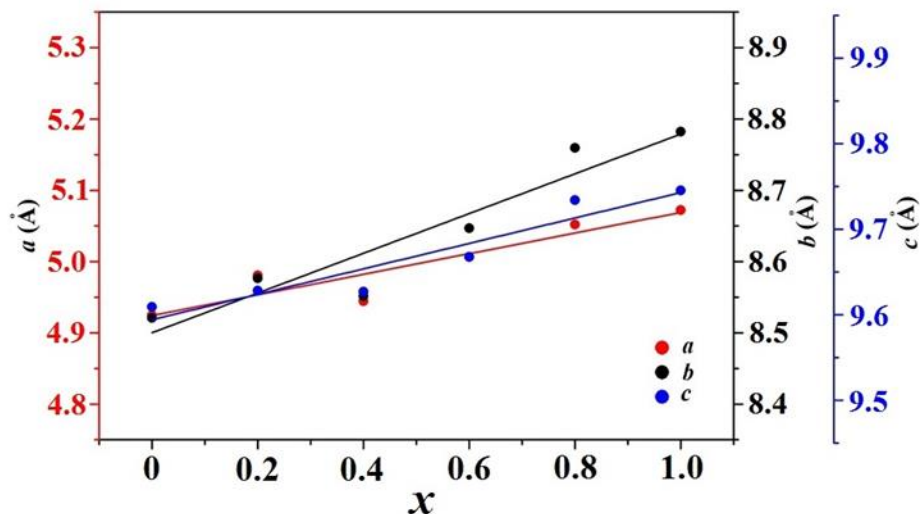


Figure 7.4 Unit cell parameters  $a$ ,  $b$ ,  $c$  of  $\text{Li}_2\text{Mn}_{1-x}\text{Ti}_x\text{O}_3$  solid solution as a function of  $x$ . The estimated errors for  $a$ ,  $b$ ,  $c$  are less than the size of the points in the figure.

Unit cell volume increases with increasing  $x$  (Fig. 7.5(a)). The  $c/a$  ratio is relatively constant and just slightly decreases with  $x$  (Fig. 7.5(b)).

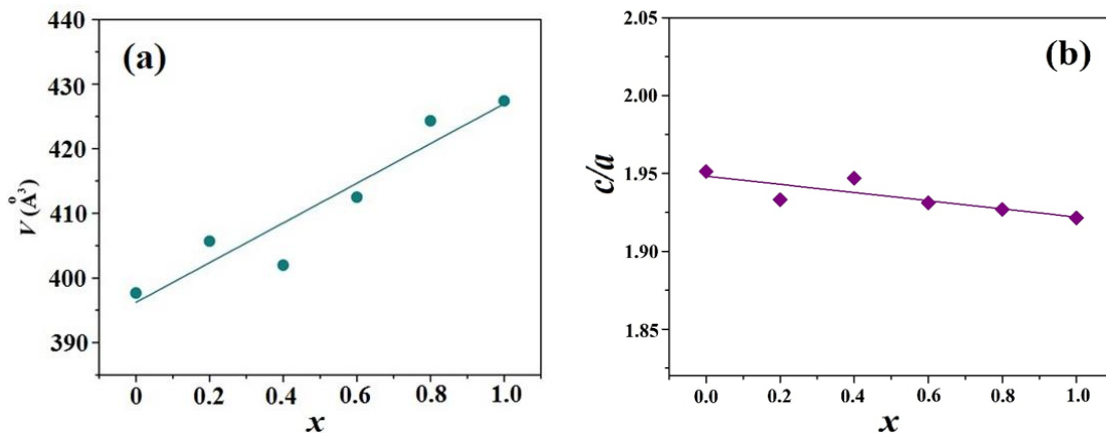


Figure 7.5 (a) Unit cell volume ( $V$ ) as a function of  $x$ ; (b)  $c/a$  value as a function of  $x$ . The estimated errors for  $V$  and  $c/a$  ratio are less than the size of the points in the figure.

Optical properties were characterized to study the color evolution of the solid solution.  $L^*a^*b^*$  parameters were measures to describe the color of each sample.  $\text{Li}_2\text{TiO}_3$  is white,  $\text{Li}_2\text{MnO}_3$  has very dark maroon color, and samples containing manganese and titanium

together show very bright orange colors vary from light orange ( $x = 0.8$ ) to dark orange ( $x = 0.2$ ) (Fig. 7.6).



Figure 7.6 Colors of  $\text{Li}_2\text{Mn}_{1-x}\text{Ti}_x\text{O}_3$  samples.

$L^*a^*b^*$  values of the synthesized samples are given in the Table 7.1.

Table 7.1  $L^*a^*b^*$  values of  $\text{Li}_2\text{Mn}_{1-x}\text{Ti}_x\text{O}_3$  compounds.

$x$	$L^*$	$a^*$	$b^*$
<b>0</b>	24.24	11.61	5.63
<b>0.2</b>	35.93	28.56	24.56
<b>0.4</b>	38.71	30.83	29.77
<b>0.5</b>	39.26	32.62	30.62
<b>0.6</b>	38.35	32.08	29.03
<b>0.8</b>	49.15	32.92	34.77
<b>1.0</b>	82.39	1.22	2.65

One of the biggest challenges of materials chemistry today is looking for new, non-toxic and environmentally friendly red pigment. Almost all red pigments which are known are very toxic: CdSe (cadmium red),  $\text{Pb}_3\text{O}_4$  (red lead), HgS (vermilion) [30]. Colored materials based on orange-red  $\alpha\text{-Fe}_2\text{O}_3$  are widely used as inorganic pigments [31,32]. The measured  $L^*a^*b^*$  values of  $\text{Li}_2\text{Mn}_{1-x}\text{Ti}_x\text{O}_3$  series were compared with  $L^*a^*b^*$  values of  $\text{Fe}_2\text{O}_3$  red oxide (Sigma-Aldrich, 99.98%).  $\text{Fe}_2\text{O}_3$  has  $L^* = 30.32$ ,  $a^* = 30.49$ ,  $b^* = 24.66$ . The  $a^*$  parameter is responsible for the red color; bright red objects have large positive  $a^*$  values. The  $a^*$  parameters of  $x = 0.4, 0.5, 0.6$  and  $0.8$  samples are larger than measured  $a^*$  value of  $\text{Fe}_2\text{O}_3$ , thus our samples are more reddish.

Diffuse reflectance spectra measurements of the  $\text{Li}_2\text{Mn}_{1-x}\text{Ti}_x\text{O}_3$  compounds were performed. Using Kublka-Munk equation [33] the diffuse reflectance was converted into absorbance and plotted vs. wavelength. The diffuse reflectance spectra of the solid solution are given in Fig. 7.7.

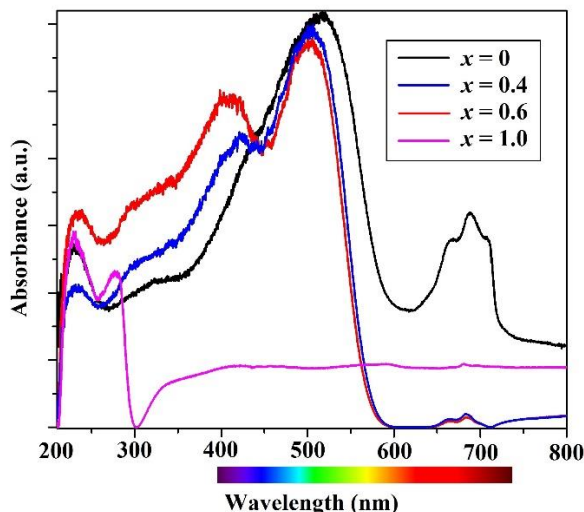


Figure 7.7 Diffuse reflectance spectra of  $\text{Li}_2\text{Mn}_{1-x}\text{Ti}_x\text{O}_3$  ( $x = 0, 0.4, 0.6, 1.0$ ) series.

All samples except white  $\text{Li}_2\text{TiO}_3$  absorb in two regions: absorption in the high energy region (200 ~ – 300 nm) is due to  $M^{4+} - \text{O}^{2-}$  charge transfer transition and the low energy peaks (325 ~ - 725 nm) are due to d-d interatomic transitions of d electrons in octahedrally coordinated  $\text{Mn}^{4+}$ . The larger the manganese concentration/smaller  $x$  value the more intense compound absorbs in low energy region and the higher low energy peaks are;  $\text{Li}_2\text{TiO}_3$  doesn't have these peaks and absorbs in the high energy region only. There is a valley of weak or no absorption between 600 and 650 nm, which causes the red or orange color of the samples.  $\text{Mn}^{4+}$  is a chromophore element.

Based on literature data [12] and Tanabe and Sugano diagram for 3d transition metals [34] we assigned all absorption peaks (d-d bands appear on the spectrum) into different transitions (Fig. 7.8).

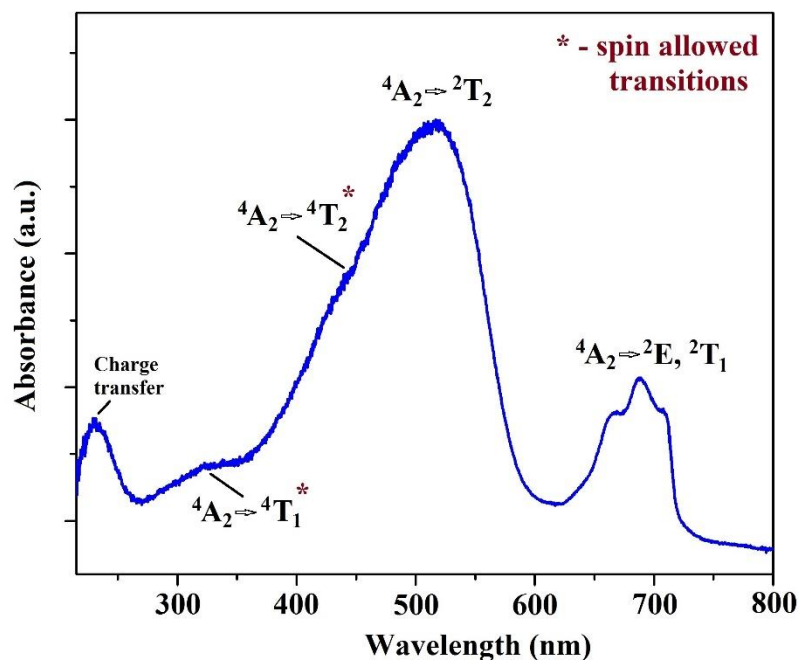


Figure 7.8 Diffuse reflectance spectra of  $\text{Li}_2\text{MnO}_3$  sample with all peaks assigned.

Crystal field splitting values for  $x = 0, 0.2, 0.5, 0.8$  and  $1.0$  samples were estimated (Table 7.2) by extrapolation of x-axis intercept at the absorption onset in diffuse reflectance plot. Crystal field splitting value increases with  $x$  and varies from  $1.90 \text{ eV}$  ( $x = 0$ ) to  $4.10 \text{ eV}$  ( $x = 1.0$ ).

Table 7.2 Estimated crystal field splitting of  $\text{Li}_2\text{Mn}_{1-x}\text{Ti}_x\text{O}_3$  compounds.

Compound	Estimated crystal field splitting (eV)
$\text{Li}_2\text{MnO}_3$ ( $x = 0$ )	2.29
$\text{Li}_2\text{Mn}_{0.8}\text{Ti}_{0.2}\text{O}_3$ ( $x = 0.2$ )	2.36
$\text{Li}_2\text{Mn}_{0.5}\text{Ti}_{0.5}\text{O}_3$ ( $x = 0.5$ )	2.41
$\text{Li}_2\text{Mn}_{0.2}\text{Ti}_{0.8}\text{O}_3$ ( $x = 0.8$ )	2.46
$\text{Li}_2\text{TiO}_3$ ( $x = 1$ )	4.39

Reflectance of the pigments is important in NIR region, because “Cool pigments” have high reflectance rate in the region and can reflect heat effectively. Our synthesized pigments reflect relatively well in NIR region ( $80 \sim 100\%$ ) and are good candidates for “Cool pigments” application (Fig. 7.9).

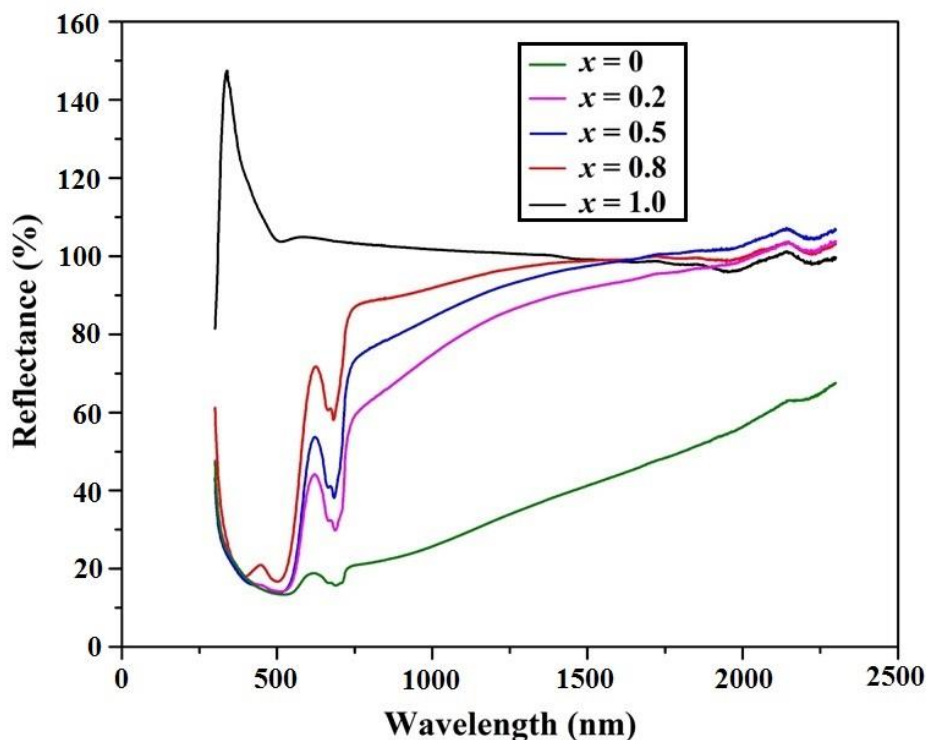


Figure 7.9  $\text{Li}_2\text{Mn}_{1-x}\text{Ti}_x\text{O}_3$  ( $x = 0, 0.2, 0.5, 0.8, 1.0$ ) reflectance vs. wavelength plots.

### 7.3 Conclusion

$\text{Li}_2\text{Mn}_{1-x}\text{Ti}_x\text{O}_3$  solid solution was synthesized and characterized by X-ray diffraction technique. The lattice parameters sequence follows an expected linear trend. Optical properties measurements were performed and compounds colors were described. Estimated crystal field splitting of the series gradually increases with increasing of  $x$ . Samples might be promising candidates for the “Cool pigments” application; they show high reflectance rate (80 ~ - 100%) in NIR region. Several samples were sent to MERCK Group Company (Germany) for the further studies.

### 7.4 Experimental Materials and Methods

Samples were prepared using standard solid state synthesis method. Stoichiometric amounts of starting materials  $\text{Li}_2\text{CO}_3$  (Sigma-Aldrich, 99.998%),  $\text{MnO}_2$  (Sigma-Aldrich, 99%) and  $\text{TiO}_2$  (Sigma-Aldrich, 99.9%) were grinded, pelletized and heated at 850–920 °C for 12–24 h. Phase purity was controlled using Rigaku Miniflex II diffractometer ( $\text{CuK}\alpha$

radiation and graphite monochromator). Konica Minolta CM-700d Spectrophotometer was used to measure  $L^*a^*b^*$  color coordinates. Diffuse reflectance spectra measurements were performed on homemade UV-VIS spectrophotometer; MgO was used as a reference. NIR reflectance data were collected using a Jasco V-670 Spectrophotometer.

## 7.5 Acknowledgements

This work has been supported by NSF grant DMR-1508527.

## 7.6 References

- [1] Goodenough, J.B., Park, K.-S., J. Am. Chem. Soc. 135 (2015) 1167.
- [2] Nitta, N., Wu, F., Lee, J.T., Yushin, G., Mater. Today 18(5) (2015) 252.
- [3] Mizushima, K. et al., Mater. Res. Bull. 15(6) (1980) 783.
- [4] Cho, J., Kim, Y.J., Park, B., Chem. Mater. 12 (2000) 3788.
- [5] Ellis, B.L., Lee, K.T., Nazar, L.F., Chem. Mater. 22 (2010) 691.
- [6] Yabuuchi, N., Ohzuku, T., J. Power Sources 119 (2003) 171.
- [7] Yan, P., Xiao, L., Zheng, J. et al., Chem. Mater. 27 (2015) 975.
- [8] Li, B., Wang, Q., Zhang, Y., Song, Z., Yang, D., Int. J. Electrochem. Sci., 8 (2013) 5396.
- [9] Numata, K., Sakaki, C., Yamanaka, S., Chem. Lett. 26(8) (1997) 725.
- [10] Yu, H., Zhou, H., J. Phys. Chem. Lett. 4 (2013) 1268.
- [11] Wang, F.X., Xiao, S.Y., Chang, Z., Li, M.X., Wu, Y.P., Holze, R., Int. J. Electrochem. Sci. 9 (2014) 6182.
- [12] Tamilarasan, S., Laha, S., Natarajan, S., Gopalakrishnan, J., J. Mater. Chem. C 3 (2015) 4794.
- [13] Chen, Y., Wang, M., Wang, J., Wu, M., Wang, C., J. Solid State Light. 1 (2014) 15.
- [14] Takahashi, T., Adachi, S., Electrochem. Solid State Lett. 12(8) (2009) J69.
- [15] Li, P., Brik, M.G., Li, L., Han, L. et al., J. Am. Ceram. Soc. 99(7) (2016) 2388.
- [16] Kim, S.J., Jang, H.S., Unithratti, S., Kim, Y.H., Im, W.B., J. Lumin. 172 (2016) 99.
- [17] Strobel, P., Lambert-Andron, B., J. Solid State Chem., 75 (1988) 90.
- [18] Jansen, V.M., Hoppe, R., Z. Anorg. Allg. Chem. 397 (1973) 279 (in German).
- [19] Riou, A., Lecerf, A., Gerault, Y., Cudennec, Y., Mat. Res. Bull. 27 (1992) 269 (in French).
- [20] Breger, J., Jiang, M., Dupre, N., Meng, Y.S., Shao-Horn, Y. et al., J. Solid State Chem., 178 (2005) 2575.
- [21] Orman, H.J., Wiseman, P.J., Acta Crystallogr. Sect. C: Cryst. Struct. Commun. 40 (1984) 12.
- [22] Mather, G.C., Dussarrat, C., Etourneau, J., West, A.R., J. Matter. Chem. 10 (2000) 2219.
- [23] Boulineau, A., Croguennec, L., Delmas, C., Weill, F., Solid State Ion. 180 (2010) 1652.
- [24] Hoffe, V.R., Serafin, M., Z. Anorg. Allg. Chem. 436 (1977) 95 (in German).

- [25] Lee, S., Park, J., Kim, J., Hong, K.-P., Song, Y., Park, J.-G., J. Phys.: Condens. Matter 26 (2014) 1.
- [26] Massarotti, V., Capsoni, D., Bini, M., Chiodelli, G., J. Solid State Chem. 131 (1997) 94.
- [27] Alvarez, G., Zamorano, R., Hairas, J., Castellanos, M., Valenzuela, R., J. Magn. Magn. Mater. 316 (2007) e695.
- [28] Dorrian, J.F., Newnham, R.E., Am. Ceram. Soc. Bull. (1969) 401.
- [29] Shannon, R.D., Acta Crystallogr. Sect. A 32 (1976) 751.
- [30] [https://en.wikipedia.org/wiki/List\\_of\\_inorganic\\_pigments#Red\\_pigments](https://en.wikipedia.org/wiki/List_of_inorganic_pigments#Red_pigments) (accessed 12.15.2016).
- [31] Marean, C.W., Bar-Matthews, M., Bernatchez, J., Fisher, E. et al., Nature 449 (2007) 905.
- [32] Bondioli, F., Ferrari, A.M., Leonelli, C. et. al., Mat. Res. Bull. 33(5) (1998) 723.
- [33] Sherif, M.E., Bayoumi, O.A., Sokkar, T.Z.N., Color Res. Appl. 22 (1997) 32.
- [34] Atkins, P.W., Shriver&Atkins' Inorganic Chemistry (5<sup>th</sup> edition), Freeman, W.H. and Company, New York, 2010, pp. 1-830.

## CHAPTER 8

### Pigments with Sillenite-Type Structure

#### Abstract

$\text{Bi}_{12-x}\text{In}_x\text{TiO}_{20}$  ( $x = 0 - 1.5$ ),  $\text{Bi}_{12-x}\text{In}_x\text{Mn}_{0.2}\text{Ti}_{0.8}\text{O}_{20}$  ( $x = 0 - 5.5$ ) and  $\text{Bi}_{12}\text{Mn}_{1-x}\text{M}_x\text{O}_{20}$  ( $M = \text{Ti, Si, Ge}$ ) solid solutions having  $\text{Bi}_{12}\text{MO}_{20}$  sillenite-type structure were synthesized through Bi-site and M-site substitutions and their properties were evaluated. The color of  $\text{Bi}_{12-x}\text{In}_x\text{TiO}_{20}$  samples varies from light yellow ( $x = 0$ ) to beige ( $x = 1.5$ ); shades of  $\text{Bi}_{12-x}\text{In}_x\text{Mn}_{0.2}\text{Ti}_{0.8}\text{O}_{20}$  series change from forest green ( $x = 0$ ) to dark sea green ( $x = 2.5$ ) and light olive drab ( $x = 5.5$ );  $\text{Bi}_{12}\text{Mn}_{1-x}\text{M}_x\text{O}_{20}$  ( $M = \text{Ti, Si, Ge}$ ) solid solutions show very similar hues from dark green ( $x = 0$ ) to forest green ( $x = 0.5$ ) and lawn green ( $x = 0.8$ );  $\text{Bi}_{12}\text{MO}_{20}$  ( $M = \text{Ti, Si, Ge}$ ) are light yellow. Tetrahedrally coordinated  $\text{Mn}^{4+}$  is a chromophore element of the series and responsible for the color. Optical properties measurements of Mn - containing samples show that combination of d-d interatomic transition in  $\text{Mn}^{4+}$  and  $\text{M}^{4+}-\text{O}^{2-}$  charge transfer is responsible for the greenish colors of the compounds. The estimated crystal field splitting values of  $\text{Bi}_{12}\text{Mn}_{1-x}\text{Ti}_x\text{O}_{20}$  series have a linear trend which follows the  $\text{Mn}^{4+}$  substitution; samples become lighter with increasing  $x$ .  $\text{Bi}_{12}\text{Mn}_{1-x}\text{Ti}_x\text{O}_{20}$  ( $x = 0.2, 0.6, 0.8$ ) compounds show paramagnetic behavior in 5–300 K temperature region, the effective magnetic moment is slightly smaller than theoretical magnetic moment of tetrahedral  $\text{Mn}^{4+}$ , which verify the possible presence of oxygen vacancies in the structure.



## 8.1 Introduction

Sillenite (Fig. 8.1) is a mineral with the  $\text{Bi}_{12}\text{SiO}_{20}$  chemical formula [1]. It was named after the Swedish chemist Lars Gunnar Sillén, who investigated bismuth – oxygen compounds [2]. The mineral might have different colors from olive – green and gray – green to yellow and reddish – brown.  $\text{Bi}_{12}\text{SiO}_{20}$  is found in Australia, Europe, China, Japan, Mexico and Mozambique [3]. Bismuth silicon oxide:  $\text{Bi}_{12}\text{SiO}_{20}$  (BSO), bismuth titanate:  $\text{Bi}_{12}\text{TiO}_{20}$  (BTO) and bismuth germanate:  $\text{Bi}_{12}\text{GeO}_{20}$  (BGO) adopt the crystal structure of sillenite.



Figure 8.1 Mineral sillenite [3].

$\text{Bi}_{12}\text{SiO}_{20}$  has cubic unit cell and crystallizes in  $I23$  space group;  $a = 9.944 \text{ \AA}$ ,  $\alpha = \beta = \gamma = 90^\circ$ ,  $V = 983.29 \text{ \AA}^3$ ,  $Z = 2$  [4].  $\text{Bi}_{12}\text{MnO}_{20}$  is isostructural to  $\text{Bi}_{12}\text{SiO}_{20}$  and also belongs to the sillenite mineral group:  $I23$  space group,  $a = 10.206 \text{ \AA}$  and  $V = 1063.08 \text{ \AA}^3$ ,  $Z = 2$  [5] (Fig. 8.2).

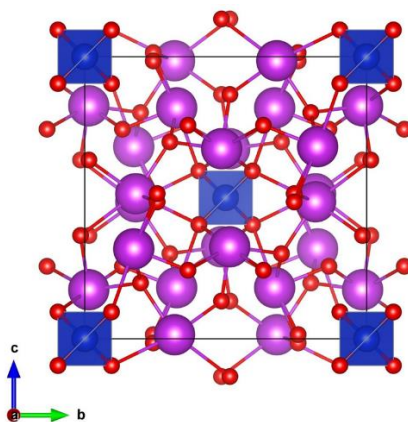


Figure 8.2 Cristal structure of  $\text{Bi}_{12}\text{MnO}_{20}$  ( $\text{Bi}^{3+}$ : magenta spheres,  $\text{Mn}^{4+}$ : blue tetrahedra,  $\text{O}^{2-}$ : red spheres).

The  $\text{Bi}_{12}\text{MnO}_{20}$  crystal structure consists of Bi—O framework, which connects the  $\text{MnO}_4$  tetrahedra.  $\text{Bi}^{3+}$  has the lone pair and distorted octahedral coordination: five oxygens form a pyramid and one lone pair is at the octahedron corner. Coordination number of manganese equals four and the atom forms an ideal tetrahedra with oxygen (Fig. 8.3).

A large number of elements with oxidation states four and others can be incorporated at the manganese positions in sillenite structure. Charge balance in this case might be achieved by oxygen vacancies, or introduction of extra interstitial oxygen in the case of metal ions with valence greater than four; sillenite is a flexible structure, which easily can adopt an oxygen vacancies or interstitial oxygen to form  $\text{Bi}_{12}\text{MO}_{20\pm\delta}$  [6,7].

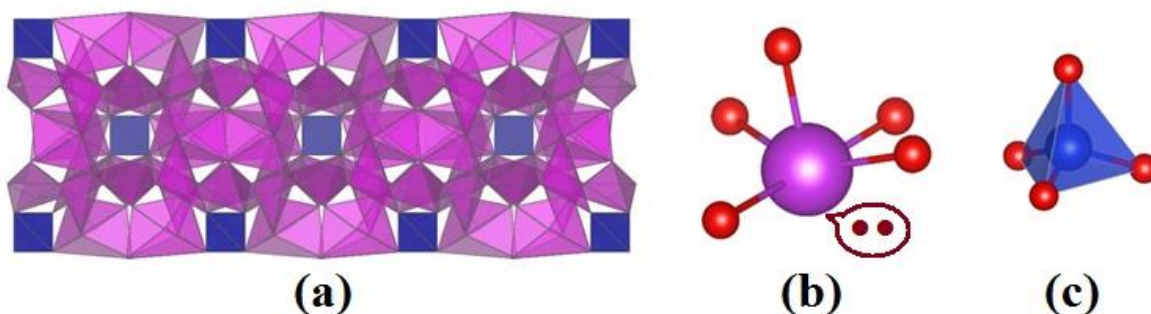


Figure 8.3 (a)  $\text{Bi}_{12}\text{MnO}_{20}$  (polyhedral view), (b)  $\square\text{BiO}_5$  distorted octahedra ( $\square$  is a lone pair) and (c)  $\text{MnO}_4$  tetrahedra.

Sillenites have a tendency to show remarkable optical [8,9], dielectric [10], photocatalytic [11] and electrical properties [12]; it is possible due to unusual coexistence of stereochemically active lone pair of  $\text{Bi}^{3+}$  and presence of non-centrosymmetry in the structure. Also Bi-containing compounds are promising substituent for toxic and not environmentally friendly lead-containing piezoelectrics [13].

Structures of several sillenite-type compounds were reported:  $\text{Bi}_{12}\text{TiO}_{20}$  [14],  $\text{Bi}_{12}\text{ZnO}_{20}$  [15],  $\text{Bi}_{12}\text{PbO}_{20}$  [16] and  $\text{Bi}_{12}\text{GeO}_{20}$  [17] and  $\text{Bi}_{12}\text{Cd}_{0.7}\text{O}_{18.7}$  [18]. Dozens of  $\text{Bi}_{12}\text{M}_x\text{O}_{20\pm\delta}$  compounds and solid solutions with different M cations were synthesized and studied [19-21]. Cr-doped single crystals of  $\text{Bi}_{12}\text{GeO}_{20}$  and  $\text{Bi}_{12}\text{SiO}_{20}$  were prepared and their optical absorption and ESR spectra were measured [22,23]. Influence of light on the magnetoelectric effect in Cr-doped  $\text{Bi}_{12}\text{TiO}_{20}$  [24] and dielectric relaxation in  $\text{Bi}_{12}\text{SiO}_{20}$ :

Cr crystals were investigated [25]. Spectroscopic and chiroptical properties of Fe-substituted sillenite crystals [26] and magnetic properties of  $\text{Bi}_{12}\text{MO}_{20}$  ( $M = \text{Fe}, \text{Co}$ ) [27] were studied. Ni [28], Ru [29,30], Nb [31], Mn, Cu, Rh, Pd, Re, Os, Ir, Zn, V – doped sillenites and  $\text{Bi}_{12}\text{Si}_{1-x}\text{Ge}_x\text{O}_{20}$  [32] single crystals were prepared and their properties were reported. Colors of some single crystals were studied.  $\text{Bi}_{12}\text{GeO}_{20}$  single crystals co-doped with Cu and V have orange color [33]. Copper produces photochromic effect and changes  $\text{Bi}_{12}\text{SiO}_{20}$  crystal color from yellow to red after daylight exposure, Mn-doped  $\text{Bi}_{12}\text{SiO}_{20}$  is yellowish-green, Cr-doped: brown-red, Ni-doped: yellow, Co-doped: yellowish-blue, Fe-doped: light-yellow; addition of Al to the listed above crystals results in bleaching of colors [34]. Gospodinov et al. [35] showed that increasing Co concentration in  $\text{Bi}_{12}\text{SiO}_{20}$  crystal changes the color from yellow to greyish-blue. Os-doped  $\text{Bi}_{12}\text{SiO}_{20}$  crystals show light yellow color, Ru-doped crystals are dark red, Ir gives blue-brown hue and Re colors  $\text{Bi}_{12}\text{SiO}_{20}$  light pink [36].  $\text{Bi}_{12.66}\text{Zn}_{0.33}\text{O}_{19.33}$  is pale yellow [37].  $\text{V}^{4+}$  and  $\text{V}^{5+}$  ions are responsible for green and orange colors of the samples [38]. Optical properties of pure and doped  $\text{Bi}_{12}\text{GeO}_{20}$  and  $\text{Bi}_{12}\text{SiO}_{20}$  single crystals were studied; the undoped crystals are yellow, and Al, Ga, P bleach the crystals color [39].

As mentioned above,  $\text{Bi}_{12}\text{MnO}_{20}$  is a structure with an unusual tetrahedral coordination of  $\text{Mn}^{4+}$ . Manganese is a chromophore element and pure  $\text{Bi}_{12}\text{MnO}_{20}$  compound shows dark green color. Several papers were published describing Mn – doped crystals and their optical properties and colors [40-42]. Bismuth manganese oxide pigments were patented [43] and  $\text{Bi}_{12}\text{MnO}_{20}$  sillenite attracts attention as a promising object for further investigations in pigments field.

In the present work we mainly focused on synthesis and optical properties studies of Mn – containing  $\text{Bi}_{12}\text{MO}_{20}$  ( $M = \text{Ti}, \text{Si}, \text{Ge}$ ) sillenite – type colored oxides since systematic study of the powder compounds were not carried out. The color of samples were tuned through Bi-site and M-site substitutions.

## 8.2 Results and Discussion

### 8.2.1 Bi-site Substitution

Two solid solutions  $\text{Bi}_{12-x}\text{In}_x\text{TiO}_{20}$  ( $x = 0 - 1.5$ ) and  $\text{Bi}_{12-x}\text{In}_x\text{Mn}_{0.2}\text{Ti}_{0.8}\text{O}_{20}$  ( $x = 0 - 5.5$ ) have been synthesized using conventional solid state synthesis through Bi-site substitution in  $\text{Bi}_{12}\text{TiO}_{20}$  and  $\text{Bi}_{12}\text{Mn}_{0.2}\text{Ti}_{0.8}\text{O}_{20}$  structures accordingly. The difference between Bi and In ionic radii allows to prepare the series (Shannon ionic radii:  $\text{Bi}^{3+}$  (CN = VI) =  $1.03\text{\AA}$  and  $\text{In}^{3+}$  (CN = VI) =  $0.800\text{\AA}$  [44]). The powder X-ray diffraction patterns of the  $\text{Bi}_{12-x}\text{In}_x\text{TiO}_{20}$  ( $x = 0 - 1.5$ ) and  $\text{Bi}_{12-x}\text{In}_x\text{Mn}_{0.2}\text{Ti}_{0.8}\text{O}_{20}$  ( $x = 0 - 5.5$ ) solid solutions are shown in Fig. 8.4 and Fig. 8.5 respectively.

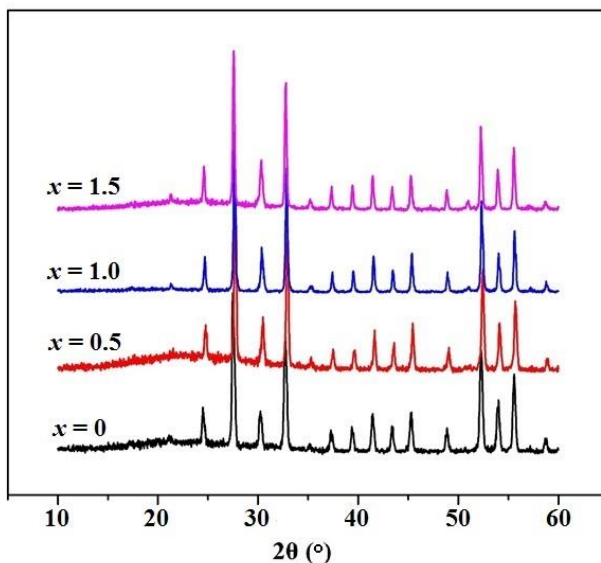


Figure 8.4 XRD patterns of  $\text{Bi}_{12-x}\text{In}_x\text{TiO}_{20}$  solid solution.

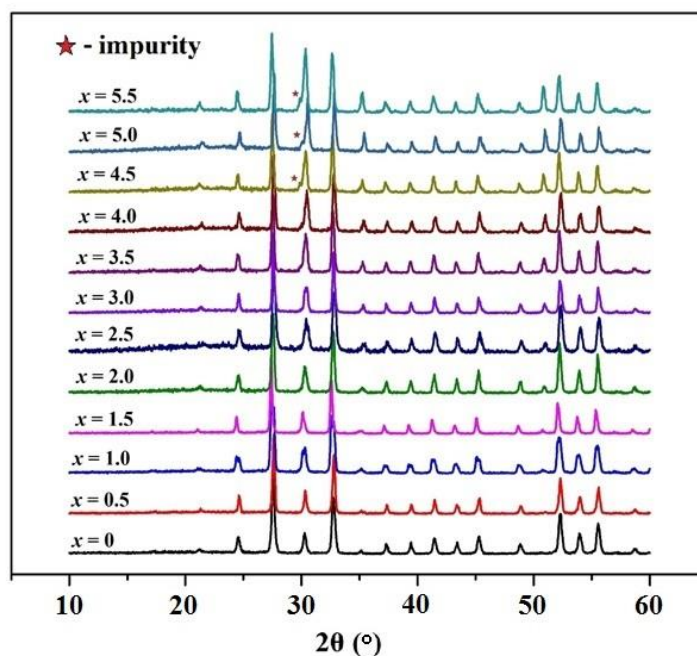


Figure 8.5 XRD patterns of  $\text{Bi}_{12-x}\text{In}_x\text{Mn}_{0.2}\text{Ti}_{0.8}\text{O}_{20}$  series.

There were no traces of impurity phases in the case of  $\text{Bi}_{12-x}\text{In}_x\text{TiO}_{20}$  solid solution; in the case of  $\text{Bi}_{12-x}\text{In}_x\text{Mn}_{0.2}\text{Ti}_{0.8}\text{O}_{20}$  series samples with  $x = 4.5 - 5.5$  have small extra peaks on XRD patterns.

Colors of  $\text{Bi}_{12-x}\text{In}_x\text{TiO}_{20}$  samples change from yellow to tan with increasing  $x$  (Fig. 8.6) and from dark lawn green to light olive color in the case of  $\text{Bi}_{12-x}\text{In}_x\text{Mn}_{0.2}\text{Ti}_{0.8}\text{O}_{20}$  series with increasing of In concentration (Fig. 8.7).



Figure 8.6 Colors of  $\text{Bi}_{12-x}\text{In}_x\text{TiO}_{20}$  compounds.

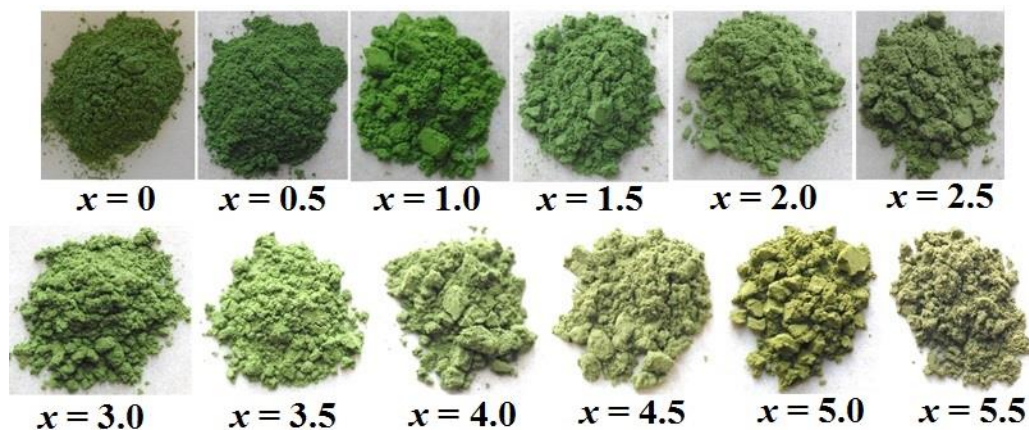


Figure 8.7 Colors of  $\text{Bi}_{12-x}\text{In}_x\text{Mn}_{0.2}\text{Ti}_{0.8}\text{O}_{20}$  solid solution.

Optical studies were performed in order to estimate the crystal field splitting as the color change through the solid solution. The diffuse reflectance was transformed to absorbance using the Kubelka-Munk relationship [45]. All samples belong to  $\text{Bi}_{12-x}\text{In}_x\text{TiO}_{20}$  solid solution have estimated band gap around 2.75 eV; they absorb radiation with energy greater than this value (purple and UV-region) and appear yellowish (Fig. 8.8). Samples from  $\text{Bi}_{12-x}\text{In}_x\text{Mn}_{0.2}\text{Ti}_{0.8}\text{O}_{20}$  series have greenish colors and show no or minimum absorption in green region on Absorbance vs. Energy plot (Fig. 8.9).

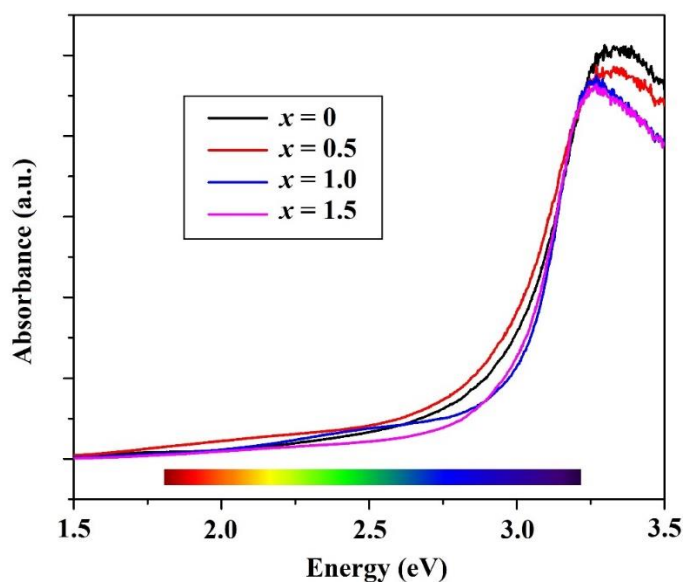


Figure 8.8 Diffuse reflectance spectra of  $\text{Bi}_{12-x}\text{In}_x\text{TiO}_{20}$ .



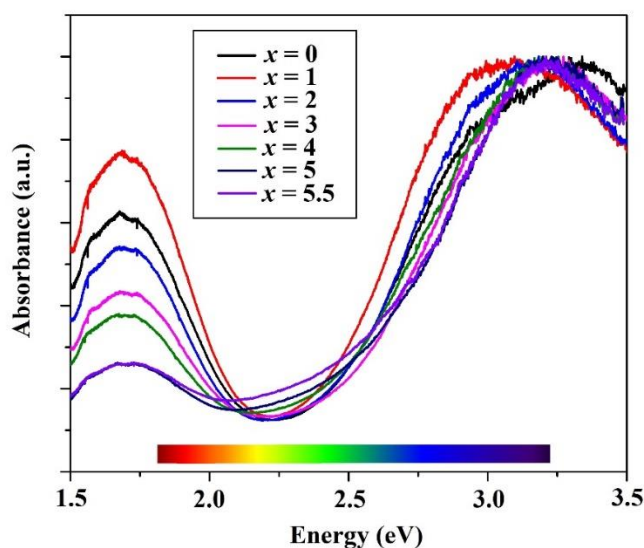


Figure 8.9 Diffuse reflectance spectra of  $\text{Bi}_{12-x}\text{In}_x\text{Mn}_{0.2}\text{Ti}_{0.8}\text{O}_{20}$  solid solution.

$\text{Bi}_{12-x}\text{In}_x\text{Mn}_{0.2}\text{Ti}_{0.8}\text{O}_{20}$  solid solution has two absorption maximums in low energy ( $\sim 1.75$  eV) and in high energy ( $\sim 3.20$  eV) regions;  $\text{Bi}_{12-x}\text{In}_x\text{TiO}_{20}$  series show only one high energy peak ( $\sim 3.25$  eV), which is due to  $\text{Ti}^{4+}\text{-O}^{2-}$  charge transfer. In case of  $\text{Bi}_{12-x}\text{In}_x\text{Mn}_{0.2}\text{Ti}_{0.8}\text{O}_{20}$  solid solution the low energy peak appears due to presence of  $\text{Mn}^{4+}$  chromophore; d-d interatomic transitions in octahedrally coordinated  $\text{Mn}^{4+}$  are responsible for this phenomenon. The larger the Mn concentration the higher the peak. Also Mn-containing samples with high  $x$  values ( $x = 4 - 5.5$ ) have charge transfer peak tailing towards the low energy region, samples color becomes lighter and more yellowish. Estimated band gap values of  $\text{Ba}_{12-x}\text{In}_x\text{Mn}_{0.2}\text{Ti}_{0.8}\text{O}_{20}$  solid solution are given in the Table 8.1. The band gap gradually increases with increasing of  $x$ ; samples become lighter.

Table 8.1 Estimated band gap of  $\text{Bi}_{12-x}\text{In}_x\text{Mn}_{0.2}\text{Ti}_{0.8}\text{O}_{20}$  series.

Compound	Estimated band gap (eV)
$x = 0$	2.36
$x = 1.0$	2.38
$x = 2.0$	2.40
$x = 3.0$	2.42
$x = 4.0$	2.44

$x = 5.0$	2.48
$x = 5.5$	2.50

All synthesized samples show relatively high reflectance in NIR region ( $\text{Bi}_{12-x}\text{In}_x\text{TiO}_{20}$ : Fig. 8.10 and  $\text{Bi}_{12-x}\text{In}_x\text{Mn}_{0.2}\text{Ti}_{0.8}\text{O}_{20}$ : Fig. 8.11) and might be promising candidates for the “Cool pigments” application.

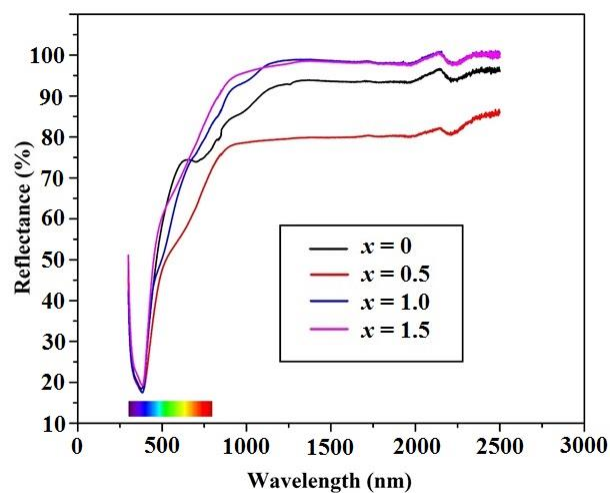


Figure 8.10 NIR reflectance spectra of  $\text{Bi}_{12-x}\text{In}_x\text{TiO}_{20}$  compounds.

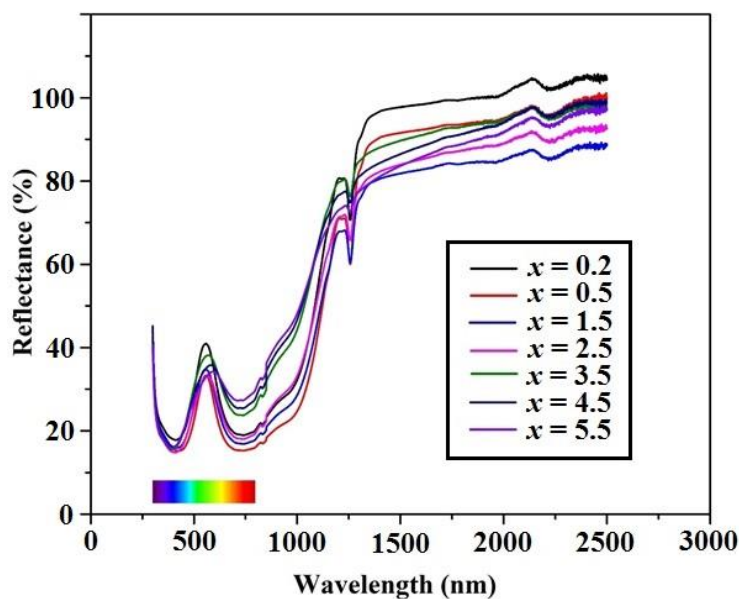


Figure 8.11 NIR reflectance spectra of  $\text{Bi}_{12-x}\text{In}_x\text{Mn}_{0.2}\text{Ti}_{0.8}\text{O}_{20}$  solid solution.



### 8.2.2 M-site Substitution

Three full solid solutions  $\text{Bi}_{12}\text{Mn}_{1-x}\text{M}_x\text{O}_{20}$  ( $M = \text{Ti, Si, Ge}$ ;  $x = 0 - 1.0$ ) were prepared and characterized. Solid state method was applied for synthesis. All samples are pure with one exception;  $\text{Bi}_{12}\text{MnO}_{20}$  phase has small impurity and there are several small extra peaks on XRD pattern. XRD patterns of  $\text{Bi}_{12}\text{Mn}_{1-x}\text{Ti}_x\text{O}_{20}$  series are shown in Figure 8.12,  $\text{Bi}_{12}\text{Mn}_{1-x}\text{Si}_x\text{O}_{20}$ : Figure 8.13,  $\text{Bi}_{12}\text{Mn}_{1-x}\text{Ge}_x\text{O}_{20}$ : Figure 8.14.

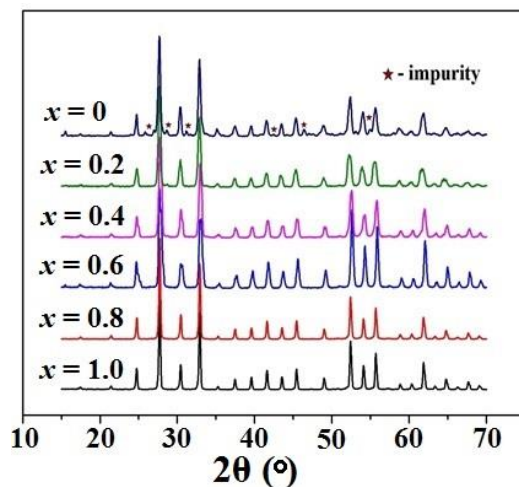


Figure 8.12 XRD patterns of  $\text{Bi}_{12}\text{Mn}_{1-x}\text{Ti}_x\text{O}_{20}$  solid solution.

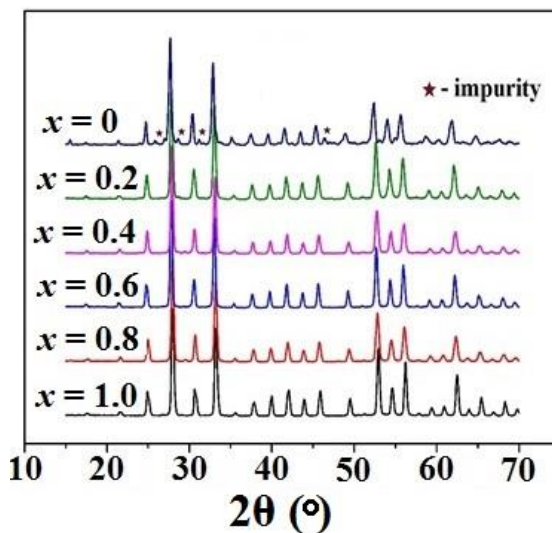


Figure 8.13 XRD patterns of  $\text{Bi}_{12}\text{Mn}_{1-x}\text{Si}_x\text{O}_{20}$  solid solution.

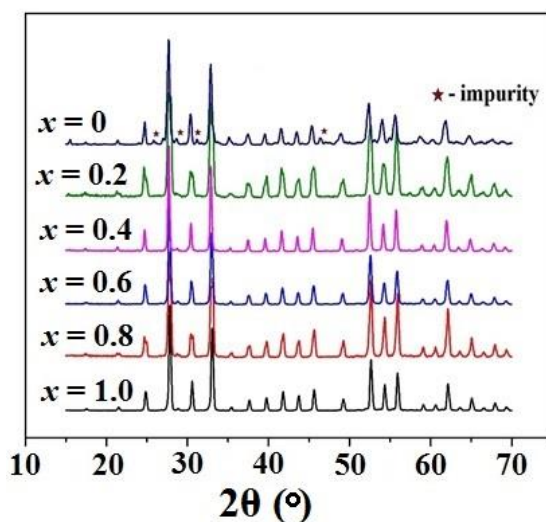


Figure 8.14 XRD patterns of  $\text{Bi}_{12}\text{Mn}_{1-x}\text{Ge}_x\text{O}_{20}$  series.

Using LeBail fitting method and GSAS software [46,47] unit cell parameters (unit cell edges and volume) for  $\text{Bi}_{12}\text{Mn}_{1-x}\text{M}_x\text{O}_{20}$  ( $M = \text{Ti}, \text{Si}, \text{Ge}$ ) solid solutions were refined. All samples were indexed to the cubic  $I23$  space group. Unit cell parameters of  $\text{Bi}_{12}\text{Mn}_{1-x}\text{Si}_x\text{O}_{20}$  progressively decrease as manganese is replaced by silicon, which was predicted regarding the difference in ionic radii (Shannon ionic radii (CN = IV):  $\text{Mn}^{4+} = 0.39 \text{ \AA}$  and  $\text{Si}^{4+} = 0.26 \text{ \AA}$  [44]). Ionic radii of Mn, Ti and Ge have similar values (Shannon ionic radii (CN = IV):  $\text{Ti}^{4+} = 0.42 \text{ \AA}$  and  $\text{Ge}^{4+} = 0.39 \text{ \AA}$  [44]), thus unit cell parameters don't vary much in case of  $\text{Bi}_{12}\text{Mn}_{1-x}\text{Ti}_x\text{O}_{20}$  and  $\text{Bi}_{12}\text{Mn}_{1-x}\text{Ge}_x\text{O}_{20}$  series (Fig. 8.15 and Fig. 8.16). In all cases the cell parameters change regularly and there is no special anomaly that would be associated to the structural transition.

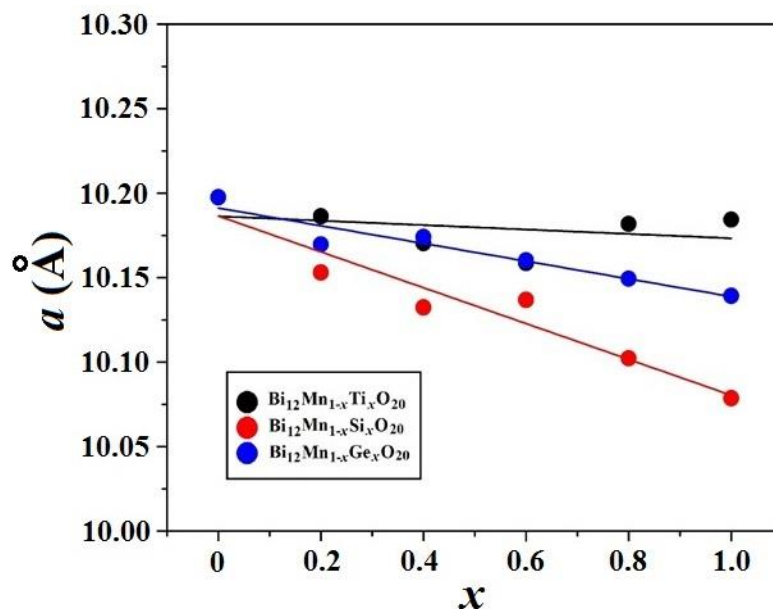


Figure 8.15 Unit cell parameters  $a$  vs.  $x$  for  $\text{Bi}_{12}\text{Mn}_{1-x}\text{M}_x\text{O}_{20}$  ( $M = \text{Ti, Si, Ge}$ ) compounds.

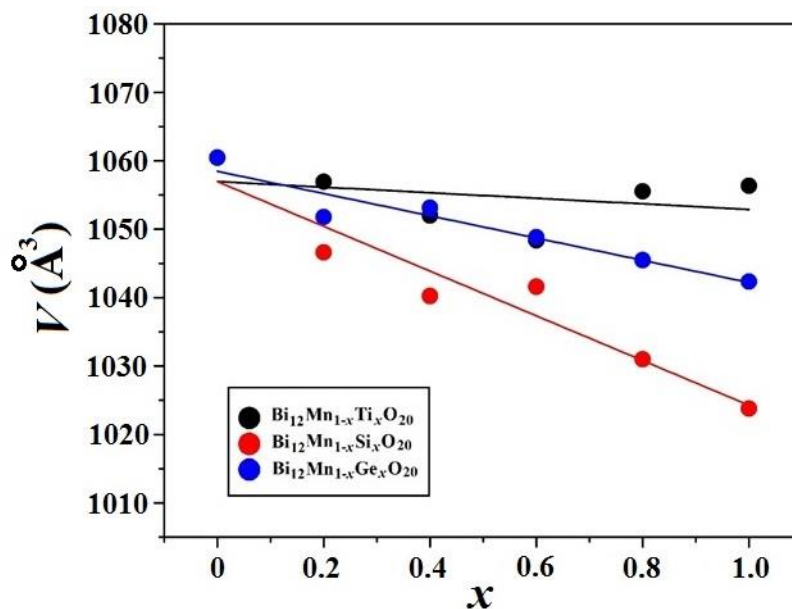


Figure 8.16 Unit cell volume ( $V$ ) of  $\text{Bi}_{12}\text{Mn}_{1-x}\text{M}_x\text{O}_{20}$  ( $M = \text{Ti, Si, Ge}$ ) series as a function of  $x$ .

All three  $\text{Bi}_{12}\text{Mn}_{1-x}\text{M}_x\text{O}_{20}$  ( $M = \text{Ti, Si, Ge}$ ) solid solutions have very similar colors (Fig. 8.17). The color vary from light yellow for samples with  $x = 1$  to lawn green ( $x = 0.5$ ) and dark green for  $x = 0$ .

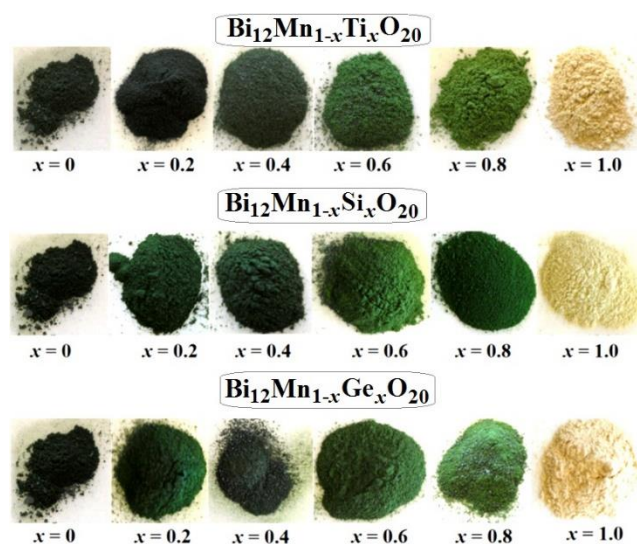


Figure 8.17 Colors of  $\text{Bi}_{12}\text{Mn}_{1-x}\text{M}_x\text{O}_{20}$  ( $M = \text{Ti}, \text{Si}, \text{Ge}$ ) compounds.

To characterize the color of each compound  $L^*a^*b^*$  parameters were measured.  $L^*a^*b^*$  values gradually increase with increasing of  $x$  value: samples become lighter, more yellowish and reddish.  $L^*a^*b^*$  parameters of  $\text{Bi}_{12}\text{Mn}_{1-x}\text{Ti}_x\text{O}_{20}$  series are shown in Fig. 8.18.

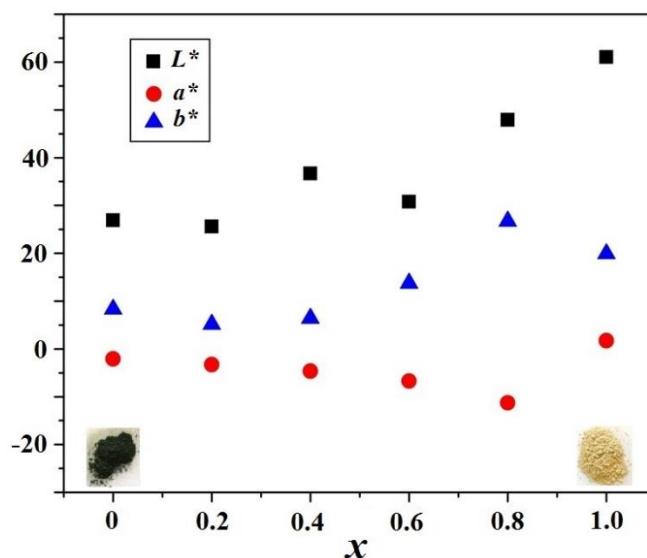
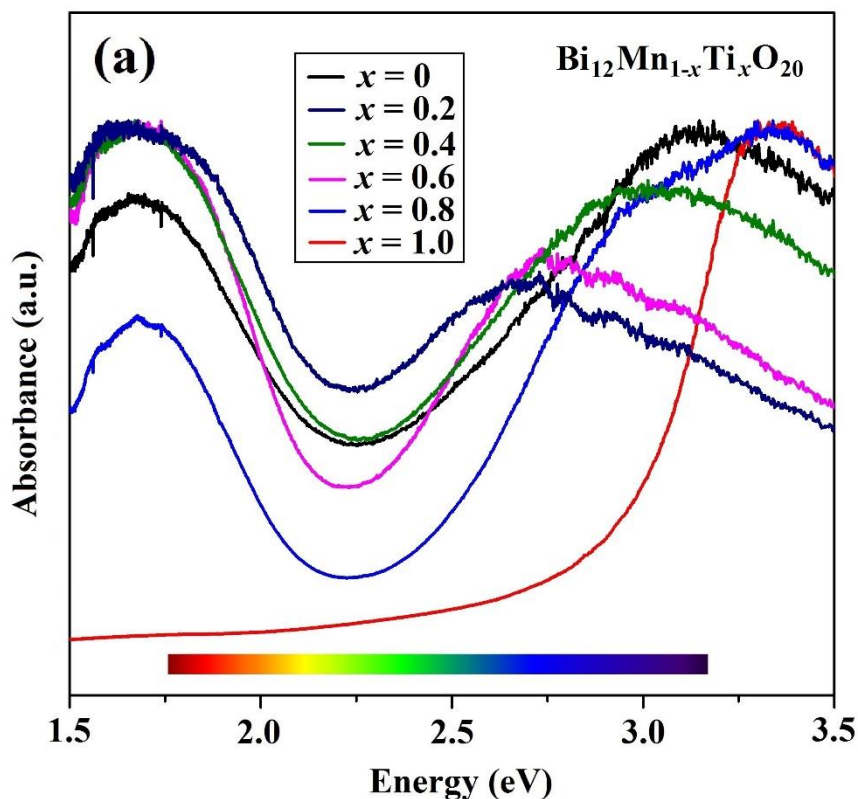


Figure 8.18  $L^*a^*b^*$  parameters of  $\text{Bi}_{12}\text{Mn}_{1-x}\text{Ti}_x\text{O}_{20}$  series.

$\text{Bi}_{12}\text{Mn}_{1-x}\text{M}_x\text{O}_{20}$  ( $M = \text{Ti}, \text{Si}, \text{Ge}$ ) solid solutions have similar diffuse reflectance spectra (Fig. 8.19). All Mn-containing samples have two maximum peaks in red-orange and in purple regions and one minimum of absorption in green region; this combination

causes the green color with different shades. The high energy peak (2.4–3.5 eV) is due to  $M^{4+}$ - $O^{2-}$  charge transfer and the low energy peak ( $\sim 1.25$  eV) is due to allowed transitions of d electrons inside  $T_d Mn^{4+}$  atom.  $Ti^{4+}$ -,  $Si^{4+}$ - and  $Ge^{4+}$ -containing compounds don't have low energy peak because these cations don't have d electrons. Gradual increase of crystal field splitting with  $x$  value and concentration of Ti, Si or Ge results in lighter shades of samples.



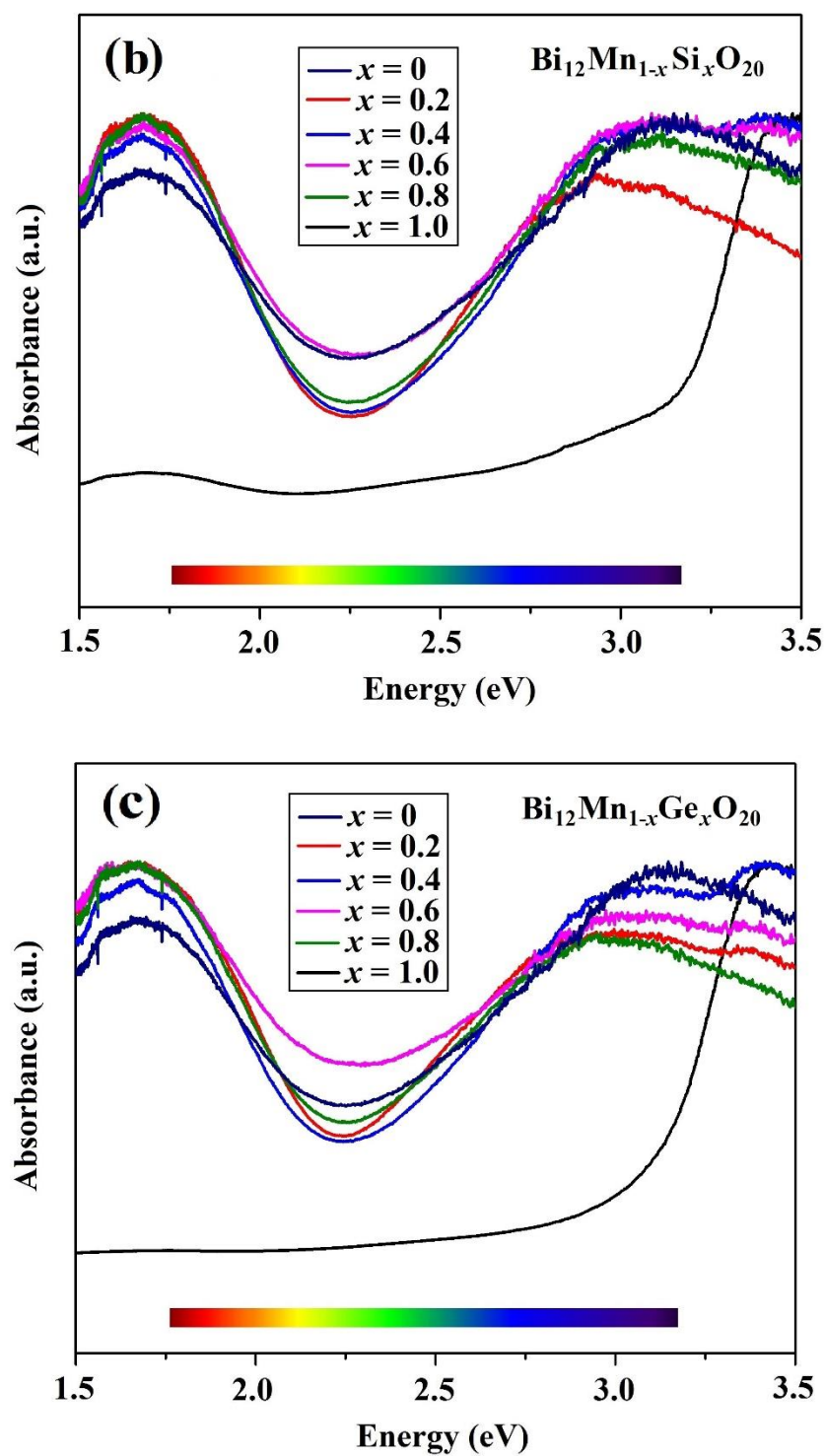
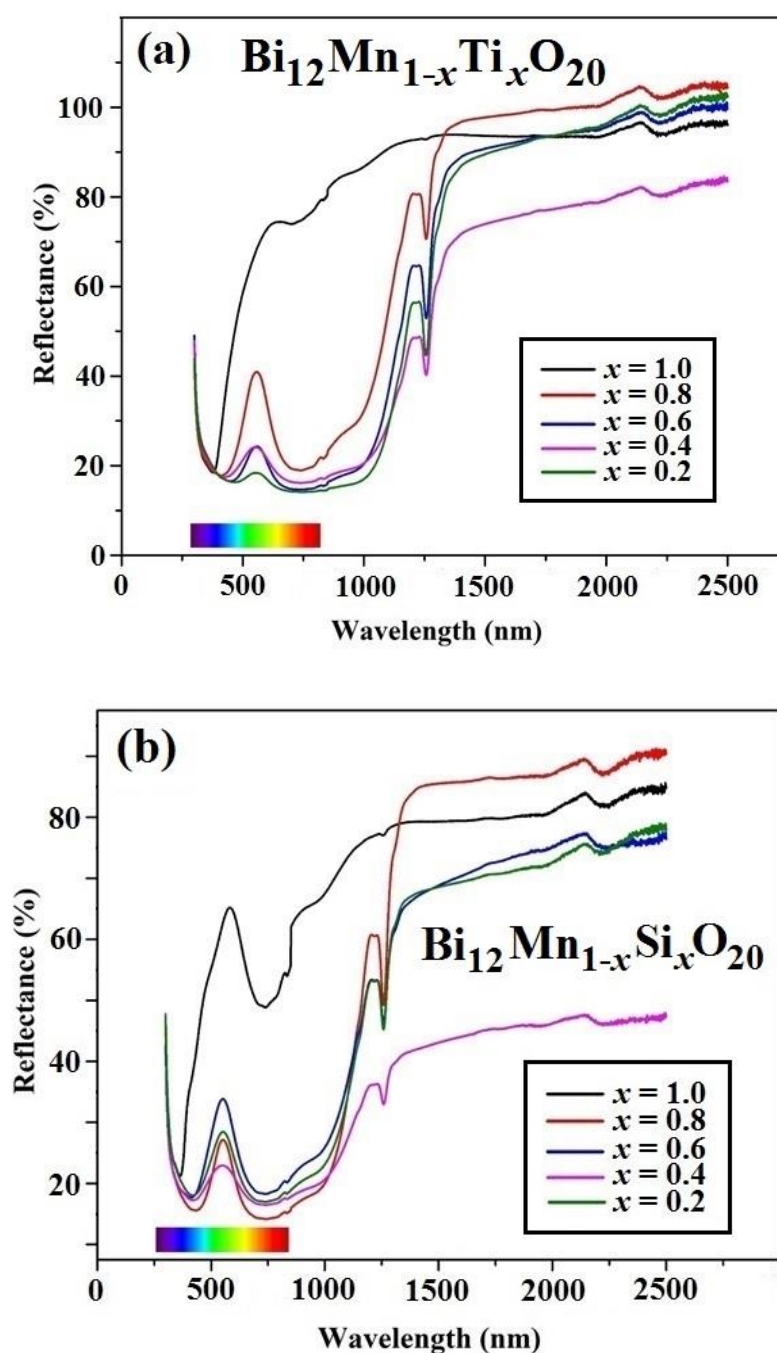


Figure 8.19 Diffuse reflectance spectra of (a)  $\text{Bi}_{12}\text{Mn}_{1-x}\text{Ti}_x\text{O}_{20}$  solid solution, (b)  $\text{Bi}_{12}\text{Mn}_{1-x}\text{Si}_x\text{O}_{20}$  series and (c)  $\text{Bi}_{12}\text{Mn}_{1-x}\text{Ge}_x\text{O}_{20}$  solid solution.

In near-IR reflectance vs. wavelength plots (Fig. 8.20) all Mn-containing samples show one sharp minimum ( $\sim 1250$  nm); this peak is inherent to d-d transitions in  $\text{Mn}^{4+}$  cation [48]. All synthesized compounds have relatively high reflectance in near-IR region (700–2500 nm).





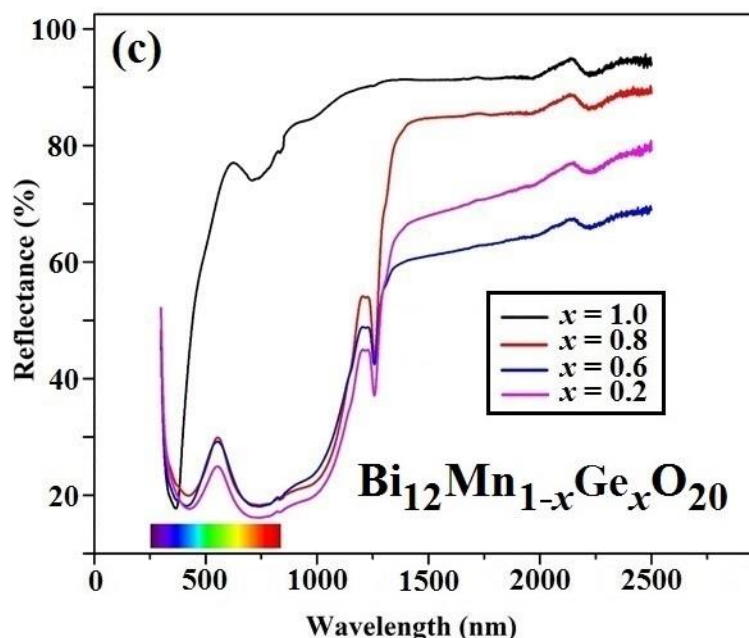


Figure 8.20 NIR reflectance spectra of (a)  $\text{Bi}_{12}\text{Mn}_{1-x}\text{Ti}_x\text{O}_{20}$  solid solution, (b)  $\text{Bi}_{12}\text{Mn}_{1-x}\text{Si}_x\text{O}_{20}$  series and (c)  $\text{Bi}_{12}\text{Mn}_{1-x}\text{Ge}_x\text{O}_{20}$  compounds.

In addition to ability to effectively reflect heat and presence of bright shade another important characteristic of pigment is existence of stable color. Some compounds have a tendency to fade in sunlight and show irreversible photochromic behavior. The sunlight exposure experiment with  $\text{Bi}_{12}\text{Mn}_{0.2}\text{Ti}_{0.8}\text{O}_{20}$  phase was performed to check the sample's color stability. The powder sample was exposed in sunlight for 9 h and  $L^*a^*b^*$  values of  $\text{Bi}_{12}\text{Mn}_{0.2}\text{Ti}_{0.8}\text{O}_{20}$  were measured before and after the experiment (Table 8.2). Based on  $L^*a^*b^*$  parameters, the color is stable; this feature makes our pigment an attractive object for further commercial applications in pigments industry.

Table 8.2  $L^*a^*b^*$  values of  $\text{Bi}_{12}\text{Mn}_{0.2}\text{Ti}_{0.8}\text{O}_{20}$  phase before and after the sunlight exposure experiment.

	$L^*$	$a^*$	$b^*$
<b>Before the experiment</b>	$45.9 \pm 0.6$	$-9.86 \pm 0.59$	$25.8 \pm 0.8$
<b>After the experiment</b>	$46.1 \pm 1.0$	$-10.1 \pm 0.2$	$26.3 \pm 0.7$

Magnetic measurements were performed for  $\text{Bi}_{12}\text{Mn}_{0.8}\text{Ti}_{0.2}\text{O}_{20}$  compound using PPMS. Molar magnetic susceptibility was measured in 5–300K temperature region. The



sample shows paramagnetic behavior in the region. Using magnetic susceptibility vs. temperature and inverse magnetic susceptibility vs. temperature plots (Fig. 8.21) Curie constant ( $C$ ), Weiss constant ( $\theta$ ) and effective magnetic moment ( $\mu_{\text{eff}}$ ) of manganese were calculated; diamagnetic correction was made [49]:  $C = 1.14$ ,  $\theta = -44.05$  K,  $\mu_{\text{eff}} = 3.04 \mu_B$ . The effective magnetic moment of manganese was found to prove the oxidation state of the element. The  $\mu_{\text{eff}}$  is slightly smaller than the theoretical value ( $\mu_{\text{th}} = 3.87 \mu_B$ ) of magnetic moment for  $\text{Mn}^{4+}$ .

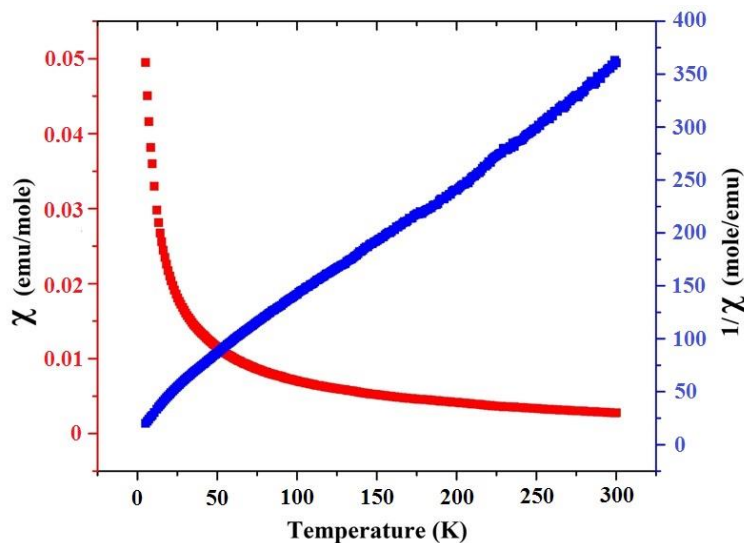


Figure 8.21 Magnetic susceptibility and inverse magnetic susceptibility of  $\text{Bi}_{12}\text{Mn}_{0.8}\text{Ti}_{0.2}\text{O}_{20}$ ; 1 emu (cgs units) =  $10^{-3}$  A m<sup>2</sup> (SI units).

To get extra details about magnetic behavior of  $\text{Bi}_{12}\text{Mn}_{1-x}\text{Ti}_x\text{O}_{20}$  system, magnetic measurements were performed for  $\text{Bi}_{12}\text{Mn}_{0.8}\text{Ti}_{0.2}\text{O}_{20}$ ,  $\text{Bi}_{12}\text{Mn}_{0.4}\text{Ti}_{0.6}\text{O}_{20}$  and  $\text{Bi}_{12}\text{Mn}_{0.2}\text{Ti}_{0.8}\text{O}_{20}$  samples at UC Santa Cruz (Dr. Ramirez's lab) using MPMS. Compounds are paramagnetic and don't show a magnetic transition in the measured temperature region (5–300K). Molar susceptibility and inverse molar susceptibility as a function of temperature graphs are shown in Figure 8.22. Plots show a linear relations at high temperature and follow Curie-Weiss law.

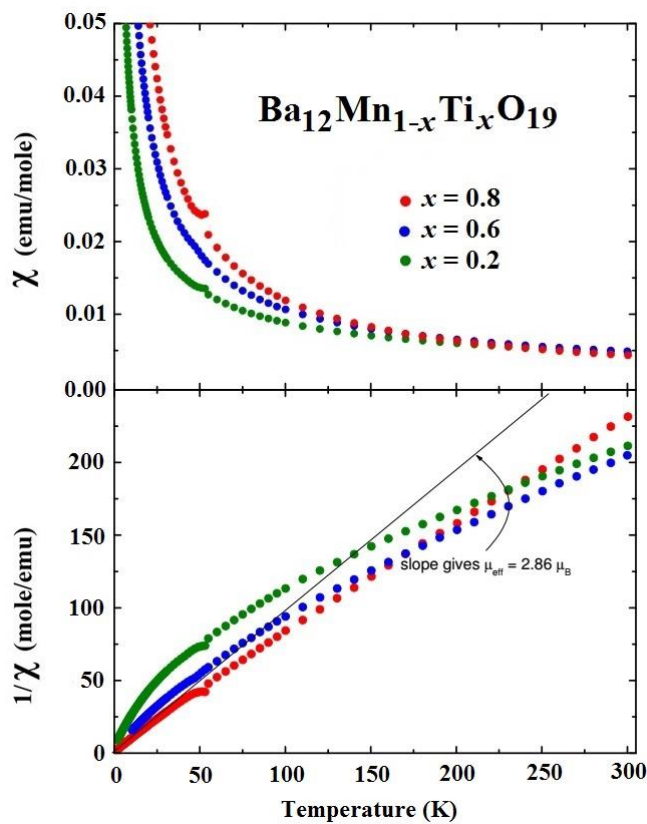


Figure 8.22 Magnetic susceptibility and inverse magnetic susceptibility as a function of temperature for  $\text{Bi}_{12}\text{Mn}_{1-x}\text{Ti}_x\text{O}_{20}$  ( $x = 0.2, 0.6$  and  $0.8$ ) samples (from Dr. Ramirez).

The  $\text{Bi}_{12}\text{Mn}_{0.2}\text{Ti}_{0.8}\text{O}_{20}$  and  $\text{Bi}_{12}\text{Mn}_{0.4}\text{Ti}_{0.6}\text{O}_{20}$  samples have  $\mu_{\text{eff}} = 2.83 \mu_B$ , for  $\text{Bi}_{12}\text{Mn}_{0.8}\text{Ti}_{0.2}\text{O}_{20}$  compound, the spins are starting to interact antiferromagnetically, and the effective magnetic moment gets reduced. The effective magnetic moment equals  $2.87 \mu_B$  corresponds to two unpaired electrons and  $\text{Mn}^{5+}$  cation, but the existence of  $\text{Mn}^{5+}$  in the sillenite-type structure has low probability as it requires an extra oxygen. Another possible explanation for the slightly reduced value of the effective magnetic moment is presence of small amount of oxygen vacancies. To make a final conclusion about the manganese oxidation state and possible presence of oxygen vacancies in the structures neutron Rietveld refinement is required to make. Neutron diffraction data were obtained at NIST for  $\text{Bi}_{12}\text{Mn}_{0.5}M_{0.5}\text{O}_{20}$  ( $M = \text{Ti, Si, Ge}$ ) samples and neutron structural refinement will be performed soon.

### 8.3 Conclusion

Several solid solutions having sillenite-type structure were prepared and studied using different methods and techniques. The samples color was tuned through Bi-site and M-site substitutions in the  $\text{Bi}_{12}\text{MO}_{20}$  structure.  $L^*a^*b^*$  parameters were measured and the colors of samples were characterized. Optical properties investigations (diffuse reflectance spectra and reflectance vs. wavelength) were performed. Mn-containing samples show greenish colors due to combination of d-d interatomic transitions in tetrahedral  $\text{Mn}^{4+}$  and  $\text{M}^{4+}\text{-O}^{2-}$  charge transfer. Samples show paramagnetic behavior and the effective magnetic moment is smaller than theoretical magnetic moment of  $\text{Mn}^{4+}$  cation; to make a final conclusion about the oxidation state of manganese and presence of oxygen vacancies neutron Rietveld refinement is needed to be performed.

### 8.4 Experimental Materials and Methods

Stoichiometric amounts of starting materials  $\text{Bi}_2\text{O}_3$  (Sigma-Aldrich, 98.0%),  $\text{In}_2\text{O}_3$  (Sigma-Aldrich, 99.998%),  $\text{TiO}_2$  (Sigma-Aldrich, 99.99%),  $\text{SiO}_2$  (Alfa Aesar, 99.5%),  $\text{GeO}_2$  (Alfa Aesar, 99.99%) and  $\text{MnO}_2$  (Sigma-Aldrich, 99%) were mixed together, ground in an agate mortar with pestle, pelletized and heated at 750–800 °C and for 12–24h. The synthesized samples were characterized by XRD using a Rigaku Miniflex II diffractometer with  $\text{CuK}_\alpha$  radiation with graphite monochromator. Powder silicon (99.999%) was used as an internal standard to refine lattice parameters of samples using LeBail method and GSAS software with EXPGUI interface. Konica Minolta CM-700d Spectrophotometer was used to measure  $L^*a^*b^*$  color coordinates. Diffuse reflectance spectra measurements were performed on homemade UV-VIS spectrophotometer (Department of Physics, OSU);  $\text{MgO}$  was used as a reference. NIR reflectance data were collected using a Jasco V-670 Spectrophotometer (Chemical Engineering Department, OSU). Magnetism measurements for  $\text{Bi}_{12}\text{Mn}_{0.8}\text{Ti}_{0.2}\text{O}_{20}$  phase were performed on a quantum design physical properties measurement system (PPMS) in the temperature range 5–300 K under magnetic field of 0.5T and zero-field cooled conditions. Magnetic measurements for  $\text{Bi}_{12}\text{Mn}_{1-x}\text{Ti}_x\text{O}_{20}$  ( $x = 0.2, 0.6, 0.8$ ) samples were made using magnetic property measurement system (MPMS) at the University of California, Santa Cruz (UCSC) at Dr. Art Ramirez lab.

## 8.5 Acknowledgements

This work has been supported by NSF grant DMR-1508527.

## 8.6 References

- [1] <http://webmineral.com/data/Sillenite.shtml#WEcAoLrK70> (accessed 12/19/2016).
- [2] Aurivillius, B., Sillen, L.G., *Nature* 155 (1945) 305.
- [3] <https://en.wikipedia.org/wiki/Sill%C3%A9nite> (accessed 12/19/2016).
- [4] Wiehl, L., Friedrich, A., Haussuehl, E. et al., *J. Phys. Condensed Matter*. 22 (2010) 1.
- [5] Delicat, U., Radaev, S.F., Tromel, M. et al., *J. Solid State Chem.* 110 (1994) 66.
- [6] Sillen, L.G., *Ark. Kemi, Mineral. Geol.* 12A (1937) 1.
- [7] Devalette, M., Meunier, G., Manaud, J.-P., Hagenmuller, P., *C.R. Math. Acad. Sci. Paris, Ser. I* 296 (1983) 189.
- [8] Shamonina, E., Kamenov, V.P., Ringhofer, K.H. et al., *Opt. Commun.* 146 (1998) 62.
- [9] Burkov, V.I., Egorysheva, A.V., Kargin, Y. F., *Cryst. Rep.* 46(2) (2001) 312.
- [10] Jeong, B.-J., Joung, M.-R., Kim, J.-S., Nahm, S. et al., *J. Am. Ceram. Soc.* 96(12) (2013) 3742.
- [11] Hou, D., Hu, X., Wen, Y. et al., *Phys. Chem. Chem. Phys.* 15 (2013) 20698.
- [12] Ilinskii, A., Prutskij, T., Silva-Andrade, F. et al., *Mod. Phys. Lett. B* 15(17-19) (2001) 749.
- [13] Shen, C., Zhang, H., Zhang, Y. et al., *Crystals* 4 (2014) 141.
- [14] Efendiev, S.M., Kulieva, T.Z., Lomonov, V.A. et al., *Phys. Stat. Sol.* 74(1) (1982) K17.
- [15] Kirik, S.D., Kutvitskii, V.A., Koryagina, T.I., *Zh. Struktur. Khim.* 26(4) (1985) 90 (in Russian).
- [16] Murray, A.D., Catlow, C.R.A., *J. Solid State Chem.*, 62 (1986) 290.
- [17] Radaev, S.F., Simonov, V.I., *Kristallografiya*, 37(4) (1992) 914.
- [18] Zyryanov, V.V., *Zh. Struktur. Khim.* 45 (2004) 480 (in Russian).
- [19] Skorikov, V.M., Kargin, Y.F., Egorysheva, A.V., *Inorg. Mater.* 41(1) (2005) S24.
- [20] Skorikov, V.M., *Chemistry of Piezoelectric Compounds*, Extended Abstract of Doctoral (Chem.) Dissertation, Moscow: Kurnakov Inst. Of General and Inorganic Chemistry, USSR Acad. Sci., 1985 (in Russian).
- [21] Kargin, Y.F., *Synthesis, structure, and properties of sillenite-structure bismuth oxide compounds*, Doctoral (Chem.) Dissertation, Moscow: Kurnakov Inst. Of General and Inorganic Chemistry, Russ. Acad. Sci., 1998 (in Russian).
- [22] Wardzynski, W., Szymczak, H., Pataj, K., *J. Phys. Chem. Solids* 43(8) (1982) 767.
- [23] Wardzynski, W., Szymczak, H., *J. Phys. Chem. Solids* 45(8/9) (1984) 887.
- [24] Filar, K.P., Gajda, G.P., Nizhankovskii, V.I., *Phys. Status Solidi B* 253(3) (2016) 473.
- [25] Panchenko, T.V., Karpova, L.M., Duda, V.M., *Phys. Solid State* 42(4) (2000) 689.
- [26] Burkov, V.I., Kargin, Y.F., Burkova, L.T. et al., *Inorg. Mater.* 31(6) (1995) 719.
- [27] Elkhouni, T., Amami, M., Salah, A.B., *J. Supercond. Nov. Magn.* 26 (2013) 2997.
- [28] Burkov, V.I., Egorysheva, A.V., Kargin, Y.F. et al., *Inorg. Mater.* 33(4) (1997) 412.
- [29] Marinova, V., Lin, S.H., Sainov, V., Gospodinov, M., Hsu, K.Y., *J. Opt. A.: Pure Appl. Opt.* 5 (2003) S500.

- [30] Avanesyan, V.T., Paima, K.I., *Phys. Solid State* 58(8) (2016) 1560.
- [31] Nogueira, A.E., Lima, A.R.F., Longo, E., Leite, E.R., Camargo, E.R., *J. Nanopart. Res.* 16 (2014) 2653.
- [32] Belyaev, V.A., Kolosov, E.E., Shilova, M.V., *Inorg. Mater.* 17(10) (1981) 1427.
- [33] Nistor, S.V., Stefan, M., Goovaerts, E. et al., *J. Magn. Reson.* 259 (2015) 87.
- [34] Petrova, D., Gospodinov, M., Sveshtarov, P., *Mat. Res. Bull.* 30(10) (1995) 1201.
- [35] Gospodinov, M., Doshkova, D., *Mat. Res. Bull.* 29(6) (1994) 681.
- [36] Marinova, V., Veleva, M., Petrova, D. et al., *J. Appl. Phys.* 89(5) (2001) 2686.
- [37] Sekhar, H., Rao, D.N., *J. Mater. Sci.: Mater. Electron.* 24 (2013) 1569.
- [38] Mel'nikova, T.I., Kuz'micheva, G.M., Rybakov, V.B. et al., *J. Struct. Chem.* 52(3) (2011) 510.
- [39] Grabmaier, B.C., Oberschmid, R., *Phys. Stat. Sol. (a)* 96 (1986) 199.
- [40] Senulienė, D., Babonas, G., Sileika, A. et al., *Litovskii Fizicheskii Sbornik, Akademiia nauk Litovskoi SSR*, 27(1) (1987) 71 (in Russian).
- [41] Wardzynski, W., Szymczak, H., Borowicz, M.T., Pataj, K., *J. Phys. Chem. Solids* 46(10) (1985) 1117.
- [42] Burkov, V.I., Egorysheva, A.V., Kargin, Y.F., Volkov, V.V., *Inorg. Mater.* 32(7) (1996) 762.
- [43] Sakoske, G.E., Sarver, J.E., Novotny, M., Bismuth manganese oxide pigments, US Patent, WO 2000037362 A1, 2000.
- [44] Shannon, R.D., *Acta Cryst. A* 32 (1976) 751.
- [45] Sherif, M.E., Bayoumi, O.A., Sokkar, T.Z.N., *Color Res. Appl.* 22 (1997) 32.
- [46] Larson, A.C., Von Dreele, R.B., General structure analysis system (GSAS), Los Alamos Natl. Lab. Rep. LAUR (2014) 86.
- [47] EXPGUI, a graphical user interface for GSAS: Toby, B.H., *J. Appl. Crystallogr.* 34 (2001) 210.
- [48] Volkov, V.V., Egorysheva, A.V., Kargin, Y.F., Skorikov, V.M., *Inorg. Mater.* 29(11) (1993) 1364.
- [49] Bain, G.A., Berry, J.F., *J. Chem. Educ.* 85 (2008) 532.

## CHAPTER 9

### General Conclusions and Future Work

The research results described in this thesis are demonstrated that various crystalline structures can be used as parent compounds to synthesize materials with interesting colors and optical properties. The hue of inorganic oxides might be engineered and tuned by different sites substitutions. New pigments are waiting to be discovered, especially new red pigment to replace toxic cadmium red ( $\text{CdSe}_{1-x}\text{S}_x$ ), red lead ( $\text{Pb}_3\text{O}_4$ ) and cinnabar/vermilion ( $\text{HgS}$ ) which are the most famous red inorganic pigments nowadays.

We have studied and discussed the synthesis, structure, color, optical, magnetic and dielectric properties of apatite-type, hibonite-type,  $\text{Li}_2\text{Mn}_{1-x}\text{Ti}_x\text{O}_3$  ( $x = 0-1.0$ ) and sillenite-type colored oxides which have a potential for application as pigments due to their stability, durability, bright colors, low cost and relatively high reflectance in the NIR region.

In  $A_5M'_{3-x}M_x\text{O}_{12}X$  ( $A = \text{Sr, Ba}$ ;  $M' = \text{Mn, Cr}$ ;  $M = \text{V, P}$ ;  $X = \text{F, Cl}$ ) apatite-type compounds  $\text{Mn}^{5+}$  and  $\text{Cr}^{5+}$  are chromophore elements which are mainly responsible for the color. Phases with high concentration of the chromophores are dark green, the color changes to turquoise and light turquoise with decreasing of manganese and chromium amount. Due to high first ionization potential of A-site elements, Mn and Cr can hold an unstable 5+ oxidation state in tetrahedral coordination.

Hibonite-type colored oxides  $A\text{Al}_{12-x}M_x\text{O}_{19}$  ( $A = \text{Ca, Sr, RE}$  (rare earths) or any combination thereof;  $M = \text{Ni, Fe, Mn, Cr, Cu}$  coupled with one of the following: Ga, In, Ti, Sn, Ge, Nb, Ta, Sb) show various colors:  $\text{Ni}^{2+}$  containing hibonites are blue with different shades, combination of  $\text{Cu}^{2+}$  with  $\text{Ti}^{4+}$ ,  $\text{Mn}^{2+}$ ,  $\text{Mn}^{3+}$  and  $\text{Fe}^{3+}$  samples have ochre and brownish hues,  $\text{Fe}^{2+}$  gives greenish colors, phases with small  $\text{Cr}^{3+}$  concentration are rosy brown, compounds having larger amount of  $\text{Cr}^{3+}$  are greenish. Hibonite structure has five different crystallographic positions of M-site and is prospective host for diverse atoms, what makes it a perspective parent compound to work with.

$\text{Mn}^{4+}$  cation can impart different tints depending on its crystallographic position: in case of octahedral coordination ( $\text{Li}_2\text{Mn}_{1-x}\text{Ti}_x\text{O}_3$  solid solution) the color is bright orange (it

varies from dark orange ( $x = 0.2$ ) to light orange ( $x = 0.8$ )) and compounds with tetrahedrally coordinated manganese ( $\text{Bi}_{12}\text{Mn}_{1-x}\text{M}_x\text{O}_{20}$ ;  $M = \text{Ti, Si, Ge}$ ) are green (from dark green ( $x = 0$ ) to light green ( $x = 0.8$ )).

Research is the endless process and any investigation can be continued. The several possible ways to proceed the research projects presented in the thesis are provided below. For  $\text{CaAl}_{12-x}\text{M}_x\text{O}_{19}$  ( $M = \text{Fe, Mn, Cr and Cu}$ ) hibonite-type colored oxides, it might be promising to check how A-site substitutions ( $A = \text{Sr, Ba, RE (rare earth)}$  and any combination thereof with Ca) affect the color of the samples. In order to determine a degree of stacking faults present in  $\text{Li}_2\text{Mn}_{1-x}\text{Ti}_x\text{O}_3$  ( $x = 0\text{--}1.0$ ) system the DIFFaX program can be applied. It can model different percentage of stacking faults in the structure and calculate a theoretical diffraction pattern for the sample. Then the experimental XRD pattern can be compared to the theoretical one and degree of actual stacking disorder might be found. To study Mn-site distribution, confirm manganese oxidation state and check the presence of oxygen vacancies in  $\text{Bi}_{12}\text{Mn}_{1-x}\text{M}_x\text{O}_{20}$  ( $M = \text{Ti, Si, Ge}$ ) series, neutron diffraction and structural refinement need to be performed for several family members.

## Bibliography

- Abrahams, S.C., Marsh, P., Brandle, C.D., *J. Chem. Phys.* 86(7) (1987) 4221.
- Adams, D.M., *Inorganic solids. An introduction to concepts in solid-state structural chemistry*, John Wiley & Sons, Inc., New York, 1974, pp. 1-352.
- Ahn, S.D., Jung, H.S., Choo, D.C. et al., *J. Electrochem. Soc.* 157(6) (2010) J238.
- Aleshko-Ozhevskii, O.P., Faek, M.K., Yamzin, I.I., *Sov. Phys. Crystallogr.* 14(3) (1969) 367.
- Altay, A., Carter, C.B., Rulis, P., Ching, W.-Y., Arslan, I., Guelguen, M.A., *J. Solid State Chem.* 183(8) (2010) 1776.
- Alvarez, G., Zamorano, R., Hairas, J., Castellanos, M., Valenzuela, R., *J. Magn. Magn. Mater.* 316 (2007) e695.
- Ardit, M., Borcanescu, S., Cruciani, G., Dondi, M., Lazau, I., Pacurariu, C., Zanelli, C., *J. Am. Ceram. Soc.* 99(5) (2016) 1749.
- Armstrong, J.T., Meeker, G.P., Huneke, J.C., Wasserburg, G.J., *Geochim. Cosmochim. Acta* 46(4) (1982) 575.
- Arora, A., Narang, S.B., *J. Mater. Sci.: Mater. Electron.* 27 (2016) 10157.
- Atkins, P.W., Shriver&Atkins' *Inorganic Chemistry* (5<sup>th</sup> edition), Freeman, W.H. and Company, New York, 2010, pp. 1-830.
- Aurivillius, B., Sillen, L.G., *Nature* 155 (1945) 305.
- Avanesyan, V.T., Paima, K.I., *Phys. Solid State* 58(8) (2016) 1560.
- Bai, G., Tsang, M.K., Hao, J., *Adv. Opt. Mater.* 3 (2015) 431.
- Baikie, T., Ahmad, Z., Srinivasan, M. et al., *J. Solid State Chem.* 180(5) (2007) 1538.
- Bain, G.A., Berry, J.F., *J. Chem. Educ.* 85 (2008) 532.
- Baker, W.E., *Am. Mineral.* 51 (1966) 1712.
- Batista, J.A.L., Ribeiro, M.J.P.M., Cordeiro da Costa, M.G.C., US Patent PT103889, A20090521, 2009.
- Beck, H.P., Douiheche, M., Haberkorn, R., Kohlmann, H., *Solid State Sci.* 8 (2006) 64.
- Beckett, J.R., Live, D., Tsay, F.D., Lawrence, G., Stolper, E., *Geochim. Cosmochim. Acta* 52(6) (1988) 1479.
- Beckett, J.R., Stolper, E., *Meteorit. Planet. Sci.* 29(1) (1994) 41.
- Bednorz, J.G., Muller, K.A., *Z. Phys. B Con. Mat.* 64(2) (1986) 189.
- Belyaev, V.A., Kolosov, E.E., Shilova, M.V., *Inorg. Mater.* 17(10) (1981) 1427.
- Bergstein, A., White, W.D., *J. Electrochem. Soc.* 118(7) (1971) 1166.
- Bermanec, V., Holtstam, D., Sturman, D., Criddle, A.J., Black, M.E., Nezilovite Scavnicar, S., *Can. Mineral* 34 (1996) 1287.
- Biernat, K., Malinowski, A., Gnat, M., *Biofuels – economy, environment and sustainability*, Z. Fang (Ed.), Intech, 2013, pp. 1-386.
- Boechat, C., Eon, J.-G., Rossi, A., et al., *J. Phys. Chem. A* 2 (2000) 4225.
- Bondioli, F., Ferrari, A.M., Leonelli, C. et. al., *Mat. Res. Bull.* 33(5) (1998) 723.
- Borromei, R., Oleari, L., Day, P., *J. Chem. Soc.* 77 (1981) 1563.
- Boulineau, A., Croguennec, L., Delmas, C., Weill, F., *Solid State Ion.* 180 (2010) 1652.
- Breger, J., Jiang, M., Dupre, N., Meng, Y.S., Shao-Horn, Y. et al., *J. Solid State Chem.*, 178 (2005) 2575.
- Brixner, L., Weiher, J.F., *Inorg. Chem.* 7 (1968) 1474.



- Burkov, V.I., Egorysheva, A.V., Kargin, Y. F., Cryst. Rep. 46(2) (2001) 312.
- Burkov, V.I., Egorysheva, A.V., Kargin, Y.F. et al., Inorg. Mater. 33(4) (1997) 412.
- Burkov, V.I., Egorysheva, A.V., Kargin, Y.F., Volkov, V.V., Inorg. Mater. 32(7) (1996) 762.
- Burkov, V.I., Kargin, Y.F., Burkova, L.T. et al., Inorg. Mater. 31(6) (1995) 719.
- Burns, R.G., Burns, V.M., Virginia, J. Geophys. Res., B 89(Suppl.) (1984) C313.
- Burns, R.G., Mineralogical applications of crystal field theory (2<sup>nd</sup> edition), Putnis, A., Liebermann, R.C. (Ed.), Cambridge University Press, 2005, pp. 1-576.
- Burns, R.G., Mixed Valency Syst.: Appl. Chem. Phys. Biol. 343 (1991) 175.
- Buvaneswari, G., Varadaraju, U.V., J. Solid State Chem. 149 (2000) 133.
- Carlston, R.C., J. Chem. Ed. 42(2) (1965) 117.
- Cheetham, A.K., Day, P. (Ed.), Solid state chemistry: techniques, Oxford University Press, Oxford, 1987.
- Chen, Y., Wang, M., Wang, J., Wu, M., Wang, C., J. Solid State Light. 1 (2014) 15.
- Chernorukov, N.G., Knyazev, A.V., Bulanov, E.N., Inorg. Mater. 47(2) (2011) 172.
- Cho, J., Kim, Y.J., Park, B., Chem. Mater. 12 (2000) 3788.
- Chun, S.H., Chai, Y.S., Jaiswal-Nagar, D., Haam, S.Y., Kim, I., Phys. Rev. Lett. 104 (2010) 037204.
- Cinibulk, M.K., J. Am. Ceram. Soc. 81(12) (1998) 3157.
- Cohen, R.E., Krakauer, H., Ferroelectrics, 136(1-4) (1992) 65.
- Collomb, A., Obradors, X., Isalgue, A., Fruchart, D., J. Magn. Magn. Mater. 69(3) (1987) 317.
- Collongues, R., Gourier, D., Kahn-Harari, A., Lejus, A.M., Thery, J., Vivien, D., Annu. Rev. Mater. Sci. 20 (1990) 51.
- Comer, J.J., Croft, W.J., Kestigian, M., Carter, J.R., Mater. Res. Bull. 2(3) (1967) 293.
- Cooray, P.G., Am. Mineral. 55 (1970) 2038.
- Costa, G., Ribeiro, M.J., Hajjaji, W., Seabra, M.P., Labrincha, J.A., Dondi, M., Cruciani, G., J. Eur. Ceram. Soc. 29 (2009) 2671.
- Cullity, B.D., Elements of X-ray diffraction (2<sup>nd</sup> edition), Addison Wesley Publishing Company, Inc., MA, 1978, pp. 1-531.
- Curien, H., Guillemin, C., Orcel, J. et al., Comptes Rendus de l'Academie des Sciences, Paris (1956) 2845.
- Dardenne, K., Vivien, D., Huguenin, D., J. Solid State Chem. 146 (1999) 464.
- Dardenne, K., Vivien, D., Ribot, F. et al., Eur. J. Solid State Inorg. Chem. 35 (1998) 419.
- Davis, M. (Ed.), Dielectric materials handbook, ML Books International, 2010, pp. 1-316.
- Delicat, U., Radaev, S.F., Tromel, M. et al., J. Solid State Chem. 110 (1994) 66.
- Devalette, M., Meunier, G., Manaud, J.-P., Hagenmuller, P., C.R. Math. Acad. Sci. Paris, Ser. I 296 (1983) 189.
- Dondi, M., Cruciani, G., Guarini, G., Matteucci, F., Raimondo, M., Ceram. Int. 32(4) (2006) 393.
- Dorrian, J.F., Newnham, R.E., Am. Ceram. Soc. Bull. (1969) 401.
- Doyle, P.M., Berry, A.J., Schofield, P.F., Mosselmans, J.F.W., Geochim. Cosmochim. Acta 187 (2016) 294.
- Doyle, P.M., Schofield, P.F., Berry, A.J., Walker, A.M., Knight, K.S., Amer. Mineral. 201 (1999) 1369.

- Doyle, P.M., Schofield, P.F., Berry, A.J., Walker, A.M., Knight, K.S., *Am. Mineral.* 99 (2014) 1369.
- Doynov, M.I., Bozadjiev, R.L., Dimitrov, T.I., Bozadjiev, L.S., *Oxid. Commun.* 34(3) (2011) 726.
- Du, L.S., Stebbins, J.F., *J. Phys. Chem. B* 108(12) (2004) 3681.
- Dyar, M.D., Solberg, T.C., Burns, R.G., *Lunar Planet. Sci. XVII* (1986) 194.
- Ebnabbasi, K., Chen, Y., Geiler, A., Harris, V., Vittoria, C., *J. Appl. Phys.* 111 (2012) 07C719.
- Ebnabbasi, K., Mohebbi, M., Vittoria, C., *Appl. Phys. Lett.* 101 (2012) 062406.
- Ebnabbasi, K., Mohebbi, M., Vittoria, C., *J. Appl. Phys.* 113 (2013) 17C703.
- Ebnabbasi, K., Vittoria, C., Widom, A., *Phys. Rev. B* 86 (2012) 024430.
- Efendiev, S.M., Kulieva, T.Z., Lomonov, V.A. et al., *Phys. Stat. Sol.* 74(1) (1982) K17.
- Elkhouni, T., Amami, M., Salah, A.B., *J. Supercond. Nov. Magn.* 26 (2013) 2997.
- Elliott, J.C., Wilson, R.M., Dowker, S.E.P., *Adv. X-ray Anal.* 45 (2002) 172.
- Ellis, B.L., Lee, K.T., Nazar, L.F., *Chem. Mater.* 22 (2010) 691.
- EXPGUI, a graphical user interface for GSAS: Toby, B.H., *J. Appl. Crystallogr.* 34 (2001) 210.
- Fielder, D.A., Albering, J.H., Besenhard, J.O., *J. Solid State Electrochem.* 2 (1998) 413.
- Figgis, B.N., Lewis, J., *Prog. Inorg. Chem.*, Eds. Cotton FA 6 (1964) 37.
- Filar, K.P., Gajda, G.P., Nizhankovskii, V.I., *Phys. Status Solidi B* 253(3) (2016) 473.
- Fleet, M.E., *Mineral. Mag.* 40 (1976) 531.
- Forster, K., Greenblatt, M., Pifer, J., *J. Solid State Chem.* 30 (1979) 121.
- Gasperin, M., Saine, M.C., Kahn, A., Laville, F., Lejus, A.M., *J. Solid State Chem.* 54(1) (1984) 61.
- Geiger, C.A., Kleppa, O.J., Mysen, B.O., Laitimer, J.M., Grossman, L., *Geochim. Cosmo. Acta*, 52 (1988) 1729.
- Giannini, M., Ballaran, T.B., Langenhorst, F., *Am. Mineral.* 99 (2014) 2060.
- Giannini, M., Ballaran, T.B., Langenhorst, F., Bischoff, A., *Meteoritics & Planetary Sci.* 46 (2011) A77.
- Girolami, G.S., *X-ray crystallography*, Univ. Science Books, 2015, pp. 1-502.
- Goodenough, J.B., Park, K.-S., *J. Am. Chem. Soc.* 135 (2015) 1167.
- Gospodinov, M., Doshkova, D., *Mat. Res. Bull.* 29(6) (1994) 681.
- Gourier, D., Laville, F., Vivien, D., *J. Solid State Chem.* 61 (1986) 67.
- Grabmaier, B.C., Oberschmid, R., *Phys. Stat. Sol. (a)* 96 (1986) 199.
- Graetsch, H., Gerbert, W., *Z. Kristallogr.* 211(1) (1996) 25.
- Greenwood, N.N., *Ionic crystals, lattice defects, and non-stoichiometry* Butterworths, London, 1968
- Grey, I.E., Madsen, I.C., Haggerty, S.E., *Am. Mineral.* 72 (1987) 633.
- Grisafe, D.A., Hummel, F.A., *J. Solid State Chem. Part B. Color* 2 (1970) 167.
- Guifang, J., Hu, Y., Li, C. et al., *Mater. Res. Bull.* 48 (2013) 2598.
- Guillemin, C., Prouvist, J., Wintenberger, M., *Bull. Soc. Franc. Miner. Crist. LXXVIII* (1955) 301 (in French).
- Haberey, F., Leckebusch, R., Rosenberg, M., Sahl, K., *J. Cryst. Growth* 61 (1983) 284.
- Hainschwang, T., Notari, F., Massi, L., Armbruster, T., Rondeau, B., Fritsch, E., Nagashima, M., *Gems Gemol.* 46(2) (2010) 135.

- Hajjaji, W., Costa, G., Zanelli, C., Ribeiro, M.J., Seabra, M.P., Dondi, M., Labrincha, J.A., J. Eur. Ceram. Soc. 32(4) (2012) 753.
- Hajjaji, W., Seabra, M.P., Labrincha, J.A., Dyes Pigm. 83 (2009) 385.
- Han, J., Brearley, A.J., Keller, L.P., Meteorit. Planet Sci. 50(12) (2015) 2121.
- Harder, M., Muller-Buschbaum, H., Z. Naturforsch B Chem. Sci. 32(7) (1977) 833 (in German).
- Harindranath, K., Viswanath, K.A., Chandranb, C.V., Bräuniger, T., Madhuc, P.K., Ajithkumar, T.G., Joy, P.A., Solid State Commun. 150 (2010) 262.
- Hata, M., Marumo, F., Iwai, S., Aoki, H., Acta Crystallogr. Sect. B 35 (1979) 2382.
- Herren, M., Gudel, H.U., Chem. Phys. Lett. 183 (2001) 98.
- Hibonite: Hibonite Mineral Information and Data. Hudson Institute of Mineralogy.
- Hippel, A.R.V., Dielectric materials and applications, Artech House, MA, 1995, pp. 1-456.
- Hoffe, V.R., Serafin, M., Z. Anorg. Allg. Chem. 436 (1977) 95 (in German).
- Holtsman, D., Phys. Chem. Miner. 23(7) (1996) 452.
- Hormillosa, C., Healy, S., Stephen, T., Brown, I.D., Bond Valence Calculator, Version 2.0 (1993) <http://www.ccp14.ac.uk> (accessed 09/09/2016).
- Hou, D., Hu, X., Wen, Y. et al., Phys. Chem. Chem. Phys. 15 (2013) 20698.
- Housecroft, C.E., Sharpe, A.G., Inorganic chemistry (4<sup>th</sup> edition), Pearson, 2012, pp. 1-1256.
- <http://colory.ru/colorhistory/> (accessed 12.02.2016).
- <http://en.wikipedia.org/wiki/Turquoise> (accessed 09/12/2016).
- <http://slideplayer.com/slide/5888177/> (accessed 12.02.2016).
- [http://tqmsystems.nl/uploads/Understand\\_Color\\_en.pdf](http://tqmsystems.nl/uploads/Understand_Color_en.pdf) (accessed 12.04.2016).
- <http://web.mit.edu/course/6/6.732/www/opt.pdf> (accessed 12.03.2016).
- <http://webmineral.com/data/Sillenite.shtml#.WEcAoLlrK70> (accessed 12/19/2016).
- <http://www.agta.org/gemstones/variation-ruby.html> (accessed 12.02.2016).
- [http://www.minsocam.org/MSA/K12/K\\_12.html/MSA/collectors\\_corner/arc/color.htm](http://www.minsocam.org/MSA/K12/K_12.html/MSA/collectors_corner/arc/color.htm) (accessed 12.02.2016).
- <http://www.piketech.com/files/pdfs/DiffuseAN611.pdf> (accessed 12.04.2016).
- <http://www.slideshare.net/solohermelin/color-theory-39956038> (accessed 12.02.2016).
- [http://www.uio.no/studier/emner/matnat/kjemi/KJM3100/v06/undervisningsmateriale/optical1\\_lect21\\_pw.pdf](http://www.uio.no/studier/emner/matnat/kjemi/KJM3100/v06/undervisningsmateriale/optical1_lect21_pw.pdf) (accessed 12.02.2016).
- <http://www.webexhibits.org/causesofcolor/8.html> (accessed 12.02.2016).
- <http://www.webexhibits.org/causesofcolor/9.html> (accessed 12.03.2016).
- <https://bitcointalk.org/index.php?topic=1333253.0> (accessed 12.02.2016).
- [https://en.wikipedia.org/wiki/Ceramic#By\\_usage](https://en.wikipedia.org/wiki/Ceramic#By_usage) (accessed 12.01.2016).
- [https://en.wikipedia.org/wiki/Cobalt\\_blue](https://en.wikipedia.org/wiki/Cobalt_blue) (accessed 01/04/2017).
- <https://en.wikipedia.org/wiki/Dielectric> (accessed 12.04.2016).
- <https://en.wikipedia.org/wiki/Emerald> (accessed 01/04/2017).
- <https://en.wikipedia.org/wiki/File:Sapphire.png> (accessed 12.02.2016).
- [https://en.wikipedia.org/wiki/Lab\\_color\\_space](https://en.wikipedia.org/wiki/Lab_color_space) (accessed 12.04.2016).
- [https://en.wikipedia.org/wiki/List\\_of\\_inorganic\\_pigments](https://en.wikipedia.org/wiki/List_of_inorganic_pigments) (accessed 12.03.2016).
- [https://en.wikipedia.org/wiki/List\\_of\\_inorganic\\_pigments#Red\\_pigments](https://en.wikipedia.org/wiki/List_of_inorganic_pigments#Red_pigments) (accessed 12.15.2016).
- <https://en.wikipedia.org/wiki/Pigment> (accessed 12.03.2016).

- <https://en.wikipedia.org/wiki/Sill%C3%A9nite> (accessed 12/19/2016).
- <https://www.britannica.com/science/oxide> (accessed 12.01.2016).
- <https://www.pinterest.com/pin/184999497165632389/> (accessed 12.04.2016).
- Hyde, B.G., Andersson, S., Inorganic crystal structures, John Wiley & Sons, Inc., New York, 1989, pp. 1-430.
- Ihinger, P.D., Stolper, E., Earth Planet Sci. Lett. 78(1) (1986) 67.
- Ilin, V.G., Rastrene, A.I., Neimark, I.E., Ukr. Khim. Zh. 36(7) (1970) 675.
- Ilinskii, A., Prutskij, T., Silva-Andrade, F. et al., Mod. Phys. Lett. B 15(17-19) (2001) 749.
- Iqbal, M.J., Ashiq, M.N., Gomez, P.H., Munoz, J.M., J. Magn. Magn. Mater. 320 (2008) 881.
- Ishiwata, S., Taguchi, Y., Murakawa, H., Onose, Y., Tokura, Y., Science 319 (2008) 1643.
- Ishiwata, S., Taguchi, Y., Tokunaga, Y., Murakawa, H., Onose, Y., Tokura, Y., Phys Rev B 79 (2009) 180408(R).
- Ivanyuk, E.V., Astrelin, I.M., Suprunchuk, V.I., Russian J. Appl. Chem. 72(9) (1999) 1508.
- Iyi, N., Göbbels, M., J. Solid State Chem. 122 (1996) 46.
- Iyi, N., Inoue, Z., Takekawa, S., Kimura, S., J. Solid State Chem. 54(1) (1984) 70.
- Iyi, N., Takekawa, S., Kimura, S., J. Solid State Chem. 85 (1990) 318.
- Jansen, V.M., Hoppe, R., Z. Anorg. Allg. Chem. 397 (1973) 279 (in German).
- Jeong, B.-J., Joung, M.-R., Kim, J.-S., Nahm, S. et al., J. Am. Ceram. Soc. 96(12) (2013) 3742.
- Jiang, P., Li, J., Ozarowski, A., Sleight, A.W., Subramanian, M.A., Inorg. Chem. 52 (2013) 1349.
- Jiang, P., Li, J., Sleight, A.W., Subramanian, M.A., Inorg. Chem., 50 (2011) 5858.
- Jiles, D., Introduction to magnetism and magnetic materials, CRC Press, USA, 1998, pp. 1-570.
- Jirak, D.Z., Krupka, M., Pollert, E., Cryst. Res. Technol. 22(4) (1987) K71.
- Johnson, P.D., Prener, J.S., Kingsley, J.D., Science 141 (1963) 1179.
- Ju, G., Hu, Y., Chen, L., Wang, X., J. of Photochem. Photobiology A: Chem. 251 (2013) 100.
- Ju, G., Hu, Y., Li, C., Wang, X., J. of Appl. Phys. 3 (2012) 113508.
- Kablukov, V.I., Sukhov, A.V., Kaminskaya, N.A., Fetisov, G.N., Russian Patent No. 2023716 (30 November 1994).
- Kadyrova, Z.R., Sirazhiddinov, N.A., Tuganova, S.K., Inorg. Mater. 33(3) (1997) 300.
- Kahn, A., Lejus, A.M., Madsac, M., Théry, J., Vivien, D., Bernier, J.C., J. Appl. Phys. 52 (1981) 6864.
- Kao, K.C., Dielectric phenomena in solids (1<sup>st</sup> edition), Academic Press, Cambridge, 2004, pp. 1-579.
- Kargin, Y.F., Synthesis, structure, and properties of sillenite-structure bismuth oxide compounds, Doctoral (Chem.) Dissertation, Moscow: Kurnakov Inst. Of General and Inorganic Chemistry, Russ. Acad. Sci., 1998 (in Russian).
- Keil, K., Fuchs, L.H., Earth Planet. Sci. Lett. 12 (1971) 184.
- Kihara, K., Donnay, G., Canad. Miner. 23 (1985) 647654.
- Kim, G., Lee, B.-H., Kor. J. Mater. Res. 24(1) (2014) 43 (in Korean).
- Kim, S.J., Jang, H.S., Unithratti, S., Kim, Y.H., Im, W.B., J. Lumin. 172 (2016) 99.

- Kimura, K., Ohgaki, M., Tanaka, K., Morikawa, H., Marumo, F., J. Solid State Chem. 87 (1990) 186.
- Kimura, T., Goto, T., Shintani, H., Ishizaka, K., Arima, T., Tokura, Y., Nature 426 (2003) 55.
- Kimura, T., Lawes, G., Ramirez, A.P., Phys. Rev. Lett. 94 (2005) 137201.
- Kingery, W.D., Introduction to Ceramics, New York: John Wiley & Sons, Inc., 1960, pp. 1-719.
- Kingsley, J.D., Prener, J.S., Segall, B., APS 137 (1965) 189.
- Kirik, S.D., Kutvitskii, V.A., Koryagina, T.I., Zh. Struktur. Khim. 26(4) (1985) 90 (in Russian).
- Kitagawa, Y., Hiraoka, Y., Honda, T., Ishikura, T., Nakamura, H., Kimura, T., Nat. Mater. 9 (2010) 797.
- Knyazev, A.V., Bulanov, E.N., Korshunov, A.O., Krashenninnikova, O.V., Inorg. Mater. 49(11) (2013) 1133.
- Knyazev, A.V., Bulanov, E.N., Lapshin, A.N., Vestnik of Lobachevsky State University of Nizhni Novgorod 3 (2012) 87 (in Russian).
- Knyazev, A.V., Chernorukov, N.G., Bulanov, E.N., Materials Chem. and Phys. 132 (2012) 773.
- Knyazev, A.V., Chernorukov, N.G., Bulanov, E.N., Vestnik of Lobachevsky State University of Nizhni Novgorod 6 (2010) 82 (in Russian).
- Knyazev, A.V., Maczka, M., Bulanov, E.N., Ptak, M., Belopolskaya, S.S., Dyes and Pigments 91(3) (2011) 286.
- Kohn, J.A., Eckart, D.W., J. Appl. Phys. 35 (1964) 968.
- Kojima, H., Sugimoto, M., Ferromagnetic Materials, Eds. Wolfarth, E.P., North-Holland, Amsterdam 3 (1982) 305.
- Kreber, E., Gonser, U., Trauiwein, A., Harris, F.E., J. Phys. Chem. Solids 36 (1975) 265.
- Kruzhlov, A.V., Gavrilov, F.F., Kordyukov, N.I. et al., Z. Prikladnoj Spectroskopii 21 (1974) 631 (in Russian).
- Kubelka, P., Munk, F.Z., Tech. Phys. 12 (1931) 593.
- Kukushkina, G.N., Demidovskaya, A.N., Irklievskaya, O.T., Mokhort, V.N., Kurlovich, T.I., Stepanova, L.N., Gizun, N.M., U.S.S.R. Patent No. 1273338 (30 November 1986).
- Kukushkina, G.N., Demidovskaya, A.N., Irklievskaya, O.T., Mokhort, V.N., Kurlovich, T.I., Stepanova, L.N., Petrusev, V.L., U.S.S.R. Patent No. 1281534 (7 January 1987).
- Larkin, P., Infrared and Raman spectroscopy; principles and spectral interpretation (1<sup>st</sup> edition), Elsevier, 2011, pp. 1-230.
- Larson, A.C., Von Dreele, R.B., General Structure Analysis System (GSAS), Los Alamos National Laboratory Report LAUR (1994) 86.
- Laufec, F., Romanskala, Haloda, J., Cisarova, I., J. Czech Geol. Soc. 51(3-4) (2006) 271.
- Laville, F., Lejus, A.M., J. Cryst. Growth 63(2) (1983) 426.
- Laville, F., Perrin, M., Lejus, A.M., Gasperin, M., Moncorge, R., Vivien, D., J. Solid State Chem. 65(3) (1986) 301.
- Lee, S., Park, J., Kim, J., Hong, K.-P., Song, Y., Park, J.-G., J. Phys.: Condens. Matter 26 (2014) 1.
- Leite, A., Costa, G., Hajjaji, W. et al., Dyes Pigm. 81 (2009) 211.
- Lejus, A.M., Laville, F., Thery, J., Mater. Res. Bull. 23(6) (1988) 913.

- Leontsev, S.O., Eitel, R.E., *Sci. Tech. Adv. Mater.* 11(4) (2010) 1.
- Levinson, R., Berdahl, P., Akbari, H., *Sol. Energ. Mat. Sol. Cells* 89(4) (2005) 351.
- Li, B., Wang, Q., Zhang, Y., Song, Z., Yang, D., *Int. J. Electrochem. Sci.*, 8 (2013) 5396.
- Li, C., Li, Y., Wang, X., *Materials Chem. and Phys.* 139 (2013) 220.
- Li, J., Medina, E.A., Stalick, J.K., Sleight, A.W., Subramanian, M.A., *Z. Naturforsch. B Chem. Sci.* 71(5) (2016) 475.
- Li, J., Medina, E.A., Stalick, J.K., Sleight, A.W., Subramanian, M.A., *Prog. Solid State Chem.* (2016) 1.
- Li, J., Singh, U.S., Schladt, T.D. et al., *Chem. Mater.* 20 (2008) 6567.
- Li, P., Brik, M.G., Li, L., Han, L. et al., *J. Am. Ceram. Soc.* 99(7) (2016) 2388.
- Li, Y.J., Ma, Y.Y., Ye, S., Hu, G.P., Zhang, Q.Y., *Mater. Res. Bull.* 51 (2014) 1.
- Lines, M.E., *Phys. Rev. B* 15 (1977) 388.
- Luo, H., Rai, B.K., Mishra, S.R., Nguyen, V.V., Liu, J.P., *J. Magn. Magn. Mater.* 324 (2012) 2602.
- Ma, C., *Am. Mineral* 95 (2010) 188.
- Magione, M., Subramanian, M.A., *Appl. Phys. Lett.* 93 (2008) 032902.
- Mamatha, C., Krishnaiah, M., Prakash, C.S., Rewetkar, K.G., *Procedia Mat. Sci.* 5 (2014) 780.
- Mao, H.H., Hillert, M., Selleby, M., Sundman, B., *J. Amer. Cer. Soc.* 89 (2006) 298.
- Marean, C.W., Bar-Matthews, M., Bernatchez, J., Fisher, E. et al., *Nature* 449 (2007) 905.
- Marinova, V., Lin, S.H., Sainov, V., Gospodinov, M., Hsu, K.Y., *J. Opt. A.: Pure Appl. Opt.* 5 (2003) S500.
- Marinova, V., Veleva, M., Petrova, D. et al., *J. Appl. Phys.* 89(5) (2001) 2686.
- Massarotti, V., Capsoni, D., Bini, M., Chiodelli, G., *J. Solid State Chem.* 131 (1997) 94.
- Mateika, D., Laudan, M., *J. Cryst. Growth* 46(1) (1979) 85.
- Mather, G.C., Dussarrat, C., Etourneau, J., West, A.R., *J. Matter. Chem.* 10 (2000) 2219.
- Meier, W.M., Villiger, H., *Z. Kristallogr.* 129 (1969) 411.
- Mel'nikova, T.I., Kuz'micheva, G.M., Rybakov, V.B. et al., *J. Struct. Chem.* 52(3) (2011) 510.
- Merker, V.L., Wondratshek, H., *Z. Anorg. Allg. Chem.* 300 (1959) 41 (in German).
- Mizoguchi, H., Sleight, A.W., Subramanian, M.A., *Inorg. Chem.* 50 (2011) 10.
- Mizushima, K., et al., *Mater. Res. Bull.* 15(6) (1980) 783.
- Muir, S.W., Rachdi, O.D., Subramanian, M.A., *Mater. Res. Bull.* 47(3) (2012) 798.
- Muller, U., *Inorganic Structural Chemistry* (2<sup>nd</sup> edition), John Wiley & Sons, Ltd, 2007, pp. 1-268.
- Murray, A.D., Catlow, C.R.A., *J. Solid State Chem.*, 62 (1986) 290.
- Na, E.H., Lee, J.H., Ahn, S.J., Hong, K.P., Koo, Y.M., Jang, H.M., *J. Magn. Magn. Mater.* 324 (2012) 2866.
- Na, E.H., Song, S., Koo, Y.-M., Jang, H.M., *Acta Mater.* 61 (2013) 7705.
- Nagashima, M., Armbruster, T., Hainschwang, T., *Mineral. Mag.* 74(5) (2010) 871.
- Nakamoto, K., *Mir, Moscow* (1991) 121 (in Russian).
- Nassau, K., *The physics and chemistry of color* (2<sup>nd</sup> edition), Wiley-Interscience, 2001, pp. 1-496.
- Nikolskiy, A.B., Suvorov, A.V., *College Chemistry textbook*, Saint Petersburg: Khimizdat, 2001, pp. 1-512 (in Russian).

- Nistor, S.V., Stefan, M., Goovaerts, E. et al., *J. Magn. Reson.* 259 (2015) 87.
- Nitta, N., Wu, F., Lee, J.T., Yushin, G., *Mater. Today* 18(5) (2015) 252.
- Noginov, M.A., Loutts, G.B., Bonner, C.E. et al., *JOSA B* 17 (2000) 1329.
- Nogueira, A.E., Lima, A.R.F., Longo, E., Leite, E.R., Camargo, E.R., *J. Nanopart. Res.* 16 (2014) 2653.
- Numata, K., Sakaki, C., Yamanaka, S., *Chem. Lett.* 26(8) (1997) 725.
- O'Brien, D.L.J., Preparation of environmentally-friendly inorganic pigments, PhD thesis, Loughborough University, 2005.
- O'Keeffe, M., Eutax; <http://www1.iucr.org/sincris-top/logiciel/prg-eutax.html> (accessed 02/17/2016).
- O'Neill, H.S.C., Dollase, W.A., Rose II, C.R., *Phys. Chem. Minerals* 18 (1991) 302.
- Obradors, X., Collomb, A., Pernet, M., Samaras, D., Joubert, J.C., *J. Solid State Chem.* 56(2) (1985) 171.
- Okube, M., Yoshizaki, J., Toyoda, T., Sasaki, S., *J. Appl. Cryst.* 49 (2016) 1433.
- Okumura, K., Ishikura, T., Soda, M., Asaka, T., Nakamura, H., Wakabayashi, Y., Kimura, T., *Appl. Phys. Lett.* 98 (2011) 212504.
- Orman, H.J., Wiseman, P.J., *Acta Crystallogr. Sect. C: Cryst. Struct. Commun.* 40 (1984) 12.
- Orna, M.V., *J. Chem. Ed.* 5(8) (1987) 478.
- Ounnunkad, S., Phanichphant, S., Winotai, P., Tang, I.-M., *Phys. Stat. Sol. (b)* 244(6) (2007) 2190.
- Ounnunkad, S., Winotai, P., Phanichphant, S., *J. Electroceram.* 16 (2006) 357.
- Paluszkiwicz, C., Slosarczyk, A., Pijocha, D. et al., *J. Mol. Struct.* 976 (1-3) (2010) 301.
- Panchenko, T.V., Karpova, L.M., Duda, V.M., *Phys. Solid State* 42(4) (2000) 689.
- Pasero, M., Kampf, A.R., Ferraris, C., Pekov, I. et al., *Eur. J. Mineral* 22 (2010) 163.
- Pausch, H., Mueller-Buschbaum, H., *Z. Naturforsch B Chem. Sci.* 31(8) (1976) 1148 (in German).
- Pekov, I.V., Britvin, S.N., Zubkova, N.V., Pushcharovsky, D.Y., Pasero, M., *Eur. J. Mineral.* 22(6) (2010) 869.
- Peterson, D.L., Helfferich, F., Blytas, G.C., *J. Phys. Chem. Solids* 26(5) (1965) 835.
- Petricek, V., Dusek, M., Palatinus, L., *Z. Kristallogr. – Cryst. Mater.* 229 (2014) 345.
- Petrova, D., Gospodinov, M., Sveshtarov, P., *Mat. Res. Bull.* 30(10) (1995) 1201.
- Pishch, I.V., Biryukova, K.E., Slepukhova, L.V., U.S.S.R. Patent No. 1065358 (7 January 1984).
- Prakash, C.S., Kulkarni, D.K., *Indian J. Pure Appl. Phys.* 32 (1994) 361.
- Radaev, S.F., Simonov, V.I., *Kristallografiya*, 37(4) (1992) 914.
- Rakotondrazafy, M.A.F., Moine, B., Cuney, M., *Contrib. Mineral. Petrol.* 123 (2) (1996) 190.
- Ramirez, A.P., Subramanian, M.A., Gardel, M. et al., *Solid State Commun.* 115(5) (2000) 217.
- Rao, J.S.R.K., Raju, R.D., *J. Indian Geo. Assoc.* 13 (1971) 79.
- Reinen, D., Lachwa, H., Allmann, R., *Z. Anorg. Allg. Chem.* 542 (1986) 71 (in German).
- Riou, A., Lecerf, A., Gerault, Y., Cudennec, Y., *Mat. Res. Bull.* 27 (1992) 269 (in French).
- Robinson, K., Gibbs, G.V., Ribbe, P.H., *Science* 172 (1971) 567.
- Roh, Y.H., Hong, S.T., *Acta Crystallogr.* 61 (2005) i140.

- Rout, S.S., Bischoff, A., *Meteorit. Planet. Sci.* 43(7) (2008) A134.
- Rozova, M.G., Shpanchenko, R.V., *Elements of structural inorganic chemistry* (textbook), Moscow State University: Moscow, 2001 (in Russian).
- Saber, D., Lejus, A.M., *Mater. Res. Bull.* 16(10) (1981) 1325.
- Sakoske, G.E., Sarver, J.E., Novotny, M., Bismuth manganese oxide pigments, US Patent, WO 2000037362 A1, 2000.
- Sandiumenge, F., Gali, S., Rodriguez, J., *Mat. Res. Bull.* 23 (1988) 685.
- Sanna, S., Schmidt, W.G., *IEEE Trans. Ultra. Ferroelec. Freq. Cont.* 59 (2012) 1925.
- Sato, M., Tanaka, T., Ohta, M., *J. Electrochem. Soc.* 141 (1994) 1851.
- Sawaguchi, E., Maniwa, H., Hoshino, S., *Phys. Rev.* 83 (1951) 1078.
- Sawaguchi, E., Shirane, G., Takagi, Y., *J. Phys. Soc. Jpn.* 6 (1951) 333.
- Schanda, J., *Colorimetry: Understanding the CIE system*, 1<sup>st</sup> ed., Wiley-Interscience, 2007.
- Schrader, B. (Ed.), *Infrared and Raman spectroscopy: methods and applications*, VCH, Weinheim, Germany, 1995, pp. 1-765.
- Schulman, J.H., Compton, W.D., *Color centers in solids*, Oxford: Pergamon Press, 1962, pp. 1-368.
- Schwanitz, S.U., Buschbaum, H.M., *Monatsh. Chem.* 113 (1982) 1079 (in German).
- Scott, M.A., Henerson, B., Gallaghen, H.G., Han, T.P.J., *J. Phys. Condens. Matter* 9 (1997) 9893.
- Scott, R.A., Lukehart, C.M. (Ed.), *Application of physical methods to inorganic and bioinorganic chemistry*, John Wiley & Sons, Ltd., UK, 2007, pp. 1-385.
- Sekhar, H., Rao, D.N., *J. Mater. Sci.: Mater. Electron.* 24 (2013) 1569.
- Senulienė, D., Babonas, G., Sileika, A. et al., *Litovskii Fizicheskii Sbornik, Akademiia nauk Litovskoi SSR*, 27(1) (1987) 71 (in Russian).
- Sereda, B.P., Soloshenko, A.A., Popov, B.A., Sekirazh, V.M., Churkin, V.I., Pakhomov, B.A., *Trudy Ural'skogo Nauchno-Issledovatel'skogo Khimicheskogo Instituta* 27 (1973) 190 (in Russian).
- Shamonina, E., Kamenov, V.P., Ringhofer, K.H. et al., *Opt. Commun.* 146 (1998) 62.
- Shang, M., Geng, D., Yang, D., Kang, X., Zhang, Y., Lin, J., *Inorg. Chem.* 52 (2013) 3102.
- Shannon, R.D., *Acta Crystallogr. Sect. A* 32 (1976) 751.
- Shcherbov, D.P., Plotnikova, R.N., *Zavod. Lab.* 42(12) (1976) 1429.
- Shen, C., Zhang, H., Zhang, Y. et al., *Crystals* 4 (2014) 141.
- Sherif, M.E., Bayoumi, O.A., Sokkar, T.Z.N., *Color Res. Appl.* 22(1) (1997) 32.
- Shevell, S.K., *The science of color* (2<sup>nd</sup> edition), Elsevier Science, 2003, pp. 1-350.
- Sillen, L.G., *Ark. Kemi, Mineral. Geol.* 12A (1937) 1.
- Simon, S.B., Davis, A.M., Grossman, L., *Meteorit. Planet. Sci.* 36(3) (2001) 331.
- Simon, S.B., Grossman, L., Hutcheon, I.D., Phinney, D.L., Weber, P.K., Fallon, S.J., *Am. Mineral.* 91(10) (2006) 1675.
- Skorikov, V.M., *Chemistry of Piezoelectric Compounds*, Extended Abstract of Doctoral (Chem.) Dissertation, Moscow: Kurnakov Inst. Of General and Inorganic Chemistry, USSR Acad. Sci., 1985 (in Russian).
- Skorikov, V.M., Kargin, Y.F., Egorysheva, A.V., *Inorg. Mater.* 41(1) (2005) S24.
- Slagtern, A., Fjellvaag, H., *Eur. J. Solid State Inorg. Chem.* 33(11) (1996) 1241.
- Sleight, A.W., *Prog. Solid State Chem.* 37 (2009) 251.



- Smith, A.E., Mizoguchi, H., Delaney, K., Spaldin, N.A., Sleight, A.W., Subramanian, M.A., *J. Am. Chem. Soc.* 131 (2009) 17084.
- Smith, A.E., Sleight, A.W., Subramanian, M.A., *Mater. Res. Bull.* 46 (2011) 1.
- Sorensen, O.T. (Ed.), *Non-stoichiometric oxides*, New York: Academic Press, Incorporated, 1981, pp. 1-60.
- Strobel, P., Lambert-Andron, B., *J. Solid State Chem.*, 75 (1988) 90.
- Subramanian, M.A., *Dielectrics lecture slides*, 2014.
- Subramanian, M.A., Li, J., Sleight, A.W., UC Patent WO2015131036, A120150903, 2015.
- Subramanian, M.A., *Magnetic properties lecture slides*, 2014.
- Subramanian, M.A., Shannon, R.D., *Mat. Res. Bull.* 24 (1989) 1477.
- Suchow, L., *J. Electrochem. Soc.* 108 (1961) 847.
- Sudarsanan, K., Young, R.A., *Acta Crystallogr., Sect. B: Struct. Sci.* 36 (1980) 1525.
- Takahashi, T., Adachi, S., *Electrochem. Solid State Lett.* 12(8) (2009) J69.
- Tamilarasan, S., Laha, S., Natarajan, S., Gopalakrishnan, J., *J. Mater. Chem. C* 3 (2015) 4794.
- Tan, G.-L., Wang, M., *J. Electrocer.* 26 (2011) 170.
- Tebble, R.S., Craik, D.J., *Magnetic materials*, John Wiley & Sons, Inc., New York, 1969.
- Thuery, P., Laville, F., Tronc, E., Lejus, A.M., Vivien, D., *Rev. Chim. Mineral.* 22(2) (1985) 216.
- Tilley, R.J.D., *Understanding solids: the science of materials* (2<sup>nd</sup> edition), John Wiley & Sons, Ltd, 2004, pp. 1-616.
- Toby, B.H., EXPGUI: a graphical user interface for GSAS, *J. Appl. Crystallogr.* 34 (2001) 210.
- Tokunaga, Y., Kaneko, Y., Okuyama, D., Ishiwata, S., Arima, T., Wakimoto, S., Kakurai, K., Taguchi, Y., Tokura, Y., *Phys. Rev. Lett.* 105 (2010) 257201.
- Tokura, Y., *Curr. Opin. Solid State Mater. Sci.* 3 (1998) 175.
- Townes, W.D., Fang, J.H., Perrotta, A.J., *Z. Kristallogr.* 125 (1967) 437.
- Tro, N.J., *Chemistry: a molecular approach* (3<sup>rd</sup> edition), Prentice Hall, 2013, pp. 1- 1081.
- Tronc, E., Laville, F., Gasperin, M., Lejus, A.M., Vivien, D., *J. Solid State Chem.* 81(2) (1989) 192.
- Ulianov, A., Kalt, A., Pettke, T., *Eur. J. Mineral.* 17 (2005) 357.
- Utsumi, S., Yoshida, D., Momozawa, N., *J. Phys. Soc. Jpn.* 76 (2007) 034704.
- Utsunomiya, A., Tanaka, K., Morikawa, H., Marumo, F., Kojima, H., *J. Solid State Chem.* 75 (1988) 197.
- Verstegen, J.M.P.J., Sommerdijk, J.L., Verriet, J.G., *J. Lumin.* 6(5) (1973) 425.
- Vinnik, D.A., Zharebtsov, D.A., Mashkovtseva, L.S. et al., *J. Alloys Compd.* 615 (2014) 1043.
- Vivien, D., Lejus, A.M., Thery, J., Collongues, R., Aubert, J.J. et al., *C. R. Acad. Sci. Paris (II)* 298(6) (1984) 195.
- Volkov, V.V., Egorysheva, A.V., Kargin, Y.F., Skorikov, V.M., *Inorg. Mater.* 29(11) (1993) 1364.
- Wagner, T.R., *J. Solid State Chem.* 136(1) (1998) 120.
- Wagner, T.R., O'Keeffe, M., *J. Solid State Chem.* 73(1) (1988) 211.

- Wang, F.X., Xiao, S.Y., Chang, Z., Li, M.X., Wu, Y.P., Holze, R., *Int. J. Electrochem. Sci.* 9 (2014) 6182.
- Wang, L., Wang, D., Cao, Q., Zheng, Y., Xuan, H., Gao, J., Du, Y., *Sci. Rep.* 2 (2012) 223.
- Wardzynski, W., Szymczak, H., Borowicz, M.T., Pataj, K., *J. Phys. Chem. Solids* 46(10) (1985) 1117.
- Wardzynski, W., Szymczak, H., *J. Phys. Chem. Solids* 45(8/9) (1984) 887.
- Wardzynski, W., Szymczak, H., Pataj, K., *J. Phys. Chem. Solids* 43(8) (1982) 767.
- Weller, M.T., *Inorganic Materials Chemistry*, Oxford university press, 1994, pp. 1-88.
- West, A.R., *Solid state chemistry and its applications* (2<sup>nd</sup> edition), Willey & Sons, Ltd, 2014, pp. 1-556.
- White, T.J., Dong, Z.L., *Acta Crystallogr. Sect. B* 59 (2003) 1.
- Wiehl, L., Friedrich, A., Haussuehl, E. et al., *J. Phys. Condensed Matter.* 22 (2010) 1.
- Wu, P., Zeng, Y.Z., Wang, C.M., *Biomaterials* 25 (2004) 1123.
- [www.mindat.org](http://www.mindat.org) (accessed 11/01/2016).
- Xia, Z., Liang, Y., Huang, W. et al., *J. Mater. Sci. Mater. Electron.* 24 (2013) 5111.
- Xiao-Long, J., *J. of Luminescence* 4 (2014) 409 (in Chinese).
- Xu, Y., Mackenzie, J.D., *J. Non-Crys. Solids* 246 (1999) 136.
- Yabuuchi, N., Ohzuku, T., *J. Power Sources* 119 (2003) 171.
- Yan, P., Xiao, L., Zheng, J. et al., *Chem. Mater.* 27 (2015) 975.
- Yoo, H.S., Vaidyanathan, S., Kim, S.W., Jeon, D.Y., *Opt. Mater.* 31 (2009) 1555.
- Yu, H., Zhou, H., *J. Phys. Chem. Lett.* 4 (2013) 1268.
- Yue, S.J., Cui, D.P., Xue, B. et al., *Mechanics and Materials* 401 (2013) 796.
- Zyryanov, V.V., *Zh. Struktur. Khim.* 45 (2004) 480 (in Russian).